

UNIVERSITY OF OKLAHOMA
GRADUATE COLLEGE

COMPUTATIONAL ELECTROMAGNETICS APPLIED TO SCATTERING
OBSERVED BY POLARIMETRIC WEATHER RADAR

A DISSERTATION
SUBMITTED TO THE GRADUATE FACULTY
in partial fulfillment of the requirements for the
Degree of
DOCTOR OF PHILOSOPHY

By
DJORDJE MIRKOVIĆ
Norman, Oklahoma
2015

COMPUTATIONAL ELECTROMAGNETICS APPLIED TO SCATTERING
OBSERVED BY POLARIMETRIC WEATHER RADAR

A DISSERTATION APPROVED FOR THE
SCHOOL OF ELECTRICAL AND COMPUTER ENGINEERING

BY

Dr. Dušan Zrnčić, Co-chair

Dr. Yan Zhang, Co-Chair

Dr. Richard Doviak

Dr. Phillip Chilson

Dr. Hjalti Sigmarsson

Dr. Jeffrey Kelly

© Copyright by DJORDJE MIRKOVIĆ 2015
All Rights Reserved.

DEDICATION

Мојим родитељима и породици у знак захвалности за љубав и истрајност у стварању мене као човека.

To my parents and family in appreciation for the love and devotion in making me the man I am today.

ACKNOWLEDGEMENTS

The dissertation in front of you represents the confluence of energy which was gifted to me. For that I am endlessly grateful to my family, doctoral committee members and numerous friends and colleagues at NSSL.

To my doctoral committee, namely Dr. Dušan Zrnić, Dr. Yan (Rockee) Zhang, Dr. Richard (Dick) Doviak, Dr. Phillip (Phil) Chilson, Dr. Hjalti (H) Sigmarsson, Dr. Jeffrey (Jeff) Kelly, I owe great appreciation for the “trouble” they dealt with.

My mentor, Dr. Dušan Zrnić is the man to whom I owe most of my gratitude. Number of hours he has spent teaching me, not just scientific, but life knowledge, cannot be counted. From discussions on Hamlet to thoughts of prota Zrnić, from time spent excersising to hours spent above the book with paper and pen. I am thankfull to God for his mentorship and care. Without him these doctoral studies would not be the same.

Thanks go to my advisor, Dr. Rockee Zhang for making sure that every single detail is properly taken care of. For making my graduate student life less bureaucratically complicated, and above all for the positive attitude toward any issue I have faced during the past 3 years.

Dr. Dick Doviak, the man of endless patience and profound knowledge, dedicated weeks of his life reviewing very first drafts of my dissertation. Even more I thank him for all hours spent in many scientific and academic discussions with me.

I am grateful to Dr. Phil Chilson, who intrigued me with the field of aeroecology. His great personality and huge support helped me achieve goals for which I would

otherwise be misunderstood or declined. Not to mention how all “crazy” ideas were completely plausible to him.

Dr. Hjalti Sigmarsson helped me survive as an atypical European in the Oklahoma scenery. Thank you for so many moments of laughter and valuable discussions which helped me understand the environment better than I would on my own. His meticulous review and valuable comments have improved the manuscript.

Dr. Jeff Kelly stepped in to be a part of my committee and dealt with the paperwork on the short notice. I greatly appreciate all the hustle he had to go through with the EM guy that speaks no biology language and writes in the electrical engineering “slang”. And finally I thank him for the time he took to explain how things work and how I can improve myself.

Besides the committee members infinite appreciation I owe to my friend Dr. Valery Melnikov for the professional and every other help in past years. I was lucky to meet someone like him and get the chance to share my thoughts and ideas. To Dr. Alexander Ryzhkov I am grateful for numberless times we spent talking about various topics in philosophy, research, and life.

I wish to thank Dr. Terry Schuur, Mr. Jacob Carlin, for the “trouble” of having me as a colleague and for the hours of work they have spent reviewing my writings.

Ms. Masha Elaković and Biljana Vukotić are acknowledged for the devotion and hospitality I have always received whenever lucky enough to be around them.

I thank Mr. Hoyt Burcham for the help in software development and debugging and I appreciate support of the Radar Research and Development Division managers: Mike Jain, Douglas Forsyth, and Kurt Hondl, as well as our secretary Ms. Tonia Rollins.

To my friend, and soon to be Dr. Petar Bukovčić, I am indebted because the time on this endeavor would not be even closely enjoyable if I have not had him to jump in and help whenever needed.

Dr. Radivoje Biljić, Dr. Antonije Djordjević and Dr. Branko Kolundžija provided advices and spent time teaching me how to understand the electrical engineering instead of just learning it. Their influence on my academic journey finally brought me to where I am today.

Finally, I thank my whole family on both sides of the Atlantic Ocean. To my mum and dad, to my aunty Goga, and to my US parents Renu and Brett, to my brother Derek, to my only grandparents left Kamala and Dr. Raj Chhikara and all others which may not be with us anymore that left traces and invested their time and efforts in making me a person I am today.

It is impossible to express how thankful I am to all of you.

Хвала Вам!

TABLE OF CONTENTS

Acknowledgements	iv
Table of Contents	vii
List of tables	xi
List of Figures.....	xii
Abstract.....	xxv
1. Introduction	1
1.1 History of the weather radar	7
1.2 Structure of the Dissertation	14
2. Electromagnetic scattering	16
2.1 Approximate techniques for calculation of scattering elements	21
2.1.1 Rayleigh Approximation	23
2.1.2 Geometrical Optics.....	25
2.1.3 Physical Optics	27
2.1.4 T-Matrix	28
2.1.5 Discrete Dipole Approximation	30
2.2 Exact techniques for calculation of scattering elements (Computational electromagnetics tools).....	32
2.2.1 Tools based on differential form solution	33
2.2.2 Tools based on integral form solution	37

2.3	Dual polarization (polarimetric) scattering.....	39
2.3.1	Geometry of polarimetric scattering.....	40
2.4	The backscattered covariance matrix.....	42
2.5	Meteorological polarimetric variables from the backscattered covariance matrix.....	44
3.	Modeling of meteorological scattering.....	48
3.1	Importance of modeling of hydrometeor scattering	50
3.2	Current modeling procedures.....	52
3.2.1	Precipitation modeling.....	53
3.2.2	Scatterer modeling (Modeling of scattering matrix elements)	54
3.2.3	Calculation of polarimetric variables	58
3.3	Evaluation of the modeling approach	62
3.3.1	Backscattering rule and its applicability.....	65
4.	Realistic modeling of hydrometeor scatterers	72
4.1	Computational electromagnetic modeling of realistic hydrometeor scatterers using exact modeling techniques.....	76
4.1.1	Modeling of scatterers using WIPL-D software.....	80
4.1.2	Modeling of physical hydrometeors using the WIPL-D software.....	83
4.1.3	WIPL-D coordinate system and hydrometeor based coordinate system..	88
4.2	Evaluation of the scattering results obtained using WIPL-D	97

4.2.1	Spherical models	98
4.2.2	Spheroidal models	99
4.2.3	Modeling of realistic ice spheroids having high axis ratio.....	108
5.	Polarimetric variable simulator	112
5.1	Technical description.....	112
5.1.1	Simulator input	115
5.1.2	Hydrometeor scattering library.....	119
5.1.3	Simulation process.....	120
5.1.4	Calculation of the polarimetric variables	122
5.1.5	Simulation output	125
5.2	Polarimetric Variable Simulator Results	127
5.2.1	Effect of roughness on the co-polar correlation coefficient and backscatter differential phase	128
5.2.2	Differential reflectivity and linear depolarization ratio in large hail.....	132
5.2.3	Circular depolarization ratio in hail.....	139
5.2.4	Polarimetric variables from WSR-88D network	142
5.3	Conclusions.....	145
6.	Biological scatterers	148
6.1	Modeling of the Brazilian free-tailed bat (<i>Tadarida brasiliensis</i>) using WIPL-D software	149

6.2	Laboratory measurements of the Brazilian free-tailed bat RCS with polarimetric calibration	152
6.3	Comparison of the modeled and measured results (evaluation of the modeling approach)	157
6.4	Biota observations using polarimetric weather radars	163
6.5	Conclusions.....	168
7.	Conclusion and future work	169
	References	174
	Appendix A: List of notations	181
	Appendix B: Polarimetric Variables calculated using the PVS	183
	Polarimetric variables calculated using the PVS.....	183
	Radar reflectivity factor.....	183
	Differential reflectivity.....	189
	Co-polar correlation coefficient	199
	Backscatter differential phase.....	209
	Linear Depolarization Ratio	220
	Circular Depolarization Ratio.....	230

LIST OF TABLES

Table 6.1 - Measured values of the co-polar and cross-polar scattering coefficients $ s_{XY} _{meas}^2$ for the calibration sphere	157
Table 6.2 - NOXP radar parameters	165

LIST OF FIGURES

Figure 2.1 - Lorenz - Mie solution for a cross section of an impenetrable (PEC) sphere, created using WIPL-D CEM tool.....	22
Figure 2.2 – Polarimetric scattering elements; f_a is the scattering matrix element for polarization parallel to the hydrometeor’s symmetry axis and f_b is the scattering element for polarization perpendicular to the symmetry axis.	24
Figure 2.3 - Coordinate system centered on a scatterer.....	41
Figure 3.1 - Accuracy evaluation of the backscattering rule. Exact values of s_{hh} for a raindrop are depicted with a solid curve. Approximation values using the backscattering rule (Angular Moments) are depicted with dashed lines.....	66
Figure 3.2 - Accuracy evaluation of the backscattering rule. Exact values of s_{hh} for a “dry” hailstone are depicted with a solid curve. Approximation values using the backscattering rule (Angular Moments) are depicted with dashed lines.....	67
Figure 3.3 - Accuracy evaluation of the backscattering rule. Exact values of s_{hh} for a “wet” hailstone are depicted with a solid curve. Approximation vales using the backscattering rule (Angular Moments) are depicted with dashed lines.....	68
Figure 3.4 – Maximal error or $\text{Re}(s_{hh})$ and $\text{Im}(s_{hh})$ for "dry" hailstone having the axis ratio of 0.7. Exact values are depicted with a solid curve. Approximation values using the backscattering rule (Angular Moments) are depicted with dashed lines.....	70
Figure 4.1 - Hailstones collected after a hailstorm in Bonn, Germany (July, 5 th , 2015).74	74
Figure 4.2 - Models of physical hydrometeors illustrating implementation of the same number of bilinear surfaces in modeling of smooth and rough surfaces.....	81
Figure 4.3 – Simple spheroidal two layer model having the inner core dielectric permittivity ϵ_1 (red) and outer shell dielectric permittivity ϵ_2 (blue).....	84
Figure 4.4 - Single layer spheroidal hailstone models with axes ratios of 0.6, 0.7 and 0.8.	85

Figure 4.5 - Dual layer spheroidal hailstone models with axes ratios of 0.6, 0.7 and 0.8.	85
Figure 4.6 - Single layer spheroidal hailstone models with axes ratios of 0.05, 0.1, 10 and 20.	85
Figure 4.7 - Physical models of rough hydrometeors having uniform random distribution of protuberances 2%, 6%, 10%, 14% of radius (first row) and modified random distribution of protuberances (second row).....	87
Figure 4.8 - Dual-layer hydrometeor model illustrating implementation of the Rasmussen formulation for the maximum water coating for a specific hailstone size. The water coating (transparent) is modeled to follow the surface topology of the hailstone ice core (yellow).....	88
Figure 4.9 – Spheroidal hydrometeor model with incident E_φ (red) and E_θ (blue fields, hydrometeor horizontal cardinal plane (red plane) and symmetry axis (purple/red); a) co-aligned WIPL and hydrometeor coordinate system with azimuth and elevation angles defined; b) rotated hydrometeor’s coordinate system around the y axis of the WIPL coordinate system with azimuth angles defined and WIPL elevation angle defining the rotation angle; c) rotation of the incident fields, original fields (dashed) rotated fields (solid); d) changing the incident field direction for set of WIPL azimuth and elevations angles causes same viewing angle as in the case of model rotation.....	90
Figure 4.10 - WIPL-D and polarimetric coordinate system angles where the xOy is the plane of polarization, directions of propagation (green line), spheroidal hydrometeor’s axis of symmetry (red line) and projection of the axis of symmetry to the plane of polarization (solid yellow line).....	93
Figure 4.11 - Relation of the scattering elements for opposite directions.....	95
Figure 4.12 – Magnitudes of the real and imaginary parts of s_{hh} obtained using WIPL-D, and T-Matrix. The scatterers are ice spheres with dielectric permittivity $\epsilon_r=3.16-j0.02$	99
Figure 4.13 - Comparison of T-Matrix and WIPL-D results for raindrop of equivolume diameter range (1 mm to 8 mm). Real and imaginary parts of s_{hh} are plotted.....	101
Figure 4.14 - Comparison of T-Matrix and WIPL-D results for raindrop of equivolume diameter range (1 mm to 8 mm). Real and imaginary parts of s_{vv} are plotted.....	102

Figure 4.15 - Comparison of T-Matrix and WIPL-D scattering element results for 10 mm equivolume water ($\epsilon_r=78.2-j12.1$) spheroid with a vertical axis of symmetry and variable axis ratio changing from oblate to very prolate spheroids for co-polar scattering of horizontally oriented E field.....	103
Figure 4.16 -Comparison of T-Matrix and WIPL-D scattering element results for 10 mm equivolume water ($\epsilon_r=78.2-j12.1$) spheroid with a vertical axis of symmetry and variable axis ratio changing from oblate to very prolate spheroids for co-polar scattering of vertically oriented E field.....	104
Figure 4.17 - Comparison of T-Matrix and WIPL-D scattering element results for 3 mm equivolume ice ($\epsilon_r=3.17-j9.6$) spheroid with a vertical axis of symmetry and variable axis ratio changing from extremely oblate to very prolate spheroids for co-polar scattering of horizontally oriented E field.....	106
Figure 4.18 - Comparison of T-Matrix and WIPL-D scattering element results for 3 mm equivolume ice ($\epsilon_r=3.17-j9.6$) spheroid with a vertical axis of symmetry and variable axis ratio changing from extremely oblate to very prolate spheroids for co-polar scattering of vertically oriented E field.....	107
Figure 4.19 - Comparison of WIPL-D and Rayleigh approximation scattering element results for 0.1 mm equivolume ice ($\epsilon_r=3.17-j9.6$) spheroid with a vertical axis of symmetry and variable axis ratio changing from spherical to extremely prolate spheroids for co-polar scattering of horizontally oriented E field.....	109
Figure 4.20 - Comparison of WIPL-D and Rayleigh approximation scattering element results for 0.1 mm equivolume ice ($\epsilon_r=3.17-j9.6$) spheroid with a vertical axis of symmetry and variable axis ratio changing from spherical to extremely prolate spheroids for co-polar scattering of vertically oriented E field.....	110
Figure 5.1 - Graphical representation of the simulation algorithm including all transient variables.....	114
Figure 5.2 - Format of the polarimetric variable simulator input file.....	115
Figure 5.3 - Illustration of the scattering library name convention.....	119
Figure 5.4 - Structure of the polarimetric variable simulator output file.....	126

Figure 5.5 - Co-polar correlation coefficient (ρ_{HV}) for wet hailstones with axis ratio of 0.6 and M-type roughness of 2% (solid blue), 6% (solid green), 10% (dashed red) and 14% (dot-dashed violet). 129

Figure 5.6 - Co-polar correlation coefficient (ρ_{HV}) for wet hailstones with axis ratio of 0.6 and R-type roughness of 2% (solid blue), 6% (solid green), 10% (dashed red) and 14% (dot-dashed violet). 130

Figure 5.7 - Backscatter differential phase (δ) for wet hailstones with axis ratio of 0.6 and M-type roughness of 2% (solid blue), 6% (solid green), 10% (dashed red) and 14% (dot-dashed violet). 131

Figure 5.8 - Backscatter differential phase (δ) for wet hailstones with axis ratio of 0.6 and R-type roughness of 2% (solid blue), 6% (solid green), 10% (dashed red) and 14% (dot-dashed violet). 132

Figure 5.9 – Vertical cross sections of polarimetric variables in a hailstorm. Top left) is Z in dBZ contours given on the color bar. Top right) is differential reflectivity with a negative pocket clearly visible above the melting layer; values in dB are indicated on the color bar. Bottom left) is the LDR with values in dB. Bottom right) is differential phase in deg. Circled is the hail region. The figure is from (Higgs, et al., 2006) 133

Figure 5.10 - Differential reflectivity (ZDR) for wet hailstones having the 2% M-type roughness and three axis ratios as indicated. 134

Figure 5.11 - Differential reflectivity (ZDR) for dry hailstones having the 2% M-type roughness and three axis ratios as indicated. 136

Figure 5.12 - Normalized radar reflectivity factors to the unit volume and 10^8 factor, for wet hailstones with 0.7 axis ratio and 2% Modified roughness protuberances. Results for 40° canting are plotted as solid curves, and 10° canting plotted as dashed lines. ... 137

Figure 5.13 - Linear depolarization ratio (LDR) for wet hailstones having the 2% M-type roughness and three axis ratios as indicated. 138

Figure 5.14 - Circular depolarization ratio (CDR) for dry hailstones having the 2% M-type roughness and axis ratio of 0.6 (solid blue), 0.7 (solid green), 0.8 (dashed red).. 140

Figure 5.15 - Circular depolarization ratio (CDR) for dry hailstones having the 2% M-type roughness and axis ratio of 0.6 (solid blue), 0.7 (solid green), 0.8 (dashed red). 141

Figure 5.16 - Differential reflectivity (ZDR) for wet hailstones having the 2% M-type roughness and axis ratio of 0.6, for fully polarimetric(AHV) radar (solid blue), and simultaneous transmission (SHV) radar at $\beta_{TX} = 0$ (solid red). 143

Figure 5.17 - Differential reflectivity (ZDR) for wet hailstones having the 2% M-type roughness and axis ratio of 0.6, for fully polarimetric (AHV) radar (solid blue), and simultaneous transmission (SHV) radar at $\beta_{TX} = 0$ (solid red). 144

Figure 6.1 – Model of a bat. a) 3-D view of the topographical surface patch model of the Brazilian free-tailed bat at radar wavelength of 3 cm. b) Detailed view of the model from above including dimensions. c) The full solid-angle vertical-polarization RCS pattern of the bat as a function of incident angle. Values corresponding to two planar cross-sections through the bat have been highlighted for the sake of reference. 150

Figure 6.2 - Laboratory equipment setup for field measurements. a) Suspended Brazilian free-tailed bat. b) Network analyzer with dual transmit and dual receive channels. c) Quad-ridged dual-polarization antennas. 153

Figure 6.3 - Comparison of observed and modeled RCS σ_{VV} values of the bat a) Illustration of the orientation of the bat carcass used for the observations with respect to the antenna position and orientation. b) The bat model is oriented to match orientation of the carcass. A trace of the modelled RCS within the plane of observation is provided for reference. c) Modelled and measured values of the RCS [dBsm,] 158

Figure 6.4 - Polar plots of modeled RCS. Co-polar a) and cross-polar b) RCS [dBsm] for cross-section through the simulated dead Brazilian free-tailed bat depicted in Fig. 6.3b..... 160

Figure 6.5 - Polar plots showing measured RCS. Co-polar a) and cross-polar b) RCS [dBsm] for the cross-section through the dead Brazilian free-tailed bat depicted in Fig. 6.2a (similar to the cross-section shown in Fig. 6.3b). 161

Figure 6.6 - Simulated and observed bat emergence. a) Conceptual representation of an emergence of Brazilian free-tailed bats. b) Values of radar reflectivity [dB η , decibel value of reflectivity relative to a reference value of 1 cm² km⁻³] obtained during a bat emergence from Frio Cave on 10 July 2010 at 0134 UTC (2034 local time). The cave is

denoted by a black dot north-northeast of the radar (origin). c) Values of radial velocity [m s^{-1}] corresponding to the data shown in (b). Red (green) colors indicate motion away from (towards) the radar. d) Values of differential reflectivity [dB] corresponding to the data shown in (b). e) Calculated values of RCS [dBsm] for horizontal (red) and vertical (blue) radar polarizations corresponding to observations made at X-band (3-cm wavelength). f) Calculated values of differential polarimetric RCS [dB] for elevation angle $\theta = -3^\circ$ obtained from the values shown in (b)(red). Z_{DR} values extracted from the measurements (d) over a 2 km range distance (blue). The black circle provides a 0-dB reference..... 164

Figure 6.7 - Picture of NOXP while deployed in Texas to observe Brazilian free-tailed bats..... 165

Figure 6.8 – a) Orientation and decomposition of H fields when crossing the model’s symmetry axis; b) comparison of the DPRCS in SHV and AHV radar operation mode for zero elevation..... 167

Figure 8.1 – Normalized radar reflectivity factor at horizontal polarization (Z_H) for dry hailstones having the axis ratio of 0.7 and M-type roughness of 2% (solid blue), 6% (solid green), 10% (dashed red) and 14% (dot-dashed violet)..... 184

Figure 8.2 - Normalized radar reflectivity factor at horizontal polarization (Z_H) for dry hailstones having the axis ratio of 0.7 and R-type roughness of 2% (solid blue), 6% (solid green), 10% (dashed red) and 14% (dot-dashed violet)..... 185

Figure 8.3 - Normalized radar reflectivity factor at horizontal polarization (Z_H) for dry hailstones having the 2% M-type roughness and axis ratio of 0.6(solid blue), 0.7 (solid green), 0.8 (dashed red)..... 186

Figure 8.4 - Normalized radar reflectivity factor at horizontal polarization (Z_H) for water coated hailstones having the axis ratio of 0.8 and M-type roughness of 2% (solid blue), 6% (solid green), 10% (dashed red) and 14% (dot-dashed violet)..... 187

Figure 8.5 - Normalized radar reflectivity factor at horizontal polarization (Z_H) for water coated hailstones having the axis ratio of 0.8 and R-type roughness of 2% (solid blue), 6% (solid green), 10% (dashed red) and 14% (dot-dashed violet)..... 188

Figure 8.6 - Normalized radar reflectivity factor at horizontal polarization (Z_H) for water coated hailstones having the 2% M-type roughness and axis ratio of 0.6(solid blue), 0.7 (solid green), 0.8 (dashed red)..... 188

Figure 8.7 - Differential reflectivity (ZDR) for dry hailstones with axis ratio of 0.6 and M-type roughness of 2% (solid blue), 6% (solid green), 10% (dashed red) and 14% (dot-dashed violet)..... 190

Figure 8.8 - Differential reflectivity (ZDR) for dry hailstones with axis ratio of 0.6 and R-type roughness of 2% (solid blue), 6% (solid green), 10% (dashed red) and 14% (dot-dashed violet)..... 190

Figure 8.9 - Differential reflectivity (ZDR) for dry hailstones with axis ratio of 0.7 and M-type roughness of 2% (solid blue), 6% (solid green), 10% (dashed red) and 14% (dot-dashed violet)..... 191

Figure 8.10 - Differential reflectivity (ZDR) for dry hailstones with axis ratio of 0.7 and R-type roughness of 2% (solid blue), 6% (solid green), 10% (dashed red) and 14% (dot-dashed violet)..... 192

Figure 8.11 - Differential reflectivity (ZDR) for dry hailstones with axis ratio of 0.8 and M-type roughness of 2% (solid blue), 6% (solid green), 10% (dashed red) and 14% (dot-dashed violet)..... 192

Figure 8.12 - Differential reflectivity (ZDR) for dry hailstones with axis ratio of 0.8 and R-type roughness of 2% (solid blue), 6% (solid green), 10% (dashed red) and 14% (dot-dashed violet)..... 193

Figure 8.13 - Differential reflectivity (ZDR) for dry hailstones having the 2% M-type roughness and axis ratio of 0.6(solid blue), 0.7 (solid green), 0.8 (dashed red). 194

Figure 8.14 - Differential reflectivity (ZDR) for wet hailstones with axis ratio of 0.6 and M-type roughness of 2% (solid blue), 6% (solid green), 10% (dashed red) and 14% (dot-dashed violet)..... 195

Figure 8.15 - Differential reflectivity (ZDR) for wet hailstones with axis ratio of 0.6 and R-type roughness of 2% (solid blue), 6% (solid green), 10% (dashed red) and 14% (dot-dashed violet)..... 196

Figure 8.16 - Differential reflectivity (ZDR) for wet hailstones with axis ratio of 0.7 and M-type roughness of 2% (solid blue), 6% (solid green), 10% (dashed red) and 14% (dot-dashed violet)..... 197

Figure 8.17 - Differential reflectivity (ZDR) for wet hailstones with axis ratio of 0.7 and R-type roughness of 2% (solid blue), 6% (solid green), 10% (dashed red) and 14% (dot-dashed violet).....	197
Figure 8.18 -Differential reflectivity (ZDR) for wet hailstones with axis ratio of 0.8 and M-type roughness of 2% (solid blue), 6% (solid green), 10% (dashed red) and 14% (dot-dashed violet).....	198
Figure 8.19 - Differential reflectivity (ZDR) for wet hailstones with axis ratio of 0.8 and R-type roughness of 2% (solid blue), 6% (solid green), 10% (dashed red) and 14% (dot-dashed violet).....	198
Figure 8.20 - Differential reflectivity (ZDR) for wet hailstones having the 2% M-type roughness and axis ratio of 0.6(solid blue), 0.7 (solid green), 0.8 (dashed red).	199
Figure 8.21 – Co-polar correlation coefficient (ρ_{HV}) for dry hailstones with axis ratio of 0.6 and M-type roughness of 2% (solid blue), 6% (solid green), 10% (dashed red) and 14% (dot-dashed violet).	200
Figure 8.22 – Co-polar correlation coefficient (ρ_{HV}) for dry hailstones with axis ratio of 0.6 and R-type roughness of 2% (solid blue), 6% (solid green), 10% (dashed red) and 14% (dot-dashed violet).	201
Figure 8.23 - Co-polar correlation coefficient (ρ_{HV}) for dry hailstones with axis ratio of 0.7 and M-type roughness of 2% (solid blue), 6% (solid green), 10% (dashed red) and 14% (dot-dashed violet).	202
Figure 8.24 - Co-polar correlation coefficient (ρ_{HV}) for dry hailstones with axis ratio of 0.7 and R-type roughness of 2% (solid blue), 6% (solid green), 10% (dashed red) and 14% (dot-dashed violet).	202
Figure 8.25 - Co-polar correlation coefficient (ρ_{HV}) for dry hailstones with axis ratio of 0.8 and M-type roughness of 2% (solid blue), 6% (solid green), 10% (dashed red) and 14% (dot-dashed violet).	203
Figure 8.26 - Co-polar correlation coefficient (ρ_{HV}) for dry hailstones with axis ratio of 0.8 and R-type roughness of 2% (solid blue), 6% (solid green), 10% (dashed red) and 14% (dot-dashed violet).	203

Figure 8.27 - Co-polar correlation coefficient (ρ_{HV}) for dry hailstones having the 2% M-type roughness and axis ratio of 0.6(solid blue), 0.7 (solid green), 0.8 (dashed red).	204
Figure 8.28 - Co-polar correlation coefficient (ρ_{HV}) for wet hailstones with axis ratio of 0.6 and M-type roughness of 2% (solid blue), 6% (solid green), 10% (dashed red) and 14% (dot-dashed violet).	205
Figure 8.29 - Co-polar correlation coefficient (ρ_{HV}) for wet hailstones with axis ratio of 0.6 and R-type roughness of 2% (solid blue), 6% (solid green), 10% (dashed red) and 14% (dot-dashed violet).	206
Figure 8.30 - Co-polar correlation coefficient (ρ_{HV}) for wet hailstones with axis ratio of 0.7 and M-type roughness of 2% (solid blue), 6% (solid green), 10% (dashed red) and 14% (dot-dashed violet).	206
Figure 8.31 - Co-polar correlation coefficient (ρ_{HV}) for wet hailstones with axis ratio of 0.7 and R-type roughness of 2% (solid blue), 6% (solid green), 10% (dashed red) and 14% (dot-dashed violet).	207
Figure 8.32 – Co-polar correlation coefficient (ρ_{HV}) for wet hailstones with axis ratio of 0.8 and M-type roughness of 2% (solid blue), 6% (solid green), 10% (dashed red) and 14% (dot-dashed violet).	208
Figure 8.33 – Co-polar correlation coefficient (ρ_{HV}) for wet hailstones with axis ratio of 0.8 and R-type roughness of 2% (solid blue), 6% (solid green), 10% (dashed red) and 14% (dot-dashed violet).	208
Figure 8.34 - Co-polar correlation coefficient (ρ_{HV}) for wet hailstones having the 2% M-type roughness and axis ratio of 0.6(solid blue), 0.7 (solid green), 0.8 (dashed red).	209
Figure 8.35 - Backscatter differential phase (δ) for dry hailstones with axis ratio of 0.6 and M-type roughness of 2% (solid blue), 6% (solid green), 10% (dashed red) and 14% (dot-dashed violet)......	210
Figure 8.36 - Backscatter differential phase (δ) for dry hailstones with axis ratio of 0.6 and R-type roughness of 2% (solid blue), 6% (solid green), 10% (dashed red) and 14% (dot-dashed violet)......	211

Figure 8.37 - Backscatter differential phase (δ) for dry hailstones with axis ratio of 0.7 and M-type roughness of 2% (solid blue), 6% (solid green), 10% (dashed red) and 14% (dot-dashed violet)..... 212

Figure 8.38 - Backscatter differential phase (δ) for dry hailstones with axis ratio of 0.7 and R-type roughness of 2% (solid blue), 6% (solid green), 10% (dashed red) and 14% (dot-dashed violet)..... 212

Figure 8.39 - Backscatter differential phase (δ) for dry hailstones with axis ratio of 0.8 and M-type roughness of 2% (solid blue), 6% (solid green), 10% (dashed red) and 14% (dot-dashed violet)..... 213

Figure 8.40 - Backscatter differential phase (δ) for dry hailstones with axis ratio of 0.8 and R-type roughness of 2% (solid blue), 6% (solid green), 10% (dashed red) and 14% (dot-dashed violet)..... 214

Figure 8.41 - Backscatter differential phase (δ) for dry hailstones having the 2% M-type roughness and axis ratio of 0.6 (solid blue), 0.7 (solid green), 0.8 (dashed red). 215

Figure 8.42 - Backscatter differential phase (δ) for wet hailstones with axis ratio of 0.6 and M-type roughness of 2% (solid blue), 6% (solid green), 10% (dashed red) and 14% (dot-dashed violet)..... 216

Figure 8.43 - Backscatter differential phase (δ) for wet hailstones with axis ratio of 0.6 and R-type roughness of 2% (solid blue), 6% (solid green), 10% (dashed red) and 14% (dot-dashed violet)..... 217

Figure 8.44 - Backscatter differential phase (δ) for wet hailstones with axis ratio of 0.7 and M-type roughness of 2% (solid blue), 6% (solid green), 10% (dashed red) and 14% (dot-dashed violet)..... 217

Figure 8.45 - Backscatter differential phase (δ) for wet hailstones with axis ratio of 0.7 and R-type roughness of 2% (solid blue), 6% (solid green), 10% (dashed red) and 14% (dot-dashed violet)..... 218

Figure 8.46 - Backscatter differential phase (δ) for wet hailstones with axis ratio of 0.8 and M-type roughness of 2% (solid blue), 6% (solid green), 10% (dashed red) and 14% (dot-dashed violet)..... 219

Figure 8.47 - Backscatter differential phase (δ) for wet hailstones with axis ratio of 0.8 and R-type roughness of 2% (solid blue), 6% (solid green), 10% (dashed red) and 14% (dot-dashed violet)..... 219

Figure 8.48 - Backscatter differential phase (δ) for wet hailstones having the 2% M-type roughness and axis ratio of 0.6(solid blue), 0.7 (solid green), 0.8 (dashed red). 220

Figure 8.49 - Linear depolarization ratio (LDR) for dry hailstones with axis ratio of 0.6 and M-type roughness of 2% (solid blue), 6% (solid green), 10% (dashed red) and 14% (dot-dashed violet)..... 221

Figure 8.50 - Linear depolarization ratio (LDR) for dry hailstones with axis ratio of 0.6 and R-type roughness of 2% (solid blue), 6% (solid green), 10% (dashed red) and 14% (dot-dashed violet)..... 222

Figure 8.51 - Linear depolarization ratio (LDR) for dry hailstones with axis ratio of 0.7 and M-type roughness of 2% (solid blue), 6% (solid green), 10% (dashed red) and 14% (dot-dashed violet)..... 223

Figure 8.52 - Linear depolarization ratio (LDR) for dry hailstones with axis ratio of 0.7 and R-type roughness of 2% (solid blue), 6% (solid green), 10% (dashed red) and 14% (dot-dashed violet)..... 223

Figure 8.53 - Linear depolarization ratio (LDR) for dry hailstones with axis ratio of 0.8 and M-type roughness of 2% (solid blue), 6% (solid green), 10% (dashed red) and 14% (dot-dashed violet)..... 224

Figure 8.54 - Linear depolarization ratio (LDR) for dry hailstones with axis ratio of 0.8 and R-type roughness of 2% (solid blue), 6% (solid green), 10% (dashed red) and 14% (dot-dashed violet)..... 225

Figure 8.55 - Linear depolarization ratio (LDR) for dry hailstones having the 2% M-type roughness and axis ratio of 0.6 (solid blue), 0.7 (solid green), 0.8 (dashed red). 226

Figure 8.56 - Linear depolarization ratio (LDR) for wet hailstones with axis ratio of 0.6 and M-type roughness of 2% (solid blue), 6% (solid green), 10% (dashed red) and 14% (dot-dashed violet)..... 227

Figure 8.57 - Linear depolarization ratio (LDR) for wet hailstones with axis ratio of 0.6 and R-type roughness of 2% (solid blue), 6% (solid green), 10% (dashed red) and 14% (dot-dashed violet).....	227
Figure 8.58 - Linear depolarization ratio (LDR) for wet hailstones with axis ratio of 0.7 and M-type roughness of 2% (solid blue), 6% (solid green), 10% (dashed red) and 14% (dot-dashed violet).....	228
Figure 8.59 - Linear depolarization ratio (LDR) for wet hailstones with axis ratio of 0.7 and R-type roughness of 2% (solid blue), 6% (solid green), 10% (dashed red) and 14% (dot-dashed violet).....	228
Figure 8.60- Linear depolarization ratio (LDR) for wet hailstones with axis ratio of 0.8 and M-type roughness of 2% (solid blue), 6% (solid green), 10% (dashed red) and 14% (dot-dashed violet).....	229
Figure 8.61 - Linear depolarization ratio (LDR) for wet hailstones with axis ratio of 0.8 and R-type roughness of 2% (solid blue), 6% (solid green), 10% (dashed red) and 14% (dot-dashed violet).....	229
Figure 8.62 - Linear depolarization ratio (LDR) for wet hailstones having the 2% M-type roughness and axis ratio of 0.6(solid blue), 0.7 (solid green), 0.8 (dashed red).	230
Figure 8.63 - Circular depolarization ratio (CDR) for dry hailstones with axis ratio of 0.6 and M-type roughness of 2% (solid blue), 6% (solid green), 10% (dashed red) and 14% (dot-dashed violet).	231
Figure 8.64 - Circular depolarization ratio (CDR) for dry hailstones with axis ratio of 0.6 and R-type roughness of 2% (solid blue), 6% (solid green), 10% (dashed red) and 14% (dot-dashed violet).	232
Figure 8.65 - Circular depolarization ratio (CDR) for dry hailstones with axis ratio of 0.7 and M-type roughness of 2% (solid blue), 6% (solid green), 10% (dashed red) and 14% (dot-dashed violet).	232
Figure 8.66 - Circular depolarization ratio (CDR) for dry hailstones with axis ratio of 0.7 and R-type roughness of 2% (solid blue), 6% (solid green), 10% (dashed red) and 14% (dot-dashed violet).	233

Figure 8.67 - Circular depolarization ratio (CDR) for dry hailstones with axis ratio of 0.8 and M-type roughness of 2% (solid blue), 6% (solid green), 10% (dashed red) and 14% (dot-dashed violet). 234

Figure 8.68 - Circular depolarization ratio (CDR) for dry hailstones with axis ratio of 0.8 and R-type roughness of 2% (solid blue), 6% (solid green), 10% (dashed red) and 14% (dot-dashed violet). 234

Figure 8.69 - Circular depolarization ratio (CDR) for dry hailstones having the 2% M-type roughness and axis ratio of 0.6 (solid blue), 0.7 (solid green), 0.8 (dashed red). 235

Figure 8.70 - Circular depolarization ratio (CDR) for wet hailstones with axis ratio of 0.6 and M-type roughness of 2% (solid blue), 6% (solid green), 10% (dashed red) and 14% (dot-dashed violet). 236

Figure 8.71 - Circular depolarization ratio (CDR) for wet hailstones with axis ratio of 0.6 and R-type roughness of 2% (solid blue), 6% (solid green), 10% (dashed red) and 14% (dot-dashed violet). 237

Figure 8.72 - Circular depolarization ratio (CDR) for wet hailstones with axis ratio of 0.7 and M-type roughness of 2% (solid blue), 6% (solid green), 10% (dashed red) and 14% (dot-dashed violet). 238

Figure 8.73 - Circular depolarization ratio (CDR) for wet hailstones with axis ratio of 0.7 and R-type roughness of 2% (solid blue), 6% (solid green), 10% (dashed red) and 14% (dot-dashed violet). 238

Figure 8.74 - Circular depolarization ratio (CDR) for wet hailstones with axis ratio of 0.8 and M-type roughness of 2% (solid blue), 6% (solid green), 10% (dashed red) and 14% (dot-dashed violet). 239

Figure 8.75 - Circular depolarization ratio (CDR) for wet hailstones with axis ratio of 0.8 and R-type roughness of 2% (solid blue), 6% (solid green), 10% (dashed red) and 14% (dot-dashed violet). 240

Figure 8.76 - Circular depolarization ratio (CDR) for dry hailstones having the 2% M-type roughness and axis ratio of 0.6 (solid blue), 0.7 (solid green), 0.8 (dashed red). 241

ABSTRACT

The primary topics of this dissertation are issues existing in the current ensemble scattering procedures. These procedures are failing to quantitatively reproduce polarimetric signatures from resolution volumes filled with ensembles of resonant size precipitation, biota, and anthropogenic scatterers. Sources of these failures are traced to the constraints on the topology that is admissible to the different modeling procedures.

The dissertation evaluates in a systematic manner the current modeling procedures focusing on limitation sources and their effects on the overall process of polarimetric variable simulation. It re-evaluates limitations of the widely used T-Matrix approach and discusses sources of instability. Based on the identified limitations, a novel computational electromagnetics (CEM) approach to scatterer modeling and polarimetric variable calculation is introduced to mitigate the current limitations. Detailed overview of the process as well as guidance on applying the CEM to the polarimetric variable calculation is presented. This is the first systematic exploration of a specific CEM solver to modeling of polarimetric radar signatures from precipitation and biota.

Finally, to demonstrate meteorological application the CEM approach is evaluated by comparison with some polarimetric radar observations of hail. Of main significance is modeling of large and giant hail having surface protuberances, or rough, irregular shape. Additionally, radar observations of biota and radar cross section (RCS) measurements are considered for aeroecology applications. As an example, the precise size and shape model of Brazilian Free-tailed bat (*Tadarida brasiliensis*) is created and compared to the RCS measurements, as well as to radar observations of bat emergence in Texas plains.

1. INTRODUCTION

From the moment of creation, awareness of the world around us comes from our senses. Empirical (sense experience) knowledge is the first to be “born”. At birth, our senses provide us with the capability to observe, feel, and hear. Our logic then gives us the capability to comprehend what we sensed. However, we must not forget that our senses are limited. One may hear, but only a part of the actual sound spectrum. One may feel, but not everything. One may see but only up to some distance and only a portion of the light spectrum. Shortly, individuals realize their own sense limitations as they develop. Luckily, mankind has an instinctive desire to learn; moreover, the most prominent scientists worked to overcome our own limitations.

Theoretical studies of the electricity and magnetism conducted by Charles-Augustin de Coulomb, Carl Friedrich Gauss, Heinrich Hertz, Michael Faraday, Andre-Marie Ampere, James Clark Maxwell, John H. Poynting among others have shaped the theory of electrodynamics, which can alleviate our limitations. As a result of their work, mankind was given a set of four equations as the foundation for one of the most researched areas in the study of physics. These four equations are known as Gauss’s Law (1), Gauss’s Law of Magnetism (2), Faraday’s Law (3) and Ampere’s Law (4). These four laws constitute a set of coupled Maxwell equations (Maxwell, 1881).

$$\nabla \cdot \mathbf{E} = \frac{\rho}{\varepsilon}; \tag{1}$$

$$\nabla \cdot \mathbf{B} = 0; \tag{2}$$

$$\nabla \times \mathbf{E} = -\frac{\partial \mathbf{B}}{\partial t}; \tag{3}$$

$$\nabla \times \mathbf{B} = \mu \mathbf{J} + \mu \varepsilon \frac{\partial \mathbf{E}}{\partial t}. \tag{4}$$

The founding equations of electromagnetics define the electric field \mathbf{E} , the magnetic field \mathbf{B} in terms of conduction currents \mathbf{J} , electric charges ρ and medium permittivity and permeability ϵ, μ . Together with the Lorentz's Law reveals an explanation to all of the macroscopic electromagnetic effects. With this foundation, all limitations of our senses can be formulated and all the answers on overcoming limitations can be found. One of the scientific visionaries, Serbian inventor Nikola Tesla, may have been one of the first to recognize endless possibilities of the Electromagnetic (EM) waves. In his article on human energy, he stated *“That communication without wires to any point of the globe is practicable with such apparatus would need no demonstration, but through a discovery which I made I obtained absolute certitude. Popularly explained, it is exactly this: When we raise the voice and hear an echo in reply, we know that the sound of the voice must have reached a distant wall, or boundary, and must have been reflected from the same. Exactly as the sound, so an electrical wave is reflected, ... Instead of sending sound-vibrations toward a distant wall, I have sent electrical vibrations toward the remote boundaries of the earth, and instead of the wall the earth has replied. In place of an echo I have obtained a stationary electrical wave, a wave reflected from afar.”* (Tesla, 1900). Clearly, he recognized that our senses “to hear” and “to see” may be extended to a further distance, by the use of the EM waves. Furthermore, as shown in Maxwell's equations, EM waves can be pointed toward a specific direction and will be reflected from any existing discontinuity of the medium they are propagate in.

Our ability to hear is then nothing more than the ability to detect mechanical waves, and our ability to see, is simply detection of scattered EM waves. With this in mind

we may realize that our senses are “instruments” that detect the existence of waves around us. Therefore, Tesla’s idea of generating EM waves will exclusively serve the purpose of nothing but a mitigation of limits imposed by our senses.

As found in Tesla’s article, it is noted that for the first time, EM waves are used for radio detection application and therefore of the *Radio Detection And Ranging* (RADAR) instrument. In light of the article, an instrument designed to improve our ability to “see” beyond the optical horizon. Under the name of RADAR such an instrument is first mentioned in November 1940 by S. M Taylor and F. R. Furth (Doviak & Zrnić, 2006). However, shortly after Tesla’s article, the first radio detection of a distant object was accomplished in 1904 using the “*Telemobiloscope*” (Hülsmeier , 1904).

Beginning with the invention of the telemobiloscope, radar instruments were built for various purposes. Among the first successful demonstrations of radar is Appleton’s continuous wave (CW) radar used to detect the ionosphere on December 11th 1924 at King’s College in London. The following one was the first pulsed radar demonstration by G. Breit in the Carnegie Institution’s laboratory for Terrestrial Magnetism and in the Naval Research Laboratory by M.A. Tuve in 1925.

Common to all of the radar research programs is that they were strictly classified. Many countries including USSR (Russia), Germany, USA, France, United Kingdom, Japan, and Italy began developing their own radar systems. By the beginning of the Second World War, often considered the scientific renaissance of the twentieth century, radars had demonstrated their capabilities to detect ships and aircrafts.

However, extensive use of radar at the start war proved that they are far more sensitive than expected. Besides the ability to detect aircrafts and ships, radar crews were capable of distinguishing echoes¹ originating from birds and weather phenomena (Eastwood, 1967). These capabilities have resulted in different applications of radars. These applications can be separated into six major areas:

- **Military** – The main driver of the radar development since the Second World War was for military purposes. The military currently uses radars for a number of tasks including target detection, recognition, tracking, missile guidance etc. With great certainty it can be concluded that most of the radar systems developed have been used for military purposes at the same time or even before they were available for civilian use.
- **Surveillance radars** – This group constitutes all surveillance radars regardless of their location. These include, Air Traffic Control (ATC) and air surveillance radars on ground; coastal (harbor) radars for observing vessels at the sea, law enforcement radio-speedometers (radars) among others.
- **Navigation and safety radars** – Radars that have navigation and safety as principal objective. Here, Collision Avoidance Radars² in automobiles, as well as radars on ships and airplanes for navigation and collision avoidance are included and so are position transponders which are standard for most vessels today.

¹ In the radar terminology word echo is commonly used to denote the displayed pattern of the returned power on the radar screen.

² Depending on the manufacturer, this system may have different name: Pre-Collision system (Toyota); Mitigation Brake System (Honda); Pre-Safe (Mercedes-Benz) etc..

- **Remote sensing** – Radars used for remote sensing and exploration of the nature and environment are considered to be part of this group³. Here we may distinguish ground penetrating radars, weather radars and radars for troposphere biota sensing (insects, birds etc.).
- **Space** – Radars and radiometers (and radio telescopes) used in space, and for space explorations constitute this group. Some of the space based radars may belong to one or two other groups. For example: radars deployed in space which primarily have a military objective are still classified in this group.
- **Other** – Radars used in industry and all other areas that do not fall in any other group.

Aside from their application, radars are differentiated by other criteria such as frequency. Throughout the dissertation different frequency bands are used. The primary concern will be the frequencies of meteorological weather radars. Radar frequency is one of the crucial factors as it directly affects angular resolution (antenna beam-width is proportional to the wavelength to maximal dimension ratio), and maximal range (due to the absorption of EM energy that is dependent of frequency). Therefore it defines the applicability of a certain frequency band for specific application. Frequency bands typically used in radar systems are⁴:

- VHF – 30 to 300 MHz – over the horizon early warning and surveillance radars;

³ Similar definition of the remote sensing group is used by Skolnik (Skolnik, 2001).

⁴ Following list is created using the information found in (Wolf, n.d.), (Doviak & Zrnić, 2006), (Skolnik, 2001).

- UHF – 300 to 1000 MHz – ballistic missile and satellite tracking radars as well as Ground Penetrating Radars and wind profiling radars;
- L – 1 to 2 GHz – long range “En Route” ATC radars, long range weather sensing for ATC;
- S – 2 to 4 GHz – ATC approach radars (Airport Surveillance Radars) as well as Weather Surveillance Radar 88 Doppler (WSR-88D);
- C – 4 to 8 GHz – missile control and ground surveillance, shorter range weather radars (European EUMETNET / OPERA radars);
- X – 8 to 12 GHz – airborne navigation and weapons control radars, micro rain weather radars, police radio speedometers (radars);
- Ku – 12 to 18 GHz – airborne weapons control and synthetic aperture (SAR), inverse SAR (ISAR) and space borne weather radars, police radio speedometers (radars);
- K – 18 to 27 GHz – short range surface movement radars, police radio speedometers (radars);
- Ka – 27 to 40 GHz – short range surface movement radars, atmospheric research and cloud sensing, police radio speedometers (radars);
- V – 40 to 75 GHz - limited applicability due to very high attenuation;

- W – 75 to 110 GHz – automotive collision avoidance and parking assistance radars, atmospheric research ice crystal sensing radars;
- Millimeter – 110 to 300 GHz – automated fire detection radars.

In order to describe radar system, besides using the application and frequency, one must include information about its topology. When a radar transmitter and receiver are collocated at one physical position system it is called a **Monostatic** radar system. When the transmission and reception portion of the radar are physically separated by a distance that is comparable to the typical target distance such system is called a **Bistatic** radar system. A system that is combination of multiple bistatic radars is called a **Multistatic** radar system.

Currently, the radars used for both civilian and military use are typically monostatic. The topology of these systems typically consists of transmission lines including sources and amplifiers of the radar signal. Switching or isolation network between transmit and a receive portion of the radar and common antenna. With the latest development of solid state electronics and signal processing the original radar topology is gradually moving toward a cost effective, fully digital system. However, there is ongoing research and an expected development period before this goal is reached.

1.1 HISTORY OF THE WEATHER RADAR

Before proceeding to the scattering and weather radar polarimetry, a short overview of weather radar history is considered. Unfortunately, historical evidence of radar

weather application has suffered due to the confidentiality of radar's very existence. Although it is well known that military applications of radars, such as air surveillance, were considered the most important defense mechanisms for the Allied Forces, there is limited documented evidence of its use. As mentioned previously, with the detection of the ionosphere by Appleton, the first actual meteorological application of radars is credited to Ryde and his attenuations studies of cloud and rain echoes in 1946 (Doviak & Zrnić, 2006). It is obvious that, when looking at topics of research published after the Second World War, radar observations of weather and other non-anthropogenic echoes caught the attention of radar community. A proof of such studies is found in Bent's publication, which elaborates on precipitation detection at Massachusetts Institute of Technology (MIT) during the war years (1942 – 1944) (Bent, 1946). Information on the observations of non-military targets during the war exist such as related to observations of biota (Eastwood, 1967) but is limited and not well documented. Toward the end of the war radar operators were versed in the detection of weather echoes using military radars. The first traces of the weather radar networks are found in 1944 in Panama and Calcutta (India) (Whiton, et al., 1998). There, military personnel began conducting weather observations using radars. The radar used for this purpose was an X-band navigation and bombing radar originally installed on heavy bombardiers (AN/APQ-13⁵), which was capable to clearly detect echoes caused by the water drops in rain. Small number of AN/APQ-13 radars was modified for ground use and installed on towers in weather stations covering Assam Valley in 1945 (Whiton, et al., 1998); (Best, 1973).

⁵ Military Joint Electronic Type Designation System (JETDS) nomenclature: AN – Army- Navy APQ-13 where letters define A-airborne, P- radar, Q- special or combination type.

Use of military radars such as AN/APQ-13 and AN/APS-10⁶ continued after the war by the Air Weather Service (part of United States Air Force) until the first radar specifically designed for weather use (AN/CPS-9) was in production in 1954 (NOAA, 2006). The X-band CPS-9⁷ radar was deployed in military bases worldwide where it served its purpose until its final replacement in 1984 (Whiton, et al., 1998). The network of APQ-13 and CPS-9 radars used for military weather observations was supposed to be substituted by the C-band AN/FPS-77⁸. However, due to the shortcomings in the FPS-77 design, these were declared unsupportable and substituted with radars that were in the meantime developed for civilian use (Whiton, et al., 1998).

The Weather Bureau (predecessor of today's National Weather Service (NWS)) obtained 25 surplus S-band AN/APS-2F aircraft radars after the war (Whiton, et al., 1998) (NOAA, 2003). These radars needed modifications which Weather Bureau could not fund, thus their deployment was delayed. First modification of the AN/APS-2F radar into Weather Surveillance Radar (WSR)-1 was in 1947 at the Washington National Airport (Whiton, et al., 1998). And it was slowly continued until a tornado event in Texas on May 11th 1953. This tornado brought to attention the necessity of weather and severe storm observations for civilian purpose. As an epilog of the Texas tornado event, the Texas Tornado Warning Conference was held on June 24th 1953. It was aimed at starting the project of creating the first civilian weather network in history, dedicated only to weather observations (NOAA, 2003). When

⁶ In JETDS APS stands for airborne, radar, detecting (range and bearing).

⁷ JETS CPS – C-Air transportable(inactivated letter),P-radar, S-Detecting (range and bearing).

⁸ JETS FPS – F-Ground, P-Radar, S-Detecting (range and bearing).

finished in 1955, the radar network consisted of 19 S-band radars designed on the concept of the surplus APS-2F radar (NOAA, 2003) and covered Texas and Louisiana Weather Bureau offices. These radars were denoted as WSR-1,-2,-3,-4 and served until 1980 (Whiton, et al., 1998).

Shortly after the WSR-1⁹ radar network was operational in April 1956 the first warning based only on the radar data was issued in Texas for the tornado that “touched down” 24 minutes after the actual warning (Whiton, et al., 1998). For the first time, based on radar observations, possible civilian casualties were avoided as students of the Texas A&M University in College Station, TX were kept inside school buildings during the tornado that hit the area.

Capabilities of the WSR-1 network in prevention of damage and human casualties in tornadic events and possibility of hurricane tracking with modified SP-1M radar resulted in the Congressional funding of the Weather Bureau for improvement of warning services in 1956 (Whiton, et al., 1998). As a result of this initiative, the Weather Bureau ordered 31 radars from Raytheon. This radar became known as the WSR-57. The WSR-57 was an S-band meteorological radar designed exclusively for Weather Bureau, it included some of the features of the CPS-9 built for the USAF by the same manufacturer (Whiton, et al., 1998). The chosen lower frequency band of WSR-57 was better suited for detection and tracking of the meteorological echoes at large distances, as it was not as affected by the attenuation as was its C-band “relative”. The WSR-57 in time became the flagship radar of the Weather Bureau and NWS, until it was replaced by the NEXRAD Doppler radar (i.e. the WSR-88D).

⁹ Here, under the notation of the WSR-1 all variations of APS-2F are considered.

During the service time of WSR-57 (until 1996) another generation of the WSR was developed in order to “fill in the gaps” in the radar network coverage and substitute old WSR-1 type radars. The radar developed for this purpose by the Enterprise Electronics was WSR-74C, where C stands for the C-band at which radar was operating. The C-band radar in this case was of sufficient range, as the system was designed as the “coverage gap filler”. However, during the substitution of the older generation WSR-1 type radars an S-band version WSR-74S was developed. The WSR-74 was the first transistor based weather radar in the network which was slowly starting to “suffer” from the shortage of vacuum tubes as the war supplies of these parts had been used (Whiton, et al., 1998). At the peak of the network, it consisted of 128 WSR-57 and WSR-74 radars covering most of the continental US.

The aging network of the vacuum tube based WSR-57 radars was starting to require extensive care in the late seventies due to obsolescence of the vacuum tubes technology. Additionally, shortcomings in the AN/FPS-77 design and lack of capability to measure wind velocity brought NWS and AWS to consider substitution of those radars with new ones capable of the wind velocity measurements. Joint effort of NWS and AWS resulted in the organization of the Joint Doppler Project (JDOP) in July 1978. Concluding the joint program, the JDOP group presented that Doppler radar is superior for weather observations increasing the warning time to 20 minutes before storm hits and reducing false alarm ratios in severe weathers. Additionally, the group stressed the capability of Doppler radars as more reliable in detection and tracking of distant storms, while providing capability to separate tornadic from non-tornadic storms using the velocity measurements (Whiton, et al., 1998). The findings

of JDOP led to finalization of the design requirements of for the next generation weather radar (NEXRAD) in 1982 (The NEXRAD Support Operation Facility, 1996). Contracts were awarded to the Sperry Corporation, Raytheon, Ford Aerospace and Westinghouse Corporation, while the validations phases took place until 1986 and the first demonstration of the NEXRAD prototype was in April-July 1988 (NOAA, 2012). The first operational prototype of the NEXRAD was delivered to the Operations Support Facility in in winter 1988 starting the era of WSR-88D (Weather Surveillance Radar '88 Doppler). Implementation of the WSR-88D and substitution of older generation radars to the weather radar network started in 1990 and continued until the last WSR-88D was installed in June 1997. First production of 13 WSR-88D units used circular polarization which was shortly changed to linear, because it was realized that change of polarization due to propagation through rain would cause significant loss of power in the intended channel for weather. Later, 147 radars with linear (horizontal) polarization were added. Together they form the current operational weather radar network of 158 radars across the United States.

Even before the deployment of the WSR-88D network first studies regarding the additional requirements to the NEXRAD were made. Consideration of the dual polarization capability for the incoming NEXRAD was published in 1984 (Sirmans, et al., 1984 (rev.1986)). These reports (Part 1 and Part 2) examine research conducted in the field of dual polarization radars and its improvements related to the quantification of precipitation, discrimination of the hydrometeor types etc. The authors stated that dual polarization (polarimetric) capability could be incorporated in the NEXRAD program without jeopardizing the existing requirements. In order to

accommodate polarimetric operation and radiation of the alternately polarized electric field pulses hardware changes would be necessary. These include installation of the orthomode coupler and a high power switch for changing polarization, and additional signal processing of received data at the two polarizations.

Unfortunately, due to the high cost of the required changes and undemonstrated utility of the technique, polarimetric capability requirement for the original NEXRAD project was not encouraged. However, favorable recommendations regarding the polarimetric upgrade of the WSR-88D network followed in the later reports in 1998 and 2002, as the novel polarimetric scheme was developed in order to avoid costly changes to the hardware. The new scheme uses simultaneous transmission of horizontal and vertical polarization and existing SIGMET's processor for the computation of the polarimetric variables (Doviak & Zrnić, 1998) (Doviak, et al., 2002). Polarimetric capability was investigated using NSSL's research WSR-88D radar based in Norman, OK designated as KOUN.

Importance and benefits of the polarimetric weather observations are identified through the improvement in quantitative precipitation, hail discrimination, identification of precipitation in winter storms, identification of electrically active storms and distinction of non-meteorological scatterers (Zrnić & Ryzhkov, 1999). All benefits ensue from analysis of the polarimetric variables that better depict the properties of the scattered EM waves. Coming from the fact that vertical-horizontal polarization basis aligns with the principal axis of several hydrometeor types maximizing the contrast between scattering properties of vertically and horizontally

polarized waves (Zrnić & Ryzhkov, 1999). In order to understand causes of this effect scattering of EM waves will be examined in the following chapter.

1.2 STRUCTURE OF THE DISSERTATION

Remainder of the dissertation is organized to build up all of the underlying theory on which the dissertation is founded. The second chapter deals with the phenomena of electromagnetic scattering and techniques used in numerical evaluations of backscattering of a dielectric object. The second chapter reviews exact, as well as approximate techniques providing a brief insight of their theory and algorithmic structure. At the very end the concept of the dual-polarization (polarimetric) scattering and the geometry accepted in the field is introduced.

The third chapter surveys current modeling of meteorological scattering. It provides the classification of the overall modeling process and evaluation of the current modeling procedures. Special attention in the chapter is focused on the issues inherent to the current modeling and the problems that the new modeling approaches should address.

The fourth chapter of the dissertation is named “Realistic modeling of meteorological scatterers”. It addresses current spheroidal based modeling and investigates its limitations. Of greatest importance is the introduction of the computational electromagnetic approach to the modeling of meteorological scatterers using the commercially available software. A thorough discussion of physical principles and adaptation of the WIPL-D software for hydrometeor modeling is given. This is followed by evaluation of the WIPL-D results. Moreover, WIPL-D is used to quantify

limits of the popular approximate solutions. Physical hydrometeor models are varied in size, shape, and dielectric properties to precisely determine limitations of the approximate tools.

A polarimetric variable simulator (PVS) is described in chapter five. The PVS uses scattering elements stored in its scattering library. The algorithm is explained, emphasizing the mathematical formulations used to achieve the highest degree of freedom in modeling. The algorithm is applied to monodispersed hail of various compositions, distribution of orientations, and roughness. The outputs of the PVS corresponding to specific hail type and size are used to explain few puzzling radar observations.

In chapter 6, the demonstrated capabilities of the computational electromagnetic tools are evaluated for cases of biological scatterers such as the Brazilian free-tailed bat (*Tadarida brasiliensis*). A unique laboratory measurement of the backscatter diagram of the bat is designed, executed, and compared with the CEM results. Also the modeled and radar observed returns from these animals are contrasted. Thus, the power of the computational EM approach in calculation of backscattering returns is extended to the field of aeroecology.

2. ELECTROMAGNETIC SCATTERING

Electromagnetic (EM) waves experience refraction and scattering along propagation paths in inhomogeneous media. If the medium contains discontinuities (such as hydrometeors or other objects) the EM wave propagating will induce currents¹⁰ on the boundary of the discontinuity disturbing wave propagation. Resulting wave after this interaction is the sum of the incident and scattered wave radiated by the induced currents (2.1).

$$\mathbf{E}_{tot} = \mathbf{E}_{inc} + \mathbf{E}_s \quad (2.1)$$

Objects along the propagation path, of the EM wave, will scatter a portion of the energy intercepted back towards the radar, thus allowing the radar to detect their presence. Therefore, it can be said that detectability of an object due to EM backscattering is one of the objects inevitable properties. Detecting objects, on the other hand depends on the detection capability of the radar, and the intensity of the backscattered wave.

Wave scattered by an object in the EM field, as mentioned, depends on the equivalent currents induced on the scatterer itself (Harrington, 1961). Ipso facto, intensity of equivalent currents induced is directly proportional to the energy that will be scattered by the object. Following from the symmetrized Maxwell's equations¹¹ induced surface currents can be determined using the induction theorem for the electric and magnetic currents at the scatterer's surface.

¹⁰ Polarization (displacement) or conduction depending on the type of the object.

¹¹ Reader is instructed to consult (Harrington, 1961) for detailed overview of symmetrized Maxwell's equations.

Using the equivalence principle (Harrington, 1961) the scattered field exterior to the object can be expressed as (2.2), (2.3):

$$\mathbf{n} \times (\mathbf{E}_{tot} - \mathbf{E}_s) = \mathbf{M}_s \Rightarrow \mathbf{M}_s = -\mathbf{n} \times \mathbf{E}_{inc} \quad (2.2)$$

$$\mathbf{n} \times (\mathbf{H}_s - \mathbf{H}_{tot}) = \mathbf{J}_s \Rightarrow \mathbf{J}_s = \mathbf{n} \times \mathbf{H}_{inc}, \quad (2.3)$$

which, by substitution of (2.1) into (2.2) and (2.3), is exactly the field incident on the object. Where \mathbf{E}_{tot} is the total field, consisting of the incident \mathbf{E}_{inc} and scattered \mathbf{E}_s fields, while \mathbf{M}_s is magnetic current, \mathbf{J}_s electric current and \mathbf{n} is the outward pointed surface vector. Thus, the equivalent current induced at any point on the object is directly proportional to vector product of the incident field and the outward directed surface vector perpendicular to the tangent plane at that point on the object. The power density scattered back from the object and measured at the antenna is used to define the Radar Cross Section.

The radar cross section (RCS), strictly is the ratio of the power density scattered by the object at infinite distance to the incident power density (2.4) (Knott, et al., 1993). Units of RCS are area [m²], or area normalized to λ^2 , where λ represents the wavelength at which particular RCS is defined. Ratio of the scattered and incident wave at infinite distance from the scatterer in the RCS definition is a scattering element (2.5).

$$RCS = 4\pi \lim_{R \rightarrow \infty} R^2 \frac{|E_s|^2}{|E_{inc}|^2} \quad (2.4)$$

$$s = \lim_{R \rightarrow \infty} R \frac{E_s}{E_{inc}} \rightarrow RCS = 4\pi |s|^2 \quad (2.5)$$

The Radar Cross Section (2.4) uses the infinite range away from target. Such requirement is a product of mathematical formalism (Knott, et al., 1993), while in the practical situation the infinite range is considered to be the far-field range where the scattered wave can be decomposed as:

$$\mathbf{E}_s(R, \varphi, \theta) = \mathbf{e}_s(\varphi, \theta) \cdot \frac{e^{-j\beta R}}{R}, \quad \beta = \frac{2\pi}{\lambda} \sqrt{\varepsilon\mu},$$

where β is the propagation coefficient, while the field is represented by normalized field vector \mathbf{e}_s having only φ and θ , azimuth and elevation components. The ε is the permittivity, μ permeability of the medium, and R is the range. For the decomposed field, the term in the numerator of the scattering element (2.5) is canceled out resulting in scattering element having the unit of $[\text{m}]^{-2}$, instead of being unit-less as it is the case with scattering parameters used in other areas of electrical engineering.

Scattered power, originated from the induced currents on an object, is radiated in all directions. However, it is important to understand that total scattered power is not isotropically radiated in the general case but angularly dependent on the scatterer's shape. Besides the shape of a scatterer, RCS depends on the material properties of the object. This is especially significant in cases of lossy dielectric objects, when a portion of the induced current's energy in the scatterer will be transferred to molecular interactions to generate heat. Finally, we can conclude that besides parameters of the scatterer itself, RCS is a function of the incidence angle, frequency and polarization of the EM wave that illuminates the scatterer.

¹² Scattering elements defined to have units of $[\text{m}]$ are aligned with work of (Doviak & Zrnić, 2006), and work cited within.

The RCS of an object can be exactly calculated, measured or approximately calculated. Solving scattering problem, in a closed analytic form, is possible only for objects of simple geometry, such as spheres, plates etc. For more complex geometry, RCS can be calculated only by numerical analysis of the scattering problem, or by using some approximations. Strictly speaking, RCS approximations are always prone to error as well as limited regarding the frequency, shape and other properties of the object.

Generally speaking, RCS measurements are always possible; however, the feasibility of measuring on certain objects can be limited. This is typically the case for objects that are prohibitively large, such as aircrafts, or especially small or unwieldy, as is the case for many flying organisms. Additionally, strict measurement of the scatterers particularly important for the weather radar applications may not be practical, due to the changes that occur to their properties during the measurement, such as, melting of frozen particles.

It is understandable that measurements of individual precipitation scatterers are very few and those of ensembles are nonexistent, because the variety of the hydrometeors is huge. Therefore, RCS calculation, and approximation techniques are widely applied in most meteorological modeling. On the other hand, precipitation is not the only scatterer type observed by weather radar. Significant effort is being put into the field of Radar Aeroecology, especially in the observation of biota using the existing network of weather radars (Chilson , et al., 2011). These biological objects are more complex, and approximations with simple spheroidal models have deficiencies

(Melnikov, et al., 2015). Solution to these issues must rely on different sets of numerical tools that are capable of making RCS prediction.

Prediction of RCS, using numerical approaches in solving Maxwell's equations, has become widely accepted over time. Contributing factors were capabilities of numerical tools, which evolved with the increase of computational power, creating new possibilities in modeling. One may notice that from the beginning two different calculation techniques have been mentioned, the exact numerical calculation of the scattering, and the approximation of scattering. Acknowledging the difference between these two approaches is very important, and it follows from the applicability, in terms of object they address, and reliability (accuracy) of these tools. Here, the tools are distinguished as:

- Computational Electromagnetics (CEM) tools using exact prediction techniques (exact techniques);
- Tools using approximate numerical techniques applicable to specific cases (approximate techniques).

Exact solution techniques (CEM) are based on a precise numerical solution of Maxwell's equations for the particular object of interest. Results obtained by CEM are in general correct for all objects, without any limitations in frequency, object's properties or the dimension to wavelength ratio. Computational complexity of these tools is usually the limiting factor in their application. Currently, with the computing power available CEM is becoming more commonly used and scattering objects can be modelled more precisely in acceptable solving time.

Computational complexity of the exact tools and impossibility to analytically solve Maxwell's equations for complex objects, resulted in the development of approximation techniques. They are developed using object, field and induced currents behavior approximations, thus limiting their use to a set of strict conditions. In the following section some of the approximations that are commonly used in hydrometeor scattering calculations are examined.

2.1 APPROXIMATE TECHNIQUES FOR CALCULATION OF SCATTERING ELEMENTS

Depending on the required accuracy and complexity of the object's shape, computationally expensive process of numerical solving Maxwell's equations might not be necessary. In these cases, for defined object types where current distribution is known a priori, modeling can be significantly simplified yielding shorter computational time, for the same accuracy of results. The most important step, in development of these approaches, is use of simplifications. Simplifications applied are typically related to the known characteristics of induced currents, major scattering contributors and symmetry. Therefore, one must always bear in mind that application of these approaches, in cases when any of the object's properties are different from ones prescribed in the development of the approach, leads to an incorrect result. Consequently, use of approximate tools is justifiable only in cases that follow same assumptions as ones used in the development of approximate tools. Approximate tools (solvers) are often discerned by the applicability region of Lorenz-Mie scattering diagram (Fig. 2.1). The Lorenz - Mie series is the exact analytical scattering solution for a homogenous sphere in the form of an infinite series of

spherical waves (Gouesbet & Gréhan, 2011). These exact results are used in comparisons with solutions provided by approximate methods. Depending on the ratio of sphere's diameter d to the wavelength λ , scattering regions could be distinguished as: Rayleigh $d < \frac{\lambda}{10}$, resonant or Mie $\frac{\lambda}{10} \leq d < 5\lambda$ and optical $d \geq 5\lambda$. Scattering from a perfect electric conductor (PEC) sphere presented in Fig. 2.1 is calculated using the WIPL-D CEM tool, which is discussed into more detail later. Results in Fig. 2.1 are computed for the sphere of fixed radius $d = 200$ mm over the frequency range from 0 to 7 GHz.

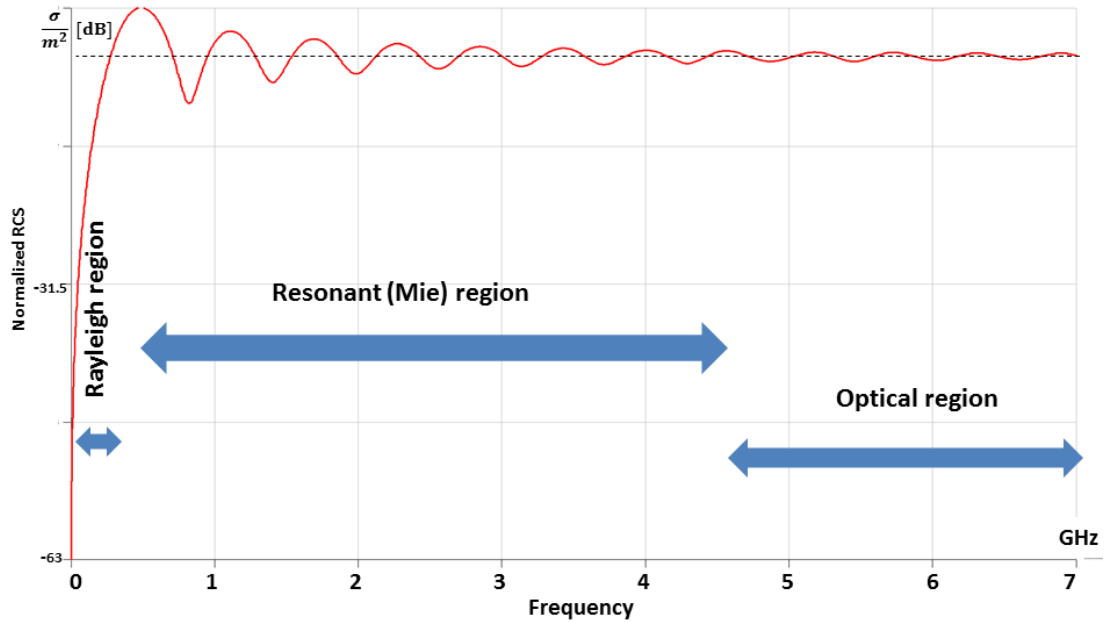


Figure 2.1 - Lorenz - Mie solution for a cross section of an impenetrable (PEC) sphere, created using WIPL-D CEM tool.

Application of approximate solvers is usually defined with respect to the region of the Lorenz-Mie scattering curve. In some cases, applicability of the approximation is defined with the position of the first or tenth Mie scattering diagram maxima. In the

following portion of this section, some of the most important approximate techniques for scattering element calculations are examined.

2.1.1 Rayleigh Approximation

The most commonly used approximation for small scatterers is the Rayleigh approximation, named after Lord Rayleigh. Rayleigh approximation has been extensively used in the modeling of meteorological scatterers as it provides accurate solutions to the scattering of raindrops. Applicability limit of the Rayleigh approximation, for the meteorological modeling is determined by the resonance parameter (RP) defined as (2.6) (Ryzhkov, et al., 2011), where D_{eq} is the particle's equivolume diameter and $|\varepsilon|$ is magnitude of the complex dielectric permittivity.

$$RP = \frac{D_{eq}\sqrt{|\varepsilon|}}{\lambda} \quad (2.6)$$

Resonance parameter corresponds to the unity at the first peak value marking the resonance (Mie) region of the scattering diagram. Depending on the accuracy needed, resonance parameter values ranging from 0.6 to 0.8 are used as a limit for application of Rayleigh approximation (Kumijan, 2012). The stricter requirement, based on the evaluation of the polarimetric radar variables, is set to be 0.25 with relaxation to 0.3-0.4 by Ryzhkov et al. (Ryzhkov, et al., 2011). Both of these requirements are derived for models of single and multilayer scatterers that are considered in meteorological simulations.

Rayleigh scattering elements for single and multilayer spheroids are defined for incidence normal to the symmetry axis (z-axis Fig. 2.2). Co-polar backscattering element, in case of polarization parallel to the spheroid's symmetry axis is f_a , while

the co-polar scattering matrix element normal to the symmetry axis of the spheroid is denoted as f_b (Van de Hulst , 1981) and (Bohren & Huffman, 1983):

$$f_{a,b} = \frac{\pi^2 D_{eq}^3}{6\lambda^2} \frac{(\epsilon_r - 1)}{1 + L_{a,b}(\epsilon_r - 1)}, \quad (2.7)$$

where $L_{a,b}$ is the shape parameter defined separately for f_a and f_b scattering element, respectively.

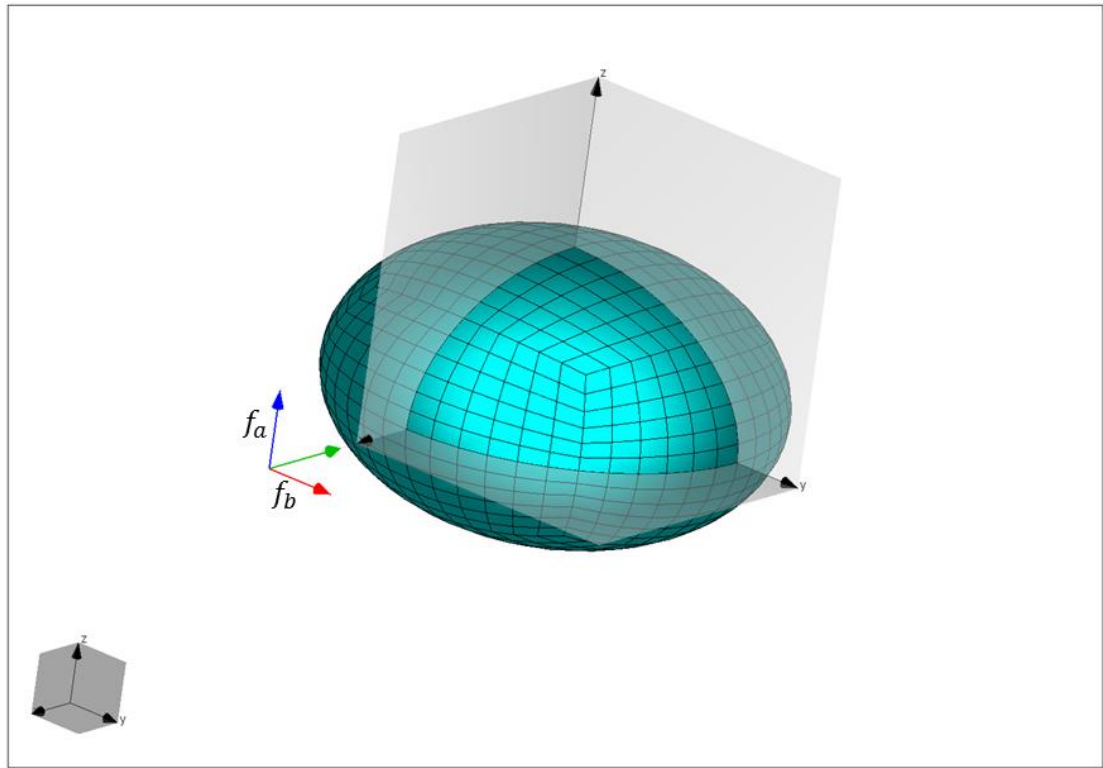


Figure 2.2 – Polarimetric scattering elements; f_a is the scattering matrix element for polarization parallel to the hydrometeor’s symmetry axis and f_b is the scattering element for polarization perpendicular to the symmetry axis.

In case of oblate spheroids $b > a$, as in Fig. 2.2, where a is the diameter parallel to the hydrometeor’s axis of symmetry, while b is diameter in the cardinal plane of the hydrometeor (normal to the axis of symmetry) parameters $L_{a,b}$ are:

$$L_a = \frac{1+g}{g^2} \left(1 - \frac{\arctan g}{g} \right); g^2 = \frac{b^2 - a^2}{a^2}, \quad (2.8)$$

$$L_b = \frac{1-L_a}{2}. \quad (2.9)$$

Contrarily, for prolate spheroids $a > b$ shape parameters are defined as:

$$L_a = \frac{1-e^2}{e^2} \left[\frac{1}{2e} \ln \left(\frac{1+e}{1-e} \right) - 1 \right]; e^2 = \frac{a^2 - b^2}{a^2}, \quad (2.10)$$

$$L_b = \frac{1-L_a}{2}. \quad (2.11)$$

Modeling of small water coated hydrometers can be done using the dual-layer Rayleigh approximation given by (2.12). Parameters v_{in} denotes the volume fraction of the inner spheroid, and ε_1 and ε_2 are complex dielectric parameters of inner and outer spheroid respectfully.

$$f_{a,b} = \frac{\pi^2 D_{eq}^3}{6\lambda^2} \frac{(\varepsilon_2 - 1)[\varepsilon_2 + L_{a,b}(1 - v_{in})(\varepsilon_1 - \varepsilon_2)] + v_{in}\varepsilon_2(\varepsilon_1 - \varepsilon_2)}{[\varepsilon_2 + L_{a,b}(1 - v_{in})(\varepsilon_1 - \varepsilon_2)][1 - L_{a,b}(\varepsilon_2 - 1)] + v_{in}\varepsilon_2(\varepsilon_1 - \varepsilon_2)L_{a,b}} \quad (2.12)$$

Formulas (2.7-2.12) are used in scattering calculations of Rayleigh particles and in the following chapters are compared to results obtained using exact techniques. Rayleigh approximation results are often used for benchmark in cases when other approximate solutions fail to converge due to the axis ratio or similar issues.

2.1.2 Geometrical Optics

Geometrical optics (GO) is one of the oldest methods for determining the RCS of an object. Its first applications are traced back to astronomers interested in light scattering. GO is used for bodies of perfect reflection, even though, with the

implementation of the conservation of energy law it can be applied to the dielectric objects. Geometrical optics is a ray tracing method based on the propagation of the equiphase fronts defined in tubular geometry. The implementation is mainly in cases where $d \gg \lambda$ or $\lambda \rightarrow 0$ without limitations regarding the reflection boundary (Knott, et al., 1993). The refracted and reflected wave angles, at oblique incidence, are defined by Snell's law, while the perfect reflection is (2.13a).

$$RCS = \pi R_1 R_2, \quad (2.13a)$$

where R_1 and R_2 are orthogonal radii of object's curvature at the surface point of reflection. Formula (2.13a) therefore represents the apparent area of the sphere regardless of actual scatterer shape. For dielectric spheres, in the limit of infinitely large diameters, backscattering cross section using the theory of GO is (2.13b) (Doviak & Zrnic, 2006).

$$RCS = \frac{\pi D}{4} \cdot \frac{|\sqrt{\epsilon_r} - 1|^2}{|\sqrt{\epsilon_r} + 1|^2} \quad (2.13b)$$

Some studies using the theory of geometrical optics were conducted in the area of hydrometeor scattering. They considered scatterers as small as $d \sim 3\lambda$ concluding that the theory of GO may produce "reasonably accurate" results in cases of raindrops and other penetrable bodies such as soap bubbles (Plummer, et al., June 1980).

Theory of geometrical optics is one of the best examples of how simplifications are applied to scattering problems. Here, backscattering accounts only for surfaces specular to the wave front while other scattering mechanisms (e.g. creeping waves

etc.) are neglected. Besides this simplification, theory of geometrical optics is very inaccurate in cases slightly curved or flat infinite surfaces (Knott, et al., 1993).

In scope of the dissertation, as well as in many cases when the requirement of dimension to wavelength $d \gg \lambda$ (optical region of Lorenz-Mie curve) ratio is not satisfied GO will not produce reliable results. For that reason theory of Physical Optics is considered.

2.1.3 Physical Optics

Approximations capable to reliably calculate scattering in the resonant region are needed, one such is the Physical optics approximation (PO). Ideas of physical optics are widely accepted, and its application is often found in more advanced iterative techniques, such as Physical Optics driven Method of Moments (Tasic & Kolundzija , 2011).

Theory of physical optics relies on the application of the far-field approximation to the Stratton-Chu equation of the electric field (Stratton, 1941). Following the induction theorem and algorithm for the calculation of the equivalent surface currents (2.1 - 2.3) scattering fields due to these currents can be resolved. Theory of PO postulates that electric and magnetic currents induced on the illuminated portion of the object will cause scattered fields. The scattered fields can be expressed by (2.14)

and (2.15), knowing that the far field derivative of the Green's function $\mathbf{g} = \frac{e^{-j\beta R}}{4\pi R} \rightarrow$

$$\nabla \mathbf{g} \cong j\beta \mathbf{r} \frac{e^{-j\beta R}}{4\pi R} \text{ (Knott, et al., 1993).}$$

$$\mathbf{E}_s = j\beta \frac{e^{-j\beta R_0}}{4\pi R} \int_S \mathbf{s} \times \left[\mathbf{n} \times \mathbf{E}_{inc} - \sqrt{\frac{\mu_0}{\epsilon_0}} \mathbf{s} \times (\mathbf{n} \times \mathbf{H}_{inc}) \right] e^{j\beta r(t-s)} dS \quad (2.14)$$

$$\mathbf{H}_s = j\beta \frac{e^{-j\beta R_0}}{4\pi R} \int_S \mathbf{s} \left[\mathbf{n} \times \mathbf{H}_{inc} + \sqrt{\frac{\epsilon_0}{\mu_0}} \mathbf{s} \times (\mathbf{n} \times \mathbf{E}_{inc}) \right] e^{j\beta r(i-s)} dS \quad (2.15)$$

In (2.14) vectors \mathbf{s} and \mathbf{n} are scattered wave direction and surface orientation vector respectively, while \mathbf{i} defines the incident wave propagation direction and ϵ_0, μ_0 are dielectric permittivity and permeability of free space. The vector cross products of surface orientation vector and incident fields define induced currents as in (2.2) and (2.3).

Theory of PO is applicable to most radar related scattering problems, as objects are usually in the far field, satisfying the PO approximation. Nonetheless, typical approximation issues arise for currents along edges that are main contributors in scattering of dendritic snowflakes or ice crystal structures, which are of interest at high frequencies. Furthermore, the PO defines induced currents only on illuminated faces of the scatterers, ignoring the contributions of currents existing in non-illuminated (shaded) regions of the scatterer. For spheroidal scatterers, so called creeping waves propagate through the shaded region around the surface of a spheroid are important contributors to the total RCS. It is exactly the backscatter contribution from the creeping wave that is neglected by the theory of PO. Thus application of PO is impractical to the meteorological scatterers which are considered to be mainly spheroidal.

2.1.4 T-Matrix

Solving for the scattering elements of particles in resonant, Mie region, is not feasible with any of the so far mentioned approximation techniques. To overcome this issue, a rigorous approach to solving Maxwell equations was required. Starting with the work

of Waterman (Waterman, 1971) a new approach to the calculation of the scattering matrix for large non-spherical particles was developed. This new, T-Matrix approach was based on the solution of the boundary condition for scattering using transition (T) matrix. An overview of the calculation using the T-Matrix approach is presented, avoiding extensive mathematical details. The T-Matrix, as one of the most widely applied approaches for calculating the elements of the backscattering matrix for various hydrometeors, is well documented in works of Mishchenko (Mishchenko, 2000), (Mishchenko, et al., 1996).

Incident and scattered waves in the far-field region are expressed as vector spherical functions in the T-Matrix. Spherical vectors allow extraction of the expansion coefficients for both, scattered and incident waves. Due to the linearity of Maxwell equations, and boundary conditions, the relation between the scattered field expansion coefficients and incident field expansion coefficients is linear. This relation is given by the transition matrix (T-Matrix) (Mishchenko, et al., 1996).

Properties of the particular transition matrix are independent of the incident wave, and depend only on the properties of the scattering object. Therefore quick calculations of scattering matrix elements at any incident angle can be made once the T-Matrix is known. The T-Matrix is independent of the polarization of the incident field; hence, polarimetric dependence of the scattering elements is obtained by decomposing the incident field vector. Fourier decomposition of the vector radiative transfer equations for incident field is elegantly done with the expansion coefficients calculating components of the phase matrix and thus solving for polarimetric scattering (Mishchenko, et al., 1996).

Computationally, the T-Matrix approach is about an order of magnitude faster than other similar approaches. This is due to the numerical efficiency and accuracy to the Extended Boundary Technique Method (EBCM) used for matching the elements of the incident and scattered expansion coefficients. It is the application of the EBCM that sets numerical limitations of the T-Matrix method. Numerical stability of the EBCM solution suffers in cases of hydrometeors having high permittivity, large size to wavelength ratio or large axes ratio, resulting in unpredictable behavior.

Besides inherited instabilities of the EBCM, numerical solutions introduce additional instabilities by limiting spherical functions of incident and scattered fields to finite order. Truncations of these functions may result in statistically small error in the original transition matrix, for which accuracy is determined by the size of the transition matrix. Unfortunately, elements of the transition matrix can differ by orders of magnitude producing the “ill-conditioned process strongly influenced by round off errors” (Mishchenko, et al., 1996). Many of the aforementioned issues can be mitigated with application of iterative processes in the EBCM evaluations; however these implementations of the T-Matrix method are beyond the scope of this dissertation. Detailed insight into the implementations of T-Matrix approach is available to the reader in the Mishchenko, et al., 1996; Mishchenko, 2000 and for multilayer T-Matrix solutions in Bringi & Seliga, 1977.

2.1.5 Discrete Dipole Approximation

The last approximate method discussed here is the Discrete Dipole Approximation (DDA) which for the purpose of scattering approximation discretizes geometry of the object. Discretization is done by implementing polarization points, which are discrete

infinitesimal building elements that acquire dipole moments in the response to the local field.

Discrete dipole approximation can be traced back to 1964 and studies of DeVoo and later in 1973 to Purcel and Pennypacker (Drane & Flatau, 1994). First applications of the DDA were related to the molecular aggregates and interstellar dust grains. Currently DDA is used in variety of applications including meteorological scattering calculations (O'Brien & Goedecke, 1988).

DDA can be applied regardless of the object's shape or wave polarization, even in cases of high particle anisotropy as each polarizable point may be assigned different dielectric properties. Dipoles used for object discretization are coupled and the main source of limitations to this method comes from the inter-dipole spacing. These limitations are especially critical in cases of objects with high refractive indexes with large inter-dipole spacing.

Numerical application of the DDA is relatively simple, because dipole moment functions are well defined. Still, the quality of approximation is highly dependent on the number of polarization points. Because the number of these points can be large, in order to accurately represent the object, mathematically simple DDA method may be less efficient than the more complex T-Matrix approach.

2.2 EXACT TECHNIQUES FOR CALCULATION OF SCATTERING ELEMENTS (COMPUTATIONAL ELECTROMAGNETICS TOOLS)

Approximate methods, discussed so far, provide computationally inexpensive solutions for strictly defined classes of problems. Still, more complex geometries cannot be accurately addressed using any of the previously mentioned approaches.

With the development of computers in the 1960s, numerical methods for solving Maxwell's equations are investigated. These numerical solutions are founded on the analytical formulation that can be evaluated for an arbitrary EM problem, avoiding any assumptions regarding the field or currents distribution, contrarily to the previous approximate solutions. Strictly speaking, numerical solutions of Maxwell's equations are in some sense "approximate" solutions; however approximations introduced in numerical cases are related only to the mathematical implementation of the calculations. Hence, these tools provide valid scattering solutions regardless of any object or wave parameters. Accuracy of these solutions is based on the coding implementation of Maxwell's equations and hardware capabilities.

Numerical solution to Maxwell's equations, defining the Computational Electromagnetics known today, is traced back to work presented by Harrington (Harrington, 1968) and Yee (Yee, 1966). Harrington's work was based on a solution of the Maxwell's equation in integral form, solving the boundary problem by application of Method of Moments (MoM). And it is considered the frequency domain solution. While Yee's approach was based on the differential form Maxwell's equations, and calculations of finite differences. And it is considered the time domain solution. Even though the differential approach is published before the MoM it

received less attention until 1985, which might be caused by a pause in Yee's work on this topic (Shaeffer, 1993). Currently, both time domain and frequency domain approaches are widely utilized, and hybrid solutions and software packages are available.

Following the historical development of the CEM both approaches will be discussed here discussing favorable applications of each method. Of particular interest is the MoM as it is the choice for the research that follows.

2.2.1 Tools based on differential form solution

The differential form of Maxwell's equations is given in Ch.1 (1-4) in vector calculus notation. This set of equations can be rewritten using definitions of vector calculus operators, Faraday's (3) and Ampere's (4) laws in this case will appear as (2.16) and (2.17)¹³.

$$\begin{bmatrix} \mathbf{i}_x & \mathbf{i}_y & \mathbf{i}_z \\ \frac{\partial}{\partial x} & \frac{\partial}{\partial y} & \frac{\partial}{\partial z} \\ E_x & E_y & E_z \end{bmatrix} = -\frac{\partial}{\partial t} \begin{bmatrix} B_x \mathbf{i}_x \\ B_y \mathbf{i}_y \\ B_z \mathbf{i}_z \end{bmatrix} \quad (2.16)$$

$$\begin{bmatrix} \mathbf{i}_x & \mathbf{i}_y & \mathbf{i}_z \\ \frac{\partial}{\partial x} & \frac{\partial}{\partial y} & \frac{\partial}{\partial z} \\ B_x & B_y & B_z \end{bmatrix} = \mu \begin{bmatrix} J_x \mathbf{i}_x \\ J_y \mathbf{i}_y \\ J_z \mathbf{i}_z \end{bmatrix} + \mu \epsilon \frac{\partial}{\partial t} \begin{bmatrix} E_x \mathbf{i}_x \\ E_y \mathbf{i}_y \\ E_z \mathbf{i}_z \end{bmatrix} \quad (2.17)$$

Equations defined by this set of functions can be numerically approximated with finite differences. Finite differences can be applied in both space and time domain and the first derivative is given as (2.18);

¹³ The medium is assumed to be isotropic, linear, and time invariant.

$$\frac{\partial f(p, \Delta p)}{\partial p} = \lim_{\Delta p \rightarrow 0} \frac{f(p + \Delta p) - f(p)}{\Delta p}, \quad (2.18)$$

where f is a function defined at point p and Δp is the discretization step for the function f . The step size is the main factor that determines the accuracy of the numerical method.

The numerical derivation step is applied in both, spatial and time meshing of the Finite Difference Time Domain (FDTD) problem, used as an example. An object of interest is approximated with a volumetric grid, consisting of predefined grid elements, usually cubes. The electric and magnetic fields are calculated at these grid elements with exact calculation points offset by half the grid element. Such offsets exist in order to accommodate Faraday's and Ampere's law as the circulation of the field vector depends on the flux through the bounded surface. From Maxwell's equations in integral form it can be seen that the electric circulation through the closed loop is equal to the change of the magnetic field while the magnetic field is proportional to the density of conduction and displacement (polarization) currents through the loop.

With the mesh element determining the accuracy and time cost of the solution, a tradeoff between the fine meshing of an object, and computational complexity, in terms of fields calculation points, has to be found. The maximal mesh element that provides satisfying accuracy and gradual change in the calculated fields is insured for mesh element size smaller than $\frac{\lambda_g}{10}$ (Yee, 1966), where λ_g is the guided wavelength in the medium where meshing is applied (i.e. in scatterer dielectric or in the free space).

The scatterer topology is of high importance for achieving precise scattering calculations. On the other hand, using the maximal mesh element might result in coarse, step like approximation of the object topology. In such situations sub-gridding is introduced to refine of the original meshing and better approximate topology representation. Sub-gridding is only introduced at locations where necessary, determined by an in software criterion. Sub-gridding the complete object would introduce unnecessary simulation time increase, due to the larger number of calculation points.

Similar to the spatial step discussed, the maximal time step has to be determined. For the numerical approximation to be accurate, requirement of the field propagation effects across the scatterer has to be satisfied on the grid dimensional level. Therefore, the time step must be short enough to account for propagation before the neighboring mesh element is affected. For the maximal mesh element step of $\frac{\lambda_g}{10}$ time step can be derived (2.19).

$$\Delta t \sqrt{\frac{1}{\mu\varepsilon}} < \frac{\lambda_g}{10} \rightarrow \Delta t < \frac{\lambda_g}{10c_g} \rightarrow \Delta t = \frac{1}{10f} \quad (2.19)$$

In the (2.19) c_g is the wave propagation speed in the medium, and f is the frequency of interest. The equation demonstrates that the time step is dictated by the frequency of interest. This observation is interesting as frequency based requirements are typically attributed to integral techniques instead of temporal techniques.

Because calculation of finite differences is not computationally intensive, the method is a desirable tool in the computational electromagnetics. Problems in the

computational effectiveness arise in open boundary (radiation) cases. As the differential solution of Maxwell's equations is based upon the finite differences the entire medium needs to be gridded. This is impractical as RCS is evaluated at infinite distance from the scatterer. Luckily, the aforementioned infinite distance criterion is relaxed to the far-field requirement for which the scattered field can be decomposed. Nevertheless, far-field depends on the maximal dimension of the object, and may still require discretization of a large volume. In order to overcome this issue, software implementations usually require the user to define complete meshing volume and thus bound space.

Adding to the complexity of the original problem, the end of a discretized volume requires a boundary condition of its own. In the original differential method approaches this boundary condition of the meshed volume tended to produce spurious reflections that jeopardize RCS calculations. A solution to this problem was introduced by the absorbing boundary condition (ABC) that eliminates spurious reflections. All of the issues mentioned led portion of the scientific community to consider FDTD impractical calculating RCS (Shaeffer, 1993).

In conclusion, the theoretical setting of the differential approach for solving Maxwell's equations is favorable and more practical in cases of closed geometries. It is considered especially favorable for solving the closed space heterogeneous problems in which the dielectric properties can be set differently at each grid element; as this is computationally expensive in integral approach solvers.

2.2.2 Tools based on integral form solution

The foundation of computational electromagnetics is based upon Yee's and Harrington's work. The EM Field solution by MoM, published by Harrington (Harrington, 1968) is the first book on the topic which defines the area of integral formulation computational electromagnetics.

Depending on the application, different types of integral equation problems can be defined. Here we distinguish Volume Integral Equations (VIE) and Surface Integral Equations (SIE). Both of them are used for solution of the scattering problem using either volumetric (VIE) or surface (SIE) induced currents. This difference comes at the computational complexity as defining an arbitrary function for volumetric distributions requires at least three coefficients (one for each axis) while, for surface distribution number of unknown coefficients is two. Thus, VIE usually has lower time efficiency compared to SIE, except for case of highly inhomogeneous media. In the remainder of the dissertation only SIE MoM is considered as scatterers of main interest are usually modeled as single or dual layer homogeneous objects.

Techniques applied for solving these equations belong to the MoM approach. MoM is the approach for solving linear operator equations, where by operator equations we consider integral field equations. The application of MoM to scattering problems is generally performed in following set of steps (Kolundzija & Djordjevic, 2002):

- Linear operator function is defined as $L(f) = g$, where L is the linear operator, g is the known function (excitation), and f is the unknown function to be determined (response/currents).

- An approximation of unknown currents by finite series of known (basis) functions multiplied by unknown coefficients (2.20). Where f_a is the approximation of the original function f , and f_i are known (basis) functions and a_i are the unknown coefficients.

$$f_a = \sum_{i=1}^N a_i f_i \quad (2.20)$$

- The approximation is then substituted into the linear operator function.
- The linear operator function is then multiplied by a set of known test (weighting) function transforming it into set of linear equations.
- The system of linear equations is then solved for the unknown coefficients.
- Induced currents are then evaluated using calculated “unknown” coefficients and known functions.

The set of linear equations is usually represented in a matrix form, which is solved for the unknown coefficients using LU (lower-upper) decomposition or similar methods (WIPL-D, 2015). Once all of the induced currents are known, the calculation of the scattering fields is relatively straight forward.

In order to provide a brief insight into the operator functions used for the calculation of scattered fields, electric and magnetic field operators $L(\mathbf{J}_s)$ and $K(\mathbf{J}_s)$ are (2.21) and (2.22) as in the Ch.3.3.4 of the (Kolundzija & Djordjevic, 2002).

$$L(\mathbf{J}_s) = \frac{\gamma^2}{4\pi} \int_S \left\{ \mathbf{J}_s(\mathbf{r}') \frac{1}{\gamma R} + \frac{\nabla_s \cdot \mathbf{J}_s(\mathbf{r}')}{\gamma} \mathbf{i}_R \left[\frac{1}{\gamma R} + \frac{1}{(\gamma R)^2} \right] \right\} e^{-\gamma R} dS' \quad (2.21)$$

$$K(\mathbf{J}_s) = -\frac{\gamma^2}{4\pi} \int_S \mathbf{J}_s(\mathbf{r}') \times \mathbf{i}_R \left[\frac{1}{\gamma R} + \frac{1}{(\gamma R)^2} \right] e^{-\gamma R} dS' \quad (2.22)$$

Where $\gamma = j\omega\sqrt{\mu\epsilon}$ is the propagation constant, \mathbf{J}_s are the induced surface currents on the surface S' . Approximated variable in the operator equations is the surface current which is approximated using (2.20). Operators are then applied to the Maxwell's

equations for fields (2.23) and (2.24), where Z is the free space impedance (Kolundzija & Djordjevic, 2002).

$$\mathbf{E} = -Z\mathbf{L}(\mathbf{J}_s) \quad (2.23)$$

$$\mathbf{H} = -\mathbf{K}(\mathbf{J}_s) \quad (2.24)$$

The implementation of the MoM to the calculation of the EM fields is a challenging and active research topic.

2.3 DUAL POLARIZATION (POLARIMETRIC) SCATTERING

Scattering is an inevitable process in each interaction of an object with EM waves, and the intensity of the scattered wave depends, among other factors, on the polarization of the incident wave. Therefore, scattered field from an object illuminated with waves of different polarization will result in different returns, depending on the polarization of the incident field. In the case of scatterer illumination with two linear and orthogonal polarizations such as E_ϕ , which will be considered horizontal (H) polarization in the text, and E_θ polarization, vertical (V) in the following text, scattering returns are described by the backscattering matrix:

$$\mathbf{S} = \begin{bmatrix} S_{hh} & S_{hv} \\ S_{vh} & S_{vv} \end{bmatrix}, \quad (2.25)$$

where scattering element S_{hh} is defined for the case of horizontal incident (horizontal transmitted by radar) and horizontal scattered (horizontal received by radar) field, S_{hv} is the vertical incident field and horizontal scattered field, S_{vh} is the horizontal incident and vertical scattered field and S_{vv} is the vertical incident and vertical

scattered field¹⁴. Each of the backscattering matrix elements is defined according to the scattering element definition (2.5).

Information about physical properties of a scatterer itself is contained in the scattered waves, and significant to the understanding of weather phenomena (Zrnica & Ryzhkov, 1999). Embedded in scattering elements is information regarding the microphysical properties of scatterers from which, under Born assumption, microphysical properties of the scatterer ensemble can be deduced (Doviak & Zrnica, 2006).

The scattering elements on the main diagonal of the scattering matrix are referred to as co-polar returns, as they are proportional to the intensity of co-polar scattered field. Off-diagonal scattering elements are called depolarization elements, as they depend on the intensity of the wave scattered in the polarization orthogonal to the incident field polarization¹⁵. Depolarization by a single scatterer, in cases of homogeneous dielectric bodies, is caused by irregular shapes or if symmetry axis of hydrometeors are not collinear with the incident electric field. This occurs in most hydrometeors and represents strong evidence of their existence as will be shown later.

2.3.1 Geometry of polarimetric scattering

Information on the particle's non-spherical shape, embedded in the depolarization scattering elements s_{hv} and s_{vh} , is coupled with the particle orientation information,

¹⁴ Convention used in electrical networks is applied here. In this case second subscript represents the orientation of incident field while first subscript is the orientation of the scattered field.

¹⁵ In case of linear polarizations that are considered in this dissertation these elements are linear depolarization coefficients. For the circular polarization these elements are called circular depolarization coefficients, representing the return in the opposite circumference from the incident wave.

which is also related to the difference of the co-polar scattering elements S_{hh} and S_{vv} . If the scatterer's orientation is collinear with the incident electric fields, its axis ratio can be determined from the intensities of the co-polar scattering elements. However, it should be noted that as the actual hydrometeor may be canted (tilted) the inferred axis ratio would be smaller and could be called apparent axis ratio.

To fully define the problem one must start with the particle centered coordinate system as in Fig. 2.3.

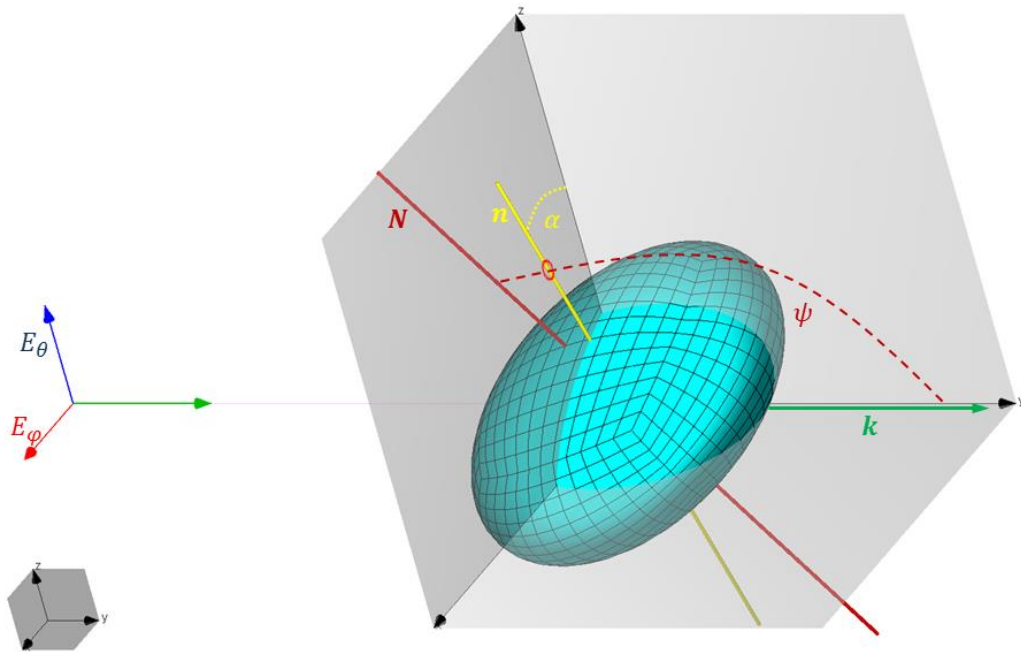


Figure 2.3 - Coordinate system centered on a scatterer.

For this coordinate system the following definitions apply: hydrometeor axis of symmetry \mathbf{N} , EM field propagation vector \mathbf{k} , and the plane of polarization xOz . The angles between the vertical axis (z in the Fig. 2.3) and projection of the hydrometeor's

symmetry axis \mathbf{n} to the plane of polarization (xOz) is the canting angle α in the plane of polarization. In the most general case hydrometeor's axis of symmetry may be out of the polarization plane. The angle between the direction of propagation \mathbf{k} and the hydrometeor's symmetry axis defines the scatterer's orientation angle ψ . For the sake of understanding, the complement to this angle is the symmetry axis deviation out of the polarization plane (canting from the plane of polarization).

Finally, the angle dependence of the scattering elements, in meteorological applications, is usually defined by canting and orientation angles. This set of angles is used in describing the angular orientation of the backscattered wave intensity.

2.4 THE BACKSCATTERED COVARIANCE MATRIX

Waves scattered by the ensembles of hydrometeors in the scattering (resolution) volumes are sequentially received by the radar antenna. An EM wave, at the ports of the antenna, produces the oscillating voltage. This voltage fluctuates in amplitude and phase about the frequency of the carrier wave, shifted by the Doppler component due to the radial movement of the scatterers inside the scattering volume. For the simplicity, herein zero Doppler shift and phase fluctuations will be considered and the demodulated voltage is considered. Under such assumptions, the voltage at the antenna ports will be given by (Dragovic , 2002):

$$\begin{bmatrix} V_h \\ V_v \end{bmatrix} = \sum_{j=1}^M \sum_{i=1}^N \frac{\lambda}{\pi} \cdot \begin{bmatrix} F_{hh} & F_{vh} \\ F_{hv} & F_{vv} \end{bmatrix} \frac{e^{-j\beta r}}{r} \cdot \begin{bmatrix} S_{hh} & S_{hv} \\ S_{vh} & S_{vv} \end{bmatrix}_{j,i} \cdot \frac{j}{2\pi} \sqrt{\frac{\mu_0}{\epsilon_0}} \frac{e^{-j\beta r}}{r} \begin{bmatrix} F_{hh} & F_{hv} \\ F_{vh} & F_{vv} \end{bmatrix} \begin{bmatrix} V_h^{(TX)} \\ V_v^{(TX)} \end{bmatrix}, \quad (2.26)$$

where, F_{xy} are co-polar and cross-polar antenna patterns, $V_{h,v}^{(TX)}$ are voltages fed to the

transmit antenna port and $V_{h,v}$ are instantaneous voltages originated from the ensemble of all scatterers in the scattering volume on reception.

Due to the nature of weather signal, mean value of received signal's voltage is zero. Thus, extraction of the information carried by the scattered waves is done by examining the second order moments of the received signals. These second order moments are linearly proportional to the ensemble averages of scattering elements' products as (Zrnić, 1991):

$$\mathbf{C} = \begin{bmatrix} \langle S_{hh}S_{hh}^* \rangle & \langle S_{hv}S_{hh}^* \rangle & \langle S_{vh}S_{hh}^* \rangle & \langle S_{vv}S_{hh}^* \rangle \\ \langle S_{hh}S_{hv}^* \rangle & \langle S_{hv}S_{hv}^* \rangle & \langle S_{vh}S_{hv}^* \rangle & \langle S_{vv}S_{hv}^* \rangle \\ \langle S_{hh}S_{vh}^* \rangle & \langle S_{hv}S_{vh}^* \rangle & \langle S_{vh}S_{vh}^* \rangle & \langle S_{vv}S_{vh}^* \rangle \\ \langle S_{hh}S_{vv}^* \rangle & \langle S_{hv}S_{vv}^* \rangle & \langle S_{vh}S_{vv}^* \rangle & \langle S_{vv}S_{vv}^* \rangle \end{bmatrix}; \quad (2.27)$$

which can be simplified to:

$$\mathbf{C} \approx_{\{S_{hv}=S_{vh}\}} \begin{bmatrix} \langle |S_{hh}|^2 \rangle & \langle S_{hv}S_{hh}^* \rangle & \langle S_{vv}S_{hh}^* \rangle \\ \langle S_{hh}S_{hv}^* \rangle & \langle |S_{hv}|^2 \rangle & \langle S_{vv}S_{hv}^* \rangle \\ \langle S_{hh}S_{vv}^* \rangle & \langle S_{hv}S_{vv}^* \rangle & \langle |S_{vv}|^2 \rangle \end{bmatrix}, \quad (2.28)$$

where angle brackets denote ensemble averaging over hydrometeors' properties and asterisk is used for complex conjugates as all of the scattering elements are complex. The full 4x4 covariance matrix can be reduced under the condition $S_{hv} = S_{vh}$ to the 3x3 covariance matrix given by (2.28).

Elements of the reduced covariance matrix are complex; however the diagonal elements represent the magnitudes of the ensemble averages of scatterers while the off-diagonal elements contain both magnitude and phase information.

2.5 METEOROLOGICAL POLARIMETRIC VARIABLES FROM THE BACKSCATTERED COVARIANCE MATRIX

Scattering elements contain physical information about particles and therefore, their ensemble averages carry bulk physical information about the ensemble. De-embedding of the microphysical information, from the scattering elements constituting the covariance matrix, is done by analyzing the polarimetric variables obtained by the fully polarimetric radar.

The covariance matrix has six independent elements (Ioannidis & Hammers, 1979) that by themselves or combined comprise the backscattering polarimetric variables as follows:

The second order moment of the horizontal co-polar scattering element (\mathbf{C}_{11}) is proportional to the power scattered in the co-polar H field. The power scattered defines the Horizontal polarization radar Reflectivity factor given by the (2.29).

$$Z_h = \frac{4\lambda^4}{\pi^4 |K_W|^2} \langle |s_{hh}|^2 \rangle C_D, \quad (2.29)$$

where the dielectric factor of water $K_W = \frac{\epsilon_{H_2O} - 1}{\epsilon_{H_2O} + 2}$ (Doviak & Zrnic, 2006) and C_D is the overall concentration function of scatterers in one cubic meter. Definition of the dielectric factor is such that, for small scatterers, Z_h will be proportional to the Rayleigh scattering elements given by (2.7) (Kumijan, 2012).

The definition applies to the vertical power scattered as well (\mathbf{C}_{33} element of the covariance matrix) – Vertical Reflectivity factor (2.30):

$$Z_v = \frac{4\lambda^4}{\pi^4 |K_W|^2} \langle |s_{vv}|^2 \rangle C_D. \quad (2.30)$$

The ratio of the co-polar backscattered powers is called Differential Reflectivity (2.31). This variable is not part of the original nine (six, after pairs are eliminated) quantities carried by the covariance matrix. However, differential reflectivity is one of the most important variables evaluated and used in the weather radar community, because it is independent on the concentration of hydrometeors

$$Z_{dr} = \frac{\langle |s_{hh}|^2 \rangle}{\langle |s_{vv}|^2 \rangle}. \quad (2.31)$$

Powers determined by the middle elements of the full covariance matrix represent the depolarization powers. Information carried by these quantities, normalized to the co-polar powers is defined as the Linear Depolarization Ratio (L_{dr}). Although, L_{dr} can be evaluated for both polarization, commonly used is the depolarization ratio of horizontal polarization; the two are related through the differential reflectivity, and are defined as:

$$L_{dr}^{(h)} = \frac{\langle |s_{vh}|^2 \rangle}{\langle |s_{hh}|^2 \rangle}, \quad (2.32)$$

$$L_{dr}^{(v)} = \frac{\langle |s_{hv}|^2 \rangle}{\langle |s_{vv}|^2 \rangle}. \quad (2.33)$$

The off-diagonal elements of the reduced covariance matrix are in pairs, whereby one member is a conjugate of the other. Both their magnitude and phase are evaluated and used. The co-polar correlation coefficient ρ_{HV} and the differential phase δ are defined as:

$$\rho_{hv} = \frac{\langle s_{vv}s_{hh}^* \rangle}{\sqrt{\langle |s_{hh}|^2 \rangle \langle |s_{vv}|^2 \rangle}}, \quad (2.34)$$

$$\delta = \arg \rho_{hv}. \quad (2.35)$$

Remaining off-diagonal elements of the covariance matrix are used to obtain the co-cross-polar correlation coefficients (Ryzhkov, 2001) and in analogy with the co-polar correlation coefficients are defined as (2.36) and (2.37) (Zrnić, 1991); (Ryzhkov, 2001):

$$\rho_{xh} = \frac{\langle s_{hv}s_{hh}^* \rangle}{\sqrt{\langle |s_{hv}|^2 \rangle \langle |s_{hh}|^2 \rangle}}, \quad (2.36)$$

$$\rho_{xv} = \frac{\langle s_{hv}s_{vv}^* \rangle}{\sqrt{\langle |s_{hv}|^2 \rangle \langle |s_{vv}|^2 \rangle}}. \quad (2.37)$$

The usefulness of these parameters has been uncertain, although, studies indicate they have potential to reveal information about the mean canting angle of hydrometeors (Ryzhkov, 2001); (Ryzhkov, et al., 2002).

Phases of the co-cross-polarization coefficients, defined by (2.38) and (2.39) have not been widely exploited. This may be tied to the unavailability of these variables in the WSR-88D's mode of operation as well as issues related to signal strength and therefore range for which they can be evaluated.

$$\delta_{cr}^{(h)} = \arg(s_{hv} - s_{hh}^*), \quad (2.38)$$

$$\delta_{cr}^{(v)} = \arg(s_{hv} - s_{vv}^*). \quad (2.39)$$

Polarimetric variables defined so far are combinations of the elements of covariance matrix in linear basis. Besides the linear polarimetric covariance matrix, the circular

polarimetric covariance matrix can be constructed. This matrix contains products of the right and left hand circular polarization returns. One of the first polarimetric quantities measured from the elements of this matrix is the circular depolarization ratio (C_{dr}). The main feature of C_{dr} is its independence of hydrometeor orientation. Circular polarization ratio is primarily determined by the shape and dielectric composition of the hydrometeors.

Approximation of the circular depolarization ratio using the simultaneous transmission/reception linear polarimetric radar is described by Matrosov (2.40) (Matrosov, 2005).

$$C_{dr} = \frac{\langle |s_{hh} - s_{vv}|^2 \rangle}{\langle |s_{hh} + s_{vv}|^2 \rangle} = \frac{\langle |s_{hh}|^2 \rangle + \langle |s_{vv}|^2 \rangle - 2Re(\langle s_{vv} s_{hh}^* \rangle)}{\langle |s_{hh}|^2 \rangle + \langle |s_{vv}|^2 \rangle + 2Re(\langle s_{vv} s_{hh}^* \rangle)} \quad (2.40)$$

3. MODELING OF METEOROLOGICAL SCATTERING

Modeling of meteorological scattering and weather radar signatures using different types of hydrometeor models have been of interest in the meteorological community. Early approaches considered scattering of spherical particles in the Rayleigh regime and were driven by the need to improve quantitative precipitation estimates. Spherical models were quickly replaced by spheroidal models, which provide a better representation of raindrop geometry. Additional motivation for the emergence of meteorological modeling was the development of polarimetric radars. Polarimetric variables contain additional microphysical information about the precipitation being observed and therefore require more precise modeling in order to fully interpret the data. However, current modeling techniques are still based on the assumption of spheroidal shapes and only allow for different dielectric properties, dimensions and dual layers.

Significant changes to the current approaches and the development of novel tools for a larger variety of hydrometeors are still unavailable. Nevertheless, electromagnetic modeling perspectives for polarimetric meteorological modeling have been identified since the early 1990s (Zrnić & Aydin, 1992); (Aydin & Zrnić, 1992). The hydrometeor properties required at the time for scatterer modeling were the dielectric properties and shape of the object, which would resemble observed hydrometeors. Still, scatterer modeling approaches allowing more complex geometries have not replaced approximate tools based on spheroidal shapes. The issue of simplified (spheroidal) modeling was recognized by Aydin and Zrnić surveying approaches in use of scatterer modeling. Thereby, the authors pointed out that the application of the

most commonly used T-Matrix (Ch.2.1.4) is limited to the calculation of the scattering parameters only for smooth particles of sizes up to 3λ and axis ratios of about 4. In a meteorological context, this means that the application of the T-Matrix is limited to the calculation of raindrop scattering and, to some extent, of dry and melting hailstone scattering, with no ability to introduce shape perturbations.

Treatment of hydrometeors with complex geometries according to Aydin and Zrnić (Aydin & Zrnić, 1992) is possible through the application of the Discrete Dipole Approximation (Ch.2.1.5) which also faces multiple limitations. For the first time¹⁶ in the literature, the authors advocate the use of the CEM technique for the modeling of meteorological scattering applications. The CEM technique advocated is the Finite Difference Time Domain (Ch.2.2.1) which has been identified to produce “acceptable results over narrow frequency band” (Aydin & Zrnić, 1992). Unfortunately, elaboration on the use of CEM techniques is not found. The extensive time needed for the computation of the scattering matrices using any of these sophisticated tools prompted the authors to propose the storage of scattering results for different hydrometeors types. The findings of Aydin and Zrnić are of great importance to the development of the work presented herein as the issues related to the shape properties of the hydrometeors have remained unaddressed thus far; the structure of the modeling algorithm presented are applicable in the current modeling advances.

In the following section a distinction between hydrometeor scattering (meteorological scattering) and hydrometeor scatterer modeling (meteorological scatterer modeling) needs to be defined. Under hydrometeor scattering, the process of modeling ensemble

¹⁶ As far as author of this dissertation is aware of.

scattering under the Born approximation is considered (in which the power density of the incident field is not significantly altered by the scatterers in it; mutual coupling effects are neglected (Doviak & Zrnic, 2006). In the case of the later, the hydrometeor scatterer modeling considers the problem of backscattering of a singular physical hydrometeor (the calculation of the backscattering matrix).

3.1 IMPORTANCE OF MODELING OF HYDROMETEOR SCATTERING

Modeling in meteorology is applied for many different purposes, ranging from forecast models which are used daily for weather prediction to more specific model types, such as for hydrometeor scattering. Modeling hydrometeor scattering, as mentioned, became more important in order to provide a better understanding of polarimetric weather radar observations. Significant amounts of research have been conducted using the polarimetric variables to gain a better understanding of precipitation. Currently, the polarimetric variables are used in algorithms for the automatic detection and recognition of precipitation (Park, et al., 2009) as their values are determined by the number density, orientations, dielectric properties, shape and sizes of hydrometeors (Zrnić & Ryzhkov, 1999).

Polarimetric signatures are a consequence of microphysical processes, some of which can be included in the scatterer model itself. Depolarization properties of the scatterer due to its non-spherical shape and canting are typically characteristic of a hydrometeor class. This allows, for example, discrimination between different precipitation types, quantitative discrimination of hail sizes and precise differentiation of hail from pure rain. Additionally, identification of electrically active storms,

biological scatterers, and the presence of other anthropogenic scatterers such as chaff and its effects on precipitation measurements are possible using the polarimetric variables (Zrnić & Ryzhkov, 1999). Co-cross-polar correlation coefficients are applied in the quantification of the mean canting angle and distributions of hydrometeor orientation (Ryzhkov, et al., 2002; Rasmussen & Heymsfield, 1987) while recent studies have revealed the possibility of supercooled water identification at high altitudes using the Circular Depolarization Ratio approximated by the terms of the linear polarimetric covariance matrix (Ryzhkov, et al., 2014).

The capabilities of polarimetric radars are often illustrated using simple computer models in which hydrometeor properties are varied to simulate their effect on the polarimetric signatures. Such an approach is justified if the modeling replicates the process occurring in nature. On the other hand, understanding microphysical properties of scatterers in the radar resolution volume based on the values of polarimetric variables is an inverse problem that often is non-unique. Using the same method as in the calculation of the polarimetric variables, the inverse problem can be defined as follows: For a set of scattering models $\mathbf{X} \left(D, \varepsilon_{1..n}, R, \frac{b}{a}, \dots \right)_{n \times 1}$ the polarimetric signature \mathbf{P} can be reproduced if a member of the set resembles actual hydrometeor properties and per unit volume distributions $\mathbf{C}_{n \times 1}$ of scatterers within the unit volume.

Solving this inverse problem is especially important as the radar observations are not directly correlated with the hydrometeor microphysics but are the consequence of the microphysical processes. Solving the inverse problem is computationally expensive

and thus simplifications that do not jeopardize the models' physics are sought. Obviously, the quality of the microphysical retrieval depends on the quality of the model, resulting in an increased demand for more precise modeling of hydrometeors and polarimetric variables.

3.2 CURRENT MODELING PROCEDURES

Overall, the process of polarimetric variable modeling can be separated into different stages based on the type of modeling applied. These stages are identified as:

- Precipitation modeling;
- Scatterer modeling (modeling of scattering matrix elements);
- Calculation of the polarimetric variables.

Precipitation modeling involves mathematical representation of hydrometeor size distributions and types based on microphysical environment. This stage of modeling is of interest in the meteorological community and it is briefly addressed in this dissertation through the overview of the existing Hebrew University Cloud Model (HUCM).

Of primary interest are the two remaining stages which are addressed in detail in the following sections. An overview of the current approaches to modeling these processes and identification of the simplifications, issues and limitations of them will be discussed. An important portion of the dissertation is the quantification of the error introduced by the existing simplifications and their influence to the overall model accuracy.

3.2.1 Precipitation modeling

To provide an overview of the precipitation modeling and its output, the Hebrew University Cloud Model (HUCM) is briefly discussed. The primary task of the HUCM is to provide distributions of the microphysical properties of hydrometeors constituting the radar resolution volume. The microphysics of the HUCM are founded on the kinetic equations for different types of hydrometeors having different types of particles as cloud condensation nuclei (Ryzhkov, et al., 2011). Maximum sizes and fall velocities are defined for each of the hydrometeor types based on the rules of spontaneous and collisional breakup of drops, rimming, and aggregation of snow and so on. The processes implemented in the HUCM are used for determining the physical properties and hydrometeor types based on the input parameters for each of the processes including drop nucleation and diffusion growth, ice nucleation and freezing, and collisions.

The output of the model is the spectral bin size distributions for hydrometeors of each type. Such distributions define the concentration of each hydrometeor type over the dimensional range which is discretized into a finite number of bins. Spectral bin modeling of size distributions is preferred over models with bulk parameterizations due to difficulties bulk distributions face in reproducing polarimetric signatures (Ryzhkov, et al., 2011). Readers interested in a more thorough explanation of meteorological modeling and related processes are directed to Khain, et al., 2000; Khain, et al., 2004; Khain, et al., 2008; Khain, et al., 2011.

3.2.2 Scatterer modeling (Modeling of scattering matrix elements)

The modeling of hydrometers introduced from the HUCM is done via the Polarimetric Radar Observation Operator (PROO) (Ryzhkov, et al., 2011). Techniques applied in PROO vary between the Rayleigh approximation of scattering elements (Ch.2.1.1) and the T-Matrix approach (Ch.2.1.4) depending upon the resonance parameter defined by (2.6). All hydrometeor types are modeled as spheroids with variable axis ratios and dielectric properties. Scattering models are either solid ice, ice mixtures with water and air or water coated scatterers. The importance of two layer modeling of scatterers is further examined in (Ryzhkov, et al., 2011). Conclusions are drawn by examining the polarimetric variables calculated for both multilayer and uniform scatterers with the corresponding dielectric constant based on the ice density. Differences in the polarimetric variables between single layer and multilayer spheroids are especially pronounced in the case of hail which shows the tendency of producing large errors even for smaller hail (e.g. sizes of $D_{eq} = 20$ mm and axis ratio of 0.8) (Ryzhkov, et al., 2011).

The scatterer properties used in the modeling of polarimetric variables by the PROO are defined based on the hydrometeor type. The parameters describing hydrometeor shape and dielectric properties important for the work shown in the later sections of this dissertation are presented below (Ryzhkov, et al., 2011):

a. *Axis ratio of hydrometeors depending on their type*

1) Axis ratio of raindrops

According to the formulation given in (Brandes, et al., 2002) the axis ratio of raindrop spheroids is given by:

$$AR_{rd} = 0.9951 + 0.02510D_{eq} - 0.03644D_{eq}^2 + 005303D_{eq}^3 - 0.0002492D_{eq}^4, \quad (3.1)$$

where AR_{rd} is the axis ratio of the raindrop and D_{eq} is the equivolume diameter given in millimeters.

2) Axis ratio of dry hail and graupel

The axis ratio of dry (solid ice) hail and graupel according to (Straka, et al., 2000) varies between 0.6 and 0.9. Generally, the following formulation is used in modeling:

$$AR_{dh} = 1 - 0.02D_{eq}; D_{eq} < 10 \text{ mm}; \quad (3.2)$$

$$AR_{dh} = 0.8; D_{eq} \geq 10 \text{ mm}. \quad (3.3)$$

3) Axis ratio of melting hail and graupel

The axis ratio of melting hail is empirically determined in (Rasmussen, et al., 1984):

$$AR_{mh} = AR_{dh} - 5(AR_{dh} - 0.8)f_{mw}; \quad f_{mw} < 0.2;$$

$$AR_{mh} = 0.88 - 0.4f_{mw}; \quad 0.2 \leq f_{mw} < 0.8;$$

$$AR_{mh} = 2.8 - 4AR_{rd} + 5(AR_{rd} - 0.56)f_{mw}; \quad f_{mw} \geq 0.8, \quad (3.4)$$

where f_{mw} represents the mass water fraction.

b. Dielectric permittivity

- 1) The dielectric permittivity of water and solid ice (Ray, 1972) is given by:

$$\varepsilon = \left(\varepsilon_{\infty} + \frac{(\varepsilon_0 - \varepsilon_{\infty}) \left[1 + \left(\frac{\lambda_0}{\lambda} \right)^{1-\alpha} \sin\left(\frac{\alpha\pi}{2}\right) \right]}{1 + 2 \left(\frac{\lambda_0}{\lambda} \right)^{1-\alpha} \sin\left(\frac{\alpha\pi}{2}\right) + \left(\frac{\lambda_0}{\lambda} \right)^{2(1-\alpha)}} \right) - j \left(\frac{(\varepsilon_0 - \varepsilon_{\infty}) \left(\frac{\lambda_0}{\lambda} \right)^{1-\alpha} \cos\left(\frac{\alpha\pi}{2}\right)}{1 + 2 \left(\frac{\lambda_0}{\lambda} \right)^{1-\alpha} \sin\left(\frac{\alpha\pi}{2}\right) + \left(\frac{\lambda_0}{\lambda} \right)^{2(1-\alpha)}} + \frac{\sigma\lambda}{18.8496 \cdot 10^{10}} \right). \quad (3.5)$$

For water constants in (3.5):

$$\varepsilon_0 = 78.54[1 - 4.579 \cdot 10^{-3}(t - 25) + 1.19 \cdot 10^{-5}(t - 25)^2 - 2.81 \cdot 10^{-8}(t - 25)^3];$$

$$\varepsilon_{\infty} = 5.27137 + 0.021647t - 0.00131198t^2;$$

$$\alpha = -16819(t + 273) + 0.0609265;$$

$$\lambda_0 = 0.00033836 e^{\left[\frac{2513.98}{t+273} \right]};$$

$$\sigma = 12.5664 \cdot 10^8.$$

For solid ice, the constants in (3.5) are:

$$\varepsilon_0 = 203.168 + 2.5t + 0.15t^2;$$

$$\varepsilon_{\infty} = 3.168;$$

$$\alpha = 0.288 + 0.0052t + 0.00023t^2;$$

$$\lambda_0 = 0.0009990288 e^{\left[\frac{13200}{(t+273)1.9869} \right]};$$

$$\sigma = 1.26 e^{\left[-\frac{12500}{(t+273)1.9869} \right]},$$

where λ is the wavelength of interest in cm, and t is the temperature in C° .

The scattering elements for hydrometeors with properties defined by the formulas (3.1)-(3.5), are obtained for two principal planes with the angular orientation of the hydrometeor in the polarimetric coordinate system $\alpha = 0^\circ$ and $\psi = 90^\circ$ (Fig. 2.3). The calculated scattering matrix elements for $(\alpha, \psi) = (0^\circ, 90^\circ)$ are equal to f_a and f_b defined previously. Orientation and scattering elements are same to those defined in Fig. 2.2, if the propagation is along $-x$ axis and z is the axis of hydrometeor symmetry.

In general, the orientation of hydrometeors in the scattering volume is not fixed and can be different than the one prescribed in the calculation of the scattering elements above. In PROO the scattering elements are calculated for the case of no canting (in the plane of polarization) and an orientation of the hydrometeor that is perpendicular to the propagation of the electric field ($(\alpha, \psi) = (0^\circ, 90^\circ)$). In a scattering volume, the orientation and canting (in the plane of polarization) of hydrometeors is not known, hence the backscattering matrix element values may differ from the two calculated ones. The “backscattering rule” is employed to account for the orientation (Holt & Shepherd, 1979).

According to the backscattering rule, the matrix elements for spheroids can be extrapolated from the calculated f_b and f_a . The approximation is developed under the assumptions that the original hydrometeor has no cross-polar scattering and that the hydrometeors’ symmetry axis is in the plane of polarization ($\psi = 90^\circ$). See (Holt & Shepherd, 1979) for a more detailed derivation.

The backscattering rule in the PROO is used to obtain the scattering matrix elements for an “arbitrarily oriented spheroidal particle” (Ryzhkov, 2001); (Ryzhkov, et al., 2011) which is different from the original orientation assumption. According to the literature the “backscattering rule” holds only for cases in which $\psi > 80^\circ$ at frequencies up to 35 GHz, conditions that are fulfilled by most hydrometeors with the exception of large hail (Ryzhkov, 2001).

By implementing the backscattering rule the polarimetric scattering matrix is approximated as:

$$\mathbf{S} = \begin{bmatrix} S_{hh} & S_{hv} \\ S_{vh} & S_{vv} \end{bmatrix} = \begin{bmatrix} (f_a - f_b) \sin^2 \psi \sin^2 \alpha + f_b & (f_a - f_b) \sin^2 \psi \sin \alpha \cos \alpha \\ (f_a - f_b) \sin^2 \psi \sin \alpha \cos \alpha & (f_a - f_b) \sin^2 \psi \cos^2 \alpha + f_b \end{bmatrix}. \quad (3.6)$$

If the matrix (3.6) is evaluated for the normal incidence $(\alpha, \psi) = (0^\circ, 90^\circ)$ resulting is matrix (3.7). In the (3.7) one notices the co-polar elements while the cross-polar are annulled. Such a simplification in the backscattering rule should be carefully evaluated as the behavior of co-polar and cross-polar scattering elements for spheroids may not follow such simple behavior especially in resonant sizes.

$$\mathbf{S} = \begin{bmatrix} f_b & 0 \\ 0 & f_a \end{bmatrix} \quad (3.7)$$

3.2.3 Calculation of polarimetric variables

Calculation of the polarimetric variables is the last and the most important portion of the overall modeling process. This section succinctly presents the material from

(Ryzhkov, et al., 2011) which is evaluated to provide detailed insight into current modeling procedures.

Calculation of the polarimetric variables represents the ensemble averaging of the covariance matrix elements for all the scatterers. It must account for hydrometeor concentrations and orientation distributions. Calculation of the polarimetric variables in PROO (Ryzhkov, et al., 2011) is obtained through the covariance matrix created from the approximation of the scattering matrix (3.6).

In the PROO, the reflectivity factor is evaluated using (3.8) under the assumption that the particle shape and size distributions are independent of the distribution of orientations.

$$Z_h = \frac{4\lambda^4}{\pi^4 |K_W|^2} \sum_{i=1}^M \int_0^\infty \{ |f_{bi}|^2 - 2(|f_{bi}|^2 - f_{ai}f_{bi}^* - f_{ai}^*f_{bi}) \langle \sin^2 \psi \sin^2 \alpha \rangle_i + |f_{bi} - f_{ai}|^2 \langle \sin^4 \psi \sin^4 \alpha \rangle_i \} N_i(D) dD, \quad (3.8)$$

where angular brackets denote ensemble average over orientations. The term $2(|f_{bi}|^2 - f_{ai}f_{bi}^* - f_{ai}^*f_{bi})$ is simplified to $2Re\{f_{bi}^*(f_{bi} - f_{ai})\}$, thus equation (3.8) becomes (3.9):

$$Z_h = \frac{4\lambda^4}{\pi^4 |K_W|^2} \sum_{i=1}^M \int_0^\infty \{ |f_{bi}|^2 - 2Re\{f_{bi}^*(f_{bi} - f_{ai})\} \langle \sin^2 \psi \sin^2 \alpha \rangle_i + |f_{bi} - f_{ai}|^2 \langle \sin^4 \psi \sin^4 \alpha \rangle_i \} N_i(D) dD, \quad (3.9)$$

where the summation is over M hydrometeor types (if $M = 2$ there are two hydrometeor types e.g. raindrops and wet hailstones), and integration is over $D \in (0, D_{\max})$ (for simplified notation $D = D_{eq}$) for scattering matrix elements $f_{a,b}$

having the hydrometeor density $N_i(D)$ given in units of inverse meter cubed per millimeter.

Similarly, the radar reflectivity factor for the vertical polarization is (3.10):

$$Z_v = \frac{4\lambda^4}{\pi^4 |K_W|^2} \sum_{i=1}^M \int_0^\infty \{ |f_{bi}|^2 - 2Re\{f_{bi}^*(f_{bi} - f_{ai})\} \langle \sin^2 \psi \sin^2 \alpha \rangle_i + |f_{bi} - f_{ai}|^2 \langle \sin^4 \psi \sin^4 \alpha \rangle_i \} N_i(D) dD. \quad (3.10)$$

The Linear Depolarization Ratio is (3.11):

$$L_{dr}^{(h,v)} = \frac{4\lambda^4}{\pi^4 |K_W|^2} \frac{1}{Z_{h,v}} \sum_{i=1}^M \int_0^\infty \{ |f_{ai} - f_{bi}|^2 \langle \sin^4 \psi \sin^2 \alpha \cos^2 \alpha \rangle_i \} N_i(D) dD. \quad (3.11)$$

The magnitude of the co-polar correlation coefficient is evaluated through (3.12), and the backscattered differential phase δ is evaluated from the argument of the co-polar correlation coefficient.

$$|\rho_{hv}| = \frac{4\lambda^4}{\pi^4 |K_W|^2} \frac{1}{\sqrt{Z_h Z_v}} \sum_{i=1}^M \left| \int_0^\infty \{ |f_{ai} - f_{bi}|^2 \langle \sin^4 \psi \sin^2 \alpha \sin^2 \alpha \rangle_i - f_{bi} (f_{bi}^* - f_{ai}^*) \langle \sin^2 \psi \sin^2 \alpha \rangle_i f_{bi}^* (f_{bi} - f_{ai}) \langle \sin^2 \psi \cos^2 \alpha \rangle_i \} N_i(D) dD \right|, \quad (3.12)$$

$$\delta = \arg(\rho_{hv}). \quad (3.13)$$

In this dissertation the differences in H, V propagation phases and H, V phase differences in the radar are not considered, only the intrinsic polarimetric properties of scatterers in the resolution volume are modeled.

Co-cross polar correlation coefficients are calculated using (3.14) and (3.15):

$$|\rho_{xh}| = \left(\frac{4\lambda^4}{\pi^4 |K_W|^2} \right)^{\frac{3}{2}} \frac{1}{2Z_h \sqrt{L_{dr}^{(h)}}} \sum_{i=1}^M \left| \int_0^\infty \{ |f_{ai} - f_{bi}|^2 \langle \sin^4 \psi \sin^2 \alpha \sin 2\alpha \rangle_i - \right. \\ \left. f_{bi}^* (f_{bi} - f_{ai}) \langle \sin^2 \psi \sin 2\alpha \rangle_i \} N_i(D) dD \right|, \quad (3.14)$$

$$|\rho_{xv}| = \left(\frac{4\lambda^4}{\pi^4 |K_W|^2} \right)^{\frac{3}{2}} \frac{1}{2Z_v \sqrt{L_{dr}^{(v)}}} \sum_{i=1}^M \left| \int_0^\infty \{ |f_{ai} - f_{bi}|^2 \langle \sin^4 \psi \sin^2 \alpha \sin 2\alpha \rangle_i - \right. \\ \left. f_{bi}^* (f_{bi} - f_{ai}) \langle \sin^2 \psi \sin 2\alpha \rangle_i \} N_i(D) dD \right|. \quad (3.15)$$

Depolarization phases, which are arguments of the co-cross-polar coefficients as well, can be calculated using (3.16), (3.17):

$$\delta_{cr}^{(h)} = \arg \rho_{xh}, \quad (3.16)$$

$$\delta_{cr}^{(v)} = \arg \rho_{xv}. \quad (3.17)$$

The trigonometric functions in equations (3.8) to (3.15) account for the hydrometeor orientations as follows from the scattering matrix (3.6). These trigonometric terms, for which angular brackets denote summation over ensemble particles orientations, if written as (3.18) define the ‘‘angular moments’’ (Ryzhkov, 2001); (Ryzhkov, et al., 2011).

$$A_1 = \langle \sin^2 \psi \cos^2 \alpha \rangle, \quad A_2 = \langle \sin^2 \psi \sin^2 \alpha \rangle, \quad A_3 = \langle \sin^4 \psi \cos^4 \alpha \rangle, \\ A_4 = \langle \sin^4 \psi \sin^4 \alpha \rangle, \quad A_5 = \langle \sin^4 \psi \cos^2 \alpha \sin^2 \alpha \rangle, \quad A_6 = \langle \sin^2 \psi \sin 2\alpha \rangle, \\ A_7 = \langle \sin^4 \psi \cos^2 \alpha \sin 2\alpha \rangle, \quad A_8 = \langle \sin^4 \psi \sin^2 \alpha \sin 2\alpha \rangle, \\ A_9 = A_1 - A_2 = \langle \sin^2 \psi \cos 2\alpha \rangle. \quad (3.18)$$

Angular moments are the only parameters in the PROO that account for hydrometeor orientation. Ergo, solving for their expected values is crucial for the truthful representation of the hydrometeor orientation properties and accuracy of the modeling in general. Analytical solutions to the angular moments are defined for cases resembling conceptual models and observations of the hydrometeor orientations in nature (Ryzhkov, 2001). According to Ryzhkov (Ryzhkov, 2001) these cases are fully chaotic (random) orientation, random orientation in the (hydrometeor's) cardinal plane and a two dimensional axisymmetric Gaussian distribution of orientations.

Important to consider in polarimetric variable modeling is how the set of calculated polarimetric variables is affected by each of the approximations in the simulation steps. Ipso facto, evaluation of the approximations introduced is the first step in the model evaluation.

3.3 EVALUATION OF THE MODELING APPROACH

The quality of the modeling approach can be assessed through the accuracy of the results and the speed of the simulation. The computational complexity in the modeling of polarimetric variables is mainly attributed to the calculation of the polarimetric scattering of hydrometeors. The best simulation performance is usually achieved using multiple approaches for the calculation of the polarimetric backscattering matrix within one simulator. The choice of an approach usually considers its limitations and effectiveness.

The PROO is a good example of diversity for scattering elements calculations as it uses the Rayleigh approximation and the T-Matrix approach depending on the

particle of interest. Multiple algorithms for scattering calculations improve the model's effectiveness and minimize the computational complexity and therefore simulation time. Simulators using scattering calculation diversity are faster and more immune to limitations typical to simulators with only one approach. However, as limitations are mainly due to the scattering element calculations they can be alleviated using robust CEM algorithms at the time effectiveness cost.

Limitations in the hydrometeor properties considered in the PROO are those of the T-Matrix. As mentioned in Ch.2.1.4 and discussed in (Aydin & Zrnić, 1992), the T-Matrix is limited to the calculation of scattering elements for spheroids of a maximal axis ratio around 4 and a smooth surface topology. Additionally, depending on the actual T-Matrix code, models may be limited to one or, as in PROO, two-layer hydrometeor models.

T-Matrix limitations of the maximal axis ratio are a significant deficiency in ice crystal modeling. Furthermore, the modeling of dendritic hydrometeors (snowflakes) is possible only under spheroidal shape assumptions, if the change of axis ratios is in the stable domain of the T-Matrix solution. Limitations are obvious in the calculated values of the co-polar correlation coefficient reaching a minimal value of 0.88 for a chaotic orientation of hydrometeors with varying axis ratios (Kumjian, 2013). This simulated value is substantially larger than observed values. Thus, modeling of the ensembles to resemble low observed co-polar correlation is one of the most challenging tasks in the modeling of polarimetric variables.

The co-polar correlation coefficient ρ_{HV} as elaborated by Ryzhkov in numerous publications (e.g. (Ryzhkov, 2001); (Ryzhkov, et al., 2002); (Ryzhkov, et al., 2011)) depends on the diversity of hydrometeor shapes and orientations as well as the backscattered differential phase properties of scatterers in the scattering volume. A decrease in the ρ_{HV} value is caused by scattering return differences among scatterers, and backscattered differential phase, which is usually associated with the resonant size scatterers (e.g., giant hail) and rough surface scatterers. In the first case, phase differences are due to the resonance effect and appear only at resonant sizes. For the latter case, backscattered differential phase is caused by the scattering surface as the return is a superposition of waves reflected off of each roughness. Consequently, reflected wave differences are proportional to the measure of roughness and dependent on the orientation of the polarization vector.

The inability to reproduce the correlation coefficient drop in present day modeling efforts produces significant drawbacks for quantitative studies related to the ρ_{HV} . Currently, ρ_{HV} is mainly used qualitatively for classification of scatterers while the information contained in its magnitude is not used to its full potential. Evaluation of the PROO for this inability is therefore done in the last step of the polarimetric variable simulation.

Calculation of the polarimetric variables using the PROO is based on the covariance matrix and therefore it is errorless. However, application of the backscattering rule to account for the orientation of the hydrometeors introduces a simplification that is evaluated herein.

3.3.1 Backscattering rule and its applicability

Extrapolation of the scattering element values for canted hydrometeors in the PROO violates limits set by Holt (Holt & Shepherd, 1979). Except for raindrops, precise limitation of the backscattering rule applicability or error evaluation does not exist, resulting in uncertainty of the result accuracy when the backscattering rule is used beyond its application limits (i.e., spherical raindrops up to 35GHz and orientation $\psi \leq 80^\circ$).

Quantification of the backscattering rule extrapolation error is illustrated by examples chosen to represent different types of precipitation. These are: 7.95 mm equivolume diameter raindrop at a temperature of $20\text{ }^\circ\text{C}$, axis ratio of 0.56 and dielectric permittivity of $\varepsilon = 75.6 - j8.9$; solid ice (“dry”) hailstone with an axis ratio of 0.7, physical diameter of 50 mm and dielectric permittivity of $\varepsilon = 3.16 - j0.0017$; water coated (“wet”) hailstone modeled as dual layer concentric spheroid of axis ratios 0.7 and with a physical diameter of the ice core of 50 mm. The thickness of the water coating is evaluated through the Rasmussen’s (Rasmussen & Heymsfield, 1987) formula for maximum water content prior to shedding.

Choosing these particular hydrometeors is expected to depict bounds of errors that influence polarimetric variable simulations for different hydrometeor types. The largest error for raindrops is expected for the largest equivolume diameter, while for hailstones the resonant size at the transition zone from large to giant hail is considered to be most prone to substantial extrapolation error.

Scattering elements for comparison are obtained using MoM CEM software WIPL-D (Kolundzija & Djordjevic, 2002) and the backscattering rule for horizontal polarization. In figures 3.1-3.3, scattering elements are calculated for each orientation while the backscattering rule (angular moments) extrapolation is evaluated by (3.6) using $f_{a,b}$ values also calculated by WIPL-D.

The orientations considered in Figs. 3.1-3.3 are in the $\psi \in (90^\circ, 0^\circ)$ range, allowing for simulations of vertically pointing radar observations (cloud radars, airborne radars etc.). Canting angles of $\alpha = 0^\circ$ and $\alpha = 40^\circ$ are used in comparison illustrating a decrease of the extrapolation error with increasing canting angle.

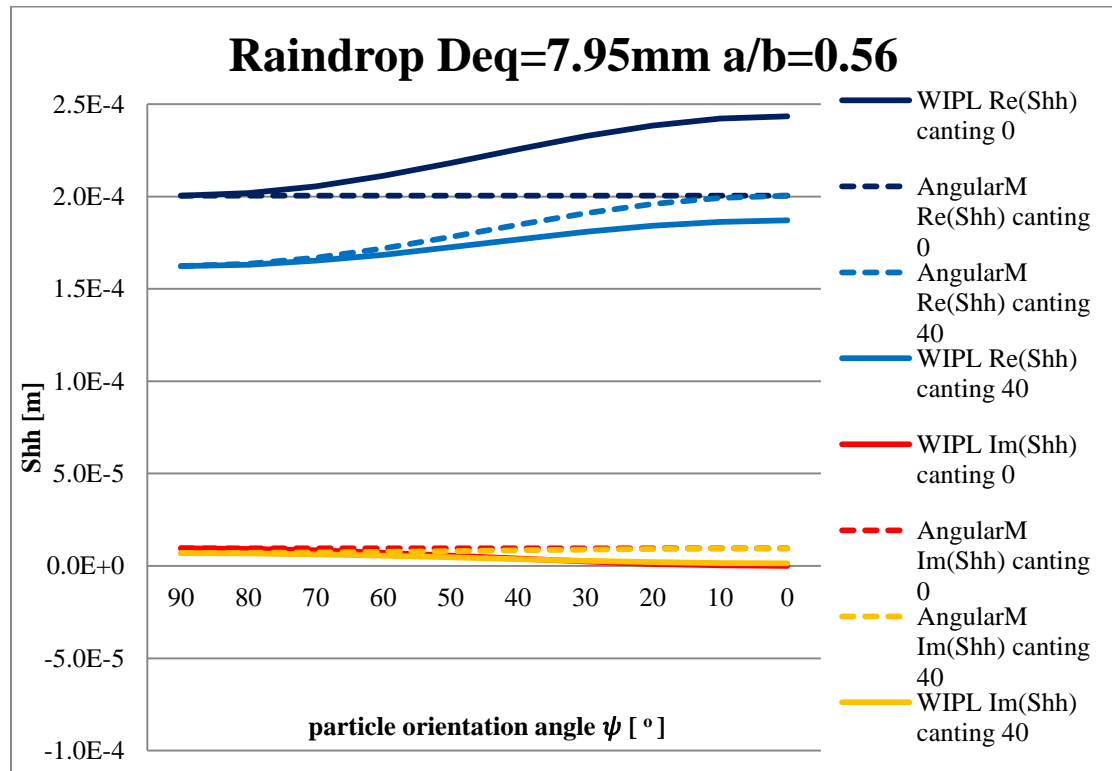


Figure 3.1 - Accuracy evaluation of the backscattering rule. Exact values of S_{hh} for a raindrop are depicted with a solid curve. Approximation values using the backscattering rule (Angular Moments) are depicted with dashed lines.

The solid curves in Fig. 3.1 represent the exact values of the scattering element S_{hh} obtained using WIPL-D software; the dashed curves are obtained using the backscattering rule (3.6). Angular orientations are given in decreasing order as the normal incidence (and the approximation starting point) is $\psi = 90^\circ$. From Fig. 3.1 follows the maximal discrepancy (error) in the extrapolation of the scattering element is for no canting and a particle orientation that is collinear with the wave propagation (for case of radars looking vertically). Nevertheless, the magnitude of the error for raindrops is not very significant as the maximal error introduced in the calculation of the radar reflectivity factor Z_H would be less than 1 dB¹⁷.

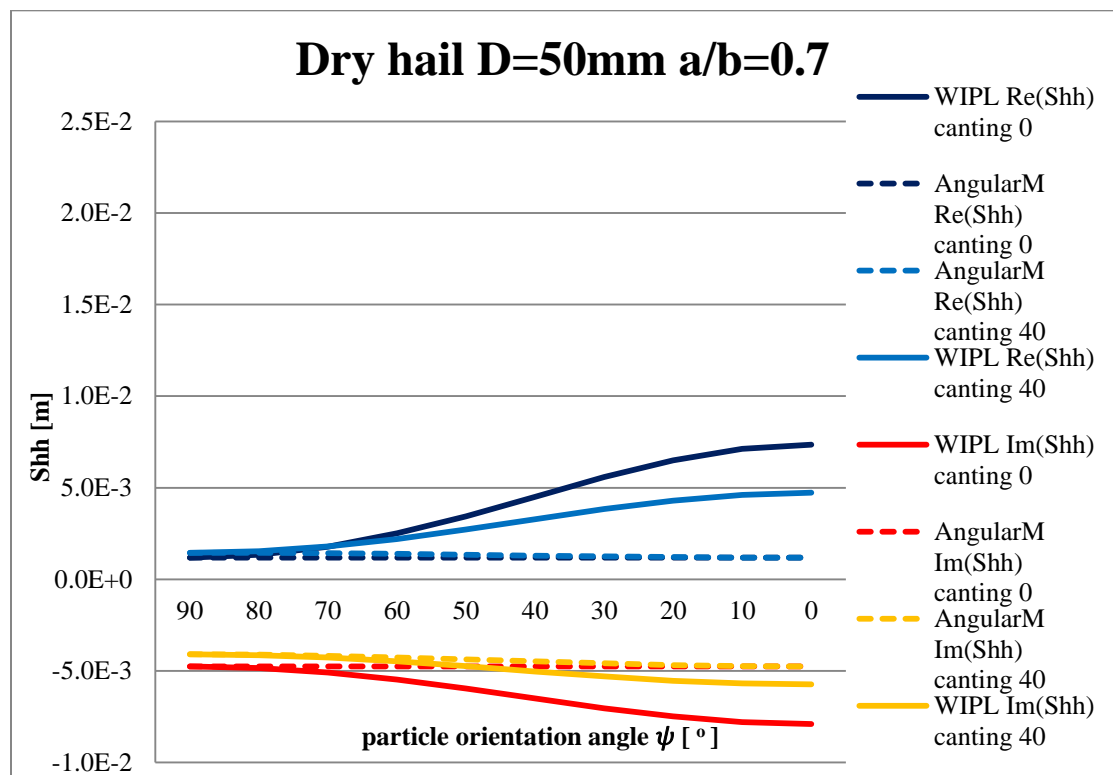


Figure 3.2 - Accuracy evaluation of the backscattering rule. Exact values of S_{hh} for a “dry” hailstone are depicted with a solid curve. Approximation values using the backscattering rule (Angular Moments) are depicted with dashed lines.

¹⁷ Value based on the calculation of the discrepancy for monodisperse size distribution and uniform raindrop orientation distribution up to $\psi \leq 75^\circ$.

The second model considered is a 50 mm “dry” hailstone (Fig. 3.2). The s_{hh} is two orders of magnitude larger than in the previous (raindrop) case while the extrapolation error behavior is similar. Maximal error for the case of no canting and $\psi = 0^\circ$ is approximately six times. Computations of horizontal radar reflectivity factor Z_H for randomly tumbling and monodisperse size distribution hailstones indicate that the backscattering rule produces negative error of about 4.2 dB.

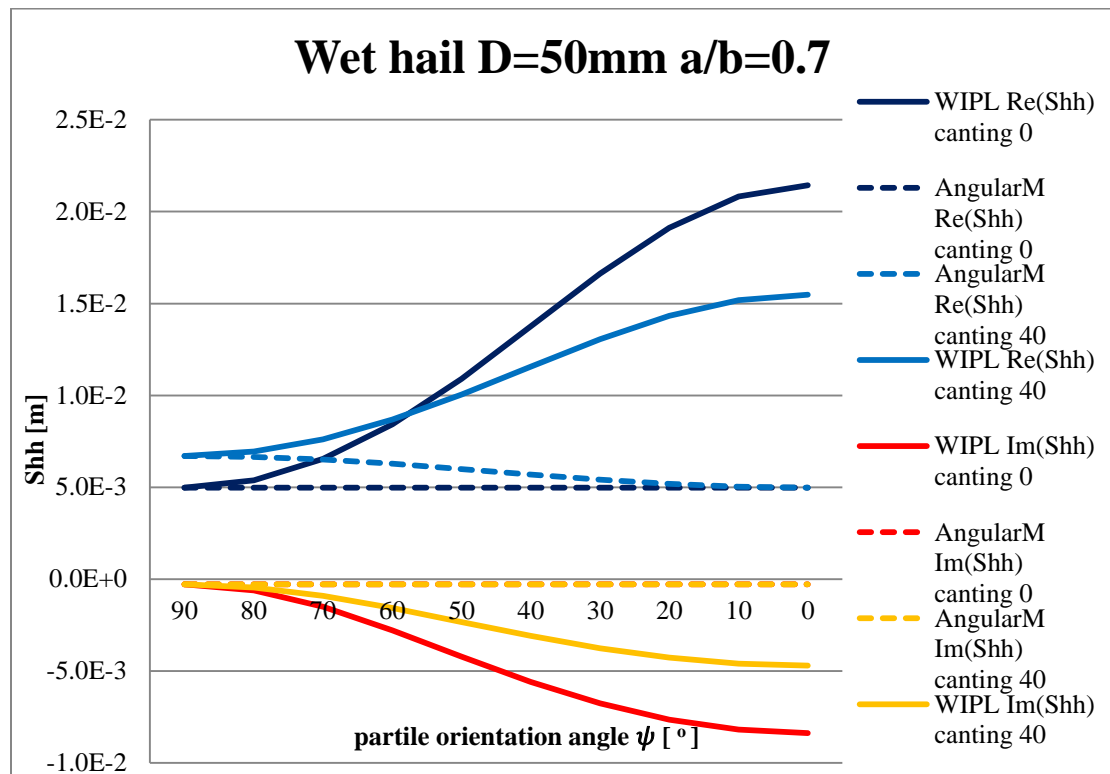


Figure 3.3 - Accuracy evaluation of the backscattering rule. Exact values of s_{hh} for a “wet” hailstone are depicted with a solid curve. Approximation vales using the backscattering rule (Angular Moments) are depicted with dashed lines.

The final model is of a “wet” hailstone with the maximal water coating prior to shedding. Comparison of the scattering elements is presented in Fig. 3.3 using the same scale as in the previous case. Both Fig. 3.2 and 3.3 illustrate the significance of water coating, as the value of the extrapolation error increases substantially. This

large extrapolation error has a substantial contribution to the error in calculation of normalized radar reflectivity factor Z_H for tumbling hail of up to -10 dB.

Large discrepancies in s_{hh} values for hydrometeor orientations aligned with the axis of symmetry ($\psi = 0^\circ$) indicates that the backscattering rule extrapolation cannot be used for high elevation angles or simulations of radars pointing vertically. Additionally, it limits the capability of proper variable calculations for randomly oriented hydrometeors, as the tumbling includes poorly extrapolated orientations.

From previous figures, the maximal extrapolation error is identified at $(\alpha, \psi) = (0^\circ, 0^\circ)$ with a tendency to increase as the magnitude of the backscattered power increases. The real and imaginary parts of the error are plotted in Fig. 3.4 for a “dry” hailstone with an axis ratio of 0.7, and at sizes between 20 and 100 mm.

The extrapolation error in Fig. 3.4 is determined as the difference of the corresponding values for extrapolated (dashed lines) and exact (solid lines) scattering elements. As expected, the envelope of the difference (error) increases with size, while the actual error value oscillates. Oscillations in the error are caused by the resonant scattering mechanisms which, for certain sizes, cause substantial error leading to a sign difference between extrapolated and exact values of the s_{hh} real and imaginary part. The discrepancy is especially pronounced for resonant diameters around 55 and 88 mm where both the real and imaginary parts of s_{hh} experience sign differences. These effects are likely to introduce a large bias in the calculation of the polarimetric variables.

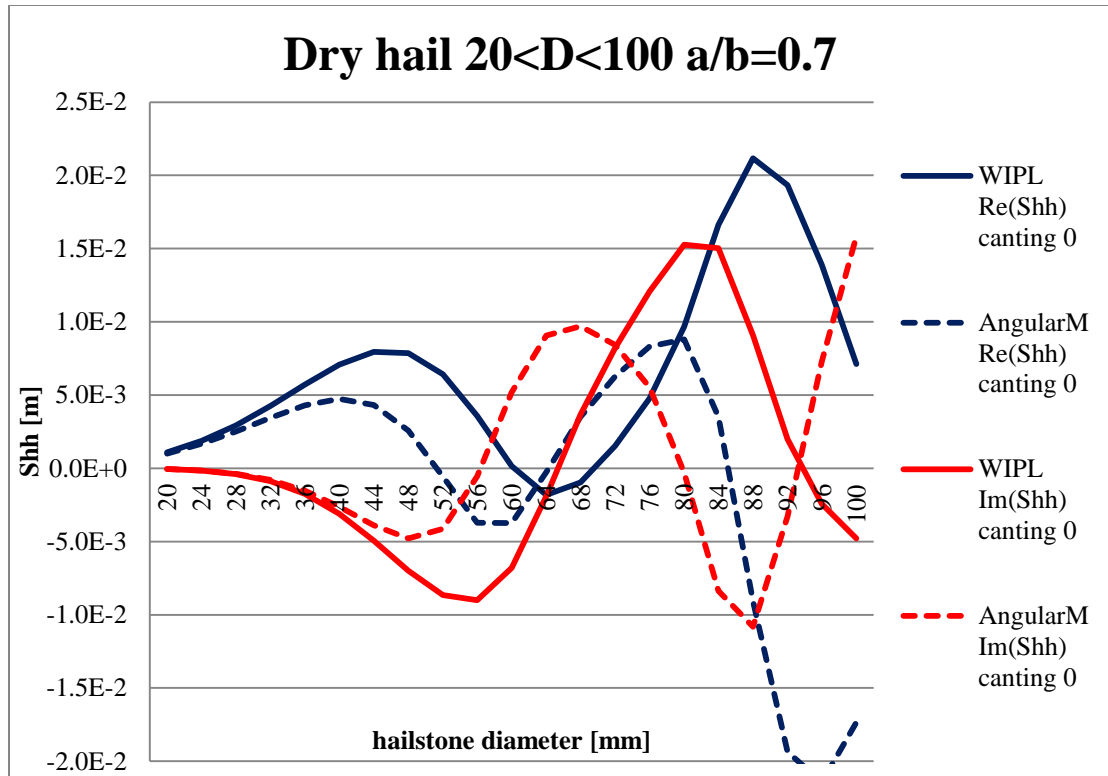


Figure 3.4 – Maximal error of $Re(s_{hh})$ and $Im(s_{hh})$ for "dry" hailstone having the axis ratio of 0.7. Exact values are depicted with a solid curve. Approximation values using the backscattering rule (Angular Moments) are depicted with dashed lines.

Large discrepancies in s_{hh} values (Fig. 3.4), both in terms of magnitude and sign, lead to the conclusion that the use of backscattering rule should be limited to particles that do not experience resonance effects and are oriented within the backscattering rule limit ($\psi \leq 80^\circ$). As the extrapolation error in the calculation of the polarimetric variables varies substantially with hydrometeor size, the overall simulation error becomes a function size distribution and therefore is hard to predict. Furthermore, extrapolation of s_{hh} values by the backscattering rule tends to decrease the s_{hh} value range making backscattering of spheroids less dependent on the orientation angle. Therefore, it may be responsible for inaccuracies in replicating the observed values of the co-polar correlation coefficient.

Constraints in modeling orientation of hydrometeors significantly affect the accuracy of the calculated polarimetric variables, as orientation is an important microphysical characteristic of every hydrometeor class. Luckily, problems introduced with the backscattering rule can be avoided if the scattering elements are calculated using the available CEM tools.

4. REALISTIC MODELING OF HYDROMETEOR SCATTERERS

Numerical modeling of the hydrometeor scattering and the calculation of polarimetric variables is typically based on spheroidal geometry models, except for a few studies of snowflakes and ice crystals. Spheroidal geometry has limitations for modeling polarimetric variables (especially ρ_{HV}), as well as other issues in case of the polarimetric radar operator (Ryzhkov, et al., 2011) (Ch.3). Deficiencies inherent to the presented modeling approaches (Ch.3) are certainly affected by the idealized modeling of hydrometeors typical for most modeling algorithms. To include these realistic scattering models, a different approach to the modeling and simulation of radar observed ensembles is required. This new approach needs to include arbitrary geometries that more closely resemble the actual hydrometeors, biota, and chaff that are observed by weather radars.

Idealized, spheroidal models are insufficient to represent the more complex geometry of natural hydrometeors, which are seldom spheroidal. Irregularity of the hydrometeor shape is best observed in snowflakes and hailstones, where observations report shapes only somewhat similar to spheroids. Surface protuberances on hailstones are caused by the natural processes. Irregularities such as lobes and protrusions are caused by preferential distribution of surface liquid water during wet growth whereas the freezing process is similar to the growing of icicles (Browning, 1966). This is in contrast to the formation of the surface protuberances in spongy hailstones which is attributed to the spongy nature of the accreted ice. Studies by Prodi (Morgan & Prodi, 1969) concluded that the creation of the surface

protuberances is due to liquid water extruded towards the surface during freezing. According to the same author, the observed phenomenon is a proof of spongy hailstone existence and evidence of spongy growth that causes surface protuberances.

Since the prevailing topology of hailstones often includes surface protuberances, one may wonder why a model concept, as is being presented here, has not already been introduced. This question is even more relevant given the fact that some polarimetric signatures are largely attributable to the irregular shape of hydrometeors (Balakrishnan & Zrnić, 1990). Perturbed surface hydrometeors were considered by Balakrishnan and Zrnić (Balakrishnan & Zrnić, 1990) who provided an approximation of the effect of protuberances on the co-polar correlation coefficient ρ_{HV} . However, their protuberance study was limited to the analytical formulation of the effect of protuberances on Rayleigh spherical scatterers and, as such, tackles only a small portion of the hydrometeor size spectrum. Even though the approach by Balakrishnan and Zrnić (Balakrishnan & Zrnić, 1990) provided the expected drop of the co-polar correlation due to surface roughness it excluded the effects of size. For small hydrometeors, backscattering phases are the same in both polarizations of the incident wave and thus affect only the magnitude of the scattering element. The backscattered differential phase was found to significantly affect ρ_{HV} (Ryzhkov, et al., 2011). It is zero for Rayleigh scatterers, but for non-Rayleigh has important contribution to the observed polarimetric variables in storms. This follows from the fact that resolution volumes seldom contain one hydrometeor type and, except for the case of severe storms, usually contain non-Rayleigh scatterers. Hydrometeors known to produce significant decrease in the co-polar correlation

coefficient are large and giant hailstones, which are known for their irregular perturbed shapes (Fig. 4.1).

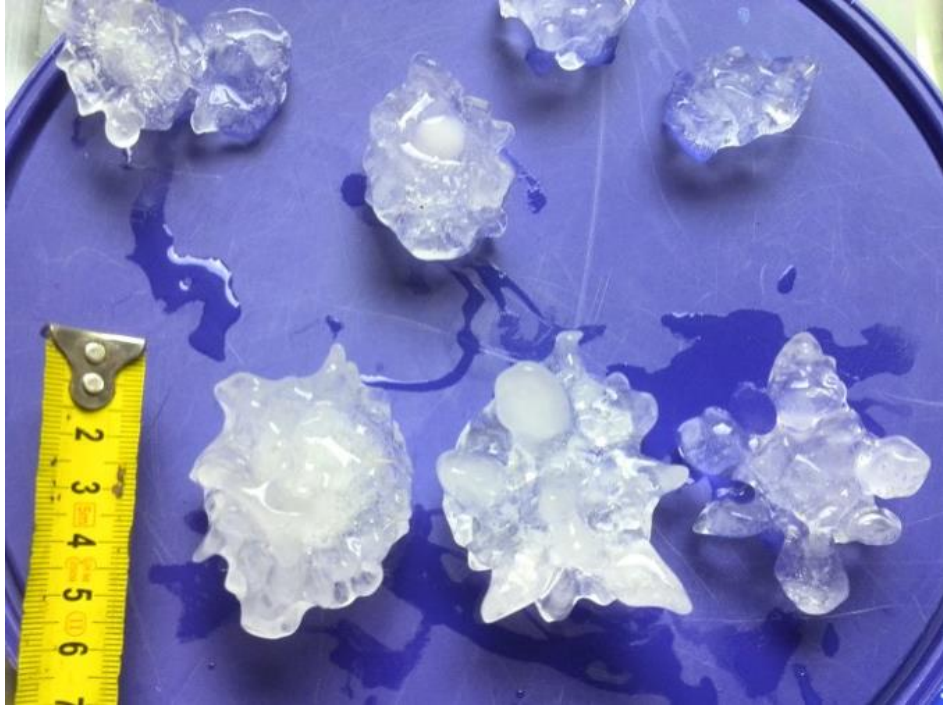


Figure 4.1 - Hailstones collected after a hailstorm in Bonn, Germany (July, 5th, 2015)¹⁸.

Different approaches of dealing with these more complex, rough spheroidal shapes are found in literature; none of those approaches, however, have ever been applied to the modeling of hydrometeors. This is likely due to the complexity of the proposed approaches, most of which exclusively discuss rough perfect electric conductor (PEC) objects (spheres) and using calculations based on approximate techniques. One of the approaches is that of Abdelezeez (Abdelazeez, 1983), who used Physical Optics theory (Ch.2.1.3); special case solutions are presented by Schiffer (Schiffer & Thielheim, 1984), for a slightly rough PEC sphere using the lowest order term of a smooth sphere solution. Another special case solution was proposed by Brykhovetski

¹⁸ Image courtesy of Dr. Alexander Ryzhkov, (NSSL/CIMMS).

(Bryukhovetski & Pazynin, 1991) who, similar to Schiffer, derived the solution of the slightly rough sphere using perturbation theory. However, none of the authors addressed scattering of the dielectric objects.

The early development of the more sophisticated computational electromagnetic tools was motivated by the growing need for antenna development. The attention paid to dielectric modeling of RCS was limited as most of the targets of interest were made of metallic materials. Presently, a wide variety of computational electromagnetic (CEM) tools are commercially available, most all of which are capable of supporting complex geometries and dielectric structures. Limitations of past CEM tools are now mitigated, allowing for modeling of most objects with satisfactory accuracy and efficiency. Limitations of the CEM tools today are in efficiency, as available computing power can handle any modeling problem.

The availability of commercial CEM tools capable of modeling any hydrometeor's scatter using the standard input/output parameters format makes these an obvious choice for the hydrometeor scattering computations. Substituting these for current approximate tools would, besides mitigating modeling limitations, introduce new systematization to the field. Most of the approximate tools were designed for particular purpose and particular group perplexing their wider use due to the lack of standard input/output format. Contrarily, commercial CEM tools are widely available so that models and results can be shared easily to supplement inter-group research.

Using CEM tools comes at a time efficiency cost. This issue was addressed by Aydin and Zrnić (Aydin & Zrnić, 1992) who proposed the creation of a hydrometeor

scattering library that would store pre-calculated hydrometeor scattering elements. The hydrometeor library was conceived as a database used for separation of the scatterers modeling from the process of polarimetric variable calculation. Thus, the library is a database of hydrometeor scattering matrices of hydrometeor types separated in such a manner that they could be easily distinguished and extracted. Each of the library content files represents a single scatterer for which polarimetric matrices are calculated over 4π steradians. This library element is herein labeled as the physical hydrometeor model.

The scattering library solves the time effectiveness issue, as the complex scattering simulations would be required only once when a particular physical hydrometeor model is added to the library. In simulations, the scattering calculations in the overall modeling process are replaced with extractions of the scattering elements from the library. Furthermore, expansion of the library is decoupled from the calculation of the polarimetric variables, enabling parallel scattering and polarimetric variable simulations.

4.1 COMPUTATIONAL ELECTROMAGNETIC MODELING OF REALISTIC HYDROMETEOR SCATTERERS USING EXACT MODELING TECHNIQUES

Simple spheroidal models provide a satisfactory interpretation of reflectivity and Z_{DR} for most precipitation types but lack the capability to replicate polarimetric signatures of large hail, insects, or birds, all of which differ substantially from oblate or prolate bodies. To overcome this deficiency, new ensemble models need to include rough, spiky hail. Previous studies (e.g. (Kumjian, 2013)) discovered that low ρ_{HV} is related

to the protuberances of the resonant size hail surface. Given the shape (topology) discrepancies for hail modeling, it is doubtful that spheroidal models are adequate for modeling more complex shapes, such as snowflakes, insects or biota.

An essential role of these complex objects is directly tied to the variety of shapes that exists in nature. This variety could be contrasted to the example of a full, three-dimensional asymmetric scatterer and a spheroidal scatterer through the number of scattering matrices needed to represent backscattering. Assume that 1° is a sufficient solid angle increment needed to completely characterize a scatterer from all viewing directions. Then the number of viewing angles is $\frac{4\pi}{\Omega^2} = \frac{4\pi}{\left(\frac{\pi}{180}\right)^2} = 41252$, which is therefore the total number of scattering matrices needed to describe the object's scatter. A scattering matrix for an asymmetric body is different for each viewing angle. Whereas, for a spheroidal model the number of different scattering matrices is 90 at most for any cut of the spheroid.

In sequent, viewing angles (orientations) discussed are described in the WIPL-D (WIPL-D, 2015) coordinate system. The WIPL-D like other CEM software, uses a spherical coordinate system with a fixed step length in the azimuth and elevation (or zenith). This results in a non-uniform distribution of viewing points (observations) over a sphere, with their density increasing towards the coordinate system poles.

The number of viewing angles (orientations) needed to describe scattering in the CEM software, using a 1° increment, is therefore 360^2 (129600), for every physical hydrometeor model. The model is defined using a set of parameters (number of layers, its spheroidal axis ratio, diameter, permittivity etc.), and stored in the

scattering library. This number of viewing angles (orientations) is for a static object. However, hydrometeors experience canting (tumbling), therefore the number of orientations including canting is as high as (360^3) . In either case (with canting or without) in terms of different scattering matrices spheroidal models exploit less than 0.00069% or 0.69‰ of the maximal number of different scattering matrices existing for non-symmetrical hydrometeor per each physical hydrometeor.

As indicated by the numbers above, the fundamental deficiency of spheroidal modeling is that it lacks the ability to mimic high differences in the scattering elements that exist in nature. This is since it provides a limited (small) amount of different scattering matrices constrained by its spheroidal topology. In other words, it provides a small maximal number of different scattering models per physical hydrometeor model. Here, it is important to understand the difference of the physical hydrometeor model and the scattering model. The first represents the hydrometeor with its shape and dielectric properties, having backscattering matrices calculated for all orientations and stored in the scattering library. The second represents an input to the polarimetric variable simulator that is a subset of the physical hydrometeor model with defined set of orientations. Therefore, one physical hydrometeor model may have many (in simulator) different scattering models that differ from one another by the user prescribed set of orientations.

An improvement in polarimetric estimates must consider the numerous scattering models that constitute an ensemble from which polarimetric variables are calculated. Starting from the variety of physical hydrometeor models for each hydrometeor type,

the total number of scattering models can be defined by (4.1) if the hydrometeor size range D_{RANGE} and size step Δd determined a priori.

$$N_D = \frac{D_{RANGE}}{\Delta d};$$

$$N = N_{layer} \cdot N_{axis} \cdot N(\alpha, \psi) \cdot N_D(D_{RANGE}, \Delta d) \cdot N_\varepsilon(\lambda, T) \cdot [N_R(\Delta r, type)]. \quad (4.1)$$

where N represents the total number of different physical hydrometeor models for one hydrometeor type (e.g., a dry hailstone), N_{layer} the number of different models governed by the number of layers, N_{axis} the number of different apparent axis ratios (proportion of the minor to major axis of a physical hydrometeor model), $N(\alpha, \psi)$ the number of canting and orientation angles per physical hydrometeor model, N_D the number of different sizes defined over the particular physical hydrometeor range, N_ε the number of different dielectric properties for different temperatures and wavelengths, and N_R the number of different irregular hydrometeor types discerned by the type of irregularity and the quantification of that irregularity. The number of different irregularities is given in brackets as this type of versatility is not available in the spheroidal modeling.

Following from the number of different physical hydrometeor models, the number of different backscattering matrices for each physical hydrometeor model can be represented. This number depends on the number of symmetries in a physical hydrometeor model. If a physical hydrometeor model does not have symmetry planes, the number of different backscattering matrices is the highest. Each plane of symmetry decreases this number in half, leading to the spheroidal and eventually spherical model that has only one scattering matrix.

The deficiency inherent to a simplified shape in approximate modeling is solved by the CEM approach, as it supports non-symmetrical complex shapes.

4.1.1 Modeling of scatterers using WIPL-D software

The CEM tool used herein is the commercial MoM software WIPL-D (WIPL-D, 2015). It is frequency domain software based on the solution of the Surface Integral Equation (SIE) for electric and magnetic fields of dielectric and metallic objects. The object's topology is defined by a combination of nodes, wires and "plates" that are used to build the surface of the object. A general representation of wires in the WIPL-D software is obtained using the conical or cylindrical wire structure, whereas the "plates" as surface elements are defined using bilinear surfaces. Bilinear surface is the nonplanar quadrilateral defined with its four vertices.

Composite structures are defined in terms of their complex dielectric parameters and thereby allow a non-restricted approach to lossy dielectrics. Equivalent electric and magnetic currents over the surface elements are approximated with higher order polynomials or rooftop basis functions, over each bilinear surface or bilinear surface portion depending on its size. Because the number of unknowns depends on the number of bilinear surfaces, minimization of the building surfaces is one of the modeling optimization goals. The modeling by bilinear surfaces allows the highest degree of topology freedom with the minimum number of building elements. Due to its general nonplanar nature, it also allows surface roughness to be easily modelled using the same number of plates as smooth models. This is unlike planar plate modeling, which requires increase in the number of building elements. As illustrated in Fig. 4.2, the number of the bilinear surfaces for smooth a) and rough b) bodies is

equal. It leads to the least number of variables per physical hydrometeor model and thus the shortest computation time.

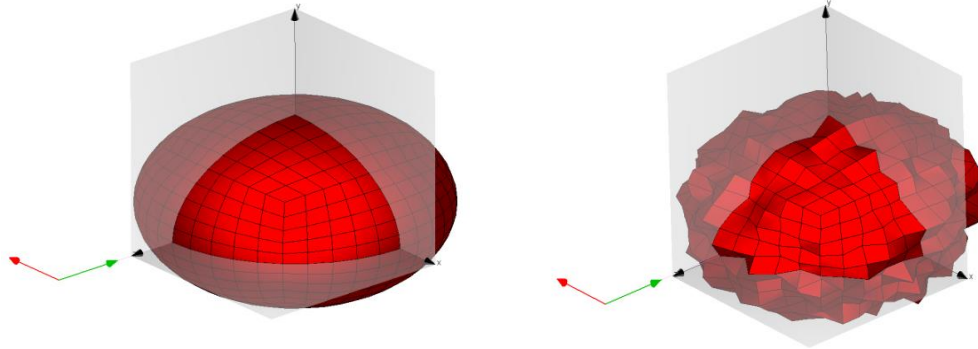


Figure 4.2 - Models of physical hydrometeors illustrating implementation of the same number of bilinear surfaces in modeling of smooth and rough surfaces.

The Surface Integral Equation (SIE) MoM software is chosen over MoM codes that use Volume integral Equation (VIE) and Finite Element Method (FEM). This decision is based on an evaluation of the amount of the unknown quantities, which are usually higher in VIE and FEM methods because they use volume elements as opposed to surface elements. In comparison with the Finite Domain Time difference methods (Ch.2.2.1), the SIE MoM is more efficient (Kolundzija & Djordjevic, 2002). This, together with the avoidance of the absorbing boundary conditions required in case of FD-TD, is a definite advantage of the chosen integral solution. The FD-TD approach is suitable for a precise representation of the variable dielectric properties resulting from, for example, the complex microphysical growth of hydrometeors. Its fundamental formulation toward closed geometry problems, however, is considered its limit for radar scattering applications.

Based on the least number of unknowns, SIE is the most desirable approach. Nonetheless, additional means of speeding up scattering calculations were considered. The scattering simulation efficiency of the WIPL-D software may be improved using parallel processing, which exploits the multiple core/thread central processor units (CPUs) in the most efficient way (WIPL-D, 2015). This parallelization option is available with most CEM software and the increase of efficiency can be from 2 to 8 times for a PC. A further increase of the simulation effectiveness can be obtained using computer clusters or supercomputers where the simulation is shared over a large number of CPUs. The WIPL-D has the option of parallelization on the graphics processor units (GPUs), which are the core of the modern gaming graphic cards. Parallelization using graphic cards is available on common PCs through hardware changes similar to those used by computer gamers. For example, installation of the specific generation of the NVidia brand graphic cards supporting CUDA cores is considered. Once the simulation machines are equipped with “gaming” graphic cards, GPU parallelization becomes available. The GPU parallelization proves to be the most efficient way to accelerate simulations as it results in decrease of simulation time up to 40 times (WIPL-D, 2015), matching the simulation times achieved on computer clusters or supercomputers. Even though the time cost now becomes comparable, the overall computation cost is tremendously higher in computations using the computer clusters or supercomputers as they are seldom dedicated to only one application, usually operating in the time share mode. Contrarily, GPU equipped computers can be dedicated to specific tasks such as

running the WIPL-D, thus making it very effective for modeling a large variety of physical hydrometeor models.

4.1.2 Modeling of physical hydrometeors using the WIPL-D software

Physical hydrometeors that cause greatest anomalies in the polarimetric signatures are those of resonant sizes that were typically modeled using the T-Matrix method. As elaborated previously, spheroidal models of hailstones are incapable of replicating their polarimetric signatures due to the hailstones irregular shapes. The primary goal of this dissertation is therefore the application of the WIPL-D software, as representative of commercially available CEM tools, to model resonant-sized hydrometeors that have a complex shape. In addition, smooth hydrometeor models are used for evaluation and verification of the results obtained by WIPL-D. Hydrometeor modeling using the WIPL-D software mitigates limitations¹⁹ existing in the approximate methods, but at a price of increased computation time. The WIPL-D scattering results are therefore stored in the scattering library.

Hydrometeor types considered are raindrops, ice crystals, dry hailstones, and water coated hailstones. These hydrometeors are modeled as single or two layer objects following the analytical expressions for their properties given by (3.1-3.5). Although multilayer modeling is not a limitation, and can be done, only one and two layer hydrometeors are considered. In two layer models the first layer represents the hydrometeor's core (usually the ice core of a hailstone) whereas the outer shell represents the core coating by a dielectric of different permittivity (usually a water

¹⁹ Generally speaking, CEM (WIPL-D) has its own limitations which for any natural hydrometeor are beyond reach if the hydrometeor is modeled properly. Limitations are mainly related to models having more than 20 layers and axis ratios for plates higher than 100.

coating in the case of a water coated hailstones) Fig. 4.3. Two layer model represents melting hydrometeors, and the need for such is elaborated by (Ryzhkov, et al., 2011).

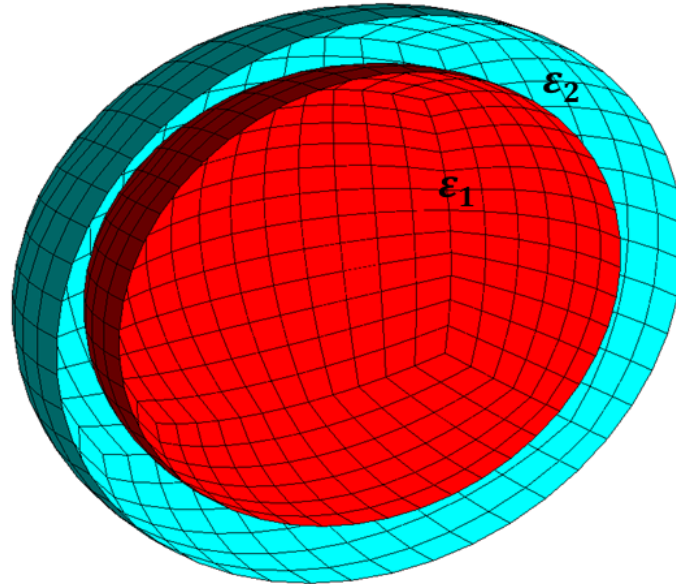


Figure 4.3 – Simple spheroidal two layer model having the inner core dielectric permittivity ϵ_1 (red) and outer shell dielectric permittivity ϵ_2 (blue).

Depending on the hydrometeor type, the axis ratio is governed by (3.1-3.4).

Therefore, in the models described herein, the following axis ratios are assigned to the different hydrometeor types:

1. Raindrops – axis ratio depend on the equivolume diameter given by (3.1) for raindrop diameters from 1 mm to 8 mm;
2. Single layer hailstones – hailstones are modeled as oblate spheroids having a horizontal to vertical axis ratio of 0.6, 0.7, and 0.8 (Fig. 4.4), for all sizes. The size range is from 5 mm up to 100 mm;

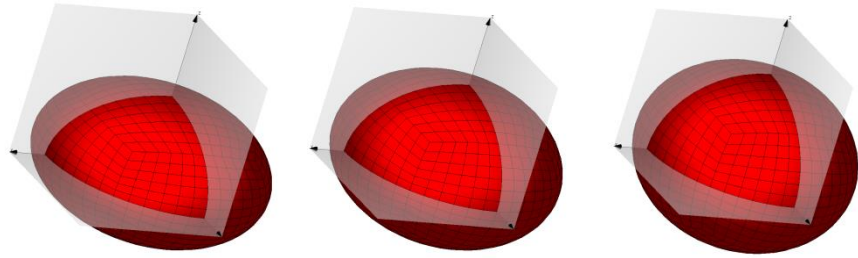


Figure 4.4 - Single layer spheroidal hailstone models with axes ratios of 0.6, 0.7 and 0.8.

3. Two layer hailstones (“wet” hailstones) – same as the single layer models (Fig. 4.5);

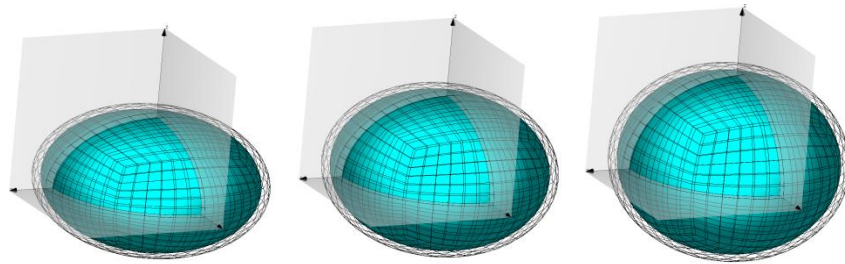


Figure 4.5 - Dual layer spheroidal hailstone models with axes ratios of 0.6, 0.7 and 0.8.

4. Ice crystals – are modeled as single layer ice spheroidal structures with axis ratios ranging from 0.05 to 20 (Fig. 4.6).

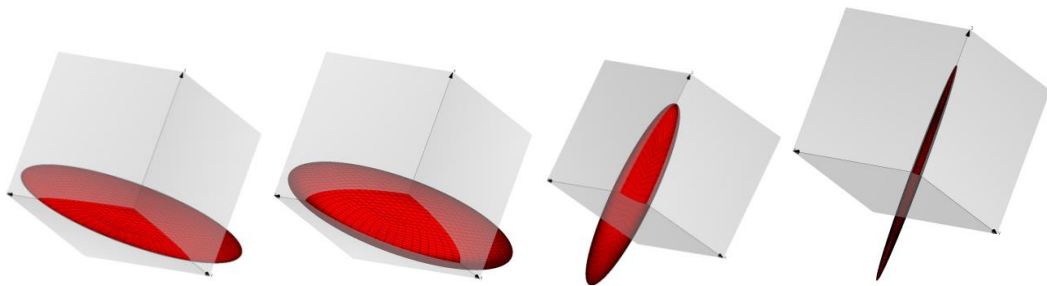


Figure 4.6 - Single layer spheroidal hailstone models with axes ratios of 0.05, 0.1, 10 and 20.

For single and two layer hailstone models, surface protrusions are introduced. All of the shapes are derived from the original spheroidal models but with different types of surface protuberances, thus creating different irregular physical hailstone models.

Although observations of irregular hailstones abound, there are no accepted hailstone models. Due to the lack of statistical information regarding the size and shape distributions of surface irregularities, a mathematical model that mimics observed shapes from different hailstone photographs is developed. This model is used to simulate a wide variety of physical hydrometeors protrusions that can have various distributions.

In the model, deviations from the spheroidal surface are introduced using two roughness types. The first is a uniform distribution of protrusions on the surface of the spherical shape $\Delta_R(\varphi_{model}, \theta_{model})$ defined by (4.2). In (4.2), R_{car} is the major axis of the base spheroid. For the second model the protuberance magnitude, $\Delta_M(\varphi_{model}, \theta_{model})$ is defined to change with respect to the point axis $R(\varphi_{model}, \theta_{model})$.

$$\Delta_R = fR_{car}, \quad (4.2)$$

$$\Delta_M = fR(\varphi_{model}, \theta_{model}), \quad (4.3)$$

where f is a random number that is generated to represent the fraction of the axis, specifying maximal roughness magnitude. Roughness values presented here are 2%, 6%, 10%, 14% of the physical hydrometeor axis (Fig. 4.7).

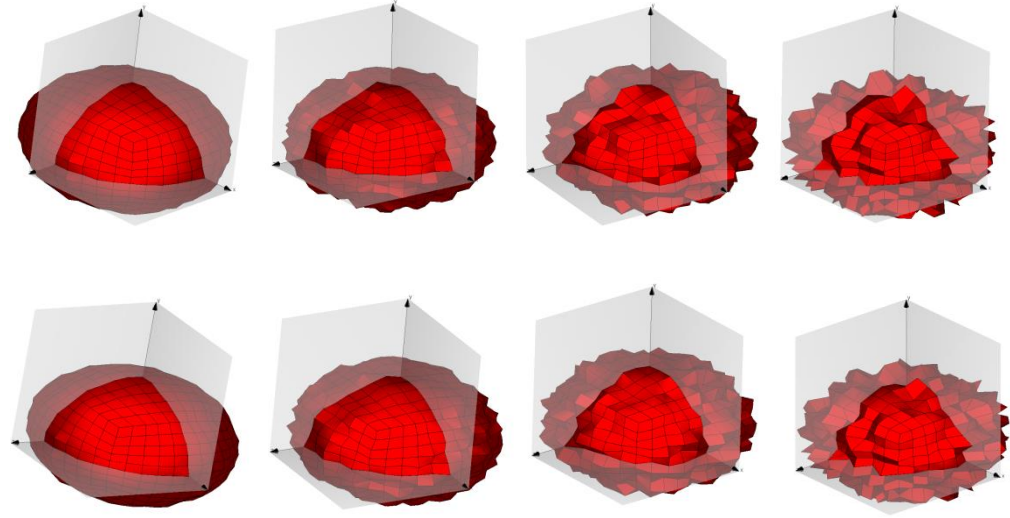


Figure 4.7 - Physical models of rough hydrometeors having uniform random distribution of protuberances 2%, 6%, 10%, 14% of radius (first row) and modified random distribution of protuberances (second row).

To avoid domain irregularities²⁰ for two layer hydrometeor models, both layers are stretched (deformed) by the same protuberance (Fig. 4.8). Multilayer objects are defined with respect to the dielectric properties (Fig. 4.3). Induced currents at each boundary are impressed at the side of the surface pointing outwards. If, in the case of water coated hailstones, the ice core surface due to the protuberances has a larger axis than the water coating (i.e., the ice core surface in contact with “air”), domain irregularity appears. Domain irregularity is caused as the boundary surface is defined to have ice as the inside dielectric with water as the outside dielectric, while in the described case boundary surface would have air on one and ice on the inner side.

The thickness of the water coating is defined using the maximal surface water content that can be obtained prior to shedding (4.4) (Rasmussen & Heymsfield, 1987).

$$m_{liquid\ H_2O} = 0.268 + 0.1389m_{ice} \quad (4.4)$$

²⁰ Accuracy of results obtained for models with irregular domains is uncertain (WIPL-D, 2015).

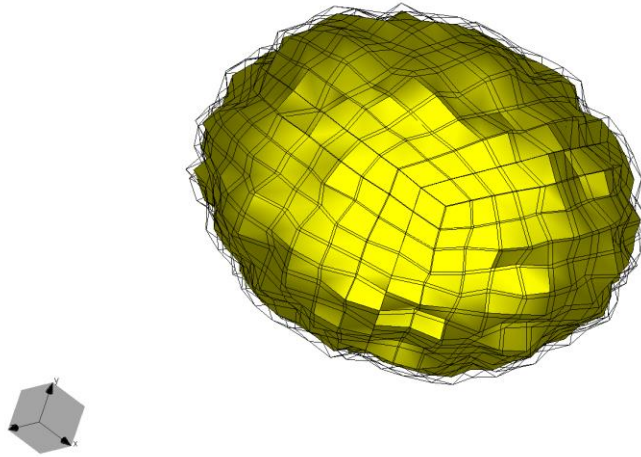


Figure 4.8 - Dual-layer hydrometeor model illustrating implementation of the Rasmussen formulation for the maximum water coating for a specific hailstone size. The water coating (transparent) is modeled to follow the surface topology of the hailstone ice core (yellow).

4.1.3 WIPL-D coordinate system and hydrometeor based coordinate system

Protuberances that are introduced to the physical hydrometeor models, as in (4.3), are defined in the hydrometeor-centered spherical coordinate system. In the WIPL-D software, the coordinate system is spherical with the polar axis along z (Fig. 4.9a). The ensemble of hydrometeors that produce the polarimetric variables has its own coordinate system, which is Cartesian with the x , and y axes parallel to the earth surface (Ch.2.3.1). Thus, to enable modeling of the meteorological phenomena, relations between the coordinate system in the modeling software (WIPL-D) and meteorological coordinate system have to be defined.

Orienting the model to account for all viewing angles is a challenging task. For a body illuminated by constant electric fields E_φ and E_θ (Fig. 4.9a), WIPL-D computes the surface currents at each elemental surface and stores them in a matrix. All couplings in this matrix are captured and backscattering matrices in all directions can

be computed from it by a single run of the software. However, if the body is rotated, the software needs to re-compute the coupling matrix, which takes by far most of the computing resources. Similarly, re-computation must be made if components of the electric field change (as in Fig. 4.9c).

A solution to the problem is obtained using the built in viewing angle sampler. In this case, as the model remains fixed in the WIPL-D coordinate system, the same coupling matrix is used for calculation of scattering matrices. Viewing angles (orientations) are positioned at meridians of the spherical coordinate system in user defined uniform azimuth and elevation steps. Furthermore from Figs. 4.9b and 4.9d is obvious that the same change in the angle of incident fields can be obtained either rotating the body in the WIPL-D coordinate system or moving the incident field on a sphere around the body.

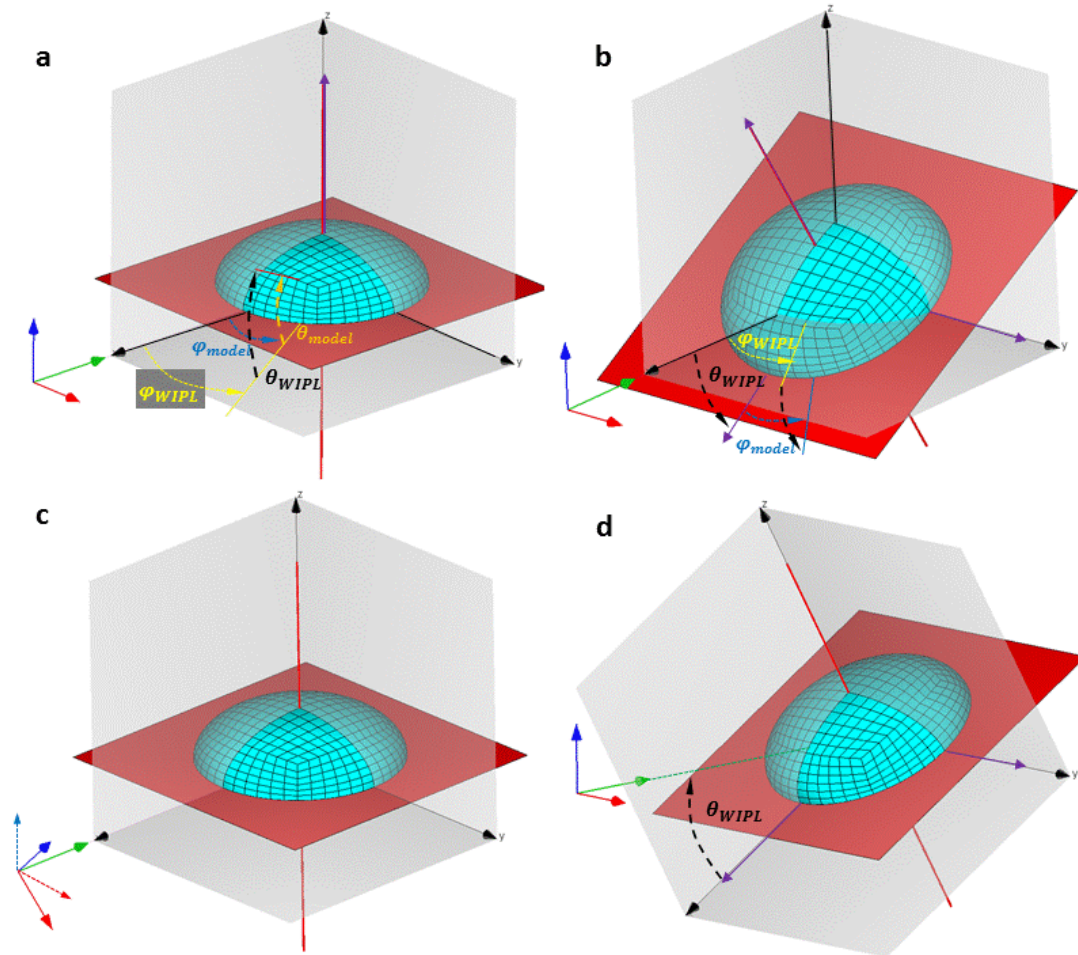


Figure 4.9 – Spheroidal hydrometeor model with incident E_ϕ (red) and E_θ (blue fields, hydrometeor horizontal cardinal plane (red plane) and symmetry axis (purple/red); a) co-aligned WIPL and hydrometeor coordinate system with azimuth and elevation angles defined; b) rotated hydrometeor’s coordinate system around the y axis of the WIPL coordinate system with azimuth angles defined and WIPL elevation angle defining the rotation angle; c) rotation of the incident fields, original fields (dashed) rotated fields (solid); d) changing the incident field direction for set of WIPL azimuth and elevations angles causes same viewing angle as in the case of model rotation.

Orientation of the rigid body in the fixed coordinate system (with respect to the coordinate system of the body) is always defined using three Euler angles, each of which defines rotation about a coordinate system axis. As the main interest of the dissertation are objects in free fall (precipitation), it is necessary to ensure that

scattering results can be obtained for physical models capable of rotating around all three axes of rotation (AoR) with respect to the electric field vector.

According to the definition accepted in the polarimetric radar community, the electric field having only E_φ component will be labeled horizontal (H), while the electric field having only E_θ component will be labeled vertical (V) (Ch.2.3). Therefore, axes of rotation for a model in WIPL-D are Cartesian axes x, y and z of the WIPL-D coordinate system.

The orientation of the model needed to account for the largest number of different orientations and canting angles has to be defined. Starting from the software (WIPL-D) coordinate system, the scattering elements are calculated for a set of φ_{WIPL} and θ_{WIPL} angles (Fig. 4.9a). These angles are defined as azimuth and elevation. Azimuth is the angle defined in xOy plane, which increases in the counter-clockwise direction starting from the x -axis, while the elevation angle θ_{WIPL} is defined between the point in space and the xOy plane (Fig. 4.9a). Similarly, the hydrometeor-centered coordinate system is defined as having the azimuth and elevation angles φ_{model} and θ_{model} in the hydrometeor's center positioned in the main cardinal plane (red in Fig. 4.9) of an oblate spheroid (co-aligned model and WIPL coordinate system Fig. 4.9a and rotated model coordinate system Fig. 4.9b), where φ_{model} and θ_{model} are defined as in WIPL-D coordinate system (Fig. 4.9a).

Fulfilling the rotational requirement mentioned above constrains the acceptable model orientation in the WIPL-D. Considering the case of co-aligned model and WIPL-D coordinate systems (as in Fig. 4.9a), yaw and rotation are defined by

WIPL-D azimuth and elevation angles with the respect to polarization vectors. However, the third degree of freedom (DoF), “roll” cannot be achieved with respect to the electric field vector (presented in Fig. 4.9c by rotation of fields). In the light of meteorological applications, and geometry of polarimetric scattering, absence of the third DoF relates to incapability of hydrometeors to cant for $\psi = 90^\circ$, which is the prevailing orientation of hydrometeors at low weather radar elevation angles. In order to introduce the third DoF, change in the original model orientation is necessary.

The two DoF issue in co-aligned WIPL-D and physical hydrometeor model coordinate systems cannot be solved without increasing the time cost of the simulation. On the other hand, hydrometeor and WIPL-D coordinate centers are independent and, as such, can be rotated in order to achieve the required three AoR. Finding a proper hydrometeor coordinate system rotation has to ensure the object’s rotation (“roll”) around the direction of wave propagation (Poynting vector). Horizontal and vertical electric field vectors (polarizations) are defined using azimuthal and elevation components and each of field’s direction changes²¹ with a change in incident angle. Consequently, there exists a point on the sphere where the vectors change their direction, with the tip of the vector creating a circular path when only one angle is changed. For the spherical coordinate system, as used in WIPL-D, two such points that define poles of the coordinate system $(\varphi_{WIPL}, \theta_{WIPL}) \in \{(\varphi, 90^\circ), (\varphi, -90^\circ)\}$ exist. In the direction of the poles, the electric field vector depends only on the azimuthal angle and is parallel to the xOy plane of the Cartesian coordinate system.

²¹ With respect to the Cartesian x, y, z coordinates.

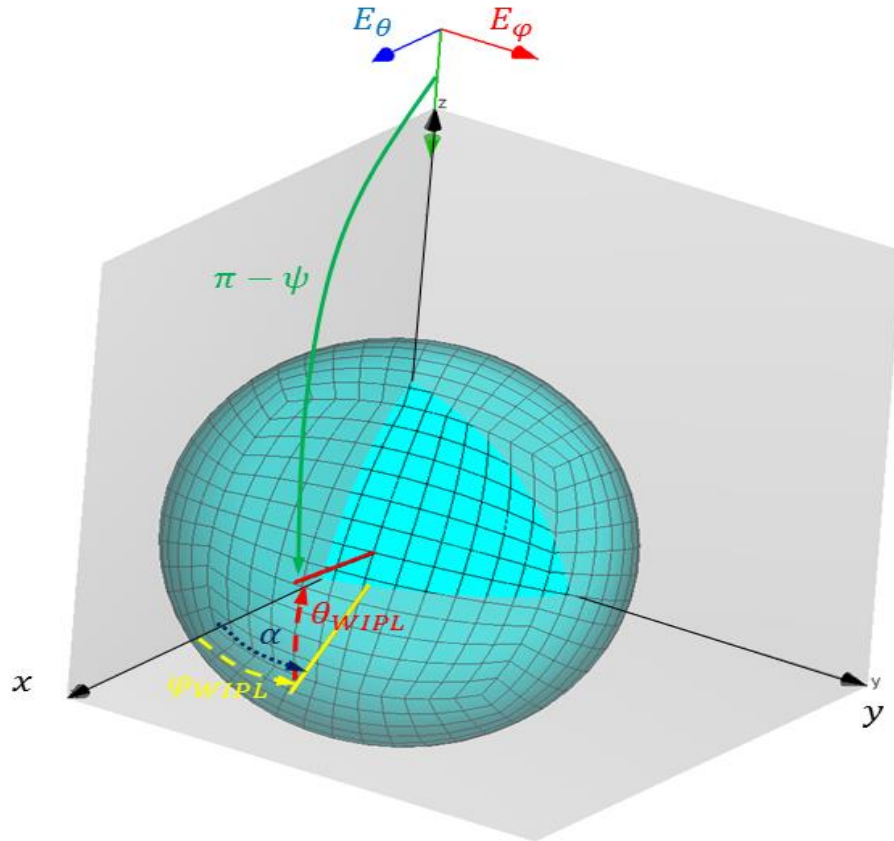


Figure 4.10 - WIPL-D and polarimetric coordinate system angles where the xOy is the plane of polarization, directions of propagation (green line), spheroidal hydrometeor's axis of symmetry (red line) and projection of the axis of symmetry to the plane of polarization (solid yellow line).

Orienting an object to face toward the $z \rightarrow +\infty$ (Fig. 4.10) allows for 3 AoR for any object. The axes of rotation are defined around Cartesian coordinate system axis in the following angle configuration²²:

1. z axis (“roll”) – for fixed value of $\theta_{WIPL} = 90^\circ$ and $0^\circ \leq \varphi_{WIPL} < 360^\circ$, the electric field vector is rotated around the z axis;
2. y axis (“tilt”) – for fixed value of $\varphi_{WIPL} = 0^\circ$ and $-180^\circ \leq \theta_{WIPL} < 180^\circ$, the electric field vector is rotated around the y axis;
3. x axis (“yaw”) – for fixed value of $\varphi_{WIPL} = 90^\circ$ and $-180^\circ \leq \theta_{WIPL} < 180^\circ$, the electric field vector is rotated around the x axis.

²² Axes of rotation are defined using WIPL-D, elevation based coordinate system.

Adjusting the hydrometeor model orientation may, as illustrated, significantly affect modeling effectiveness, especially when modeling hydrometeors where the scattering elements at all orientations are sought. Therefore, if a spheroidal physical hydrometeor model is considered, its cardinal plane should be oriented parallel to the yOz plane. A hydrometeor's axis of symmetry is, in that case, parallel (co-aligned) with the x axis of the WIPL-D coordinate system. The orientation described has three axis of rotation.

Scattering matrices of properly oriented hydrometeors are typically calculated in 65341 directions, or in 1° step increment for $0^\circ \leq \varphi \leq 360^\circ$, where both 0° and 360° angles are included²³, and for $-90^\circ \leq \theta \leq 90^\circ$, thereby creating solutions over a full solid angle. For a non-symmetric complex shape hydrometeor, the simulation will yield exactly 64 800 independent scattering matrices, as 0° is calculated twice (as 0° and 360° , for all θ). One may notice that the number of viewing angles is half of the maximal number of different scattering matrices, yet the full solid angle coverage is claimed. Such a difference is best illustrated in Fig. 4.11.

²³ Detailed explanation of including both 0° and 360° angles can be found in WIPL-D user's manual (WIPL-D, 2015) as it is of minimal importance to the work presented herein.

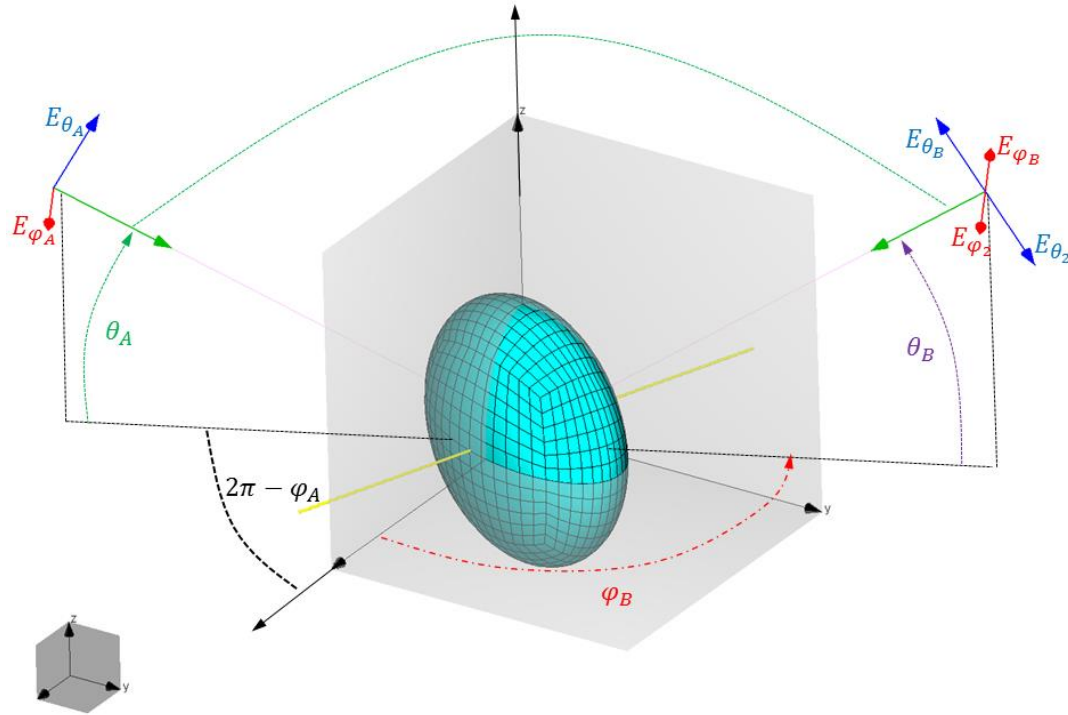


Figure 4.11 - Relation of the scattering elements for opposite directions.

Angles φ_A and θ_A define point A, increasing the elevation angle θ it crosses the polar (zenith) axis ($\theta = 90^\circ$). The position θ_2 is defined as point B having angular coordinates (φ_A, θ_2) . Point B in Fig. 4.11 is also defined by another set of angles (φ_B, θ_B) where $\varphi_B = \varphi_A + \pi$ and $\theta_B = \pi - \theta_2$. Even though both sets of angles define the same point (B), the directions of the electric field vectors defined at point B differ from one another depending on the angles used. For the point B defined by (φ_A, θ_2) , the electric field E_{θ_2} (V-pol) points toward the xOy plane, while when B is defined by (φ_B, θ_B) , the electric field vector points away from the xOy plane. The same is valid for the horizontal polarization electric field vector E_φ . It is obvious that scattering elements at point B will be the same for both cases with electric fields having only sign difference; hence their magnitudes and phases due to their angular orientation are equal.

Mathematical relationships between WIPL-D and polarimetric canting (in the plane of polarization) angle α and orientation ψ (4.4) and (4.5) are deduced from Fig. 4.10. Since the polarimetric community uses polarimetric coordinate system, relations (4.4) and (4.5) are of great importance. As previously (Ch.2.2.1) mentioned, the polarimetric coordinate system is defined with respect to the orientation of the hydrometeor and wave propagation. It is therefore independent of the scattering model implementation (notation simplification $\varphi_{WIPL} = \varphi, \theta_{WIPL} = \theta$).

$$\alpha = \varphi \tag{4.4}$$

$$\psi =$$

$$\left\{ \begin{array}{l} \pi - \arccos\left(\frac{[\cos^2 \theta (\cos^2 \varphi - \sin^2 \varphi) - \sin^2 \theta + 1]}{2 \cos \theta \cos \varphi}\right) \mid \forall \varphi, \theta \in [0, 2\pi] \quad \varphi \neq \frac{\pi}{2}, \frac{3\pi}{2} \wedge \theta \neq \frac{\pi}{2}, \frac{3\pi}{2} \\ \frac{\pi}{2} \mid \varphi = \frac{\pi}{2}, \frac{3\pi}{2} \\ \frac{\pi}{2} \mid \theta = \frac{\pi}{2}, \frac{3\pi}{2} \end{array} \right\}$$

$$\tag{4.5}$$

The relations given by (4.4) and (4.5) for canting and orientation angles are to be used for calculating the polarimetric angles when WIPL-D software is used for modeling of hydrometeor scattering. Nonetheless, these relations are valid for all hydrometeor models developed in any other CEM software that use the same elevation defined Cartesian coordinate system and physical hydrometeor model orientation as in Fig. 4.10.

4.2 EVALUATION OF THE SCATTERING RESULTS OBTAINED USING WIPL-D

The focus of this section is on evaluation of the WIPL-D accuracy in the modeling of hydrometeor scattering.

The WIPL-D software has been heavily tested, and the accuracy and overall reliability of the software have been documented (Jokanovic, et al., 2001); (Nikolic, et al., 2005). Nevertheless, a comprehensive validation of the scattering results has not been made. Moreover, the accuracy of hydrometeor modeling using any commercially available CEM is not recorded in the literature.

Herein, results calculated by approximate approaches proven accurate in modeling of hydrometeor scattering are compared to results obtained by WIPL-D software. The idea behind this comparison is to test each of the tools. Thus, WIPL-D results are compared to results of approximate solvers in regions where their approximations are defined, while approximate solvers are compared to WIPL-D results in regions where a particular approximate solver is considered inaccurate. Doing so provides an evaluation of the WIPL-D accuracy in the region where an approximation is known to hold and also quantifies the degradation of the approximate approach outside of that region.

Comparison, below is organized to follow historical complexity, as well as development of physical hydrometeor models. It starts by modeling spherical hydrometeors which, as discussed, lack polarimetric properties of natural hydrometeors. It then continues to more complex spheroidal models that are currently

used in the polarimetric radar simulators. Finally, it compares the results for high axis ratio models used mainly for hydrometeor modeling of winter precipitation (crystals), which cannot be accurately addressed by most of the tools currently in use.

4.2.1 Spherical models

The simplest and oldest physical shape model used in the modeling of meteorological scatterers is the dielectric sphere. The spherical model has a very simple closed form approximation that is valid for a large span of sizes. It usually serves as the first benchmark in the modeling of meteorological scattering. For that reason, spherical models are presented here.

A comparison of the T-Matrix and WIPL-D software results is presented in Fig. 4.12. The WIPL-D result for real part of s_{hh} is plotted in solid dark blue while the absolute value of the imaginary portion of s_{hh} is plotted as solid light blue line. The T-Matrix results are plotted as dashed lines in red for the real part of s_{hh} and orange for absolute value of imaginary s_{hh} . As stated, the absolute value of imaginary part of the complex scattering element is plotted in order to avoid differences in incident field definitions between the two codes.

For the purpose of comparison, the dielectric (ice) sphere model, which has a relative dielectric permittivity of $\epsilon_r = 3.17 - j0.0017$ at S-band (2.8 GHz), is modeled by varying the sphere diameter from 1 to 100 mm in 1 mm steps. As can be seen, the results (Fig. 4.12) show perfect agreement for the displayed range of diameter values. This is expected as both methods are fully capable of modeling spherical objects that

are at least up to one wavelength in size, which in this case is 100 mm. Scattering from larger spherical bodies is not considered because these are rare in nature.

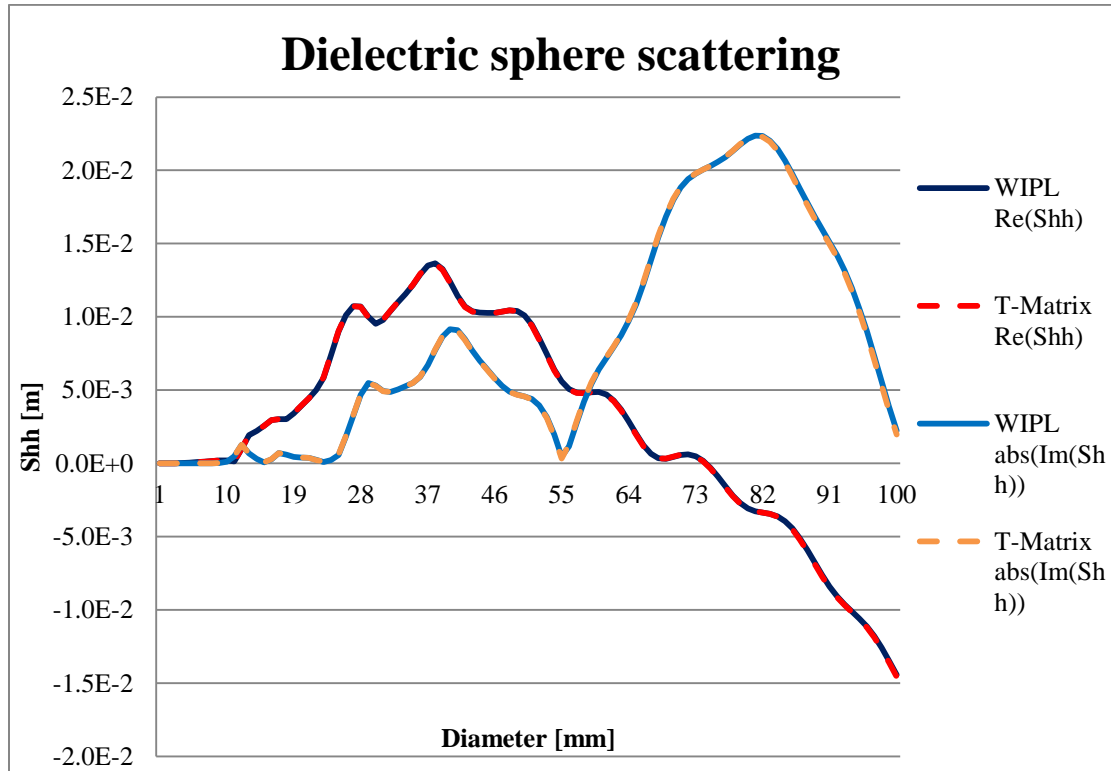


Figure 4.12 – Magnitudes of the real and imaginary parts of s_{hh} obtained using WIPL-D, and T-Matrix. The scatterers are ice spheres with dielectric permittivity $\epsilon_r=3.16-j0.02$.

4.2.2 Spheroidal models

Increasing the shape complexity from the pure spherical model leads to spheroidal shapes. These shapes are used to model raindrops, hailstones, and ice crystals for cases where accurate results using approximate methods can be produced.

Modeling of raindrops and hailstones as spheroids is usually done using the Rayleigh approximation for sizes small compared to λ and the T-Matrix method for larger sizes. A limitation of the Rayleigh solutions in size of the model calls for a more robust solution, yet the simplicity of the Rayleigh solution makes it attractive for

handling protruded spherical shapes. Generally, the T-Matrix is preferred by the meteorological community. Therefore, a comparison with T-Matrix is presented in this section.

An evaluation of the WIPL-D accuracy for the modeling of hydrometeors is considered through agreement of complex scattering element values. The electric field vectors for the horizontal (H) and vertical (V) polarizations are defined to be perpendicular to the hydrometeor's symmetry axis in case of H polarization and parallel to the hydrometeor's symmetry axis in case of vertical polarization. For all of the following benchmarks, the results are compared at the $(\alpha, \psi) = (0^\circ, 90^\circ)$, as the mean values of hydrometeor orientation and canting angle are found to be close or equal to 90° and 0° (Ryzhkov, et al., 2002).

The first hydrometeor type considered is the raindrop. Raindrops are the most frequently occurring hydrometeor type in most climate regions. Herein, raindrops are modeled at S-band for equivolume diameter range of 1 to 8 mm using the relative dielectric permittivity of liquid water $\epsilon_r = 75.59 - j8.905$, and an axis ratio defined by (3.1). Depending on the equivolume diameter, as governed by (3.1), the axis ratio is varied between 1 and 0.56. Raindrops of smaller sizes have almost spherical shape and are not considered.

Raindrop scattering elements are obtained using the T-Matrix and WIPL-D codes for both polarizations and are plotted in Figs. 4.13 and 4.14. Fig. 4.13 depicts results for horizontal (H) polarization and Fig. 4.14 presents the results for the orthogonal, vertical (V) polarization. In each figure the results obtained using the WIPL-D

software are drawn using solid curves and the T-Matrix results are presented with dashed curves. Similarly, the real part of the corresponding complex scattering element is given in blue for WIPL-D and red for T-Matrix. The absolute value of the imaginary part is plotted as light blue for the WIPL-D result and orange for the T-Matrix.

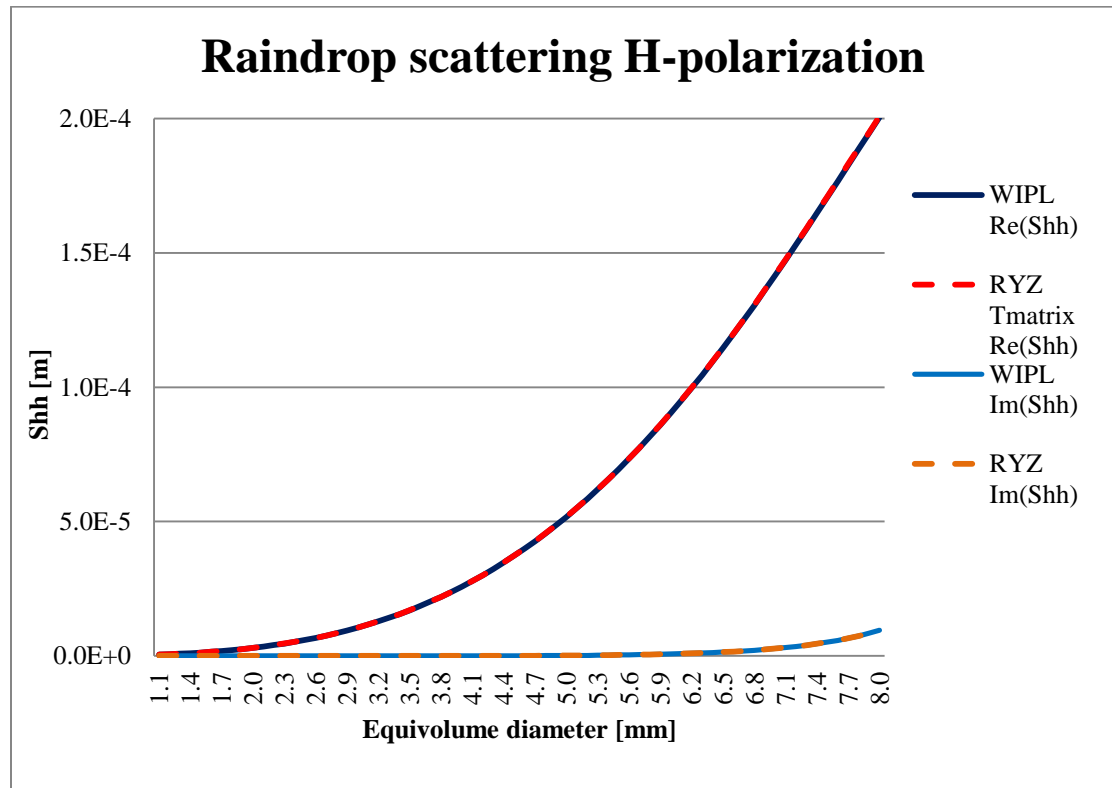


Figure 4.13 - Comparison of T-Matrix and WIPL-D results for raindrop of equivolume diameter range (1 mm to 8 mm). Real and imaginary parts of S_{hh} are plotted.

As depicted in these figures, scattering element values obtained using these two approaches are identical for all raindrop equivolume diameters. Since the T-Matrix results are well established and correct for raindrop sizes and axis ratios, it is concluded that CEM tools are fully capable for raindrop modeling.

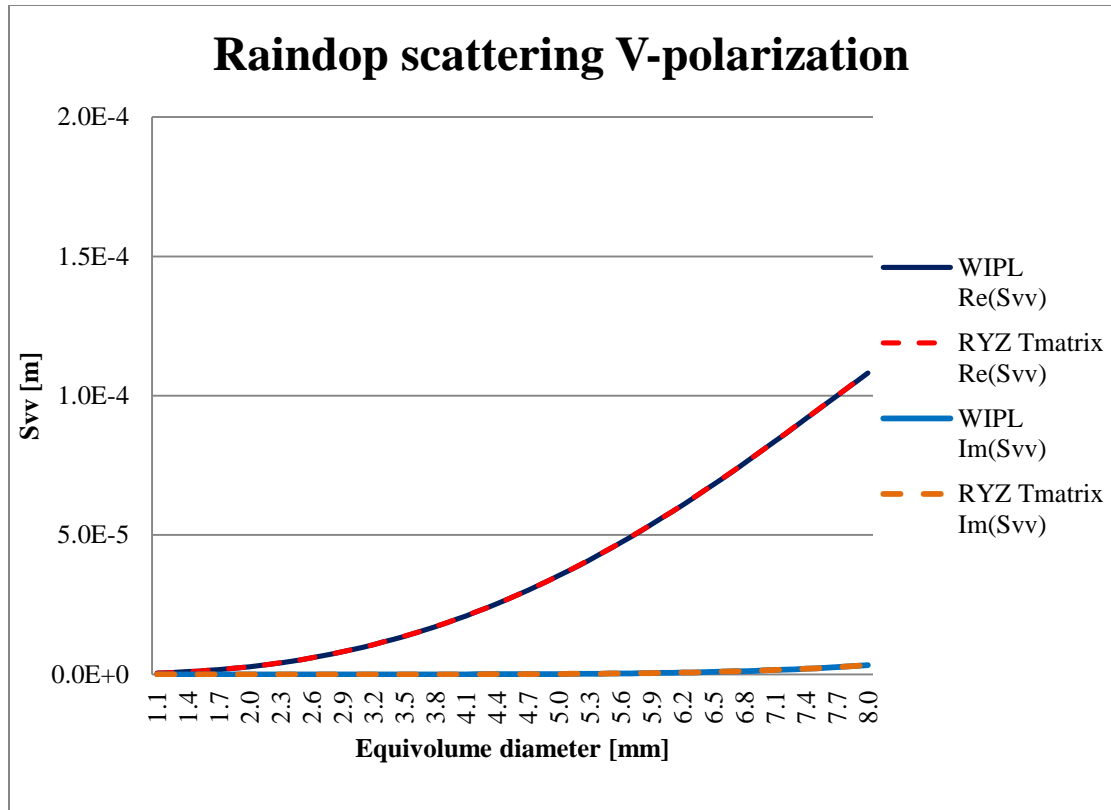


Figure 4.14 - Comparison of T-Matrix and WIPL-D results for raindrop of equivolume diameter range (1 mm to 8 mm). Real and imaginary parts of s_{vv} are plotted.

The comparison of results for raindrop models could be considered an introduction to the more general question of T-Matrix limitations and capabilities of modeling higher axis ratios in hydrometeor scattering applications. This, moreover, has special significance because the imprecise convergence limitations suggested in the literature may be reevaluated using CEM codes. This is done here for the dual-layer T-Matrix code (Bringi & Seliga, 1977) used in scatterer modeling of the polarimetric forward radar operator (Ch.3.2).

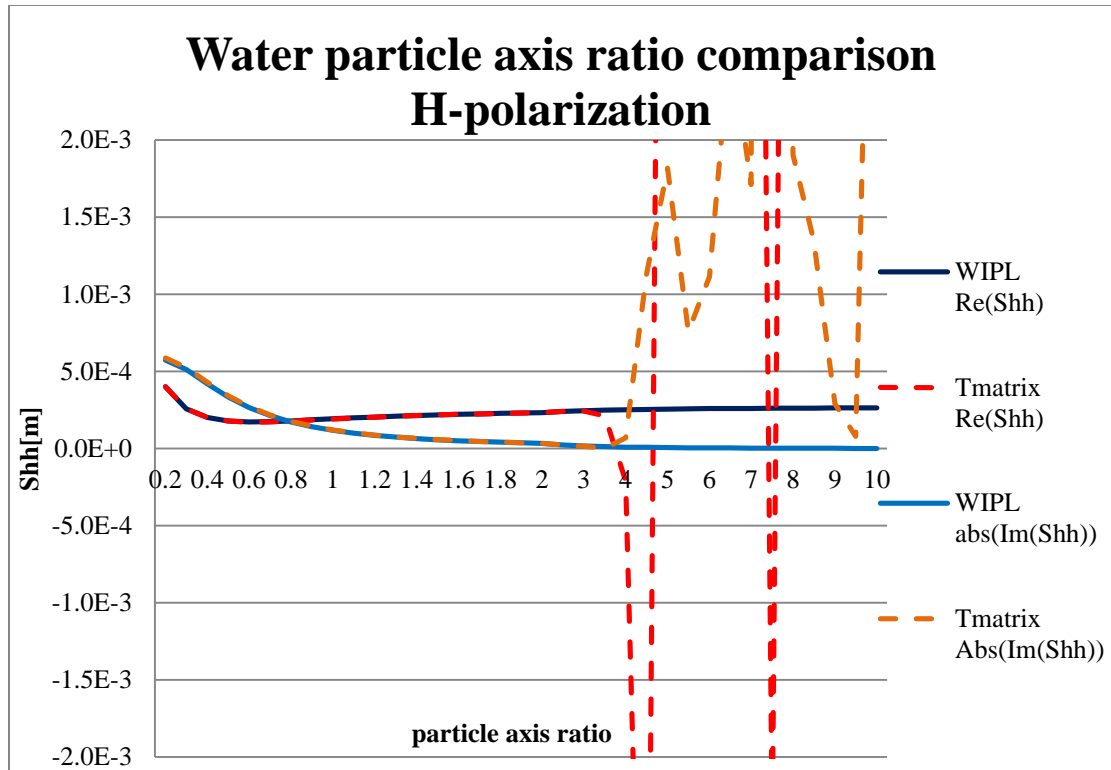


Figure 4.15 - Comparison of T-Matrix and WIPL-D scattering element results for 10 mm equivolume water ($\epsilon_r=78.2-j12.1$) spheroid with a vertical axis of symmetry and variable axis ratio changing from oblate to very prolate spheroids for co-polar scattering of horizontally oriented E field.

A raindrop scattering comparison is presented in Figs. 4.13 and 4.14 for raindrops whose equivolume diameter to axis ratio dependence is governed by the (3.1). The T-Matrix limitations are not quantified, but this issue is addressed next by modeling both water and ice particles. To start, the comparison is conducted for a water spheroid of 10 mm equivolume diameter. The simulation is carried out at S-band (2.8 GHz) using the relative dielectric permittivity $\epsilon_r = 78.3 - j12.1$ and varying the axis ratio from 0.2 up to 10, which is not realistic for raindrops. The values 8 to 10 mm are for illustration and could occur in nature only if the water is supported with an ice core. The computation, however, is done solely to determine the

limitations of the T-Matrix method in dealing with extremely eccentric spheroids. Thus, it is justified.

The results from this computation are presented in Figs. 4.15 and 4.16 for the co-polar backscattering at horizontal and vertical polarizations, respectively. For horizontal co-polar backscattering, the results are identical for axis ratios less than one (oblate spheroids). Once the axis ratio exceeds 3.5, the results diverge. The diverging results do not follow any predictable pattern but immediately start oscillating with large magnitudes for both the real and imaginary parts. Beyond the point of divergence, the behavior of the T-Matrix results is fully chaotic.

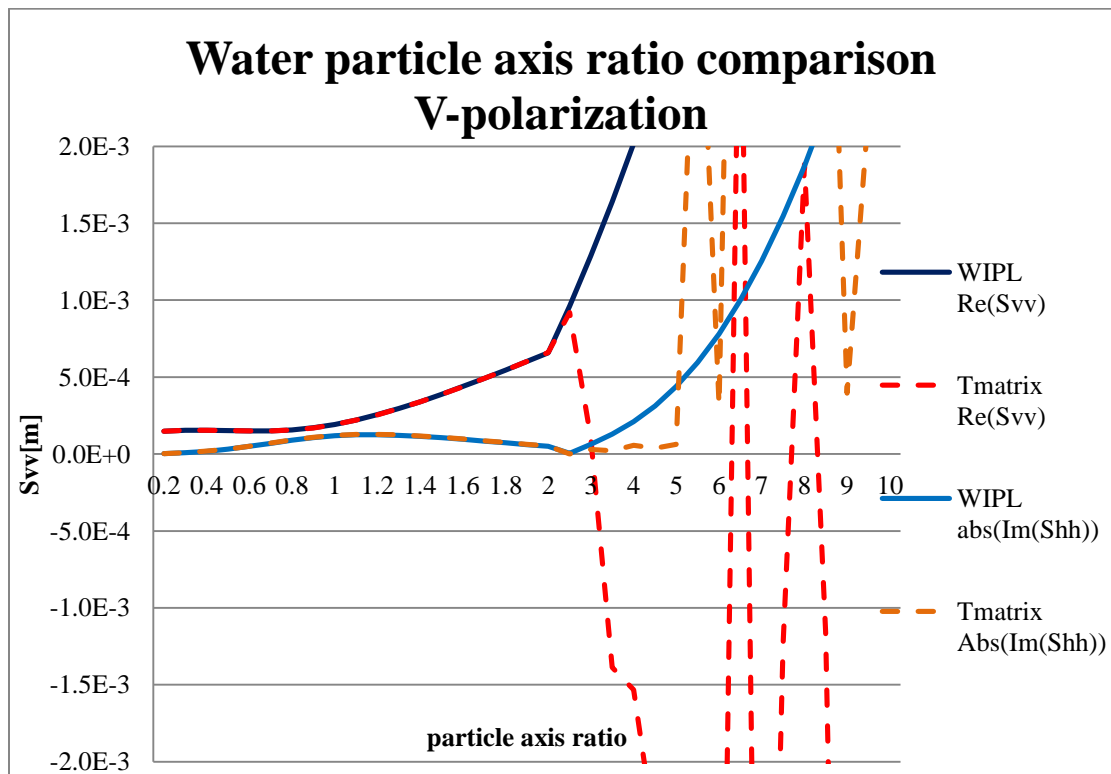


Figure 4.16 -Comparison of T-Matrix and WIPL-D scattering element results for 10 mm equivolume water ($\epsilon_r=78.2-j12.1$) spheroid with a vertical axis of symmetry and variable axis ratio changing from oblate to very prolate spheroids for co-polar scattering of vertically oriented E field.

In Fig. 4.16, the co-polar backscattering at vertical polarization is examined. As was the case for the horizontal co-polar backscattering, the T-Matrix results show good agreement for axis ratios from 0.2 up to 2. However, once the axis ratio exceeds the T-Matrix limit, their behavior is unpredictable and fully chaotic. It is interesting to note that the T-Matrix limit is smaller for vertical polarization. One may find this unexpected as prolate spheroids with an axis of symmetry parallel to the polarization vector would produce larger backscattering. Yet, the T-Matrix instability is caused by finite order of spherical function approximation. Therefore it is not tied to the actual backscattering value.

The overall conclusion that can be drawn for a relatively large, pure water particle is that the T-Matrix results may be used with certainty only for moderately spheroidal particles. Based upon this particular example, the axis ratios higher than 3 should not be considered in the T-Matrix applications. Justification of this proposed limit is illustrated in Figs. 4.15 and 4.16, where this represents the upper limit for which results in both polarizations may be considered conditionally accurate.

T-Matrix axis ratio limitations for another particle that is often found in nature, an ice particle of spheroidal geometry having fixed 3 mm equivolume diameter, are considered. The scattering elements are calculated at the W-band (90 GHz) using the relative dielectric permittivity of ice $\epsilon_r = 3.17 - j9.6$ and varying the axis ratio from 0.05 to 20 in unique steps. As in previous cases, the hydrometeor's axis of symmetry is aligned with the z axis of the WIPL-D. The simulations results are presented in Figs. 4.17 and 4.18, using the same colors and line schemes as in previous examples.

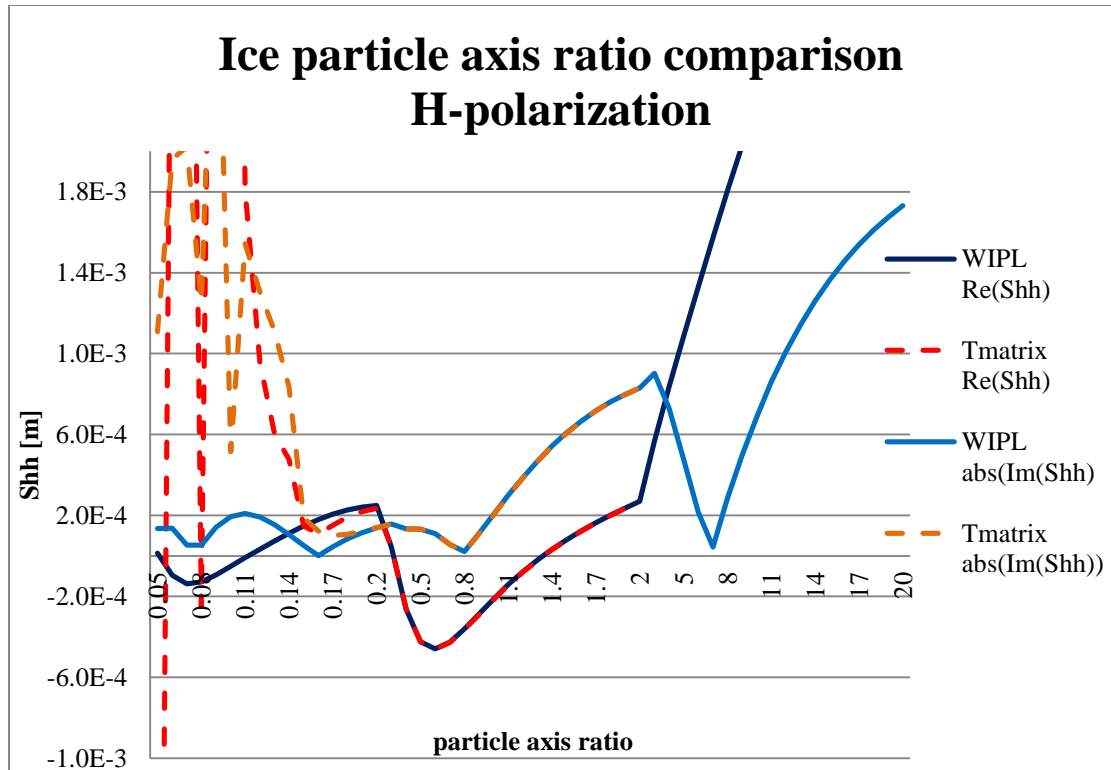


Figure 4.17 - Comparison of T-Matrix and WIPL-D scattering element results for 3 mm equivolume ice ($\epsilon_r=3.17-j9.6$) spheroid with a vertical axis of symmetry and variable axis ratio changing from extremely oblate to very prolate spheroids for co-polar scattering of horizontally oriented E field.

From Fig. 4.15, it is obvious that T-Matrix results do not converge for high axis ratios of oblate spheroids. Additionally, the results for the prolate spheroids with axis ratios higher than 3 in this particular case, do not exist because the computations used (Bringi & Seliga, 1977) failed convergence to its internal criteria at both polarizations.

Intuition and reasoning, typical for cases where the numerical error is the limiting factor to stability of results, may mislead the reader to expect better stability of the T-Matrix results for a polarization that is parallel to the hydrometeors larger axis. The results plotted in Fig. 4.17 and Fig. 4.18 counter the intuition, as the limiting factor of the T-Matrix is the truncation of spherical functions (see Ch. 2.1.4). It is obvious that

the T-Matrix becomes highly unstable for axis ratios less than 0.2, in the case presented.

Axis ratio limitation in the T-Matrix's computations is known and documented, however different T-Matrix code implementations may have different maximal axis ratio limitations. Each code requires either benchmarking in order to evaluate these values or relying on the in-code convergence evaluation criterion. In each case limitations imposed by maximal axis ratio are substantial for ice crystal known to have high axis ratios.

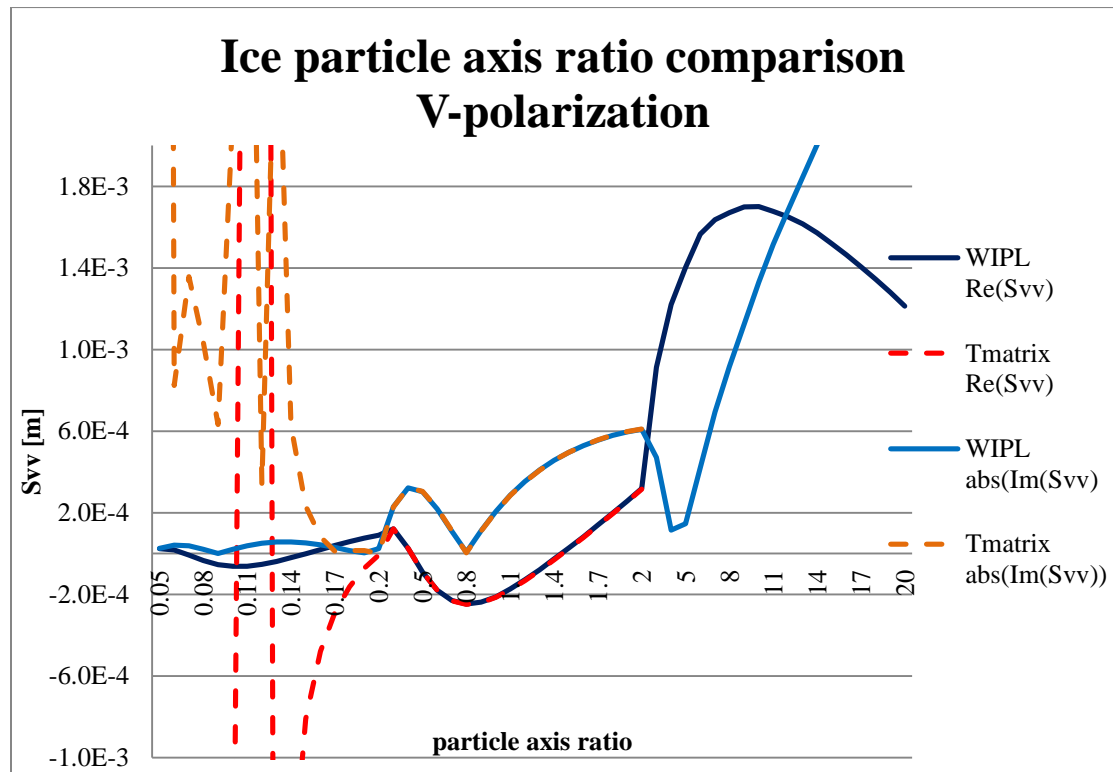


Figure 4.18 - Comparison of T-Matrix and WIPL-D scattering element results for 3 mm equivolume ice ($\epsilon_r=3.17-j9.6$) spheroid with a vertical axis of symmetry and variable axis ratio changing from extremely oblate to very prolate spheroids for co-polar scattering of vertically oriented E field.

The T-Matrix results for V polarization converge only for axis ratios larger than 0.3, which is slightly higher than in the case of horizontal polarization. Nonetheless, results for both polarizations experience similar chaotic behavior for highly oblate particles. Therefore the T-Matrix axis ratio limits can be established strictly to be 0.3 and larger for oblate and axis ratio of 3 or smaller for prolate particles. Unfortunately, an axis ratio limit for oblate particles of 0.3 may have a substantial impact on winter precipitation applications that use the T-Matrix because snowflakes are often modeled as oblate spheroids with high axis ratios.

4.2.3 Modeling of realistic ice spheroids having high axis ratio

An evaluation of the CEM method approach in modeling of high axis ratio objects for meteorological applications is conducted using an ice crystal model. An ice crystal with a variable axis ratio ranging from 1 to 20 is modeled using the relative dielectric permittivity $\epsilon_r = 3.17 - j9.6$ at the frequency of 90 GHz, which is usually used in observation of ice crystals in alto clouds, and an equivolume diameter of 0.1 mm.

Because the T-Matrix fails to converge for high axis ratios, it cannot be used for the purpose of the scattering element evaluation. The Rayleigh-Gans theory is used instead. In order to fit into the limitations of the Rayleigh-Gans approximation method, smaller ice particles are modeled. Despite the size, the calculated scattering elements have similar scientific importance as the elements of larger crystals.

A comparison of the WIPL-D and Rayleigh-Gans approximation scattering results is plotted in Figs. 4.19 and 4.20. Similar to the previous comparisons, the WIPL-D results are plotted in solid, while the Rayleigh-Gans approximation results are plotted

using dashed lines. Besides scattering elements on each of the figures, the overall radar cross section (RCS) for corresponding polarization is plotted. Here, the RCS plot is included to aid understanding, especially for the V polarization where both the real and imaginary portions of the scattering element are decreasing while, as expected, the actual magnitude is increasing.

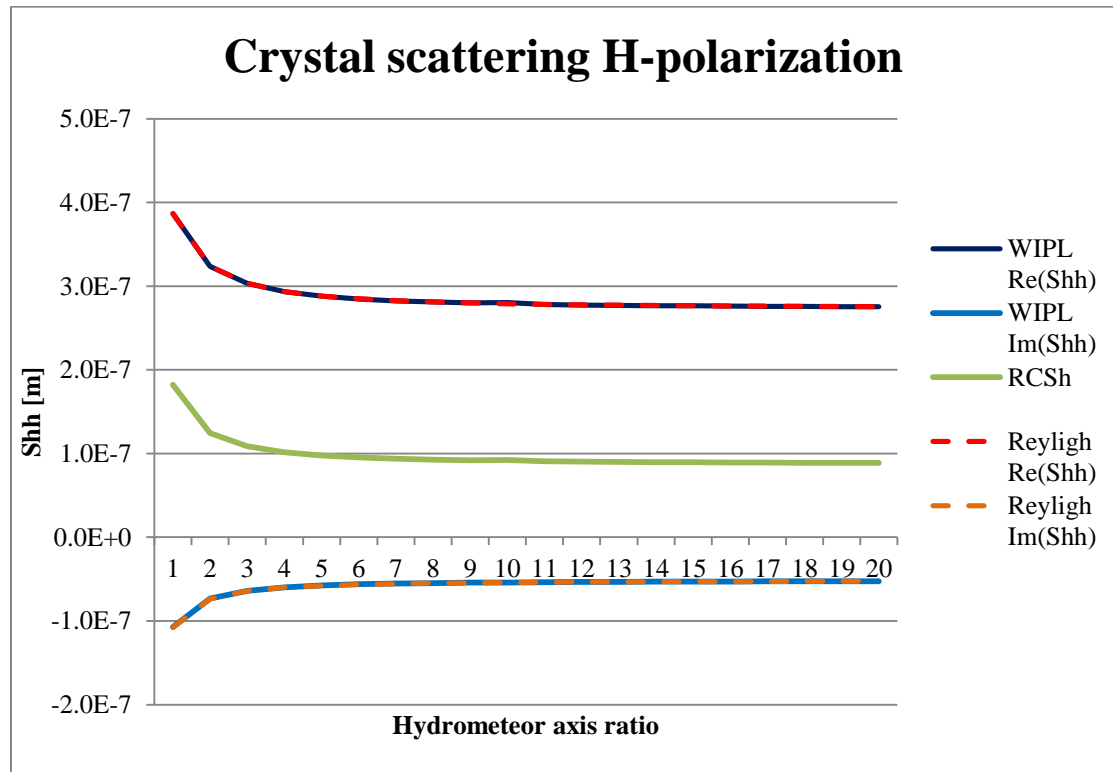


Figure 4.19 - Comparison of WIPL-D and Rayleigh approximation scattering element results for 0.1 mm equivolume ice ($\epsilon_r=3.17-j9.6$) spheroid with a vertical axis of symmetry and variable axis ratio changing from spherical to extremely prolate spheroids for co-polar scattering of horizontally oriented E field.

The scattering element values obtained using both of the approaches agree perfectly for horizontal polarization while, in the vertical polarization, a slight discrepancy in the real portion of the co-polar return exists. Such a discrepancy might be expected as low values are in place and different levels of numerical precision are present. Additionally, the number of numerical operations is very different for these two

approaches. The difference can therefore be easily assigned to the error in numerical calculations.

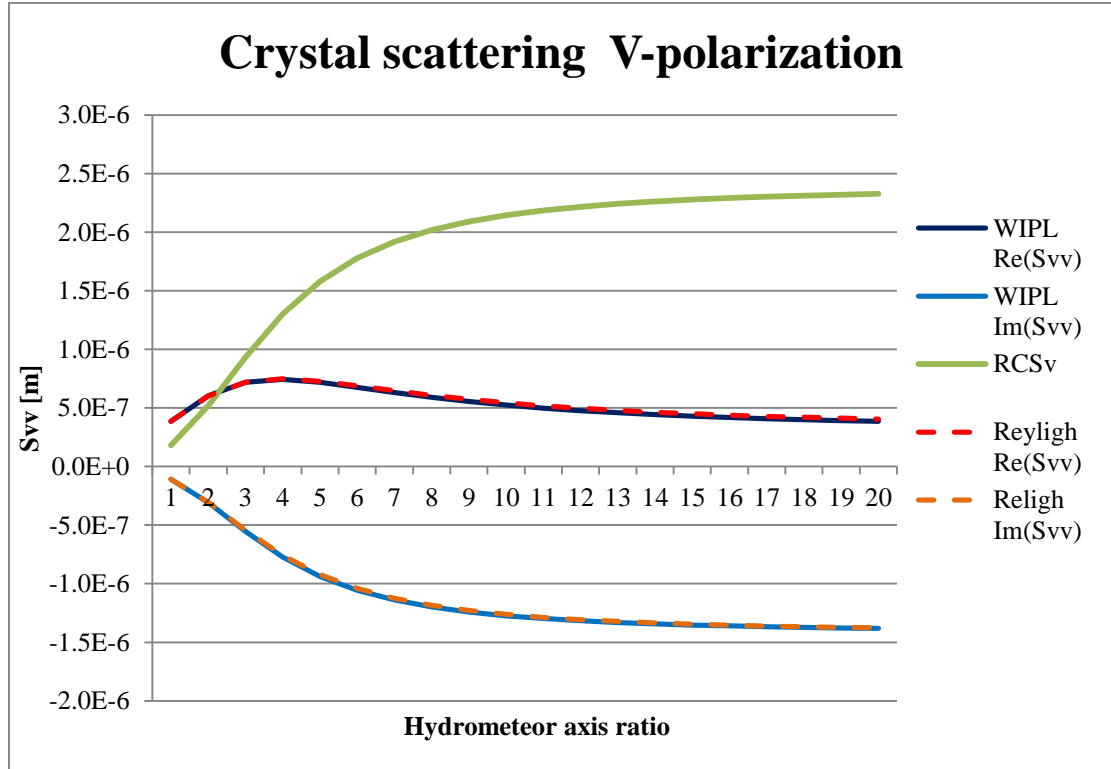


Figure 4.20 - Comparison of WIPL-D and Rayleigh approximation scattering element results for 0.1 mm equivolume ice ($\epsilon_r=3.17-j9.6$) spheroid with a vertical axis of symmetry and variable axis ratio changing from spherical to extremely prolate spheroids for co-polar scattering of vertically oriented E field.

In conclusion, the most important task addressed in this section was the evaluation of the scattering results obtained using one CEM approach the WIPL-D, as the tool of choice. The WIPL-D use for calculation of hydrometeor scattering results presented proved to be accurate. Furthermore, WIPL-D proved to be reliable in evaluating limits of the other tools that are currently being used for the same applications. Finally, it can be concluded that capabilities offered by the CEM tools are superior to capabilities of the non-CEM tools currently in use. On the other hand, the price of such “limitless” capabilities is paid in time efficiency of the CEM tools. Therefore,

for simple hydrometeors with low axis ratios the non-CEM tools may offer more efficient alternative.

5. POLARIMETRIC VARIABLE SIMULATOR

Developing the polarimetric variable simulator (PVS) is a multistage process. In the previous chapter, the scattering modeling portion of the overall process was discussed, providing a detailed overview of the scattering computations using the CEM tool WIPL-D. The calculated scattering elements are next used to obtain the polarimetric variables of the hydrometeor ensembles as with the fully polarimetric weather radar. The full description of the algorithm is presented.

5.1 TECHNICAL DESCRIPTION

The input parameters of the polarimetric variable simulator can be meteorological variables including temperature, pressure etc., however, this would require that precipitation modeling is included in the simulator. But, due to the complexity of the precipitation (cloud) models (e.g. HUCM), a scatterer (hydrometeor) size and orientation distribution will be considered known for the simulator presented herein. This distribution can be obtained using some of the precipitation (cloud) models and provided for the PVS with the necessary parameters.

Simulation for a known scatterer distribution consists of a set of tasks. Each task will be discussed in detail by providing a full technical description of the polarimetric variable simulator. The simulation starts with the extraction of the scattering elements from the scattering library. For each of the ensemble scattering models, orientations are determined from the input file and scattering products (backscattered covariance matrix elements) are averaged over a selected portion of a solid angle, creating

average particle properties with the prescribed orientation distribution. The algorithm can be visualized using Fig. 5.1.

The polarimetric variables calculated with the PVS are:

1. Reflectivity factor at horizontal polarization Z_H ,
2. Differential reflectivity Z_{DR} ,
3. Co-polar correlation coefficient ρ_{HV} ,
4. Backscatter differential phase δ ,
5. Linear depolarization ratio L_{DR} ,
6. Approximate circular depolarization ratio CDR_a .

Besides abovementioned polarimetric variables, other terms of the covariance matrix (polarimetric variables) can be calculated. Variables such as co-cross-polar correlation coefficients are not considered due to their limited use within meteorological circles. Polarimetric variables, synthesized by the simulator, are considered sufficient for evaluation and revealing the most important polarimetric signatures.

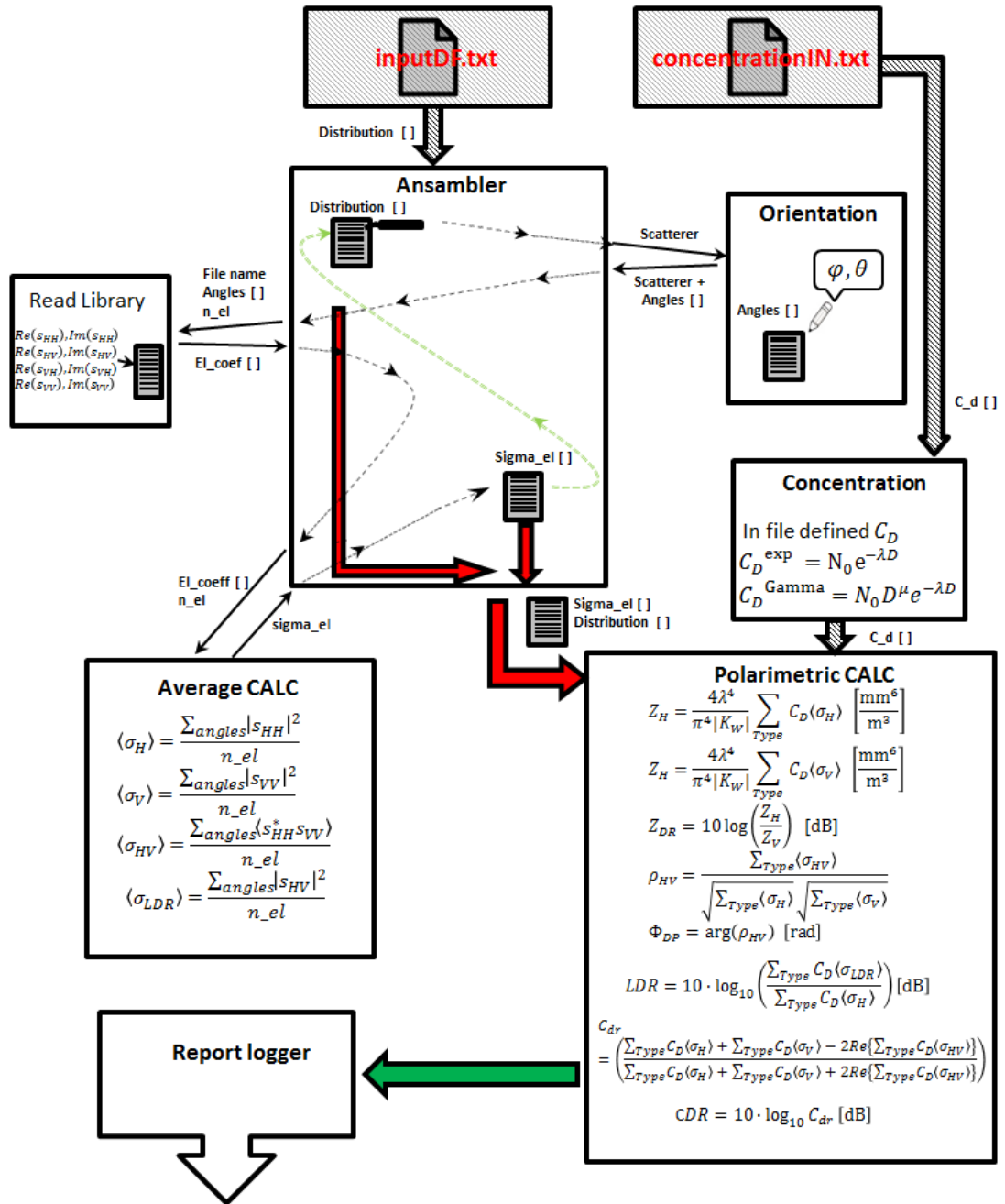
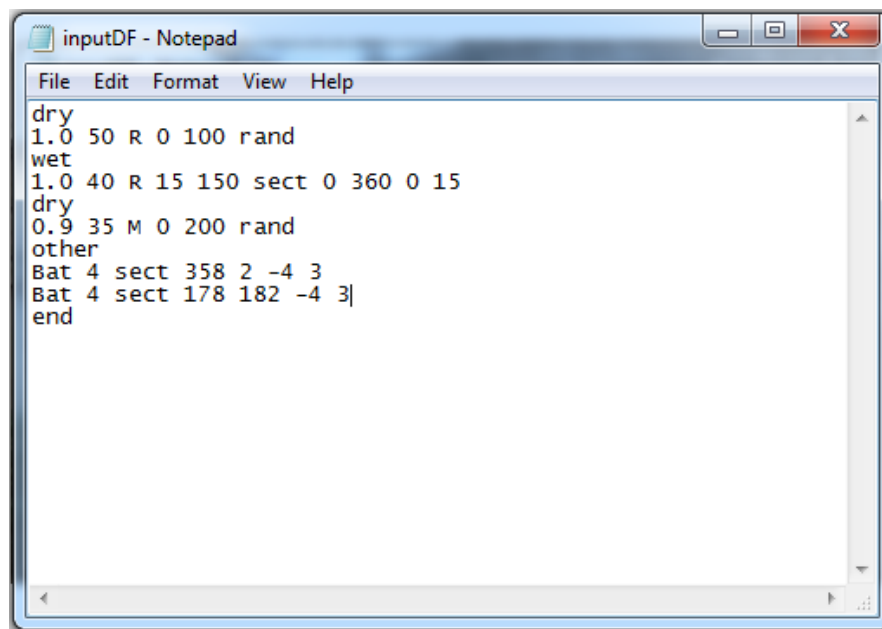


Figure 5.1 - Graphical representation of the simulation algorithm including all transient variables.

The polarimetric variable simulator presented in Fig. 5.1 consists of seven subprograms and requires two separate input text files. The inputs and subprograms will be presented with corresponding structural and mathematical processes, as well as outputs.

5.1.1 Simulator input

Defining the scattering model ensemble for the PVS is done using two input files. The first is the **inputDF.txt** which defines physical scattering models in the simulation. The **inputDF.txt** format depends on the type of the scattering model which is considered for the ensemble simulation. The format is presented using the example in Fig. 5.2.



```
inputDF - Notepad
File Edit Format View Help
dry
1.0 50 R 0 100 rand
wet
1.0 40 R 15 150 sect 0 360 0 15
dry
0.9 35 M 0 200 rand
other
Bat 4 sect 358 2 -4 3
Bat 4 sect 178 182 -4 3
end
```

Figure 5.2 - Format of the polarimetric variable simulator input file.

The first line of the file defines the type of the scattering models that follow. Simulator adds a new model for each line of the input file containing proper information required, until it reaches the name of another type or the “end” statement. Scattering models, in the simulator, are primarily distinguished as meteorological and non-meteorological (other). Because the main purpose of the PVS is meteorological applications the model types currently supported are:

- Dry hail “D”;
- Water-coated (wet) hail “W”;
- Ice crystals “C”;
- Irregular meteorological objects “I”;
- Other scatterers “O”.

Meteorological scatterers have on average spheroidal shapes that are described by its axis ratio, major axis, protrusion type and percent of the protrusion with respect to the large axis. The non-meteorological scatterers’ definition is in the scattering library (user defined) and is retrieved with its file name.

Once the scattering model is defined by the input parameter, the number of orientations to be used in the simulation needs to be specified. Orientations are either fully random (“rand”) or distributed over user specified sector of the solid angle (“sect”). The sector is defined using the WIPL-D coordinate system angles $\varphi_{start}, \varphi_{stop}$ and $\theta_{start}, \theta_{stop}$. For meteorological scatterers, these angles are obtained from polarimetric coordinate system using (4.4 and 4.5). For non-meteorological scatterers orientations depend on the orientation of the 3D model in the WIPL-D software, which is defined by the model provider.

As example the five scattering models defined by the inputDF.txt (Fig. 5.2 in sequential order) are:

1. Dry hailstone; axis ratio 1.0; diameter 50 mm; protrusion type: Random uniform; magnitude of protrusions is 0% of radius (no protrusions); 100 random orientation samples are averaged over the solid angle.
2. Wet hailstone; axis ratio 1.0; diameter 40 mm; protrusions: Random uniform; protrusions are 15% of radius; 150 orientation samples are averaged from the sector defined by $\varphi_{start} = 0^\circ$, $\varphi_{stop} = 360^\circ$ and elevation $\theta_{start} = 0^\circ$, $\theta_{stop} = 15^\circ$.
3. Dry hailstone; axis ratio 0.9; diameter 35 mm, protrusions: Modified random; protrusions are 0% of diameter; 200 random orientation samples are averaged over the solid angle.
4. Other type of scatterer with file name Bat; 4 orientations are averaged from the sector defined by $\varphi_{start} = 358^\circ$, $\varphi_{stop} = 2^\circ$ and elevation $\theta_{start} = -4^\circ$, $\theta_{stop} = 3^\circ$.
5. Other type of scatterer with file name Bat; 4 orientations are averaged from the sector defined by $\varphi_{start} = 178^\circ$, $\varphi_{stop} = 182^\circ$ and elevation $\theta_{start} = -4^\circ$, $\theta_{stop} = 3^\circ$.

The last two models are subsets of the same physical model, but different in orientations. The simulator does not check for redundancy of the physical models at input, hence, same physical model can be defined in the ensemble multiple times for different orientations. As in the example, 5th and 6th inputs represent bats flying

toward the radar (head on), and the later 6th input bats flying away from radar (head away).

The simulator implies uniform distribution of angles over the specified sector. Ipso facto, creating non-uniform distribution of orientations is done by specifying partially uniform sets of orientations. These partial sets are assigned weighting factors in the **concentrationIN.txt**.

The **concentrationIN.txt** file specifies a weighted concentration number of each scattering model of the **inputDF.txt**. The **concentrationIN.txt** file is a list of rational numbers used for weighting angularly averaged scattering models in the same order of appearance as in the **inputDF.txt**. The PVS incorporates parameter concentration functions dependent only on the scattering model diameter. Supported concentration functions are: exponential (5.1) (special case of Gamma distribution for $\mu = 0$) and Gamma distribution functions (5.2) for which input parameters²⁴ λ, μ, N_0 have to be defined.

$$C_D^{\text{exp}}(D) = N_0 e^{-\lambda D} \quad (5.1)$$

$$C_D^{\text{Gamma}}(D) = N_0 D^\mu e^{-\lambda D} \quad (5.2)$$

Following from many discussions (e.g. (Ryzhkov, et al., 2011)) one or multi parameter concentration functions in many cases fail to represent observed drop size distribution (DSD). The solution proposed by the same authors is spectral bin treatment of concentrations obtained from precipitation models. This makes spectral bins an obvious choice for the distribution input in the PVS. Additionally, as PVS is

²⁴ Those corresponding to the distribution.

introducing higher variety of hydrometeor parameters than current modeling algorithms (protuberances etc.), spectral bin distribution is revisited to account for additional degrees of freedom offered. Distribution of scatterer sizes is introduced in the model by assigning weights to each scatterer category. These are specified in the **concentrationIN.txt** file, where the weight is assigned to each scattering model defined in the **inputDF.txt**.

5.1.2 Hydrometeor scattering library

Scatterer's properties defined in the simulation input are stored in the scattering library. For each physical hydrometeor model the scattering library contains polarimetric scattering elements calculated over the entire range of solid angle. Orientations of hydrometeors are defined in the modeling software (Ch. 4.2). While, for non-meteorological scatterers orientation is left to the user (creator) to specify.

The scattering library is organized as a database of text files having the **.cft** extension. Each file, in the scattering library, corresponds to one physical model with backscattered matrices for all orientations. As in case of orientations, non-meteorological models are named by the library creator and a PVS user needs to be aware of convention used. Meteorological models are organized to follow name convention defined in Fig. 5.3.

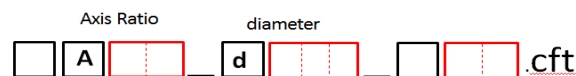


Figure 5.3 - Illustration of the scattering library name convention.

Name convention in Fig. 5.3, uses the first character to define the type of a hydrometeor (“D” dry, ”W” wet, ”C” crystal, ”I” irregular), second character is always “A” symbolizing the axis ratio which is a two digit number (decimal point is omitted). Following is the letter “d” and the three digit number for the physical hydrometeor diameter value in mm. And at the end is the character defining protuberance type (currently: “R” Rough uniform, “M” modified uniform roughness, “S” spikes) and two digits quantifying the roughness type (percentage of radius for “R” and “M”).

5.1.3 Simulation process

The simulation process starts with the import of data from the input files into the list of all scattering models – Distribution (Fig. 5.1). The Distribution list contains all scattering model data from the **inputDF.txt** file and is used for the cycling of the complete simulation process. In each simulation cycle one scattering model is taken from the list, and depending on orientation properties defined in the **inputDF.txt**, a list of specific orientation angles ($\varphi_{1p}, \theta_{1p}$) is created. The number of entries in the Angles list (Fig. 5.1) corresponds to the number of orientations specified in the **inputDF.txt**.

The list of angles, created by the Orientation subroutine, is based on the “seeded” pseudorandom process, which is bounded between the user input values in case of “sect” orientation properties or by 4π steradian if “rand” is the orientation mode. Current limitation of the code is that orientation limits have to be set in ascending

order (regarding particular angles) in the range 0 to 360 degrees for azimuth angle and -90 to 90 degrees for elevation.

Once the specific orientation angles are defined, the scattering library is searched for the corresponding physical scattering model and the corresponding polarimetric scattering elements are extracted by the Read Library subroutine. Extracted scattering elements are then averaged into the averaged scattering model represented by the scattering products (backscattered covariance matrix elements) (5.3 – 5.6):

$$\langle \sigma_H \rangle = \frac{\sum_{angles} |s_{hh}|^2}{n_{el}}; \quad (5.3)$$

$$\langle \sigma_V \rangle = \frac{\sum_{angles} |s_{vv}|^2}{n_{el}}; \quad (5.4)$$

$$\langle \sigma_{HV} \rangle = \frac{\sum_{angles} \langle s_{hh}^* s_{vv} \rangle}{n_{el}}; \quad (5.5)$$

$$\langle \sigma_{LDR} \rangle = \frac{\sum_{angles} |s_{hv}|^2}{n_{el}}. \quad (5.6)$$

Each averaged particle σ_i is associated with four scattering products (backscattered matrix elements) describing its scattering properties. Calculated products are: $\langle \sigma_H \rangle$ orientation averaged backscattering cross section at the H polarization, $\langle \sigma_V \rangle$ is the orientation averaged at the V polarization, whereas $\langle \sigma_{HV} \rangle$ and $\langle \sigma_{LDR} \rangle$ are co-polarization product cross section and cross-polar cross section. Evaluation of these terms ends the scattering model cycle. Calculated covariance matrix elements describe the averaged particle created for every scattering model at the input. Physically, an averaged scattering model is the average of n_{el} -many physical models having different orientations.

5.1.4 Calculation of the polarimetric variables

Once the particle averaging is done, the cycle is completed, and the list of the averaged moments is used for the calculation of the polarimetric variables (5.7-5.13). Formulation of the polarimetric variables may appear to be different from those defined in Ch. 2.5, in the way that summation in this case is done over the averaged particles polarimetric products σ_i instead of the scattering elements as in Ch.2.5.

$$Z_H = \frac{4\lambda^4}{\pi^4 |K_W|} \sum \sigma_i C_D \langle \sigma_H \rangle \left[\frac{\text{mm}^6}{\text{m}^3} \right] \rightarrow Z = 10 \cdot \log Z_H \text{ [dBZ]}; \quad (5.7)$$

$$Z_V = \frac{4\lambda^4}{\pi^4 |K_W|} \sum \sigma_i C_D \langle \sigma_V \rangle \left[\frac{\text{mm}^6}{\text{m}^3} \right]; \quad (5.8)$$

$$Z_{DR} = 10 \log \left(\frac{Z_H}{Z_V} \right) \text{ [dB]}; \quad (5.9)$$

$$\rho_{HV} = \frac{\sum \sigma_i C_D \langle \sigma_{HV} \rangle}{\sqrt{\sum \sigma_i C_D \langle \sigma_H \rangle} \sqrt{\sum \sigma_i C_D \langle \sigma_V \rangle}}; \quad (5.10)$$

$$\delta = \arg(\rho_{HV}) \text{ [rad]}; \quad (5.11)$$

$$L_{DR} = 10 \cdot \log_{10} \left(\frac{\sum \sigma_i C_D \langle \sigma_{LDR} \rangle}{\sum \sigma_i C_D \langle \sigma_H \rangle} \right) \text{ [dB]}; \quad (5.12)$$

$$CDR_a = 10 \cdot \log_{10} \left(\frac{\sum \sigma_i C_D \langle \sigma_H \rangle + \sum \sigma_i C_D \langle \sigma_V \rangle - 2\text{Re}\{\sum \sigma_i C_D \langle \sigma_{HV} \rangle\}}{\sum \sigma_i C_D \langle \sigma_H \rangle + \sum \sigma_i C_D \langle \sigma_V \rangle + 2\text{Re}\{\sum \sigma_i C_D \langle \sigma_{HV} \rangle\}} \right) \text{ [dB]}. \quad (5.13)$$

The first two variables, evaluated in the PVS, are radar reflectivity factors at the two polarizations. The reflectivity factor is the most important variable that has been identified with weather radars. The values of horizontal reflectivity factor for weather phenomena are in the range of -10 dBZ up to 80 dBZ (Kumjian, 2013).

Immediately following the reflectivity factors is the differential reflectivity Z_{DR} . It is independent of the concentration of the hydrometeors in the scattering volume. Typical values of Z_{DR} in precipitation according to (Kumjian, 2013) range from -1 dB

up to 6 dB; in the case of random tumbling of hydrometeors such as hail it is equal to 0 dB.

Co-polar correlation coefficient depends on both amplitude and phase of the returned signals. In physical sense, it can be understood as similitude of the signals in the H and V channels. Relation of the H and V returns represents the measure of diversity in hydrometeor properties, orientation, and shapes in the scattering volume and their contribution to the overall return signal (Kumjian, 2013). The ρ_{HV} is independent of the concentration of hydrometeors in the scattering volume. Properties affecting the co-polar correlation coefficient are changes in orientation, distributions of sizes and axis ratios and composition. Observed values of the co-polar correlation coefficient from hydrometeors are between 0.6 in cases of giant hail to unity in drizzle. Values of ρ_{HV} higher than 1 are not physical. They are usually related to the improper correction of the noise effects or small number of samples in the estimates (Ryzhkov, 2007).

The phase difference of the backscattered fields is the argument of the complex co-polar correlation coefficient. It is directly related to the resonant sizes of non-spherical hydrometeors and that makes its prediction very challenging. This is because the phase difference in small Rayleigh scatterers is null whereas in resonant size scatterers it depends on size, shape, angle of incidence, and permittivity. The backscatter differential phase is superposed to the propagation differential phase and system differential phase, and thus is hard to quantify. Therefore and also because it is insignificant in most precipitation it has not been subject of many studies. Instead, the total propagation phase shift Φ_{DP} is mainly considered in literature.

The ratio of the cross-polarized scattered power to the co-polarized scattered power is called linear depolarization ratio, L_{DR} . In the physical sense, the L_{DR} is related to the orientation (canting) of spheroidal shapes, or complex shape scatterers in the resolution volume. In most precipitation, values of L_{DR} range from -30 dB to -15 dB (Zrnić, et al., 2002). Additionally, L_{DR} accumulates due to propagation through canted or oscillating hydrometeors causing bias that is hard to correct.

The approximate circular depolarization ratio (CDR_a) is the last polarimetric variable synthesized by the PVS. To distinguish it from the true CDR ((Doviak & Zrnic, 2006); $\frac{|s_{rr}|^2}{|s_{lr}|^2}$, eq. 8.41b) the subscript a is used. In the CDR_a the contribution by the cross polar intrinsic term s_{hv} is ignored. Similarly to the L_{DR} , the CDR_a is not available on the WSR-88D network. Same as L_{DR} , CDR_a is the polarimetric variable with “memory” and can be heavily biased by propagation differential phase. Nevertheless, using equation 8.56a in (Doviak & Zrnic, 2006) without the $\cos \Phi_{DP}$ term this propagation effect can be mitigated so that the CDR_a becomes a function of Z_{DR} and ρ_{HV} . Another approximate CDR has been defined from the variables computed in the SHV mode (Matrosov, 2004) (Ryzhkov, et al., 2014). Because of its practical significance it is labeled as CDR_p a proxy CDR. The CDR_p can be computed form (5.13) by replacing $2Re\{\sum_{\sigma_i} C_D \langle \sigma_{HV} \rangle\}$ with:

$$2 \cdot \sqrt{\sum_{\sigma_i} [|\sigma_{HV}|^2 + \sigma_{LDR}^2 + 2|\sigma_{HV}| \cdot \sigma_{LDR} \cos(\Phi_{DP} + 2\beta_{TX})]} \quad \text{to which } 2 \cdot \sum_{\sigma_i} \sigma_{LDR}$$

should be added.

This expression is valid for oblate spheroids (with protuberances) that have a symmetric distribution of canting angles about a mean value of zero, as simulated herein.

Importance of the CDR is best illustrated above the melting layer where it can be used for discrimination of dry hail sizes aloft, quantification of rimming effects associated with super cooled cloud water (hazardous as produces icing to aircrafts) and studies of particle orientation (Ryzhkov, et al., 2014). CDR values recorded in literature are ranging from -30 dB up to -6 dB as illustrated in (Ryzhkov, et al., 2014).

5.1.5 Simulation output

Calculated polarimetric variables are displayed on the simulator screen in the units listed in (5.7-5.13) and stored in the simulation report. The simulation report is the final step and the last subroutine executed by the PVS. The logger subroutine in the simulator diagram (Fig. 5.1) is used to create detailed report of each simulation. The output of the logger subroutine is the **LOG_DDMMYYYY_HHMMSS.txt** file, where characters “**D**” stand for the day of the simulation, “**M**” for month, “**Y**” is the year, and the following is the simulation start time in hours “**H**”, minutes “**M**”, and “**S**” seconds. Such convention is adopted to simplify running multiple simulations in a row without possibility to overwrite data due to any input distribution or similarities.

```

LOG_09062015_170112 - Notepad
File Edit Format View Help
EM ensemble scattering simulator REPORT

Calculated values of the polarimetric variables for the ensemble are:
Zh=31.97 dBZ
Zv=38.80 dBZ
ZDR=-6.83 dB
Mag(RhoHV)=0.99615
Phase(RhoHV)=-0.000 rad
LDR=-96.63 dB
CDR=-19.53 dB

Ensamble consists of following particles:

-----
| TYPE | AXIS | Diameter[mm] | Perturbation | Roughness | No. of angles | Concentration | Orientation | Phi | Theta |
-----
| D | 9.0 | 15 | R | 99 | 5000 | 1.000e+000 | sect | 0 -360 | -10 - 10 |
-----

Legend:
TYPE: D - Dry hail      w - wet(water coated) hail      I - Irregular hail      ! - Element does NOT exist in the Library
Perturbation: R - Uniform roughness (% of radius)      M - uniform axis ratio tapered roughness (% of
No. of angles = represents the number of averaged canting angles in creation of an averaged particle of specified type
Concentration = concentration of such element type in 1m^3

Phi and Theta columns are contain start and stop values of canting angles. For RAND orientation these values are set to 0

```

Figure 5.4 - Structure of the polarimetric variable simulator output file.

A Log file is organized as in Fig. 5.4. Immediately following the headline are the calculated polarimetric variables and then the list of the ensemble properties. A table of each scatterer model input is listed including: type, axis ratio, diameter, perturbation type, quantification of the perturbation, number of angles used in angular averaging (creating the averaged scattering model), as well as concentration, orientation type and range of canting angles for the sector type of orientation. Below the ensemble is the legend of the abbreviations with a brief explanation of each parameter.

5.2 POLARIMETRIC VARIABLE SIMULATOR RESULTS

The presented results are calculated assuming the monodisperse size distribution of “dry” and water coated hailstones. Relative dielectric permittivity used for ice and water are $\epsilon_{ice} = 3.1685 - j0.02492$ and $\epsilon_{liquid\ H_2O} = 78.3 - j12.1$ respectively (Ryzhkov, et al., 2011). Hailstone axis ratios are 0.6, 0.7 and 0.8 (Knight, 1986) having protuberances of M (modified uniform) type and R (random uniform) type defined in Ch.4.2.1 with the protuberance (roughness) values of 2%, 6%, 10% and 14% of radius. Each simulation was ran for an ensemble consisting of approximately 21 000 orientations over a quasi-uniform distribution of canting angles ($-40^\circ \leq \alpha \leq 40^\circ$) at frequency of 2.8 GHz with 5 mm hailstone size increment. Hailstone diameters are along the long axis and in the 5 to 100 mm range. Orientation and canting are defined as described in Ch.4.2.2, and the incident electric fields are orthogonal and equiphase.

Polarimetric variables for all ensembles, having different axis ratios and protuberances, are presented in the Appendix B. Following, are the results illustrating significance of the work and comparison with polarimetric radar observations.

Gauging hail size aloft is one of the main motivations for the study and a pressing need for weather services. Algorithms for hail sizing are under development in the National Severe Storm Laboratory (NSSL), relying on the observational and modeled data. Still, it remains unclear what are the effects of roughness and dry versus wet hail to the variables. The CEM tools are the only viable methods for calculating scattering of protruded large hailstones, while some results (as indicated) obtained for spheroids

were already applied for the purpose (Kumijan, 2012). The goals are to include missing results for ρ_{HV} , and improve existing for Z_{DR} and δ . Additionally an attempt is made to evaluate how well these variables discriminate between small (smaller than 1 inch), large (1 to 2 inches) and giant (greater than 2 inches) hail.

Although results are presented for monodisperse size distribution, it is hypothesized that often size sorting can occur so that larger size hail fall faster. In such cases, the distribution would be relatively narrow and the results might be directly applicable to some observations.

5.2.1 Effect of roughness on the co-polar correlation coefficient and backscatter differential phase

The effects of roughness on the polarimetric variables are illustrated on the co-polar correlation coefficient and the backscatter differential phase. For example, water coated (“wet”) hailstones with a 0.6 axis ratio and having M and R type roughness are presented in Figs. 5.5 and 5.6.

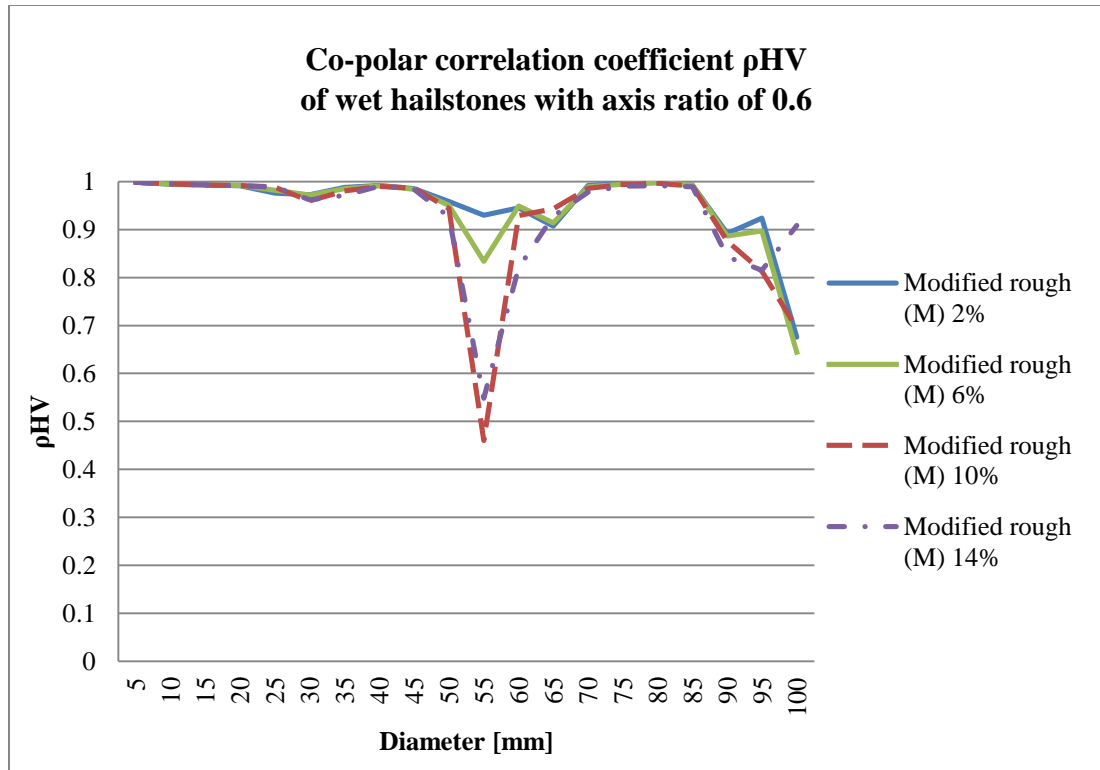


Figure 5.5 - Co-polar correlation coefficient (ρ_{HV}) for wet hailstones with axis ratio of 0.6 and M-type roughness of 2% (solid blue), 6% (solid green), 10% (dashed red) and 14% (dot-dashed violet).

Differences in the ρ_{HV} for two different protuberance types are rather small. Random R distribution of roughness produces slightly larger drop at sizes near 55 mm (0.3 compared to 0.4 for M type 10% roughness). It is interesting that the slightly less rough particles (10%) causes larger drop in RHV than the more protruded (14%) particles. This is attributed to the micro resonance effects.

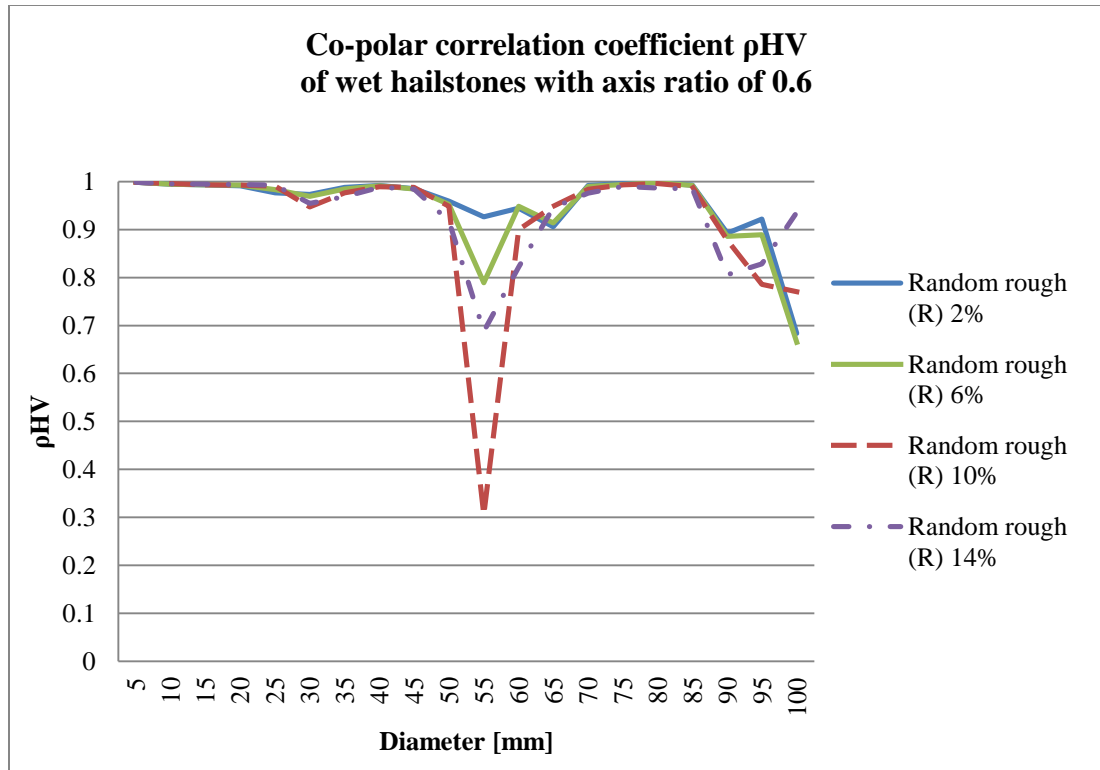


Figure 5.6 - Co-polar correlation coefficient (ρ_{HV}) for wet hailstones with axis ratio of 0.6 and R-type roughness of 2% (solid blue), 6% (solid green), 10% (dashed red) and 14% (dot-dashed violet).

The decreases at 30 mm and 55 mm hailstone sizes are also seen in the results of (Balakrishnan & Zrnić, 1990) except that magnitude of these is considerably smaller than the values in Figs. 5.5 and 5.6. For example their values of the ρ_{HV} for spongy hail of same axis ratio but due to the lack of canting and roughness produce a decrease to at most 0.83 compared to values between ~ 0.8 and 0.3 (Fig. 5.6). Balakrishnan and Zrnić identify the issue and claim that canting introduces additional drop to the correlation coefficient value. Furthermore, they produce same Z_{DR} signature for the presented particle (see 0.6 axis ratio wet hailstones in Appendix B).

The backscatter differential phase results are available in (Balakrishnan & Zrnić, 1990) only for sizes up to 60 mm, and their computation is for oblates with the minor

axis horizontally oriented in the plane of polarization. Therefore to compare with the values herein the sign of Z_{DR} and δ in (Balakrishnan & Zrnić, 1990) should be reversed and the equivalent diameter changed to the large axis. Values of the backscatter differential phase are presented in Figs. 5.7 and 5.8 for major axis up to 100 mm. The range of values between 70 and 150 degrees around 60 mm encompasses the value of 100 degrees in (Balakrishnan & Zrnić, 1990).

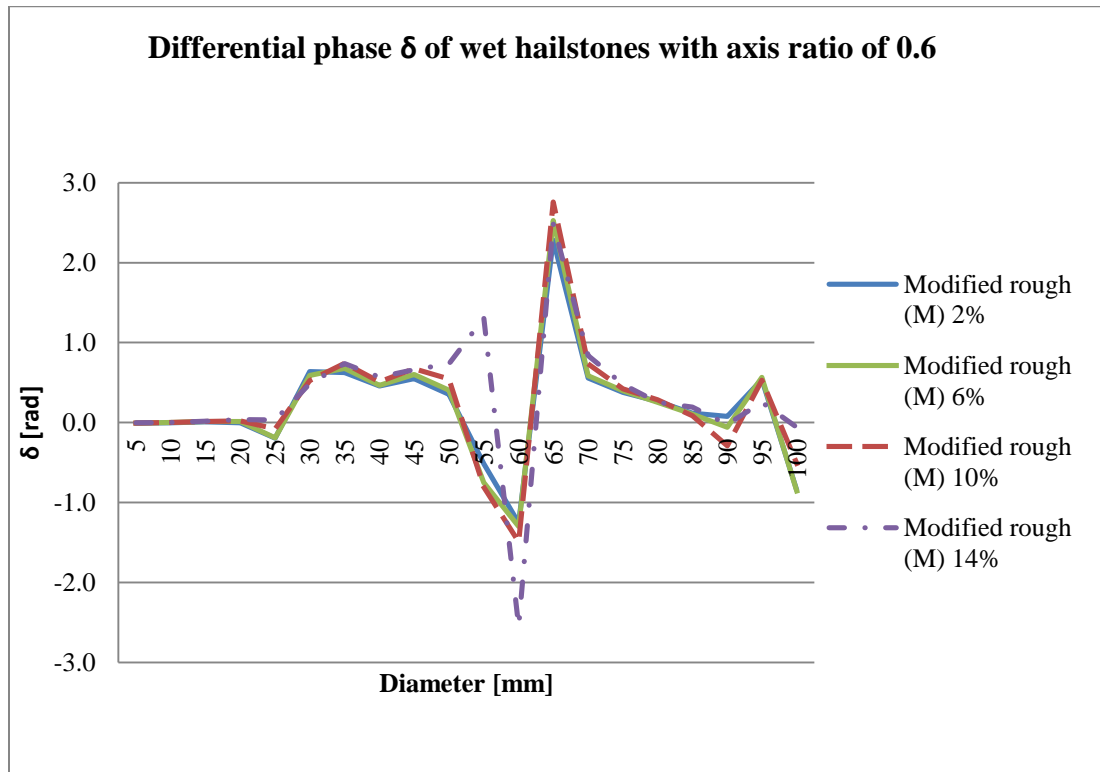


Figure 5.7 - Backscatter differential phase (δ) for wet hailstones with axis ratio of 0.6 and M-type roughness of 2% (solid blue), 6% (solid green), 10% (dashed red) and 14% (dot-dashed violet).

As it was the case for the ρ_{HV} the dependence of backscatter differential phases on roughness is modest and would be further smoothed by the distribution of sizes in regions of hail.

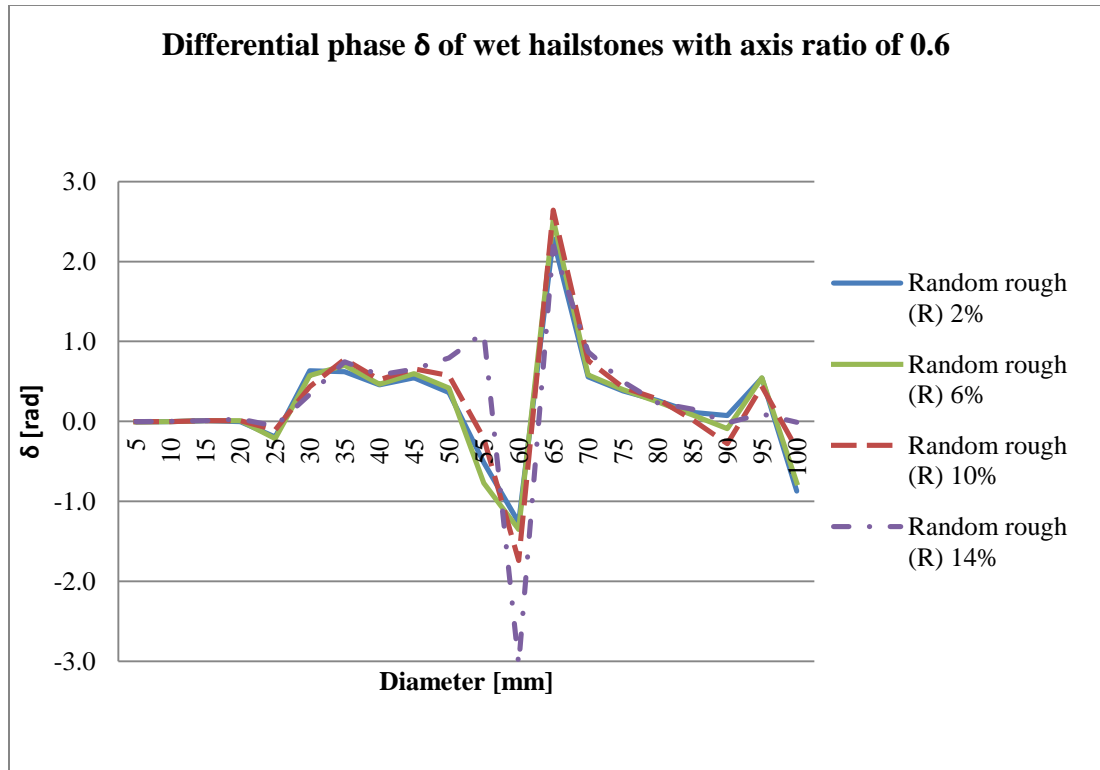


Figure 5.8 - Backscatter differential phase (δ) for wet hailstones with axis ratio of 0.6 and R-type roughness of 2% (solid blue), 6% (solid green), 10% (dashed red) and 14% (dot-dashed violet).

Because the ρ_{HV} and backscatter differential phase might be key discriminators for large and giant hail quantifying their values as functions of size and axis ratio is important. The results are presented in the Appendix B.

5.2.2 Differential reflectivity and linear depolarization ratio in large hail

Z_{DR} needs to be considered with other polarimetric variables to infer about hail presence and possibly size. At lower altitudes, below the melting layer, there is significant amount of partially melted hail with large axis ratios. Therefore, Z_{DR} values below the melting layer can be significantly positive. However, negative Z_{DR} is also observed in hail (Fig. 5.9); it can be caused by differential attenuation (Kumijan, 2012), or can be genuine. It is important to note that oblate wet hail of

about 50 mm to 70 mm size produces negative Z_{DR} . In dry hail negative net values persist between 70 and 100 mm size (Fig. 5.10).

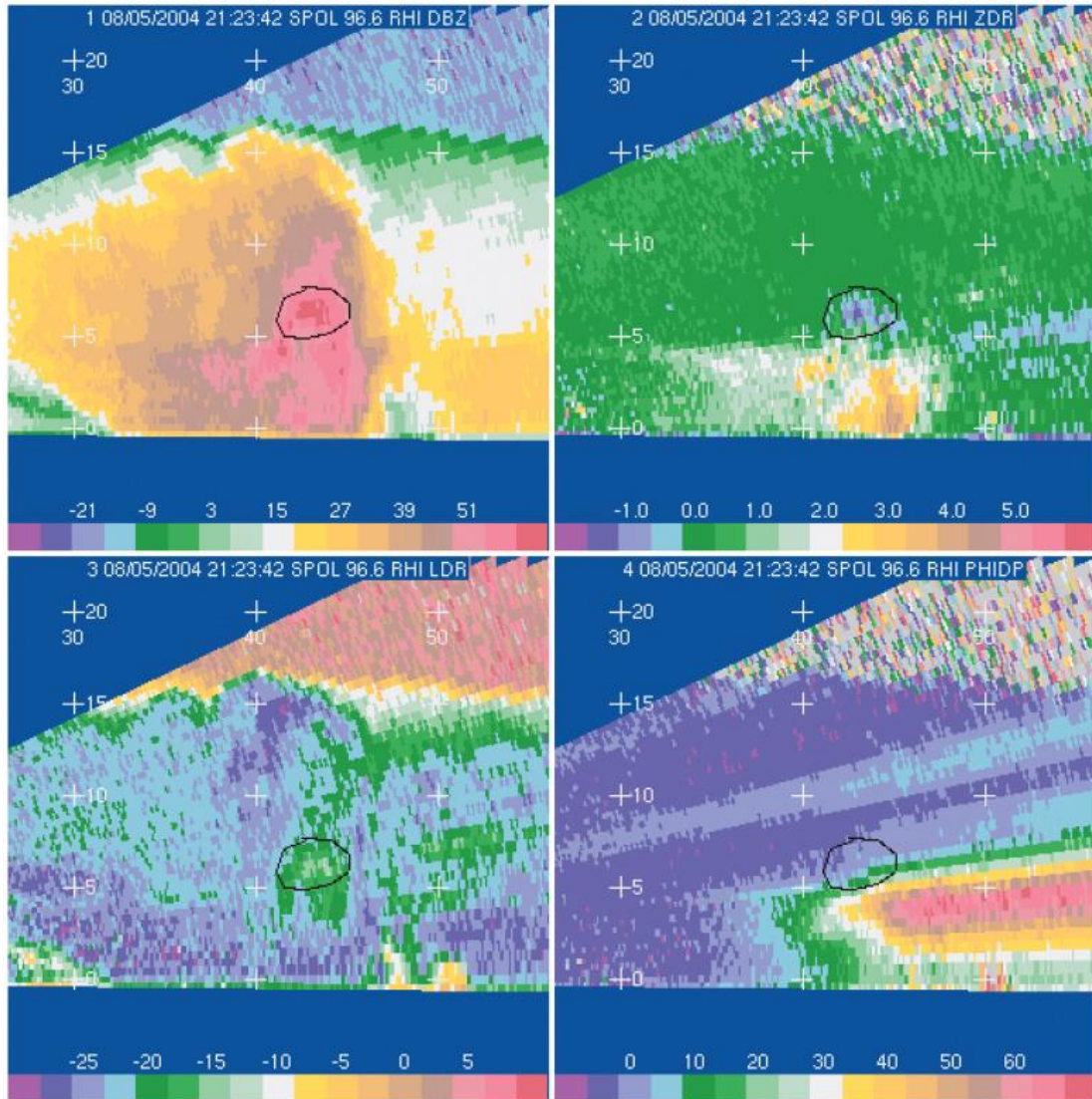


Figure 5.9 – Vertical cross sections of polarimetric variables in a hailstorm. Top left) is Z in dBZ contours given on the color bar. Top right) is differential reflectivity with a negative pocket clearly visible above the melting layer; values in dB are indicated on the color bar. Bottom left) is the LDR with values in dB. Bottom right is differential phase in deg. Circled is the hail region. The figure is from (Higgs, et al., 2006).

Researches have observed negative differential reflectivity values. One example is in Fig. 5.9 with clearly visible negative pocket of Z_{DR} (smaller than -1.5 dB) above the

melting layer. The computations of Z_{DR} in Figs. 5.10 and 5.11 would support these negative values if the hail size distribution (HSD) favors the sizes at which Z_{DR} is negative. To test this hypothesis, integration of reflectivity factors (in linear units) weighted by the HSD needs to be made. This is addressed next.

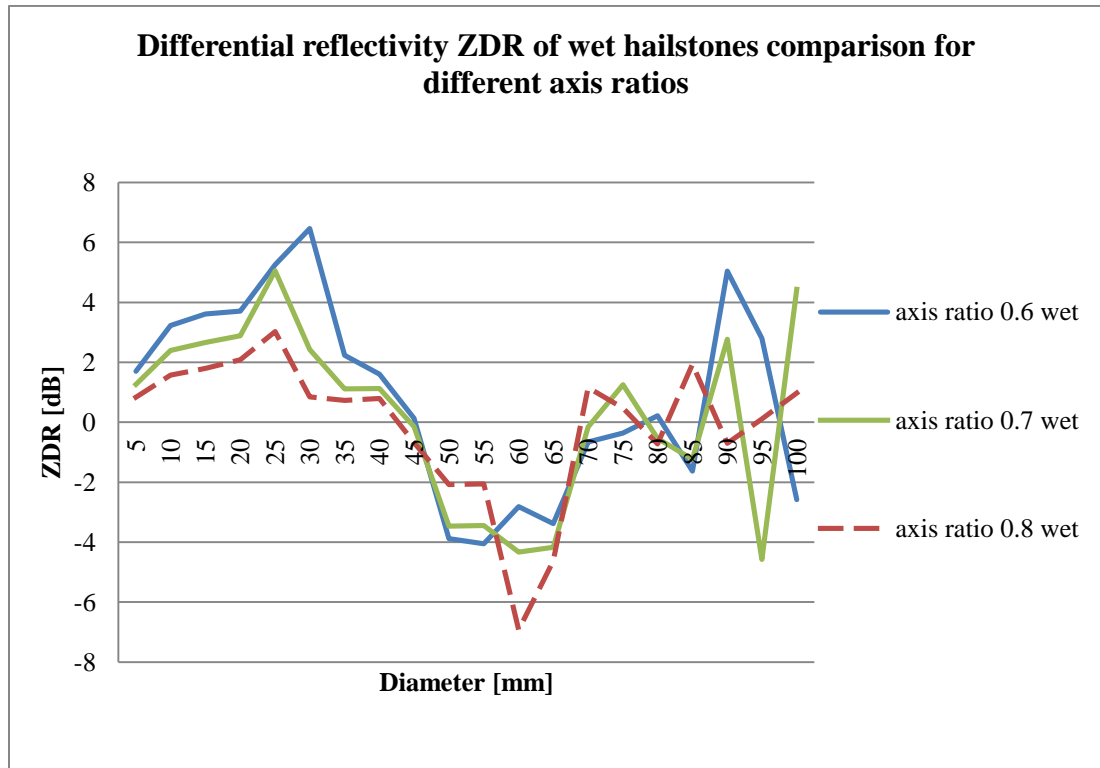


Figure 5.10 - Differential reflectivity (ZDR) for wet hailstones having the 2% M-type roughness and three axis ratios as indicated.

Present knowledge about the hail size distribution is scant. Smaller sizes are represented by an exponential function (Cheng & English, 1983). From models and observations and the work by Cheng and English, researchers conclude that one exponential function should be used for sizes less than 8 mm and spliced to it should be another exponential function to cover the sizes up to about 30 mm (Ryzhkov, et al., 2013). For even larger sizes there are no accepted forms of the HSD although it appears that the distribution is often centered on the mean (Ziegler, et al., 1983).

Thus the exponential distribution recommended by (Ryzhkov, et al., 2013) for hail size up to 30 mm by extending it to larger D_{max} values. It quickly became evident that no D_{max} could produce negative Z_{DR} . A uniform distribution of sizes up to 70 mm still would not produce negative values. Thus, examined are the values of reflectivity factors that enter into computations of Z_{DR} . These values are plotted in Fig. 5.12 for 0.7 axis ratio, wet hailstones having the 2% M-type roughness. Note that values of Z_{dr} become smaller than 1 (i.e., negative Z_{DR}) after D reaches the cross over point at about 45 mm. Then it stays smaller than 1 for sizes between 45 and 65 mm, and at these sizes the reflectivity factors are about four to five times smaller than at sizes of about 40 mm. Simply stated the integral of Z_h (from 10 mm to about 70 mm) divided with the integral of Z_v is always larger than 1. Therefore there is no way to have negative Z_{DR} unless the HSD gives most weight to the sizes between 45 and 70 mm. To elaborate further consider a two-step hail size distribution: let the first step be from 25 mm to 45 mm and have a value of a and the second from 45 to 70 mm be 1. It can be shown that a Z_{DR} of -1.5 dB would occur if $a \leq \frac{2}{27}$. This means that the concentration of hail smaller than 45 mm needs to be lower by a factor of 13.5 the concentration of hail between 45 and 70 mm. Although this is a hypothetical example, it indicates that for Z_{DR} to be negative HSD must be narrowly centered at sizes 50 to 60 mm. This conclusion is not sensitive to the distribution of canting angles as the curves for 40° and 10° (Fig. 5.12) are very similar. Moreover, the axis ratios of 0.8 and 0.6 (not shown) cause marginal difference in the cross over point.

Narrow HSDs at three different times of observations are plotted by (Ziegler, et al., 1983), their Fig. 8. These are centered around 12 mm, 24 mm, and 40 mm and are

about 10 to 20 mm wide with minimal overlap between each other. Because great care was made in collecting these samples it is safe to assume that the lack of overlap is not due to melting of the smaller sizes but to the genuine lack of these sizes. It is hypothesized that size sorting can be present in the strong updraft that supports hail growth (indicated by the convex Z in Fig. 5.9) and that it ejects small hail and levitates the large hail until ultimately its weight (gravity) exceeds the aerodynamic force of its support. Then the hail falls.

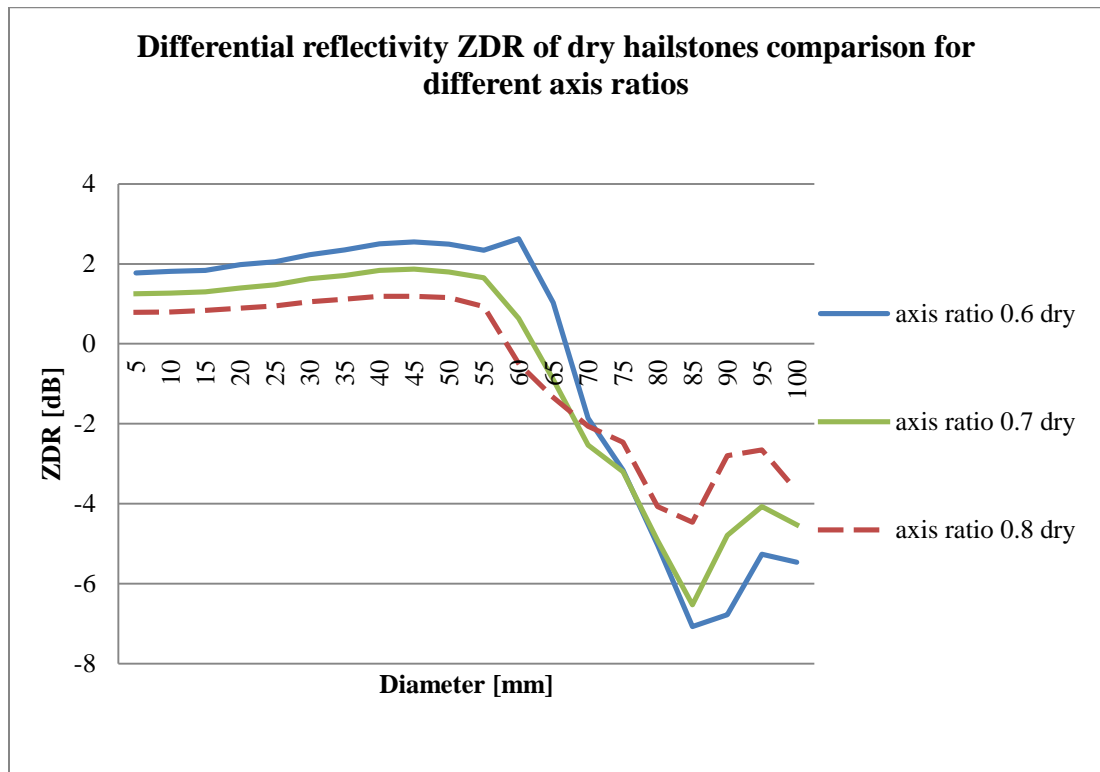


Figure 5.11 - Differential reflectivity (Z_{DR}) for dry hailstones having the 2% M-type roughness and three axis ratios as indicated.

It is significant that the pocket of negative Z_{DR} (Fig. 5.9) is above the melting layer and that the reflectivity contour has a convex shape suggesting that hail is supported by an updraft. Thus, it might be that hail there is oblate and undergoing wet growth. Dry hail of sizes larger than about 65 mm also produces negative Z_{DR} (Fig. 5.10). In

this case it is unlikely because to be dry, hail has to be ejected from the updraft into the air void of supercooled drops. The L_{DR} values of about -15 dB (Fig. 5.9) are consistent with large wet hail in the same size range; the average simulated L_{DR} is close to -15 dB (Fig. 5.13).

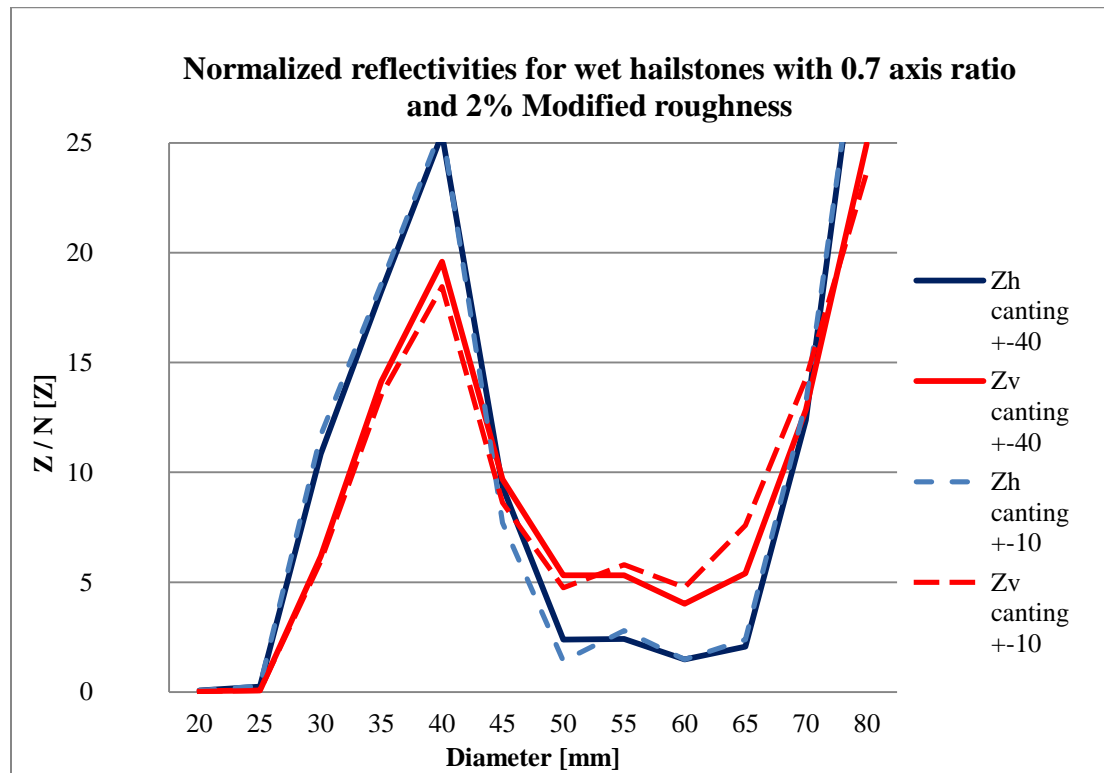


Figure 5.12 - Normalized radar reflectivity factors to the unit volume and 10^8 factor, for wet hailstones with 0.7 axis ratio and 2% Modified roughness protuberances. Results for 40° canting are plotted as solid curves, and 10° canting plotted as dashed lines.

Similar value of negative Z_{DR} just on top of the melting layer (height 4 – 6 km) $Z_{DR} \sim -2$ dB for $Z = 65$ dBZ is reported by Illingworth (Illingworth, et al., 1987). The values and location are consistent with the wet growth region of giant hail.

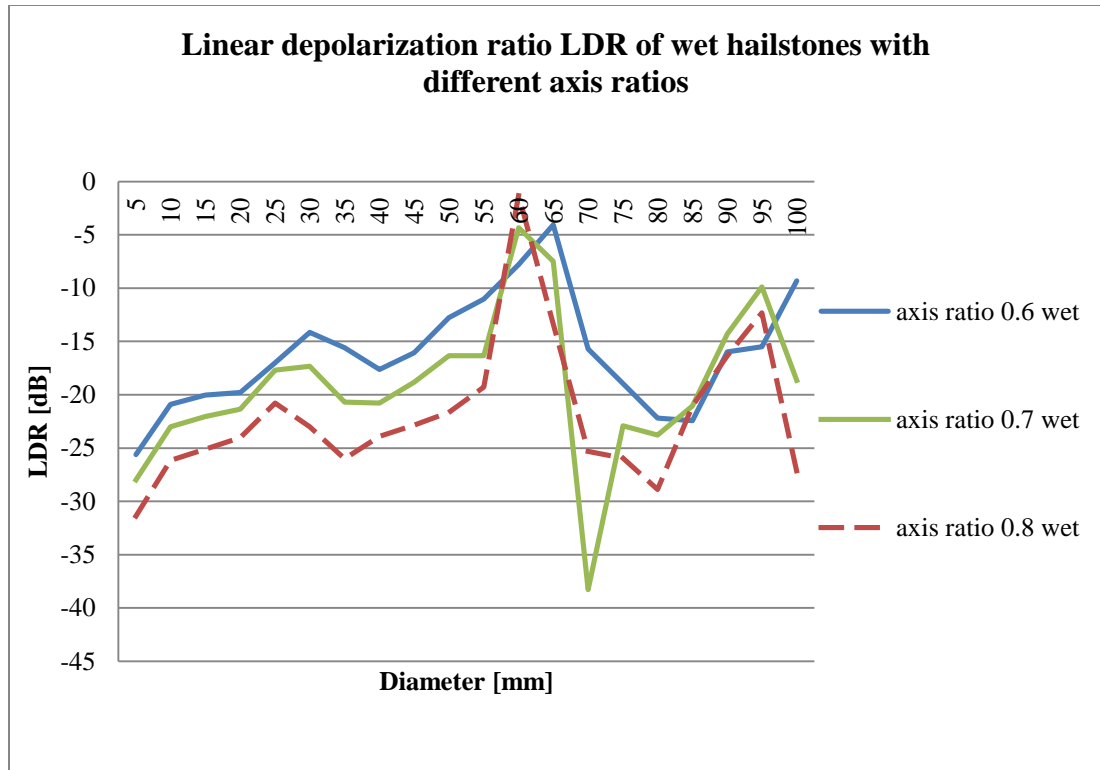


Figure 5.13 - Linear depolarization ratio (LDR) for wet hailstones having the 2% M-type roughness and three axis ratios as indicated.

Negative values of Z_{DR} in a hailstorm are discussed by Aydin who attribute these to “sizes predominantly in the 12 to 40 mm range, which fall with their larger dimensions aligned (on the average) vertically” (Aydin, et al., 1990). These authors had no additional polarimetric variables such as L_{DR} to help their interpretation. According to simulations an L_{DR} less than about -15 dB would support this interpretation (Fig. 5.13). In the case of Fig. 5.9 the juxtaposition of L_{DR} larger than -15 dB and Z_{DR} smaller than -1.5 dB clearly indicate sizes in the 45 to 65 mm range.

Also, Housson and Pointin (Housson & Pointin, 1989) report negative $Z_{DR} \sim -1.4$ dB at heights below 2.5 km in $Z = 60$ dBZ regions. Giant hail could not

grow that close to the ground but likely is melting, or hail is smaller but differential attenuation caused negative Z_{DR} .

From the Figs. 5.9 and 5.11 it is concluded that the negative Z_{DR} can be produced by the water coated hail above the melting layer having axis ratios 0.6 to 0.8 and a narrow distribution of sizes mostly larger than about 50 mm. This conclusion is corroborated with the values of the L_{DR} in Fig. 5.13, identifying the circled pocket in Fig. 5.9 as the hailstone wet growth region. Although the L_{DR} measurements are presented in the Fig. 5.9 they are not available from the WSR-88D network. Definitely more observations are needed to associate negative Z_{DR} with hail size.

5.2.3 Circular depolarization ratio in hail

Circular depolarization ratio, as the name says is the ratio of the cross-polar and co-polar returns for circular polarized radar system. The CDR is likely the first polarimetric variable definitely related to hail (Barge, 1974), and the hypothesized range of values is given by Balakrishnan and Zrnić (Balakrishnan & Zrnić, 1990). The idea of measuring CDR using the radar with simultaneous transmission/reception at X-band comes from Matrosov (Matrosov, 2004). Theoretical work carried out by Matrosov resulted in approximate formulas of the CDR containing linear scattering matrix elements (2.40). Work on the CDR is further examined by Ryzhkov (Ryzhkov, et al., 2014) who formulated the algorithm for calculation of CDR_p using WSR-88D polarimetric products. Because CDR_p is mainly affected by the size, shape and composition of particles in scattering volume it can be useful in microphysical studies. Ryzhkov et al. (Ryzhkov, et al., 2014) emphasize the capability for

determination of the hailstone sizes above the melting layer as well as quantification of rimming associated with super cooled water aloft.

The CDR_a calculated for hailstones of different axis ratio having 2% M type protuberances is presented for dry and wet hail in Figs. 5.14 and 5.15.

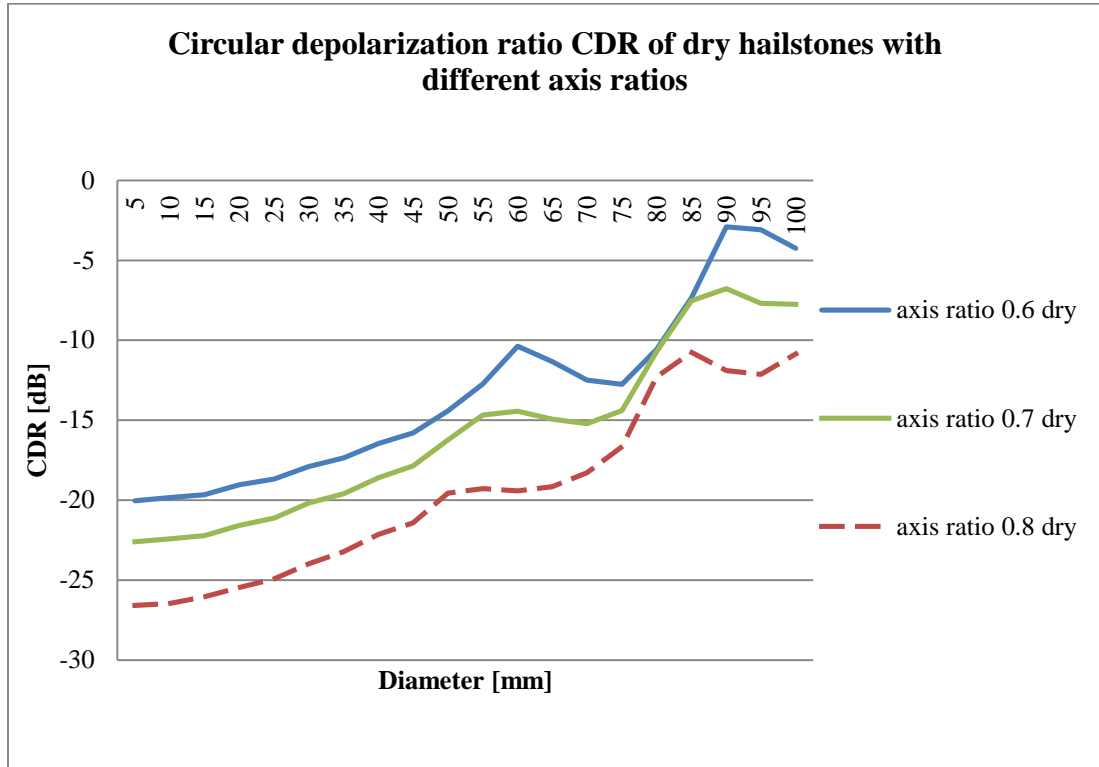


Figure 5.14 - Circular depolarization ratio (CDR) for dry hailstones having the 2% M-type roughness and axis ratio of 0.6 (solid blue), 0.7 (solid green), 0.8 (dashed red).

The monotonic trend of the CDR_a supports that dry hailstone size above the melting layer can be based on the basis of CDR almost exclusively. This is not the case for wet hailstones. The CDR, due to the more complex scattering behavior experiences positive values near resonant, 50 mm sizes.

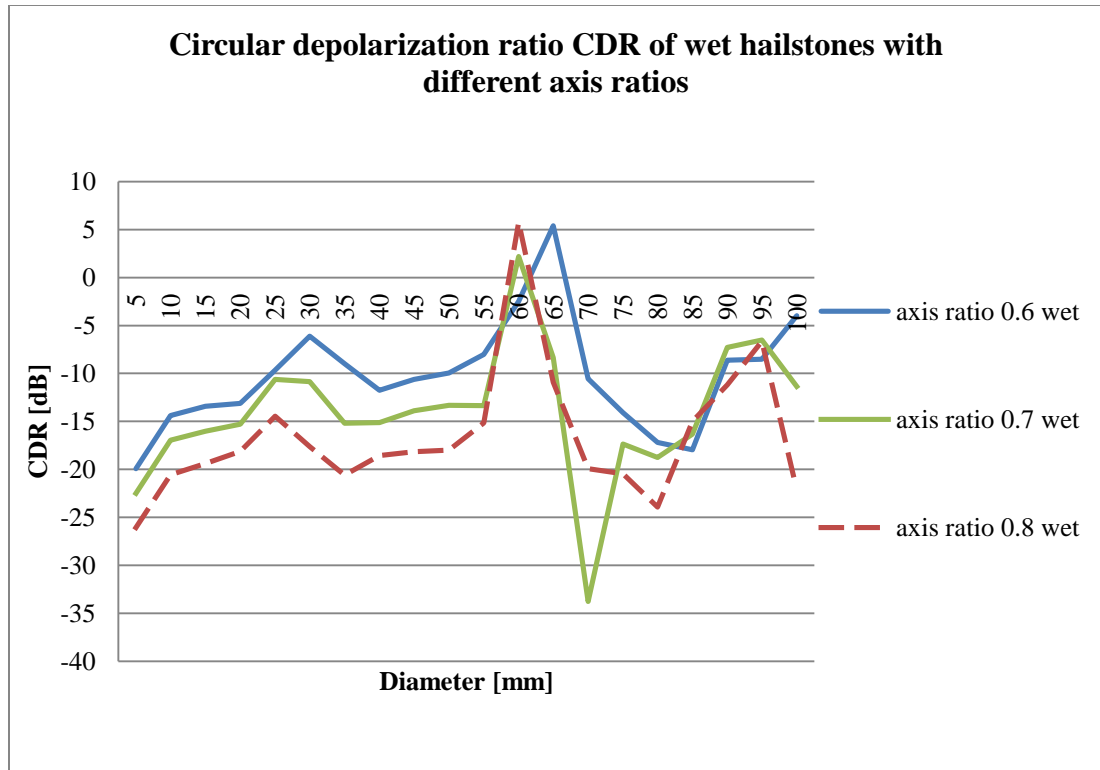


Figure 5.15 - Circular depolarization ratio (CDR) for dry hailstones having the 2% M-type roughness and axis ratio of 0.6 (solid blue), 0.7 (solid green), 0.8 (dashed red).

Positive values of CDR (dB) physically represent stronger return in the EM circular polarization of the opposite orientation of the transmitted one. This occurs when the backscatter differential phase (Fig. 5.8) is outside the -90 and +90 degrees interval.

Non monotonic nature of the wet hailstone CDR provides only qualitative information that can be used to improve hailstone size discrimination using multiple polarimetric variables. This is recognized by Balakrishnan and Zrnić (Balakrishnan & Zrnić, 1990) who identify expected CDR_a values in hail storms to be between -17 and -5 associated with ρ_{HV} values of 0.6 to 0.9. This matches a range of polarimetric variables calculated for monodisperse distributions that are smoothed through size integration.

5.2.4 Polarimetric variables from WSR-88D network

The national polarimetric weather radar network of WSR-88D radars provides polarimetric weather radar observations with 5min updates. The network operates in the simultaneous H, V polarization (SHV) transmission-reception mode and therefore variables obtained are different than ones synthesized by the PVS.

In the SHV mode, power received at each antenna port is defined as (5.14) or (5.15) while the correlation at zero time lag is (5.16):

$$P_h = \sum_{i=1}^N |s_{hh(i)} + s_{hv(i)} e^{j\beta_{TX}}|^2 C_D; \quad (5.14)$$

$$P_v = \sum_{i=1}^N |s_{vv(i)} e^{j\beta_{TX}} + s_{vh(i)}|^2 C_D; \quad (5.15)$$

$$R_{hv} = \sum_{i=1}^N (s_{hh(i)}^* + s_{hv(i)}^* e^{-j\beta_{TX}})(s_{vv(i)} e^{j\beta_{TX}} + s_{vh(i)}) C_D, \quad (5.16)$$

where β_{TX} is the transmission differential phase and C_D is the overall concentration functions of scatterers in one cubic meter. All polarimetric variables are then calculated using (5.17 - 5.20):

$$Z_h^{(SHV)} = \frac{4\lambda^4}{\pi^4 |K_W|^2} P_h; \quad (5.17)$$

$$Z_{DR}^{(SHV)} = 10 \cdot \log_{10} \frac{P_h}{P_v}; \quad (5.18)$$

$$\rho_{HV}^{(SHV)} = \frac{R_{hv}}{\sqrt{P_h} \sqrt{P_v}}; \quad (5.19)$$

$$\delta^{(SHV)} = \arg \rho_{hv}^{(SHV)}. \quad (5.20)$$

The relation between the fully polarimetric and SHV differential reflectivity is presented. The comparison of the Z_{DR} and $Z_{DR}^{(SHV)}$ (Fig. 5.16) is shown for monodisperse distribution of wet hailstones with axis ratio of 0.6 at 2.8 GHz. The $Z_{DR}^{(SHV)}$ values are obtained using the relation (5.21), where lower letter subscripts denote linear units of variables.

$$Z_{dr}^{(SHV)} = Z_{dr} \cdot \frac{1+L_{dr}}{1+Z_{dr}L_{dr}} \quad (5.21)$$

Formulation for the co-polar correlation coefficient in SHV mode can be obtained as well using (5.22).

$$\rho_{HV}^{(SHV)} = \frac{\rho_{HV} + L_{dr}\sqrt{Z_{dr}}}{\sqrt{1+L_{dr}}\sqrt{1+Z_{dr}L_{dr}}} \quad (5.22)$$

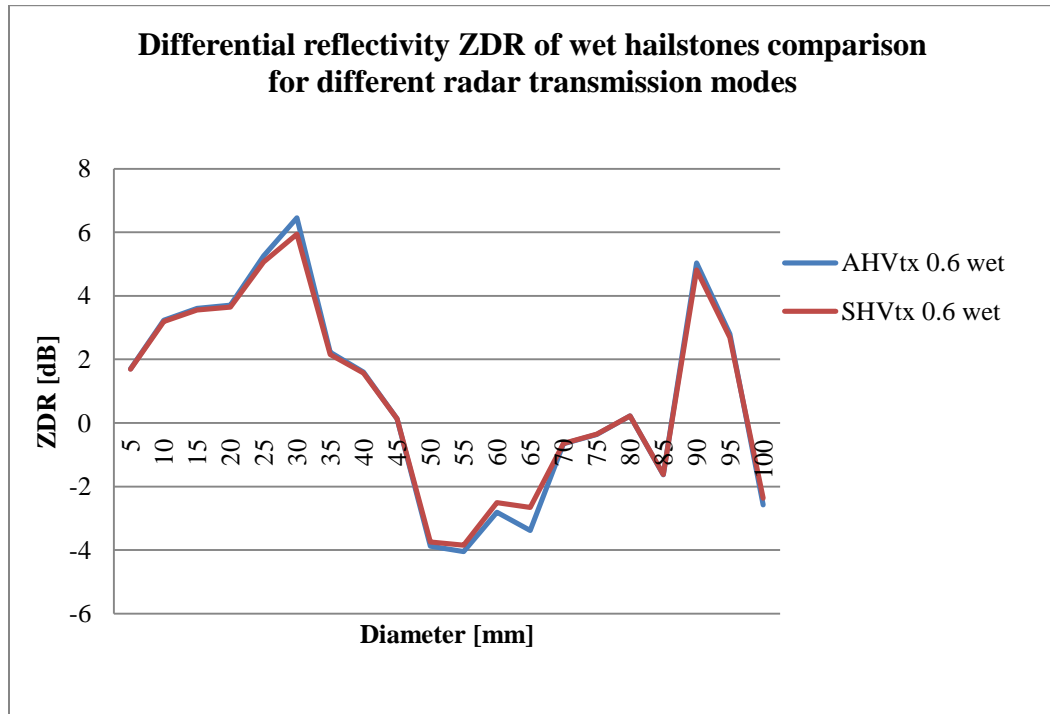


Figure 5.16 - Differential reflectivity (ZDR) for wet hailstones having the 2% M-type roughness and axis ratio of 0.6, for fully polarimetric(AHV) radar (solid blue), and simultaneous transmission (SHV) radar at $\beta_{TX} = 0$ (solid red).

The two differential reflectivities are rather similar and cannot be considered the reason for sparse reports of negative Z_{DR} signatures in hailstorms. The intrinsic Z_{DR} and $Z_{DR}^{(SHV)}$ are also very similar if hailstones are dry (Fig. 5.17). The reason is insignificant cross-coupling. The cross-coupling contribution in (5.14), as well as in (5.15) is the sum of the first and second order term in s_{hv} . For zero mean canting angle the ensemble average of the first order term is zero leaving the only the small $|s_{hv}|^2$ term in (5.20) and (5.21). Note that the simulation assumes mean canting angle is zero.

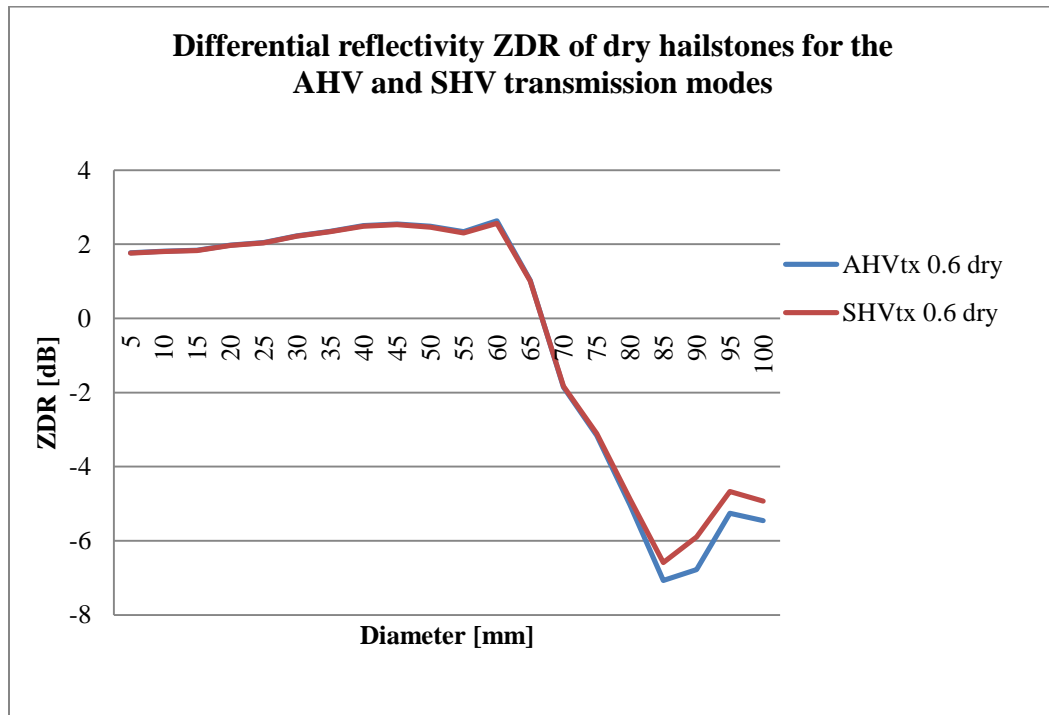


Figure 5.17 - Differential reflectivity (ZDR) for wet hailstones having the 2% M-type roughness and axis ratio of 0.6, for fully polarimetric (AHV) radar (solid blue), and simultaneous transmission (SHV) radar at $\beta_{TX} = 0$ (solid red).

5.3 CONCLUSIONS

The Polarimetric Variable Calculator (PVC) discussed in this chapter is the first application of the CEM scattering approach to calculations of the polarimetric variables. It is free of geometric and composition limitation that might be imposed by real scatterers.

In the literature, irregular shape hydrometeors (hailstones) are assumed to cause many specific polarimetric signatures in the observational data. However, prior simulators didn't address these complex shape objects. For the first time herein, the polarimetric variables are calculated for ensembles of rough surface hailstones. The results are compared to the observational data from a couple of storms probed with fully polarimetric research radars. The negative Z_{DR} , and values of L_{DR} , observed in the radar data are well replicated by the wet hailstones of resonant ~ 50 mm size, providing consistency between the two variables. The simulated, negative differential reflectivity is slightly wider in size range, and more negative than those obtained with other simulators. For either simulation results integration over the size distribution would not change the basic conclusion. If anything the magnitude of negative values would be smaller and would better agree with observations. Thus regions of negative Z_{DR} of < -1.5 dB coupled with $Z > 60$ dBZ just above the melting layer might imply giant hail in wet growth. Below the melting layer such combination could mean melting of giant hail.

The comparison between simulated polarimetric variables and research observations proves the capability of PVS to capture the essential bulk polarimetric properties of

precipitation and possibly the responsible microphysical processes. For example on the basis of simulated differential reflectivity and linear depolarization ratio the results synthesized were sufficient for identification of the hailstone wet growth pocket above the melting layer.

Furthermore, comparison of the differential reflectivity synthesized for fully polarimetric radar and for SHV radar demonstrates the differences between these systems. At zero mean canting angle, these differences are imperceptible for monodisperse size distributions, and would be even smaller for broader size distributions. Comparisons like this one are necessary to reconcile observations by fully polarimetric radars and the SHV radars.

The co-polar correlation coefficient results corroborate the need for complex shape hydrometeor modeling. The calculated decrease of the ρ_{HV} to 0.4, for monodisperse distributions, are in agreement with the observations of giant hail in hailstorms. Such low values of co-polar correlation coefficient could not be predicted with standard spheroidal models that do not support rough hail (i.e., T-Matrix). The observed decreases, are well correlated with the large variations of differential phase confirming the strong effect of the δ on ρ_{HV} .

Finally, the CDR_a results support suggestions by Ryzhkov et al. (Ryzhkov, et al., 2014) that the CDR or its proxy could be used for the discrimination of dry hail sizes above the melting layer. This needs further scrutiny and verification in the observations. However, the simulation provides a solid start in creation of algorithms for automatic hail size detection based on measured polarimetric variables.

The complete overview of the synthesized polarimetric variables for every type, axis ratio and morphology is presented in the Appendix B.

6. BIOLOGICAL SCATTERERS

Observations of airborne animals with radar date back to its early use in tracking aircraft (Lack & Varley, 1945). Today, radar has become one of the many tools used by researchers to study the behavior of flying animals in the airspace, resulting in many significant biological and ecological advances (Gauthrea & Able, 1970); (Holland, et al., 2006); (Chapman & al., 2010); (Bruderer, 1997); (Horn & Kunz, 2008); (Chapman & Reynolds, 2011); (Chilson & et al., 2011). There is a growing disparity, between the pace of emerging technological advances in radar systems and our capacity to quantitatively interpret the resulting radar measurements of wildlife. Our ability to make precise biological observations and inferences from radar data has been largely limited by a lack of understanding of how radio waves interact with volant animals. Studies of radio-wave interactions with animals have been limited to only a few species observed at select wavelengths and for single polarizations (Bruderer, 1969); (Edwards & Horughton, 1959); (Riley, 1985); (Drake, 2014). Consequently, radar biology has often employed the simplifying assumption that airborne organisms have isotropic radar cross-sections (Drake, 2014). The paucity of available biological radar cross-section data can primarily be attributed to the complexity of obtaining such measurements through laboratory and field observations. One imperative for expanding radar aeroecology beyond qualitative analysis and interpretation is development of techniques for quantifying radio wave scattering in ways that can be extended across species and for different radar wavelengths and polarizations.

Analytic equations describing the interactions of electromagnetic radiation with simple physical objects have existed since the early 1900s. However, elegant solutions for objects with even moderately more complex shapes have remained elusive. In the case of radio waves used by radar, the scattering properties of an object are characterized through the radar cross section (RCS), which is a measure of the intensity of the scattered electric field relative to that which was incident on the object (Knott, et al., 1993). Although several numerical approaches have been developed over the years to calculate RCS values for a variety of objects, as presented in Ch.2. none have been developed for animals.

Herein the radio-wave scattering properties of the Brazilian free-tailed bat (*Tadarida brasiliensis*) are examined using both laboratory observations and computer modeling using the WIPL-D software. The Brazilian free-tailed bat is commonly detected by weather radar in the southern United States due to its abundance and the heights at which it flies (Horn & Kunz, 2008) often resulting in a “cloud” of biological echo detected by the radar. The electromagnetic scattering model and measurements of the Brazilian free-tailed bat were made for two orthogonal polarizations: horizontal and vertical, important if used for identification of an object (Cloude & Pottier, 1996).

6.1 MODELING OF THE BRAZILIAN FREE-TAILED BAT (*TADARIDA BRASILIENSIS*) USING WIPL-D SOFTWARE

The Brazilian free-tailed bat was topologically modeled. Its shape is represented as a collection of adjoined dielectric plates and then a set of equations is used to find the

surface currents on each plate created by the incident electromagnetic wave (Ch.2.2.2).

Developing an organismal model it suffices to include only as much detail, i.e., as many plates, as is required to produce realistic scattered fields. But, the necessary level of detail is rarely known *a priori*. For this study, a realistic geometric bat model was used, for which details such as toes, eyeballs, and nostrils were replaced with larger, coarser plates. The final model consists of 4404 interconnected bilateral plates as shown in Fig. 6.1a, representing the body topology.

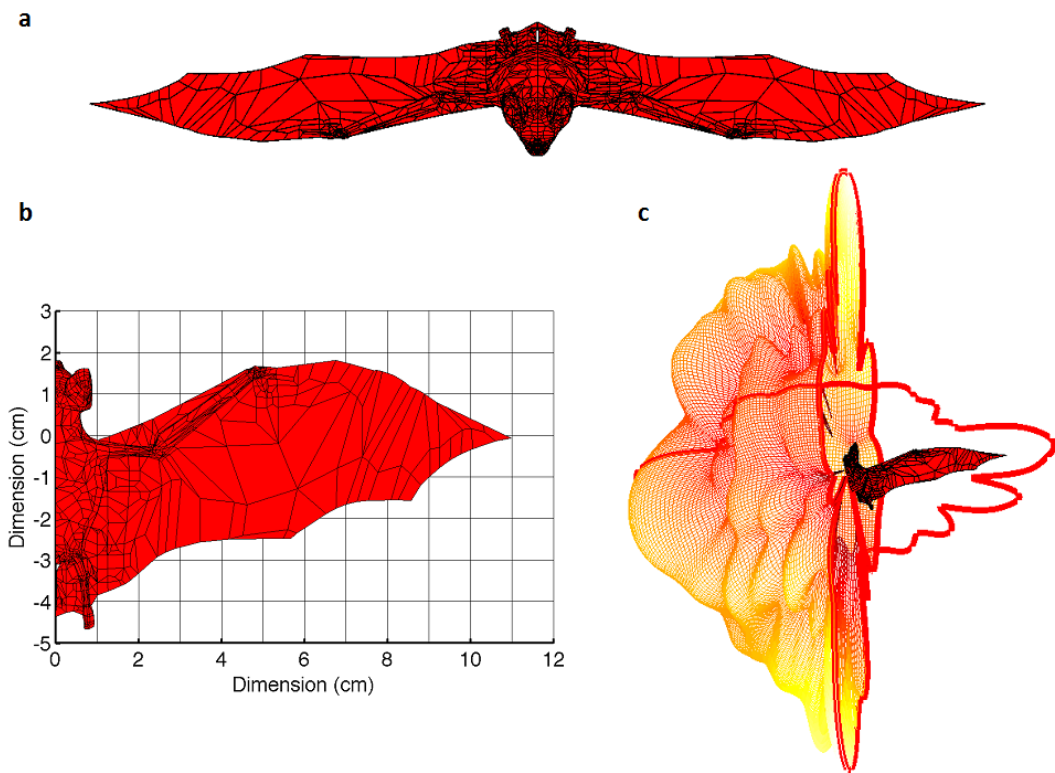


Figure 6.1 – Model of a bat. a) 3-D view of the topographical surface patch model of the Brazilian free-tailed bat at radar wavelength of 3 cm. b) Detailed view of the model from above including dimensions. c) The full solid-angle vertical-polarization RCS pattern of the bat as a function of incident angle. Values corresponding to two planar cross-sections through the bat have been highlighted for the sake of reference.

With the geometric structure of the bat defined, the next step is specification of the dielectric properties of the building elements. To facilitate comparisons between the model results and laboratory measurements, discussed in the following section, the dielectric permittivity values were set to those emulating our specimen bat. This modeled specimen was a Brazilian free-tailed bat carcass that had been collected (IACUC R09-29), frozen for temporary storage, and thawed prior to measurements. Our model was developed to match RCS signature of the dead animal, which is expected to be slightly different than the live animal RCS (Drake & Reynolds, 2012). For example, the water content of the dead animal is reduced, especially in the thin membranes of the wings and tail. One way to account for this difference was by varying the dielectric permittivity of plates in different regions of the bat. However, to avoid adding complexity an effective dielectric permittivity that represents a body-averaged value was used. As appropriate dielectric permittivity the average of wet and dry skin values (Andreuccetti, et al., 1997) is used $\epsilon_r = 29.29 - j12.89$ (Gabriel & Gabriel, 1996). Incidentally, the average of these skin values is approximately equal to the average of all other available tissue permittivity values.

The 4404 building elements making up the topological bat model require 25834 unknown coefficients to define the surface current solution. Further reduction of the computational complexity was achieved with the option of body symmetry that cut the number of unknowns by half. The symmetry option deduces the full-body current distribution as the vector sum of the original and “symmetric” induced currents.

6.2 LABORATORY MEASUREMENTS OF THE BRAZILIAN FREE-TAILED BAT RCS WITH POLARIMETRIC CALIBRATION

To assess the validity of the RCS results obtained through the WIPL-D method of moments, direct measurements of the dead Brazilian free-tailed bat specimen discussed above were made. Two major challenges complicated the RCS measurements of the carcass. First, the size and dielectric composition of the bat yield relatively weak echo signals that are easily overcome by surrounding clutter or environmental interference. Second, the body of the bat is quite frail and flaccid, making exact and consistent positioning difficult. Coupled with the low RCS, many typical methods for supporting the body (e.g., foam pedestals and supports) were simply too obstructive for this application. The following describes the hardware implementation for these measurements, and discusses our methods for overcoming the technical challenges.

Since the 1980's, network analyzers have provided the means to measure electromagnetic antenna patterns - a process technically similar to RCS measurement (Agilent Technologies, 2004). Over time, the capabilities of these devices have increased as their sizes decreased, resulting in a convenient tool for onsite RCS measurements. The network analyzer used in this analysis was the Agilent E8364B, a general-purpose network analyzer equipped with four receivers that may be decoupled from the instrument main ports via the front panel bridges. To implement direct polarimetric measurement, we decoupled the instrument ports as proposed in (Agilent Technologies, 2004) and used them to sample the desired polarization return

from the scatterer. The instrumentation setup, presented in Fig. 6.2b, shows the direct connection of the source ports to the transmitting port of the quad-ridged dual-pol antennas. Similarly, the receive line connects the antenna receiver to the network analyzer ports on the front panel. In this configuration, the received signal will be stored as the S-parameter matrix.

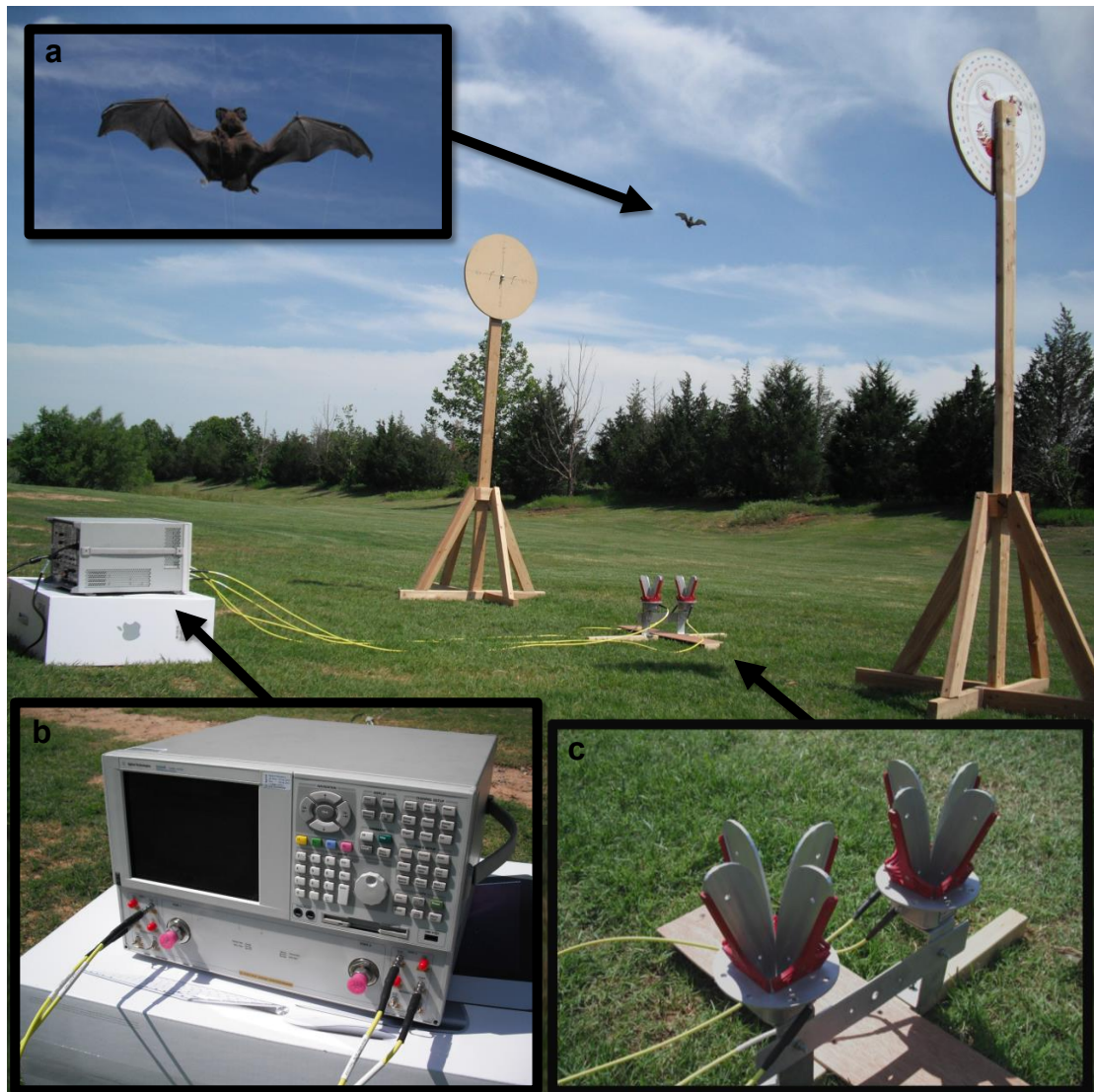


Figure 6.2 - Laboratory equipment setup for field measurements. a) Suspended Brazilian free-tailed bat. b) Network analyzer with dual transmit and dual receive channels. c) Quad-ridged dual-polarization antennas.

To ensure reliable measurements, transmit and receive antennas require precise control of the cross-polarization coupling and phase center position. The antennas used are dual-polarized, ETS Lindgren quad-ridged horns (model 3164-05). Confirmed by the laboratory measurements, these antennas provide over 24 dB of isolation between orthogonal polarizations and more than 25 dB of back-lobe suppression (Lindgren, 2010).

Obtaining a precise and reproducible body positions when measuring such a small, limp, and fragile subject is a challenging task. It is important that the apparatus suspending the bat does not interact with the measurement, either as obtrusive clutter or a source of electromagnetic coupling. Many previous measurement efforts have used polyfoam supports or enclosures, citing their negligible electromagnetic contributions (Blacksmith & Mack, 1965). While such a rig may be suitable for larger (in the RCS sense) objects, our experience has shown that the weak scattering characteristics of bats are often of the same magnitude as otherwise negligible clutter.

To eliminate clutter sources, it was opted to perform outdoor under the sky measurements in the zenith direction and constructed a planar positioning apparatus that minimized interference (Fig. 6.2). The planar positioner consists of two identical wooden structures four meters apart, with each structure made of a rotating disk atop a 2.3 m stationary post. A 360 degree protractor is fastened to each disk, providing rotations in 1-degree increments. Four 0.25 mm diameter low-permittivity monofilament lines span between the two counter facing disks, piercing the bat in several places and suspending it in the middle of the rig. Upon applying slight tension

to all lines, the bat was suspended in a rigid, flight-like body position above the antennas (Fig. 6.2).

The RCS is defined in terms of plane wave with defined phase characteristics illuminating the object of interest. Therefore, it was necessary to place the bat within the far field of the antenna, both in terms of diameter and the antenna spacing. Moreover, it was desirable to have the bat within the alias-free or unambiguous range. The settings selected in the case of our measurements placed the limit of the alias-free range at 267 m.

Post processing of the observations allows removal of unwanted artifacts in the data and thereby improvement of RCS estimation. For example, the total returned signal in measurement is a superposition of reflections from the scatterer under investigation (the bat in this case) and reflections from other objects creating stationary background signals. These signals can be measured in the absence of the scatterer under investigation. In this way the noise floor can be set to the averaged value of the time dependent signals from the background (here, -103 dBm). Moreover, to mitigate statistical errors in amplitude measurements and reduce noise ten consecutive samples of the received power were averaged in time. The temporal averaging was implemented to characterize both the background and the scattering properties of the bat. Signal post-processing using time gating was implemented to further improve the quality of the RCS measurements by better suppressing second trip reflections, especially those from the ground.

Various techniques for RCS measurement calibrations exist and rely on comparisons with cross section of objects that are either known or easily computed. Such objects are spheres, cylinders or plates composed of conducting material. Here, a conductive sphere with a diameter of 15.82 mm was used. The size of the sphere was chosen to be comparable with that of the bat to mitigate potential miscalibration for the case of low RCS due to the instrument's dynamic range nonlinearity. The true (calibration) RCS for a sphere was calculated using the WIPL-D. By performing the calculation of the calibration standard using the WIPL-D software the possibility of inherited errors in approximate methods (Ch.2.1) was removed, which could otherwise affect the quality of calibration.

Calibration of the RCS amplitude was by the substitution technique (Knott, et al., 1993). That is, the calibration standard (sphere) was substituted for the object (bat) and measurements were made at each polarization. The same suspension system, used to position the bat above the antennas during the RCS measurements, was used for the calibration sphere which was placed at the center-of-mass position of the bat. Measured values of the co-polar and cross-polar scattering elements $|s_{XY}|_{meas}^2$ collected at 10 GHz for the 15.82 mm diameter sphere are given in Data Table 6.1. The subscripts X and Y denote the polarization of the incident and scattered wave, respectively. The calculated (expected) co-polar values for the calibration sphere are $|s_{XX}|_{cal}^2 = -52.13$ dBsm, decibel value of the RCS relative to a reference value of 1 m^2 . Measured values of s_{XY} for the calibration sphere are not expected to be exactly the same for the different channels (polarizations) because of imbalances between channels. Moreover, because the sphere does not backscatter cross-polarized field, the

calibration technique is used to check the cross-polar isolation. This isolation is simply the ratio between the measured co-polar and cross-polar powers.

Table 6.1 - Measured values of the co-polar and cross-polar scattering coefficients $|s_{XY}|_{meas}^2$ for the calibration sphere

	H_{inc}	V_{inc}
H_{scat}	-80.42 dB	-104.73 dB
V_{scat}	-102.09 dB	-80.94 dB

Using the data in table scattering elements are calculated as:

$$|s_{XY}|_{est}^2 = |s_{XY}|_{meas}^2 + |s_{XY}|_{corr}^2, \quad (6.1)$$

where $|s_{XY}|_{corr}^2$ denotes the offset determined through the calibration procedure. For the co-polar terms $|s_{hh}|_{corr}^2 = 28.29$ dB and $|s_{vv}|_{corr}^2 = 28.81$ dB. Calibration was not able to provide offset values of the cross-polar terms; however, it was found that $|s_{hv}|_{off}^2 = |s_{vh}|_{off}^2 = 35$ dB gave good agreement between the measured and modeled values of $|s_{hv}|^2$ and $|s_{vh}|^2$. Thus, calculated is the RCS in units of dBsm from the estimated scattering coefficients as:

$$\sigma_{XY} = 10 \cdot \log 4\pi + |s_{XY}|_{est}^2. \quad (6.2)$$

6.3 COMPARISON OF THE MODELED AND MEASURED RESULTS (EVALUATION OF THE MODELING APPROACH)

Scattering matrix elements relate physical characteristics of a body to the magnitude and phase of scattered radiation. Consequently the body's symmetries are expected to map into symmetric properties of the RCS. Moreover, knowing that reciprocity of

radio-wave scatter is a preserved property for linear media, cross-polarization scattering elements are expected to be identical, i.e., $s_{hv} = s_{vh}$. Such symmetries can be used in interpreting observed and modeled RCS data and any discrepancies, which may relate to measurement error or unwanted received signals. The correlation of cross-polar scattering elements is an especially sensitive parameter and thus provides a reliable criterion to assess measurement integrity.

An initial comparison of the measured and modeled RCS values, σ_{VV} , of the bat is presented in Fig. 6.3c.

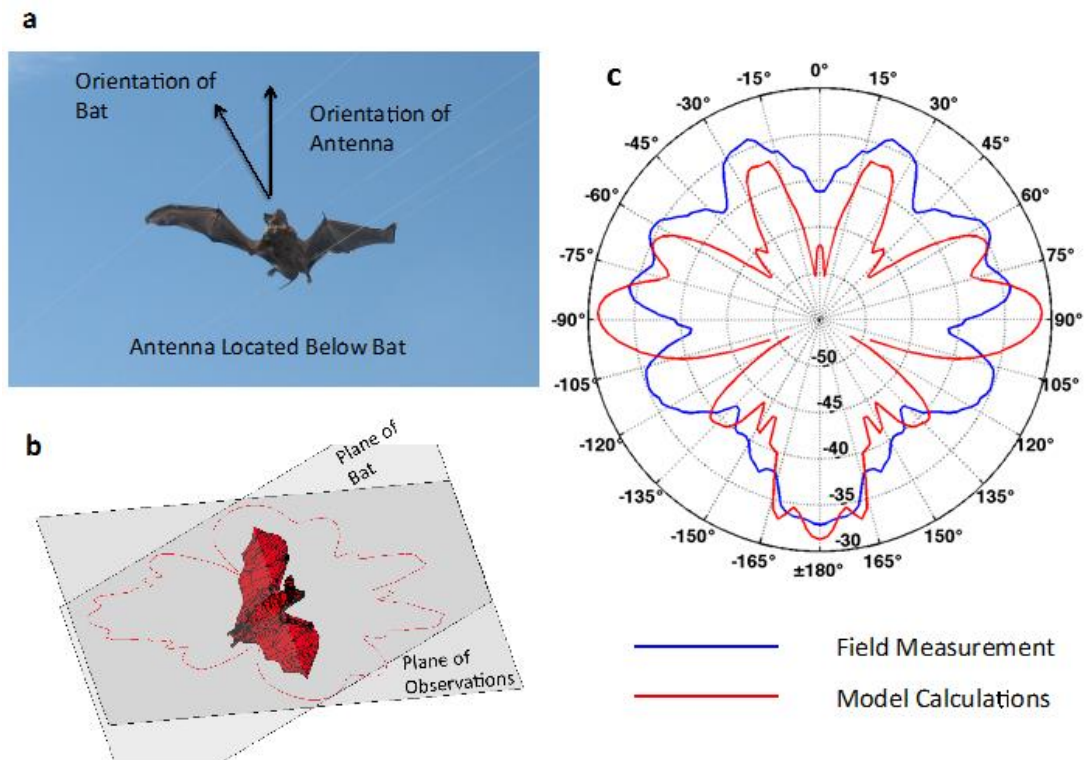


Figure 6.3 - Comparison of observed and modeled RCS σ_{VV} values of the bat a) Illustration of the orientation of the bat carcass used for the observations with respect to the antenna position and orientation. b) The bat model is oriented to match orientation of the carcass. A trace of the modelled RCS within the plane of observation is provided for reference. c) Modelled and measured values of the RCS [dBsm].

In general the RCS data presented in Fig. 6.3c show good agreement in both shape and magnitude. This is evident in the ranges of $+135^\circ$ to -135° and -75° to $+75^\circ$; although, in the later region, the modeled values are on the average 3dB less than those from the measurements. There are notable differences across the remainder of azimuth angles: although lobes in the measured and modeled RCS values are offset in angle, the corresponding magnitudes do exhibit relatively good agreement.

The modeled RCS data presented in Fig. 6.3c corresponds to a single planar cut through the body of the bat Fig. 6.3b. It was not possible to suspend the measured bat (Fig. 6.3a) such that it identically matches the geometry of the modeled bat. The measured bat is at an angular offset of 35° from the zenith as in Fig. 6.3a, resulting in measurements being taken in the slanted plane (plane of observations in in Fig. 6.3b). Consequently, some discrepancies between the modeled and measured RCS data were anticipated. Moreover, some differences in size and dielectric permittivity are expected between the modeled and measured bat. Taking these factors into account, it is submitted that the modeled RCS, especially the number and position of main local maxima, show good agreement with those obtained through measurements.

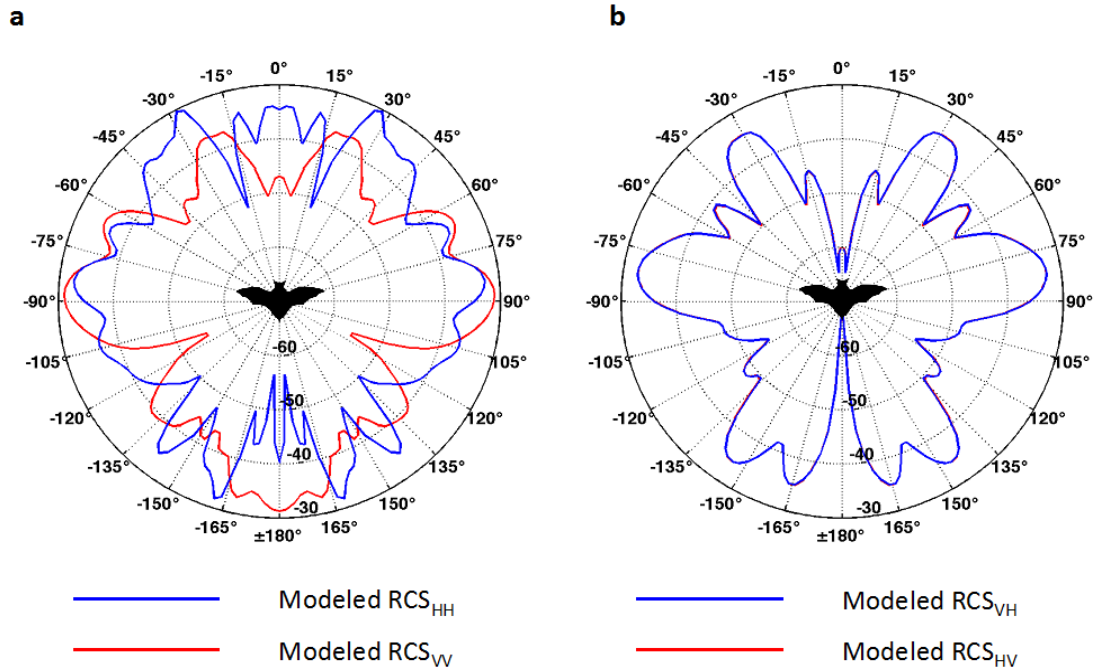


Figure 6.4 - Polar plots of modeled RCS. Co-polar a) and cross-polar b) RCS [dBsm] for cross-section through the simulated dead Brazilian free-tailed bat depicted in Fig. 6.3b.

Modeled and measured RCS of the bat corresponding to co- and cross-polarizations are presented in Figs. 6.4 and 6.5. Since the σ_{VV} is already considered here the focus is on σ_{HH} . The overall magnitudes of the modeled and measured RCS are similar; however, the shapes do not agree as well as in case of σ_{VV} . Understanding this discrepancy requires considering the scattering surfaces that contribute to the overall RCS diagram (Knott, 2006). The electric field vector for the horizontal polarization is incident along the bat's body including the wings. Therefore, it is more susceptible to differences in the body orientation, size, and permittivity than the vertical polarization. As previously mentioned, an effective dielectric constant was used for the entire body of the modeled bat. For the measured case the dielectric constant varies across the body. For example, the wings, which are mainly composed of skin, were relatively dry compared to the rest of the body, resulting in a lower permittivity

and corresponding weaker reflections than predicted by the model. This effect exists in the modeled RCS for vertical polarization as well; however, it is not as noticeable as for the horizontal polarization, again because of the relative contribution of the wings to the modeled scatter for the two polarizations. Although the agreement between the modeled and measured values of σ_{HH} are not as good as for σ_{VV} (partly due to the reasons provided); the results do provide further support to the claim that the main scattering properties of the bat are reproduced by the model within the WIPL-D environment.

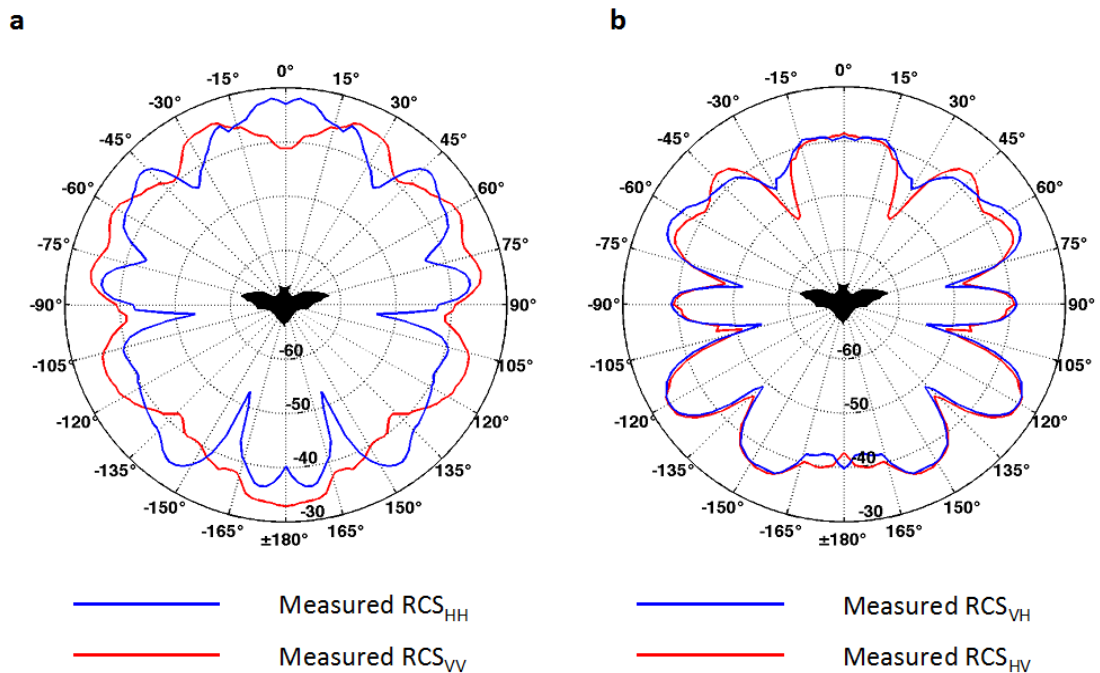


Figure 6.5 - Polar plots showing measured RCS. Co-polar a) and cross-polar b) RCS [dBsm] for the cross-section through the dead Brazilian free-tailed bat depicted in Fig. 6.2a (similar to the cross-section shown in Fig. 6.3b).

Finally the cross-polarization RCS modeled and measured data is considered. Often, cross-polarization terms are not considered or discussed in the published literature; however, for the case of biological scatter these terms can be significant (Melnikov,

et al., 2015). Cross-polarization scatter is caused by currents of perpendicular polarization induced on the body of the bat and therefore is sensitive to the geometric features of the animal. Moreover, comparison of the cross-polar terms provides a good criterion to assess measurement quality; since, s_{hv} and s_{vh} are expected to be equal because of reciprocity conditions.

We show the modeled and measured cross-polarization diagrams of RCS in Figs. 6.4b and 6.5b, respectively. The measured cross-polar RCS for HV and VH agree quite well (Fig. 6.5b) and serve to validate our experimental procedure. As expected, the two cross-polar RCS for the modeled case are identical (Fig. 6.4b). Although the measured cross-polar RCS have not been properly calibrated we see that the number of maxima (lobes) is the same for the modeled (Fig. 6.4b) and measured (Fig. 6.5b) cross-polar terms. The main discrepancies are associated with the head tail regions of the bat.

In summary, some differences between the modeled and measured RCS do exist (and to some extent are expected), but the overall conclusion is that the comparison validates the modeling methodology. Obtaining quality RCS information for animals using experimental techniques is a slow process requiring considerable care and effort. Thus the modeling framework presented here should significantly enhance the ability to collect RCS information for a variety of species at different radar wavelengths and polarizations.

6.4 BIOTA OBSERVATIONS USING POLARIMETRIC WEATHER RADARS

To extend the analysis beyond the controlled conditions of the laboratory, computational scattering model is utilized to interpret actual radar observations of a collective ensemble of Brazilian free-tailed bats in flight. These bats are insectivorous and form large colonies located in caves, under bridges, in buildings, and similar locations. At dusk they typically emerge from their roost in a tight flight pattern and initially ascend to high altitudes to avoid predation by raptors. They then disperse radially as they descend and begin to forage for insects (Horn & Kunz, 2008) (Williams, et al., 1973)(Fig. 6.6a).

The Brazilian free-tailed bats were observed in central Texas, USA using the NOAA X-band polarimetric (NOXP) shown in Fig. 6.7 mobile radar (Schuur, et al., 2014). Table 2 lists the radar specification.

The radar was located about 12 km from Frio Cave, TX, USA. Here, considered is the radar data from a single 360° azimuthal scan at a fixed elevation angle of 3° taken about 15-20 min after the first bats emerged. Results are presented in Figs. 6.6b-6.6d as radar reflectivity [dB η], radial velocity - a measure of the speed of the bats relative to the radar, and differential reflectivity: The bats, corresponding to larger values of reflectivity, can be seen as they emerge from Frio Cave (Fig. 6.6b). A divergent pattern (bats dispersing radially from cave) along with low-level easterly winds can be identified in the radial velocity data (Fig. 6.6c). The pattern seen in the differential reflectivity for the bats appears to be related to the divergent signature in their velocity.

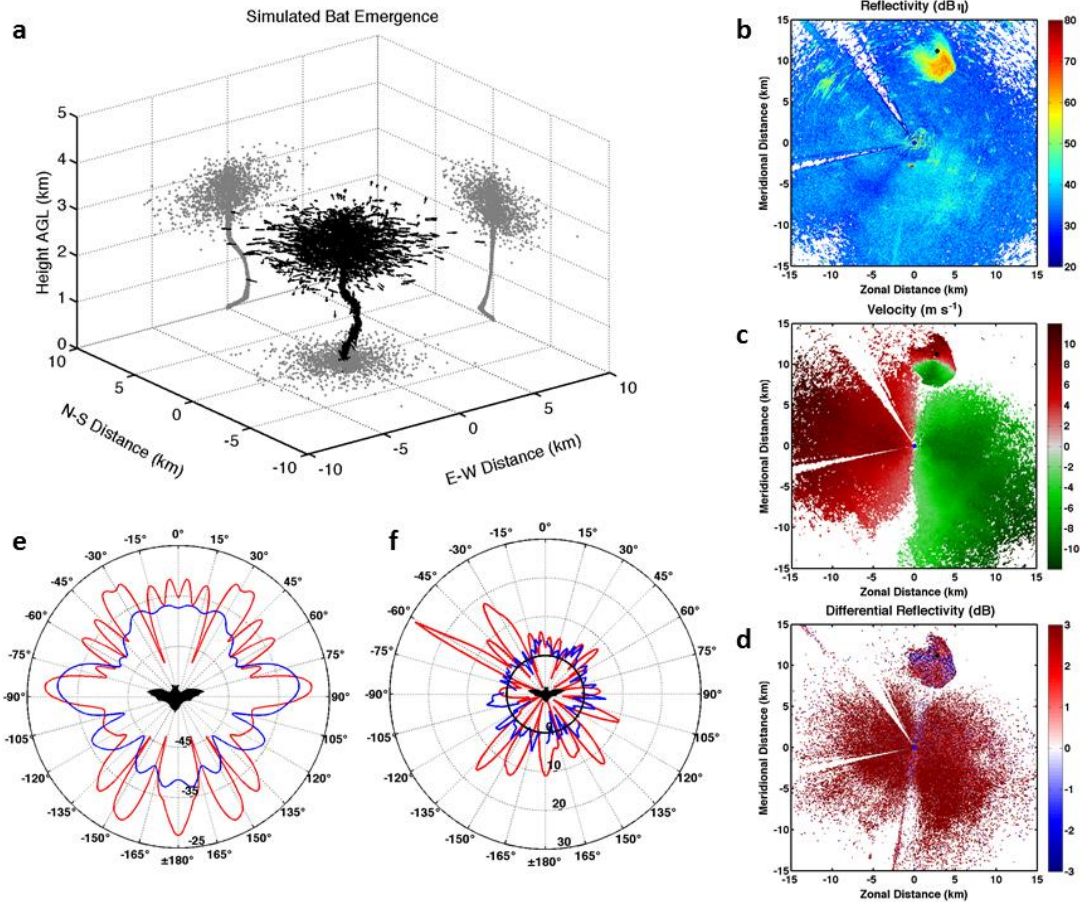


Figure 6.6 - Simulated and observed bat emergence. a) Conceptual representation of an emergence of Brazilian free-tailed bats. b) Values of radar reflectivity [$\text{dB}\eta$, decibel value of reflectivity relative to a reference value of $1 \text{ cm}^2 \text{ km}^{-3}$] obtained during a bat emergence from Frio Cave on 10 July 2010 at 0134 UTC (2034 local time). The cave is denoted by a black dot north-northeast of the radar (origin). c) Values of radial velocity [m s^{-1}] corresponding to the data shown in (b). Red (green) colors indicate motion away from (towards) the radar. d) Values of differential reflectivity [dB] corresponding to the data shown in (b). e) Calculated values of RCS [dBsm] for horizontal (red) and vertical (blue) radar polarizations corresponding to observations made at X-band (3-cm wavelength). f) Calculated values of differential polarimetric RCS [dB] for elevation angle $\theta = -3^\circ$ obtained from the values shown in (b)(red). Z_{DR} values extracted from the measurements (d) over a 2 km range distance (blue). The black circle provides a 0-dB reference.

Table 6.2 - NOXP radar parameters

Radar Parameter	Value
Wavelength	3.2 cm
Transmit power per polarization	50 kW
Antenna beam width (3-dB)	0.90°
Antenna gain	45 dB
Minimum detectable signal	-112 dBm
Minimum detectable Z at 60 km	7.5 dBZ



Figure 6.7 - Picture of NOXP while deployed in Texas to observe Brazilian free-tailed bats²⁵.

²⁵ Courtesy of Dr. Phillip Chilson.

To explore the pattern in differential reflectivity, the bat's RCS at both polarizations is calculated from the model corresponding to the animal's orientation relative to the radar (Fig. 6.6e). It should be stressed that bat's RCS presented in Fig 6.6e and Fig. 6.4 is not the same. These two graphs represent differently oriented models; as mentioned, results in Fig.6.4 are calculated in the observation plane (Fig. 6.3b), while the RCS (Fig. 6.6e) is calculated in the plane of bat (Fig. 6.3b). It is assumed that most of the bats within the radar sampling volume were flying level with the ground. The ratio of the RCS for the two polarizations (differential polarimetric RCS in dB) is shown in Fig. 6.6f (red). Depending on the radar operation mode SHV or AHV DPRCS will exhibit different properties. While for the research radars operating in the AHV mode DPRCS (5.7-5.9) is symmetric, as expected from the body symmetry, the DPRCS for the SHV operation mode is asymmetric. The cross-polar components in (5.14-5.18), which are the same order of magnitude as the co-polar ones in biota, experience the change of phase ($\pm\pi$) in H polarization once it crosses the symmetry plane. Phase change occurs as the H polarization changes the sign which makes it asymmetric in neighboring quadrants (Fig. 6.8a). Therefore the DPRCS in the SHV and AHV mode are compared in the plain of the bat (elevation $\theta = 0^\circ$) in Fig. 6.8b.

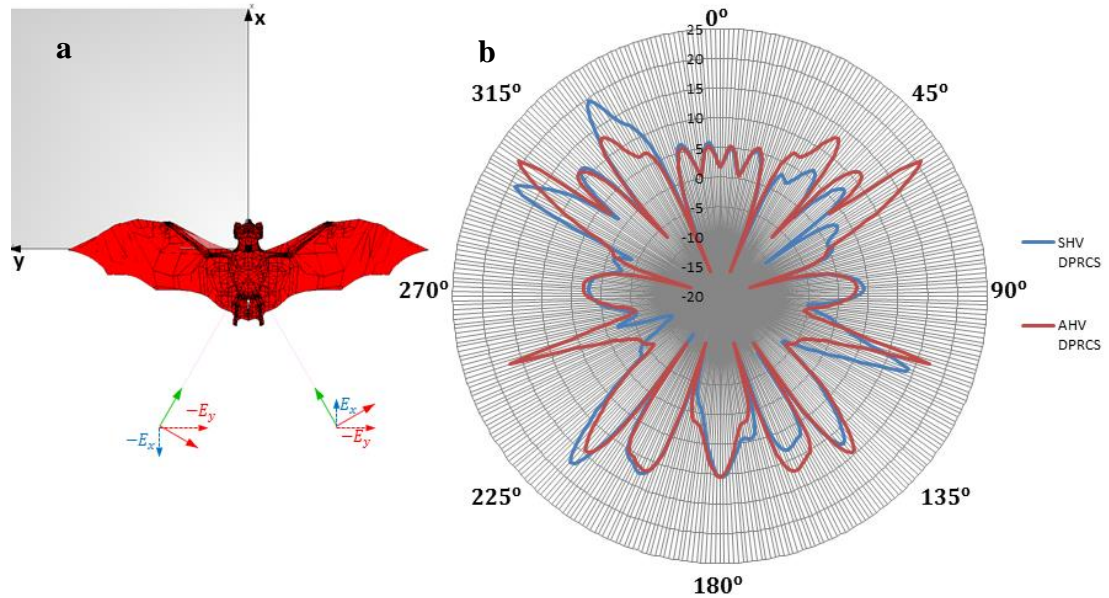


Figure 6.8 – a) Orientation and decomposition of H fields when crossing the model’s symmetry axis; b) comparison of the DPRCS in SHV and AHV radar operation mode for zero elevation.

Based on the azimuthal variation in RCS, we predict this ratio (in dB) to be mostly positive when the bats are flying towards or away from the radar and negative when the bats are observed from the side. This is consistent with the pattern in differential reflectivity that we observe for the bats (Fig. 6.6d), which are dispersing radially from the cave. For the sake of easy comparison, Z_{DR} signature of the bats ensemble is extracted from the Fig. 6.6d and averaged over 2 km range and plotted in Fig.6.6f (blue curve), showing good resemblance. It should be noted that our radar observations represent an ensemble average of the bats. Moreover, the simulated bat (Fig. 6.1) is static whereas the observed animals in flight will have a range of different body positions. Therefore some discrepancies are expected.

6.5 CONCLUSIONS

It is shown for the first time that numerical electromagnetic models, such as those incorporating the method-of-moments technique, can produce robust and realistic full solid-angle radio-wave RCS data of a flying animal (here, the Brazilian free-tailed bat) at orthogonal polarizations. Although tested and validated for a single radar wavelength ($\lambda = 3$ cm) and for one type of animal, the method is general. This is an important consideration because weather radars are increasingly used to monitor the activity of volant organisms over large spatial and temporal scales (Dokter & et al., 2011); (Kelly & et al., 2012). Moreover, many weather radars are being upgraded to include polarimetric operation. In the United States the network of weather surveillance radars (NEXRAD) has already undergone such an upgrade (Doviak, et al., 2000). Validating results of numerical model justifies the substitution of the complex measurement process with numerical modeling for volant animals. Electromagnetic modeling of volant animals could have a dramatic impact on the field of radar aeroecology, for example, in estimating numbers of organisms in the atmosphere and possibly genus based on radar observations.

7. CONCLUSION AND FUTURE WORK

This dissertation presents a systematic evaluation of current modeling procedures focusing on limitation sources and their effects to the overall process of polarimetric variable simulation. It re-evaluates limitations of the widely used T-Matrix approach and discusses sources of instability. Constraints obtained for the T-Matrix align with published values although slightly different limits might be imposed on results from other implementations of the T-Matrix code.

To overcome limitations in scattering tools and approximations used in the polarimetric variable simulators, a novel computational CEM based approach is proposed. For that purpose a CEM solver, herein the robust commercially available WIPL-D, is systematically explored. The goal of the study was to improve modeling of the polarimetric radar signatures and thus explain their meaning. The obtained results are out of reach of the non-CEM methods and prove the robustness and usefulness of the approach.

To use the CEM, a physical model of the hydrometeors must be designed and adapted within the CEM's structure. Doing so is part of the novelty in this dissertation and it involved devising coordinate transformations and manipulations to achieve desired changes in hydrometeor orientation while reducing the computation time.

The CEM approach is verified using accepted modeling tools, such as T-Matrix and Rayleigh approximation. The comparison was conducted for various sizes and shapes of scatterers, including raindrops, spheroidal hailstones, and ice crystals. Verifications proved the superiority of the CEM over the approximate tools, as the scattering

results of CEM remained stable and accurate at all considered sizes, axis ratios, and radar frequencies. This is in contrast to the T-Matrix which revealed intrinsic limitation in dealing with axis ratios larger than about 3 for most types of hydrometeors.

The developed CEM polarimetric variable simulator (CEM-PVS) combines results from scattering computations and theory to obtain ensemble scattering under the Born assumption. The approach makes no approximations to orientations, composition, or topology of scatterers. Therefore it is applicable to modeling of polarimetric signatures of arbitrary scatterers. The orientation distribution and concentration are the required inputs. Of particular interest are the polarimetric signatures of irregular shape hailstones. For the first time, polarimetric variables are calculated for protuberated, resonant size hailstones. Numerical simulations of these ensembles reproduce polarimetric signatures observed in storms. It is shown that the large decrease of the co-polar correlation efficient occurs at resonant size or if the sum of the hailstone size and its protuberance equals the resonant size. Modeling of these irregular shapes is necessary because about 84% of observed hailstones are somewhat spheroidal while the remainder is roughly conical. In either case a CEM approach is the only one suitable for computing scattering parameters from such scatterers.

The substantially negative Z_{DR} and juxtaposed significant L_{DR} values observed in radar data were well replicated using the CEM-PVS. Thus, it is inferred that the observations correspond to giant hail of size 45-65 mm undergoing wet growth. The claim of such narrow distribution is further evaluated by computing the differential reflectivity for wider size distribution and by estimating the relative number densities of hailstones

needed to achieve the observed negative Z_{DR} . It ensued that the number of hailstones in the 45 – 65 mm range has to be at least an order of magnitude larger than the number of smaller hailstones to explain the observation. The comparison between simulated polarimetric variables and research observations proves the capability of PVS to capture the essential bulk polarimetric properties of precipitation and possibly the responsible microphysical processes. Furthermore, comparison of the differential reflectivity expected from a fully polarimetric radar and from an SHV radar demonstrates that in case of hail the differences between the results are not significant. Finally, the co-polar correlation coefficient results corroborate the need for complex shape hydrometeor modeling. The low values cannot be predicted with standard spheroidal models that do not support rough hail, while the observed decreases, are well correlated with the large change of differential phase.

The CEM-PVS has the potential to provide better replicate of the polarimetric variables in precipitation where some hydrometeors are comparable to the radar wavelength. Accurate estimates of these are necessary to improve understanding of the precipitation physics and interpretation of the dominant microphysical processes ongoing in the resolution volume. This new computational method could help assimilation of radar data into numerical weather prediction models; for example giant hail in wet growth might be identified based on the values of the polarimetric variables predicted by the CEM-PVS. Future applications of the CEM-PVS in meteorology hinge on simulation of the realistic hydrometeor distributions so that these resemble the ones observed in storms. Polarimetric variables calculated using CEM-PVS in those cases should reproduce features observed by radar. If not, it could

alert researches that some physical process has not been accounted for in the simulation.

The scatterer based modeling in the CEM-PVS, besides its meteorological application, introduces capability for quantitative studies in the field of Aeroecology. This is spurred by the now ubiquitous presence of polarimetric weather radars. Because the scattering regime of birds or bats at the 10 cm wavelength is resonant the only way to explain polarimetric measurements off these scatterers is via simulations. The CEM tools, WIPL-D particularly, proved its capabilities in modeling of biological scatterers when compared with the polarimetric RCS measurements of the Brazilian Free-tailed bat (*Tadarida brasiliensis*). To make the comparison an experiment was devised. It was a measurement whereby a bat was suspended above two orthogonally polarized EM sources located outdoors and emitting in the zenith direction. A judicious calibration and interference rejection was applied in the measurements. The measured and computed backscatter polar diagrams demonstrated remarkable similarity in locations of the lobes. Thus, not only has the accuracy of the CEM approach to modeling of biota been proven, but the isotropic RCS approximation used in aeroecology studies was shown by the model and in observations to be inadequate to explain the azimuthal change. The dynamic range in azimuth of the RCS is more than 20dB and exhibits a complicated pattern which the model can predict reliably. Therefore, future application of WIPL-D or similar techniques in the field of aeroecology is very likely. Development of numerical scattering models for migratory and other bird species, often reported by agroecologists and ornithologists, is the first step toward development of algorithms

for radar based estimation of the species number and possible determination of the species types. Similar algorithms are needed for estimating the density of large insects and their flight orientation.

To conclude, application of the CEM approach and the PVS to modeling of ensemble scattering provides abundance of research opportunities to study precipitation types, as well as biota or anthropogenic scatterers. Realistic scatterer models are capable of contributing to the aspiration for better and more precise quantitative and qualitative scatterer recognition algorithms using polarimetric radars. Some of the topics that can be addressed in the future are ellipsoidal 3D hail models and sensitivity of the polarimetric variables to the change in the spread of canting angles. Examination of archived polarimetric data from hailstorm should be made to establish how often negative Z_{DR} similar to the modeled ones appear. Are such negative values definite indicators of giant hail? Models of birds that could reproduce the azimuthal dependence of polarimetric variables, specifically Z_{DR} and backscatter differential phase need to be developed keeping in mind that measurements in the SHV and AHV mode produce different results. The bat model assumed the animal has wide open wings which would be the case on some flyers in the flock and only at some specific instances in time. It is very likely that the distribution of wing positions is uniform between open and retreated wings. Modeling this continuum of change is possible but rather time consuming. This could be also done for birds and is definitely a possibility for further studies.

REFERENCES

- Abdelazeez, M. K., 1983. Wave scattering from a large sphere with rough surface. *IEEE Antennas and Propagation*, March, 31(2), pp. 375-379.
- Agilent Technologies, 2004. *New Network Analyzer Methodologies in Antenna/RCS Measurements*. [Online]
Available at: <http://cp.literature.agilent.com/litweb/pdf/5989-1937EN.pdf>
[Accessed 2014].
- Andreuccetti, D., Fossi, R. & Petrucci, C., 1997. *Internet Electromagnetic tissue properties database*. [Online]
Available at: <http://niremf.ifac.cnr.it/tissprop/>
[Accessed 2014].
- Aydin, K., Zhao, Y. & Seliga, T. A., 1990. A differential reflectivity radar hail measurement technique: Observations during the Denver hailstorm 13 June 1984. *Journal of Atmospheric and Oceanic Technology*, Volume 7, pp. 104-113.
- Aydin, K. & Zrnić, D. S., 1992. Modeling polarimetric signatures of precipitation. *ACES Newsletter*, November, 7(3), pp. 22-25.
- Balakrishnan, N. & Zrnić, D. S., 1990. Use of polarization to characterize precipitation and discriminate large hail. *Journal of Atmospheric Sciences*, 1 July, 47(13), pp. 1525-1539.
- Barge, B. L., 1974. Polarization Measurements of precipitation backscatter in alberta. *Journal de Recherches Atmospheriques*, 8(N 1-2), pp. 163-173.
- Bent, A. E., 1946. Radar detection of precipitation. *Journal of Meteorology*, pp. 78-84.
- Best, W. J. H., 1973. Radars over hump - Recollections of the first weather radar network.. *Bull. of the American Meteo. Soc.*, Volume 54, pp. 205-208.
- Blacksmith, P. J. & Mack, R. B., 1965. On measuring the radar cross section of ducks and chickens. *Proc. IEEE*, Volume 53, pp. 1125-1125.
- Bohren, C. F. & Huffman, D. R., 1983. *Absorption and Scattering of Light by Small Particles*. New York, NY: John Wiley and Sons.
- Brandes, E. A., Zhang, G. & Vivekanandan, J., 2002. Experiments in rainfall estimation with a polarimetric radar in a subtropical environment. *Journal of Applied Meteorology*, Volume 41, pp. 674-685.
- Bringi, V. N. & Seliga, T. A., 1977. Scattering from axisymmetric dielectrics or perfect conductors imbedded in an axisymmetric dielectric. *IEEE Trans. Antennas and Propagation*, July, pp. 575-580.

- Browning, K. A., 1966. The lobe structure of giant hailstones. *Quart. Journal of Royal Meteorological Society*, Volume 92, pp. 1-14.
- Bruderer, B., 1969. Zur registrierung und interpretation von echosignaturen an einem 3-cm-Zielverfolgungsradar. *Der Ornithologische Beobachter*, Volume 66, pp. 70-88.
- Bruderer, B., 1997. The study of bird migration by radar Part 2: Major achievements. *Naturwissenschaften*, Volume 84, pp. 45-54.
- Bryukhovetski, A. S. & Pazynin, L. A., 1991. *Scalar wave scattering by a rough sphere: Bourret's approximation for the coherent field of a point source*. s.l., IEEE Proceedings-H, pp. 147-150.
- Chapman, J. W. & Reynolds, V. A., 2011. Recent insights from radar studies of insect flight. *Annual Rev. Entomology*, pp. 337-356.
- Chapman, J. W. & al., e., 2010. Flight orientation behaviors promote optimal trajectories in high-flying insects. *Science*, pp. 682-685.
- Cheng, L. & English, M., 1983. A relationship between hailstone concentration and size. *Journal of the Atmospheric sciences*, Volume 40, pp. 204-214.
- Chilson, P. B. et al., 2011. Estimating animal densities in the aerosphere using weather radar: To Z or not to Z. *Ecosphere*, 3(77).
- Chilson, P. B. & et al., 2011. Partially cloudy with a chance of migration: Weather radars and Aeroecology. *Bulletin of the American Meteorological Society*, Volume 93, pp. 669-686.
- Cloude, S. R. & Pottier, E., 1996. A review of target decomposition theorems in radar polarimetry. *IEEE Trans. Geosci. Remote Sensing*, Volume 34, pp. 498-518.
- Dokter, A. & et al., 2011. Bird migration flight altitudes by a network of operational weather radars. *J R Soc Interface*, Volume 8, pp. 30-42.
- Doviak, R. J. et al., 2000. Considerations for Polarimetric upgrades to operational WSR-88D radars. *Journal of Atmospheric and Oceanic Technology*, Volume 17, pp. 257-278.
- Doviak, R. J., Carter, J., Melnikov, V. & Zrnić, D. S., 2002. *Modification to the research WSR 88D to obtain polarimetric data*, Norman, OK: National Severe Storm Laboratory.
- Doviak, R. J. & Zrnic, D. S., 2006. *Doppler Radar and Weather Observations*. Mineola, NY:
- Doviak, R. & Zrnić, D. S., 1998. *Polarimetric upgrades to improve rainfall measurements*, Norman, OK: National Severe Storm Laboratory NOAA.
- Dragovic, M., 2002. *Antennas and Propagation of radio waves (Antene i prostiranje radio talasa)*. Belgrade: Academic Mind.
- Drake, V. A. & Reynolds, D. R., 2012. *Radar Entomology*. Oxfordshire OX10 8DE: CABI.

- Drake, V. A., 2014. Estimation of unbiased insects densities and density profiles with vertically pointing entomological radars. *Int. Journal Remote Sensing*, pp. 4630-4654.
- Drane, B. T. & Flatau, P. J., 1994. Discrete-dipole approximation for scattering calculations. *Journal of American optics society*, april, 11(4), pp. 1491-1450.
- Eastwood, E., 1967. *Radar Ornithology*. London: Methuen&Co Ltd.
- Edwards, J. & Horughton, E. W., 1959. Radar Echoing area polar diagrams of Birds. *Nature*, p. 1059.
- Gabriel , L. S. & Gabriel , C., 1996. The dielectric properties of biological tissues: III. Parametric models for dielectric spectrum of tissues. *Physics in medicine and biology*, Volume 41, p. 2271.
- Gauthrea, S. A. & Able, K. P., 1970. Wind and direction of nocturnal songbird migration. *Nature*, Volume 228, p. 476.
- Gouesbet, G. & Gréhan, G., 2011. *Generalized Lorenz-Mie Theories*. Verlag Berlin: Springer.
- Harrington, R. F., 1961. *Time-harmonic electromagnetic fields*. New York, NY: McGraw-Hill.
- Harrington, R. F., 1968. *Field Computation by Method of Moments*. New York, NY: Macmilan.
- Higgs, W., Ahijevych, D., Amador, J. & et al., 2006. THE NAME 2004 FIELD CAMPAIGN. *BAMS*, pp. 79-94.
- Holland, R., Wikelski, M. & Wilicove, D., 2006. How and why do insects migrate. *Science*, pp. 794-796.
- Holt, A. R. & Shepherd, J., 1979. Electromagnetic scattering by dielectric spheroids in the forward and backward directions. *J. Phys.A Math. Gen*, Volume 12, pp. 159-166.
- Horn, J. W. & Kunz, T. H., 2008. Analyzing NEXRAD doppler radar images to assess nightly dispersal patterns and population trends in Brazilian free-tailed bat (*Tadarida brasiliensis*). *Integrative and comparative biology*, Volume 48, pp. 24-39.
- Housson, D. & Pointin, Y., 1989. *Quantitative Estimation of the hailfall intensity with a dual polarization radar and hailpad network*. s.l., Radar Meteorology Conference, pp. 10.11-10.15.
- Hülsmeier , C., 1904. Deutschen Reiche, Patent No. 165546.
- Ioannidis, G. A. & Hammers, D. E., 1979. Optimum antenna polarizations for target discrimination in clutter. *Transactions on Antennas and Propagation*, Volume AP-27, pp. 357-363.

- Jokanovic, B., Maricic, A. & Kolundzija, B., 2001. Analysis of parasitic effects in double-Y baluns. *IEE Proceedings Microwave Antennas Propagation*, 148(4), pp. 239-245.
- Kelly, J. & et al., 2012. Quantifying animal phenology in the aerosphere at a continental scale using NEXRAD weather radars. *Echosphere*, Volume 3, p. art 16.
- Khain, A. P., Benmoshe, N. & Pokorovsky, A., 2008. Factors determining the impact of aerosols on surface precipitation from clouds: Attempt of classification. *Journal of Atmospheric Science*, Volume 65, pp. 1721-1748.
- Khain, A. P. et al., 2000. Notes on the state of the art numerical modeling of cloud microphysics. *Atmospheric research*, Volume 55, pp. 159-224.
- Khain, A. P. et al., 2004. Simulation of effects of atmospheric aerosols on deep turbulent convective clouds using a spectral microphysics mixed phase cumulus cloud model. Part I: Model description and possible applications. *Journal of Atmospheric Science*, Volume 61, pp. 2963-2982.
- Khain, A. P. et al., 2011. The role of CCN in precipitation and hail in mid-latitude storm as seen in simulation using spectral (bin) microphysics model in a 2D frame. *Atmospheric Research*, Volume 99, pp. 129-146.
- Knight, C. N., 1986. Hailstone shape factor and its relation to radar interpretation of hail. *Journal of Climate and Applied Meteorology*, Volume 25, pp. 1956-1960.
- Knott, E. F., 2006. *Radar Cross Section Measurements*. Raleigh, NC: SciTech.
- Knott, E., Shaeffer, J. F. & Tuley, M. T., 1993. *Radar Cross Section*. Norwood, MA: Artech House.
- Kolundzija, B. M. & Djordjevic, A. R., 2002. *Electromagnetic Modeling of Composite*. Boston: Artech House.
- Kumjian, M. R., 2012. *Doctoral dissertation: The impact of precipitation physical process on the polarimetric radar variables*. Norman, OK: The University of Oklahoma.
- Kumjian, M. R., 2013. Principles and Applications of Dual-Polarization Part I: Description of the Polarimetric Variables. *Journal of Operational Meteorology*, November, pp. 226-242.
- Lack, D. & Varley, G. C., 1945. Detection of birds by radar. *Nature*, Volume 156, p. 446.
- Lindgren, E., 2010. *Model 3164 Open Boundary Wuaad-Ridged Horns*, s.l.: ETS Lindgren.
- Matrosov, S., 2004. Depolarization estimates from linear H and V measurements with weather radars operating in simultaneous transmission - simultaneous receiving mode. *Journal of Atmospheric and Oceanic Technology*, Volume 21, pp. 574-583.

- Matrosov, S., 2005. Depolarization estimates from linear H and V measurements with weather radars operating in simultaneous transmission - simultaneous receiving mode. *Journal of Atmospheric and Oceanic Technology*, Volume 21, pp. 574-583.
- Matson, R. J. & Huggis, A. W., 1980. The direct measurement of the sizes, shapes, and kinematics of falling hailstones. *Journal of the Atmospheric Science*, Volume may, pp. 1107-1122.
- Maxwell, J. C., 1881. *A treatise on electricity and magnetism*. Oxford: Clarendon Press.
- Melnikov, V. M., Istok, M. J. & Westbrook, J. K., 2015. Asymmetric radar echo patterns from insects. *Journal of Atmospheric and Oceanic Technology*, pp. 659-674.
- Mishchenko, M. I., 2000. Calculation of the amplitude matrix for a nonspherical particle in a fixed orientation. *Applied Optics*, pp. 1026-1031.
- Mishchenko, M. I., Travis, L. D. & Mackowski, D. W., 1996. T-matrix computations of light scattering by nonspherical particles: A review. *J. Quant. Spectrosc. Radiat. Transfer*, pp. 535-575.
- Morgan, G. & Prodi, F., 1969. A laboratory observation of hailstone "lobe" formation following the termination of spongy growth by accretion. *Journal of Applied Meteorology*, October, Volume 8, pp. 840-843.
- Nikolic, M. M., Djordjevic, A. R. & Nehorai, A. R., 2005. Microstrip antennas with suppressed radiation in horizontal directions and reduced coupling. *IEEE Transactions on Antennas and Propagation*, 53(11), p. 3469 – 3476.
- NOAA, 2003. *HISTORIC TORNADO WARNING CONFERENCE LAUNCHED NATION'S*. [Online]
Available at: <http://www.noaanews.noaa.gov/stories/s1163.htm>
- NOAA, 2006. *NOAA Legacy Time Line 1900-1969*. [Online]
Available at: http://www.history.noaa.gov/legacy/time1900_1.html
- NOAA, 2012. *NEXRAD/WSR-88D HISTORY*. [Online]
Available at: <http://www.roc.noaa.gov/WSR88D/PublicDocs/NEXRAD.pdf>
- O'Brien, S. G. & Goedecke, G. H., 1988. Scattering of millimeter waves by snow crystals equivalent homogenous symmetric particles. *Applied Optics*, Volume 27, pp. 2439-2444.
- Park, H., Ryzhkov, A. V., Znić, D. S. & Kim, K.-E., 2009. The Hydrometeor Classification Algorithm for the Polarimetric WSR-88D: *WEATHER AND FORECASTING*, June, 24(June), pp. 730-750.
- Plummer, D. K., Hinton, L. E., Knott, E. F. & Ray, C. J., June 1980. *Nonmetallic chaff study*,
- Rasmussen, R. M. & Heymsfield, A. J., 1987. Melting and shedding of graupel and hail Part I: Model physics. *Journal of Atmospheric Science*, Volume 44, pp. 2754-2763.

- Rasmussen, R. M., Levizzani, V. & Pruppacher, H. R., 1984. A wind tunnel study on the melting behavior of atmospheric ice particles III: Experiment and theory for spherical ice particles of radius $>500\mu\text{m}$. *Journal of Atmospheric Science*, Volume 41, pp. 381-388.
- Ray, P., 1972. Broadband complex refractive indices of ice and water. *Applied Optics*, Volume 11, pp. 1836-1844.
- Riley, J. R., 1985. Radar cross section of insects. *Proc. IEEE*, Volume 73, pp. 228-232.
- Ryzhkov, A., Pinsky, M., Pokrovsky, A. & Khain, A., 2011. Polarimetric Radar Observation Operator for a Cloud Model with Spectral Microphysics. *American Meteorological Society*, Volume 50, pp. 873-894.
- Ryzhkov, A. V., 2001. Interpretation of Polarimetric Radar Covariance Matrix for Meteorological Scatterers: Theoretical Analysis. *J. of Atmospheric and Oceanic Technology*, pp. 315-328.
- Ryzhkov, A. V., 2007. The impact of beam broadening on the quality of radar polarimetric data. *J. Atmospheric Oceanic Technology*, Volume 24, p. 729-744.
- Ryzhkov, A. V., Kumjian, M. R., Ganson, S. M. & Khain, A. P., 2013. Polarimetric Characteristics of melting hail. Part I: theoretical Simulations using spectral microphysical modeling. *Journal of Applied Meteorology and Climatology*, pp. 2849-2871.
- Ryzhkov, A. V. et al., 2014. *Measurements of circular depolarization ratio with the radar with simultaneous transmission/reception*. Garmish Partenkirchen, ERAD.
- Ryzhkov, A. V., Zrnic, D. S., Vivekanandan, J. & Brandes, E. A., 2002. Polarimetric radar observations and interpretation of co-cross-polar correlation coefficients. *J. of American Meteorological Society*, March, Volume 19, pp. 340-354.
- Schiffer, R. & Thielheim, K. O., 1984. Scattering of scalar waves by an impenetrable rough sphere. *Optica Acta*, 31(10), pp. 1085-1100.
- Schuur, T. et al., 2014. Precipitation observation with NSSL's X-band Polarimetric radar during the SNOW-V10 campaign. *Pure Applied Geophys.*, pp. 95-112.
- Shaeffer, J. F., 1993. Exact prediction techniques. In: *Radar Cross Section*. Boston: Artech House.
- Shamoun-Barnes, J. & et al., 2014. Continental-scale radar monitoring of the areal movements of animals. *Movement Ecology*, 9(2).
- Sirmans, D., Zrnić, D. S. & Sachidananda, M., 1984 (rev.1986). *Doppler Radar Dual Polarization Considerations for NEXRAD, NOAA/NSSL Report, Part I*, Norman: National Severe Storm Laboratory (NOAA).

- Straka, J. M., Zrnić, D. S. & Ryzhkov, A. V., 2000. Bulk hydrometeor classification and quantification using polarimetric radar data: Synthesis of relations. *Journal of Applied Meteorology*, Volume 39, pp. 1341-1372.
- Stratton, J. A., 1941. *Electromagnetic theory*. New York, NY: McGraw-Hill.
- Tasic, M. & Kolundzija, B., 2011. Efficient Analysis of Large Scatterers by Physical Optics Driven Method of Moments. *IEEE Antennas and Propagation*, pp. 2905 - 2915 .
- Tesla, N., 1900. The problem of increasing human energy. *The Century Magazine*, June, pp. 175-210.
- The NEXRAD Support Operation Facility, 1996. *NEXRAD System/Segment Specification*, Norman: The NEXRAD Support Operation Facility.
- Van de Hulst, H. C., 1981. *Light Scattering by small particles*. New York: Dover.
- Waterman, P. C., 1971. Symmetry, unitarity, and geometry in electromagnetic scattering. *Physics Rev.*, pp. 825-839.
- Whiton, R. C. et al., 1998. History of operational use of weather radar by U.S. weather services. Part I: The pre-NEXRAD era. *Journal of American Meteorological Society*, pp. 219-243.
- Williams, T. C., Ireland, L. C. & Williams, J. M., 1973. High altitude flights of the free-tailed bat, *Tadarida brasiliensis*, observed with radar. *Journal of Mammalogy*, Volume 54, pp. 807-821.
- WIPL-D, 2015. *WIPL-D*. [Online]
Available at: www.wipl-d.com
- Yee, K. S., 1966. Numerical Solution of Initial Boundary Value Problems Involving Maxwell equations in isotropic media. *Trans. on Antennas and Propagation*, pp. 302-307.
- Ziegler, C. L., Ray, P. S. & Knight, N. C., 1983. Hail Growth in an Oklahoma Multicell Storm. *Journal of the Atmospheric Sciences*, Volume 40, pp. 1768-1792.
- Zrnić, D. S., 1991. Complete polarimetric and Doppler measurements with a signal receiver radar. *Journal of Atmospheric and Oceanic Technology*, February, Volume 8, pp. 159-165.
- Zrnić, D. S. & Aydin, K., 1992. Polarimetric signatures of precipitation. *ACES Newsletter*, July, 7(2), pp. 12-13.
- Zrnić, D. S. et al., 2002. Polarimetric radar observations and interpretation of co-cross polar correlation coefficient. *J. Of Atmospheric and Oceanic Technology*, Volume 19, pp. 340-353.
- Zrnić, D. S. & Ryzhkov, A., 1999. Polarimetry for weather surveillance radars. *Bulletin of the American Meteorological Society*, March, 80(3), pp. 389-406.

APPENDIX A: LIST OF NOTATIONS

E	–	The electric field
B	–	The magnetic field
μ	–	Magnetic permeability of the material
ϵ, ϵ_r	–	Dielectric permittivity, relative dielectric permittivity
J_s	–	Electric surface currents
M_s	–	Magnetic surface currents
n	–	Surface vector pointer outwards
λ	–	Wavelength
D_{eq}	–	Equivolume diameter
$f_{a,b}$	–	Scattering elements at normal incidence for vertical and horizontal polarization
β	–	Wave propagation factor
RP	–	Resonance parameter
S	–	Backscattering matrix
K_w	–	Dielectric factor of water
α	–	Canting angle in the plane of polarization

- ψ – Orientation angle between the hydrometeor's symmetry axis and plane of polarization Fig 2.3.
- AR – Axis ratio, hydrometeor type is given as subscript
- β_{TX} – Transmit differential phase
- $F_{hh,vv}$ – Co-polar antenna radiation pattern
- $F_{hv,vh}$ – Cross-polar antenna radiation pattern
- \mathbf{C} – Backscattering covariance matrix
- C_D – The overall concentration function (function is product of angular weighting and concentration functions)
- AHV – Alternate Horizontal and Vertical transmission
- SHV – Synchronous Horizontal and Vertical transmission

APPENDIX B: POLARIMETRIC VARIABLES CALCULATED USING THE PVS

POLARIMETRIC VARIABLES CALCULATED USING THE PVS

In this Appendix polarimetric variables calculated using the PVS are presented for each polarimetric variable separately. Separate plots are given based on protuberance type, axis ratio and morphology of the hydrometeors for each polarimetric variable.

Radar reflectivity factor

The radar reflectivity factor of the rough solid (“dry”) ice hydrometeors is plotted in Figs. 8.1 and 8.2. The same axis ratio of all hydrometeors is 0.7 and protuberances are 2%, 6%, 10% and 14% of the hydrometeor radius. In Fig. 8.1 only M-type protuberances (Ch.4.1.2) are considered, while in Fig. 8.2 R-type protuberances are presented. It is obvious that for the smaller ice particles the reflectivity factor increases monotonically up to the point of first resonance (i.e., local maximum slightly below 50 mm). Once the resonant scattering regime is in place it becomes obvious that larger hydrometeors may produce lower radar reflectivity factor than slightly smaller ones.

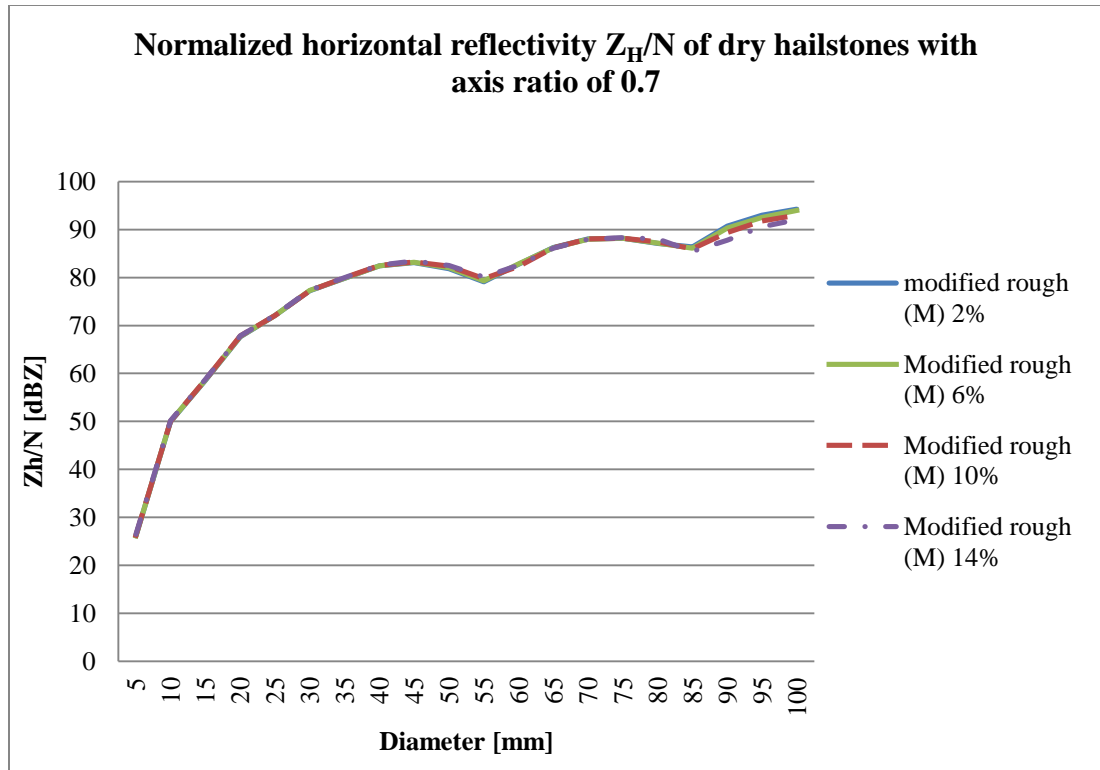


Figure 8.1 – Normalized radar reflectivity factor at horizontal polarization (Z_H) for dry hailstones having the axis ratio of 0.7 and M-type roughness of 2% (solid blue), 6% (solid green), 10% (dashed red) and 14% (dot-dashed violet).

The results presented in Figs. 8.1 and 8.2 are almost identical, thus it is concluded that radar reflectivity factor value is not affected by the protrusion magnitude and distribution on hydrometeor surface.

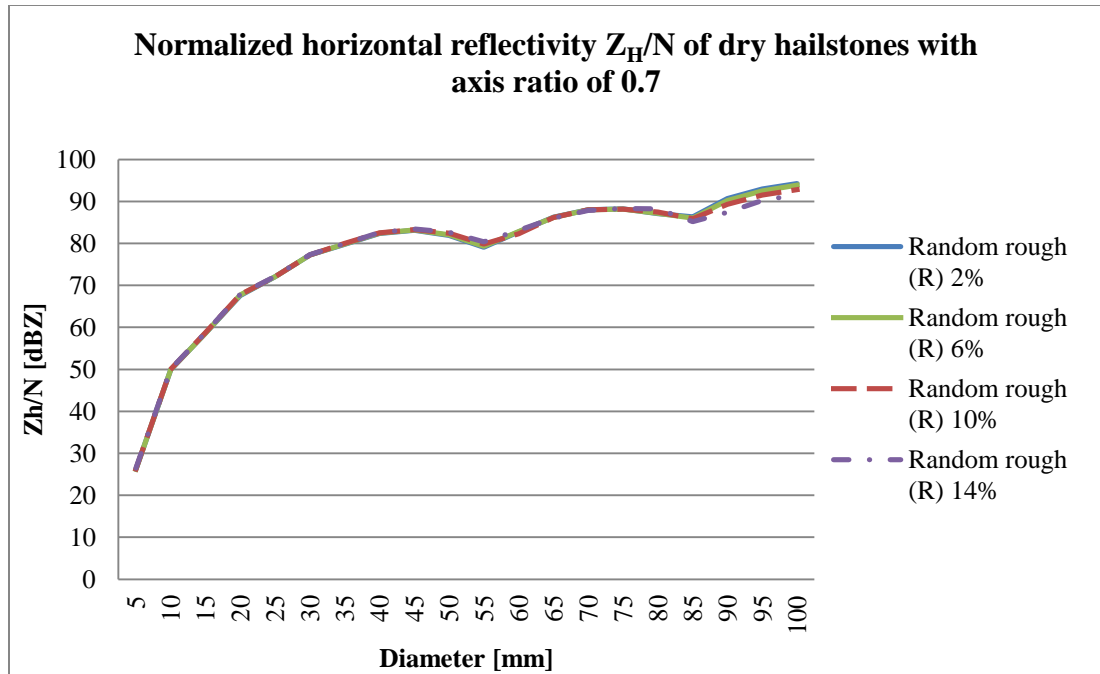


Figure 8.2 - Normalized radar reflectivity factor at horizontal polarization (Z_H) for dry hailstones having the axis ratio of 0.7 and R-type roughness of 2% (solid blue), 6% (solid green), 10% (dashed red) and 14% (dot-dashed violet).

Next the influence of the hydrometeors' axis ratio on the reflectivity factor is examined (Fig. 8.3).

Radar reflectivity factor, for the case of different hydrometeor axis ratios tends to shift the position of the first resonance maximum toward lower sizes. This is expected, and it is due to the hydrometeor's volume, which is not the same for particles having the same physical diameter (major axis) and different axis ratio. Because the physical diameter, major axis, is used instead of the equivolume diameter.

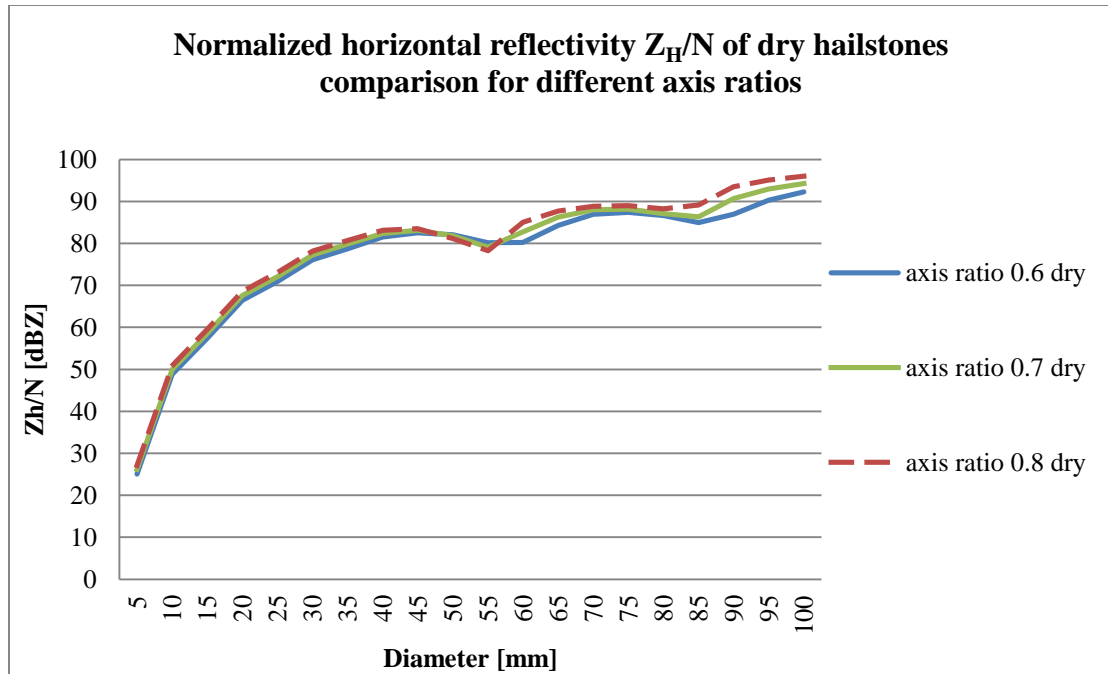


Figure 8.3 - Normalized radar reflectivity factor at horizontal polarization (Z_H) for dry hailstones having the 2% M-type roughness and axis ratio of 0.6 (solid blue), 0.7 (solid green), 0.8 (dashed red).

The curves are in excellent agreement with those presented by (Kumijan, 2012), (Ryzhkov, et al., 2013), in shape and magnitude with those presented in Figs.8.1-8.3.

Due to the partial melting, occurring in the atmosphere or acquisition of water due to different growth mechanisms during the freefall of hailstones, thin water film is created on their surface. Increase in the dielectric permittivity caused by the liquid water coating causes significant increase in the reflectivity factor. Values calculated for the water coated hail of axis ratio 0.8 and different protrusion types are presented in Figs. 8.4 and 8.5. Similar to the dry ice the differences caused by protrusion amplitudes and types are minimal and noticeable only in the first resonance minima at about 55 mm. For larger protrusion value the width of the first resonance minima tends to increase. This is expected because the protrusions cause a spread in the

horizontal dimension. Such behavior of this region sensitive to the actual value of the hydrometeor size is expected as surface protrusions may result in the effects that would result in higher apparent diameter of the hydrometeor when illuminated by the EM wave. On the other hand differences due to the different distribution of the protrusions do not produce any noticeable effect in the radar reflectivity factor.

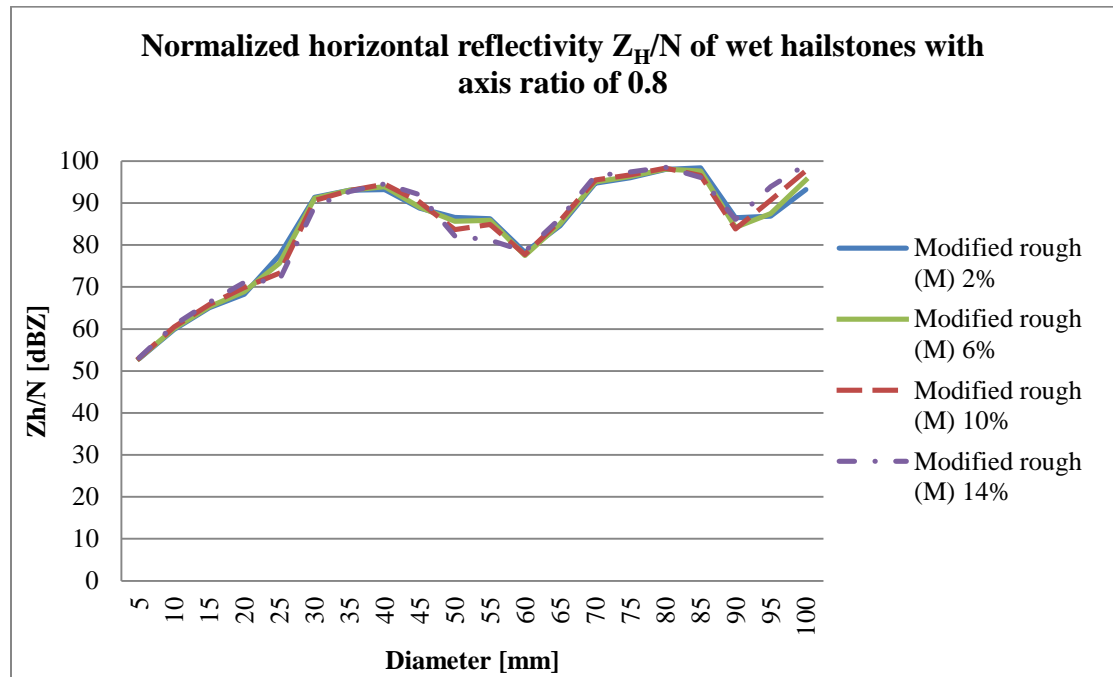


Figure 8.4 - Normalized radar reflectivity factor at horizontal polarization (Z_H) for water coated hailstones having the axis ratio of 0.8 and M-type roughness of 2% (solid blue), 6% (solid green), 10% (dashed red) and 14% (dot-dashed violet).

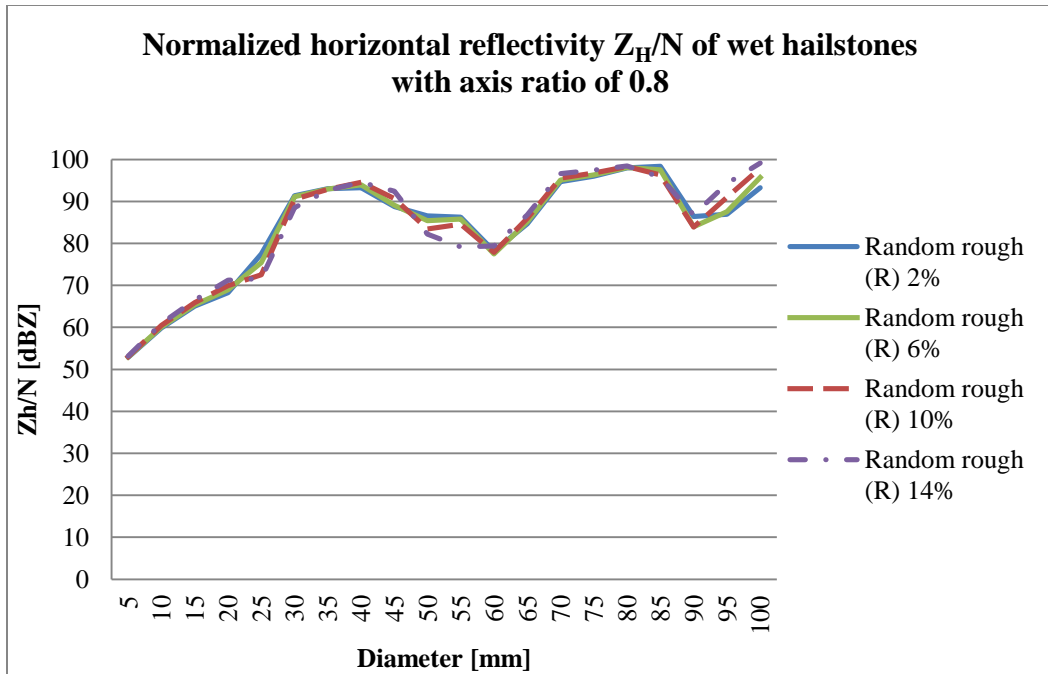


Figure 8.5 - Normalized radar reflectivity factor at horizontal polarization (Z_H) for water coated hailstones having the axis ratio of 0.8 and R-type roughness of 2% (solid blue), 6% (solid green), 10% (dashed red) and 14% (dot-dashed violet).

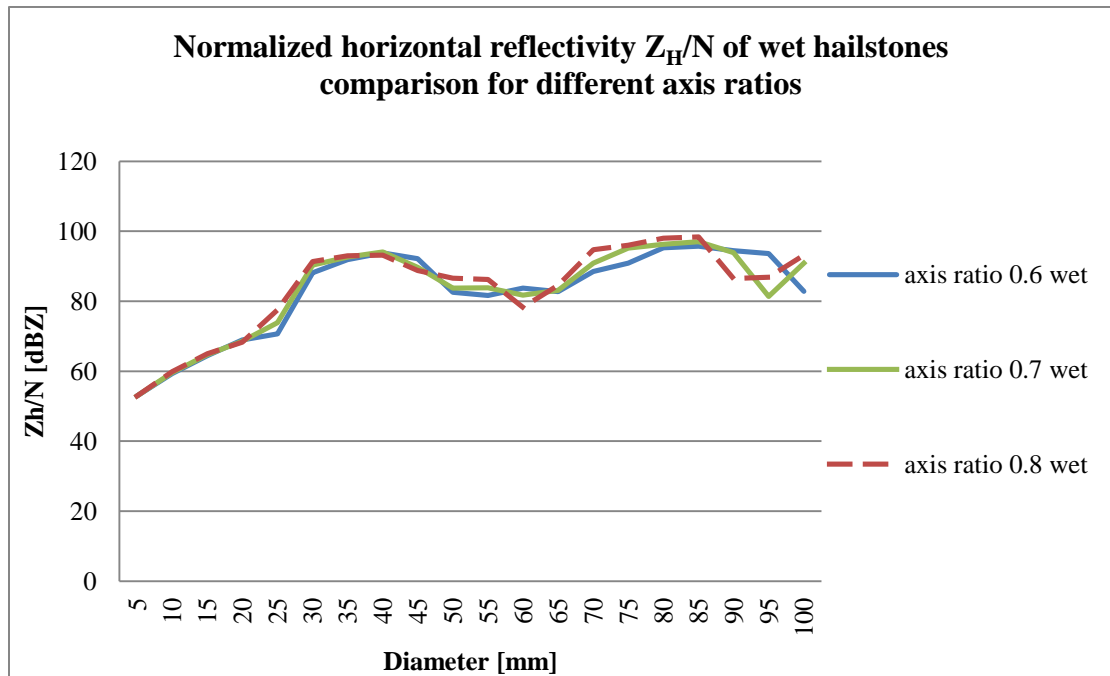


Figure 8.6 - Normalized radar reflectivity factor at horizontal polarization (Z_H) for water coated hailstones having the 2% M-type roughness and axis ratio of 0.6 (solid blue), 0.7 (solid green), 0.8 (dashed red).

From the presented figures, it can be concluded that the most significant effects on the radar reflectivity factor are caused by the change of the dielectric constant, due to the water coating. As well as with increase of the hydrometeor volume due to increase in horizontal dimension. No other significant effects appeared due to the surface protuberances.

Differential reflectivity

In the resonant scattering regime, scattering behavior is more complex making the ratio of two resonant scattering returns even more complex. With the increase of the major axis, hailstone volume increases. For oblate hailstones resonance is first reached in the horizontal polarization as the axis is larger. This is followed by the resonance in the vertical polarization while at the same time H resonant return decreases.

Figures 8.7 and 8.8 present the differential reflectivity for monodisperse distribution of dry hailstones with axis ratio of 0.6 for different protuberance types and values. It is immediately evident that the increase of the protuberance value will be affecting values of maximal and minimal Z_{DR} as well as causing fluctuations at about 15 and 50 mm in Fig. 8.7 and pronounced in Fig. 8.8. These resonances could be attributed to some higher order resonance modes (micro resonances) which could appeared due to the slight difference in size caused by the protrusions. This explanation is the one best resembling the data plotted as such resonances are more pronounced in uniform random rough R- type of protrusions and only for higher protuberances values.

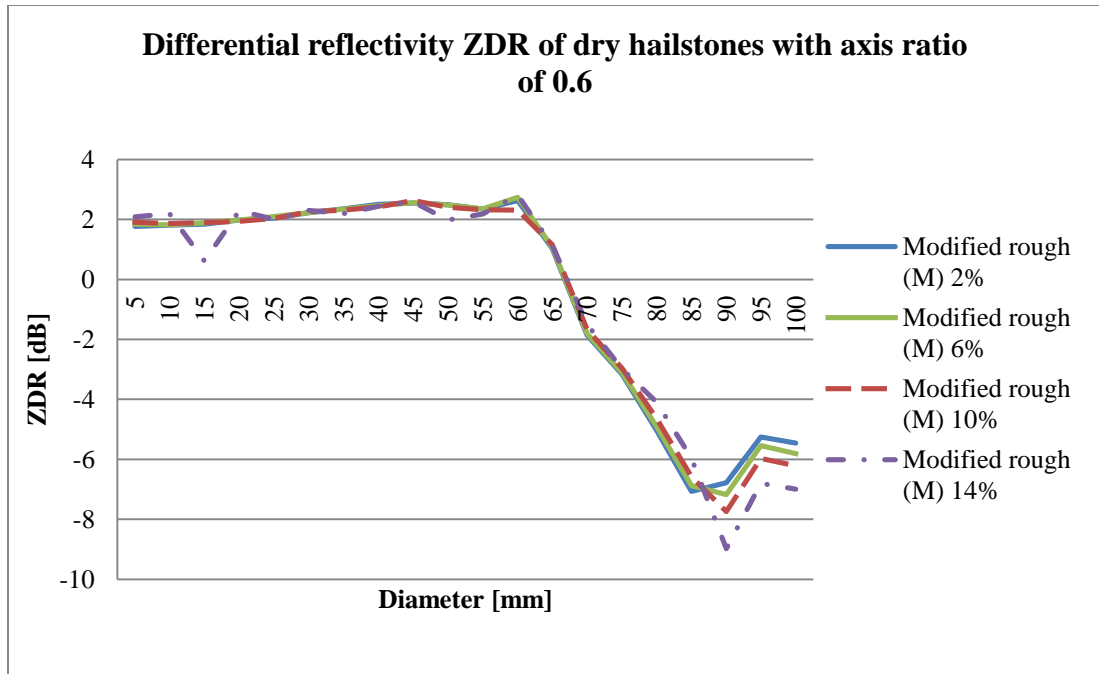


Figure 8.7 - Differential reflectivity (ZDR) for dry hailstones with axis ratio of 0.6 and M-type roughness of 2% (solid blue), 6% (solid green), 10% (dashed red) and 14% (dot-dashed violet).

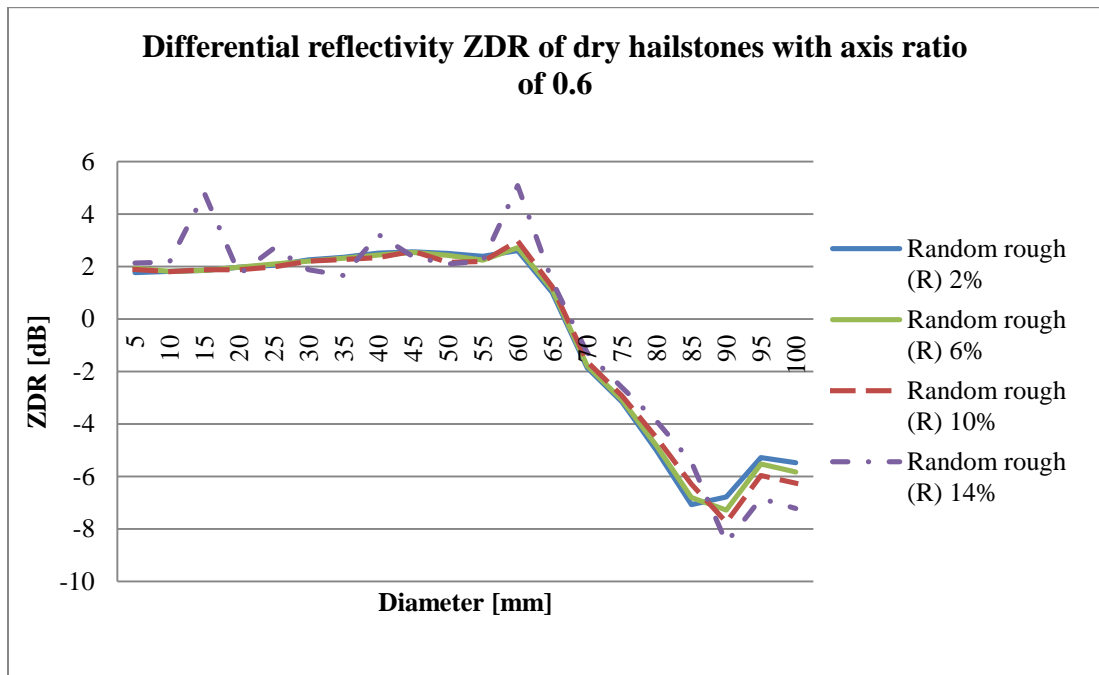


Figure 8.8 - Differential reflectivity (ZDR) for dry hailstones with axis ratio of 0.6 and R-type roughness of 2% (solid blue), 6% (solid green), 10% (dashed red) and 14% (dot-dashed violet).

In the case of dry hailstones having the axis ratio of 0.7 (Figs. 8.9 and 8.10) some of the effects observed in the 0.6 axis ratio hailstones are missing. Again, protrusion value has affected the maximal Z_{DR} values but micro resonance effects are not observed. Effects of protrusions in the cases illustrated in Figs. 8.9 and 8.10 are slight changes of diameters at which Z_{DR} changes sign (due to the shift in resonance extinction, which is different depending on the type of protuberances).

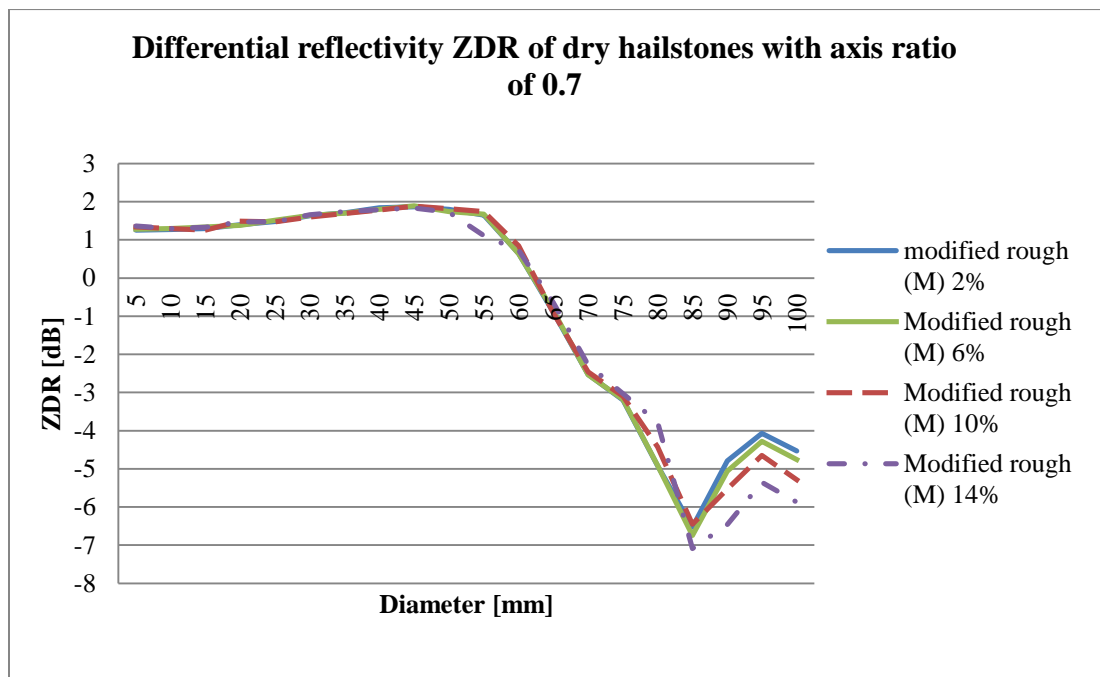


Figure 8.9 - Differential reflectivity (ZDR) for dry hailstones with axis ratio of 0.7 and M-type roughness of 2% (solid blue), 6% (solid green), 10% (dashed red) and 14% (dot-dashed violet).

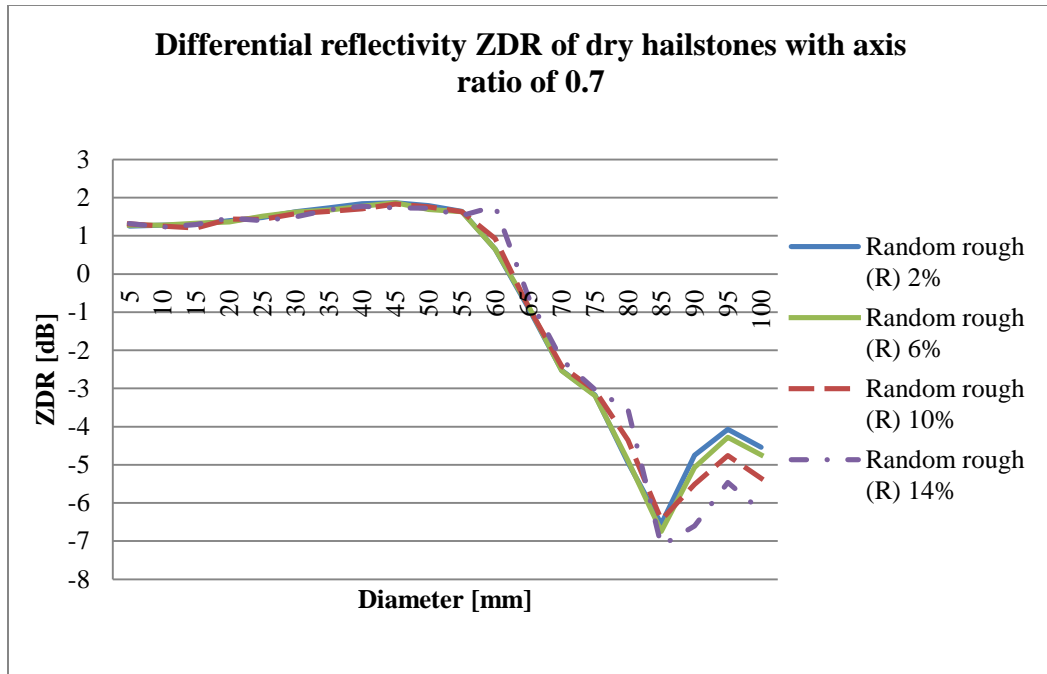


Figure 8.10 - Differential reflectivity (ZDR) for dry hailstones with axis ratio of 0.7 and R-type roughness of 2% (solid blue), 6% (solid green), 10% (dashed red) and 14% (dot-dashed violet).

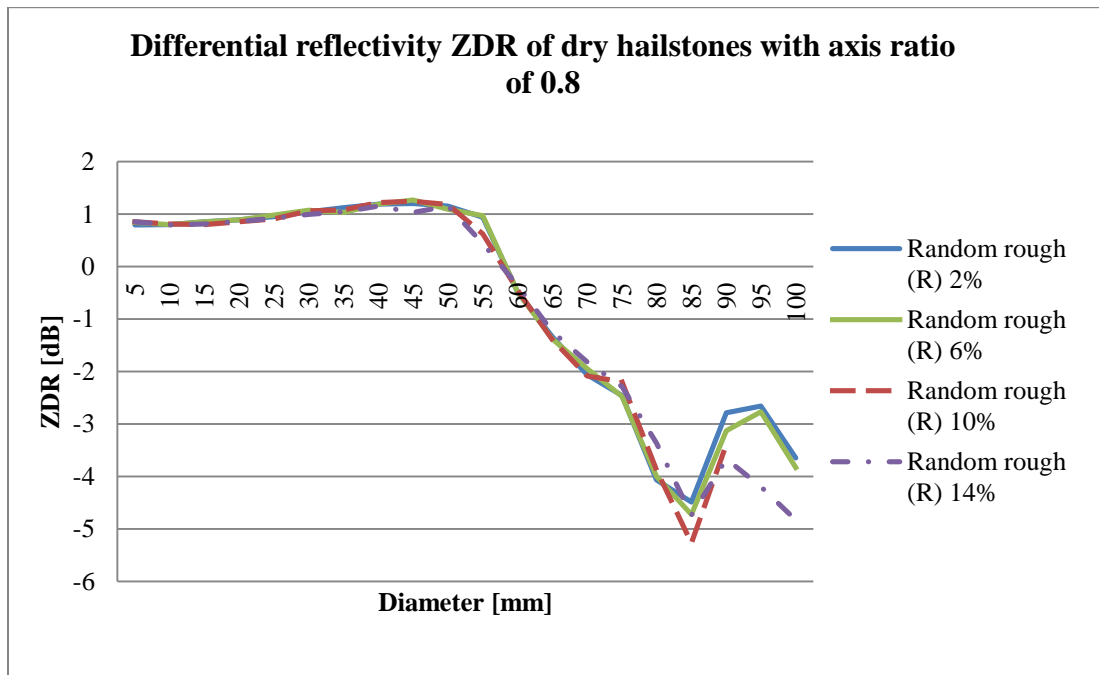


Figure 8.11 - Differential reflectivity (ZDR) for dry hailstones with axis ratio of 0.8 and M-type roughness of 2% (solid blue), 6% (solid green), 10% (dashed red) and 14% (dot-dashed violet).

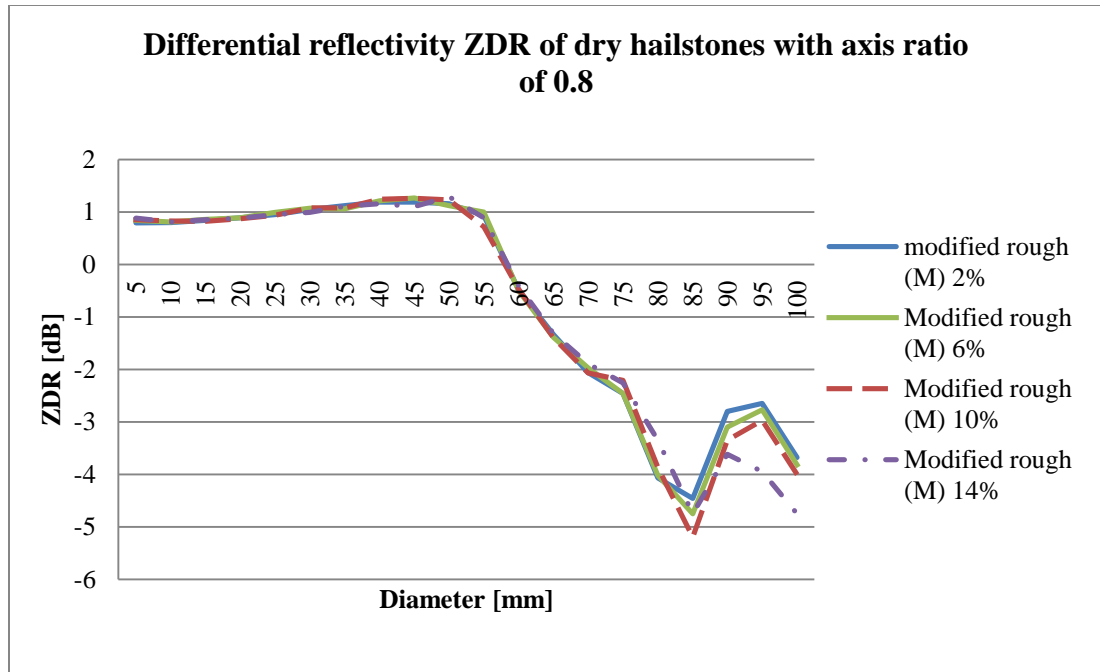


Figure 8.12 - Differential reflectivity (ZDR) for dry hailstones with axis ratio of 0.8 and R-type roughness of 2% (solid blue), 6% (solid green), 10% (dashed red) and 14% (dot-dashed violet).

Comparison of the differential reflectivity values for different axes ratios of dry hailstones with the M-type protuberances are plotted in Fig. 8.13. As expected, axis ratios closer to unity are producing lower Z_{DR} values. The difference in the position of the sign shift is due to definition of physical diameter, instead of the equivolume diameter.

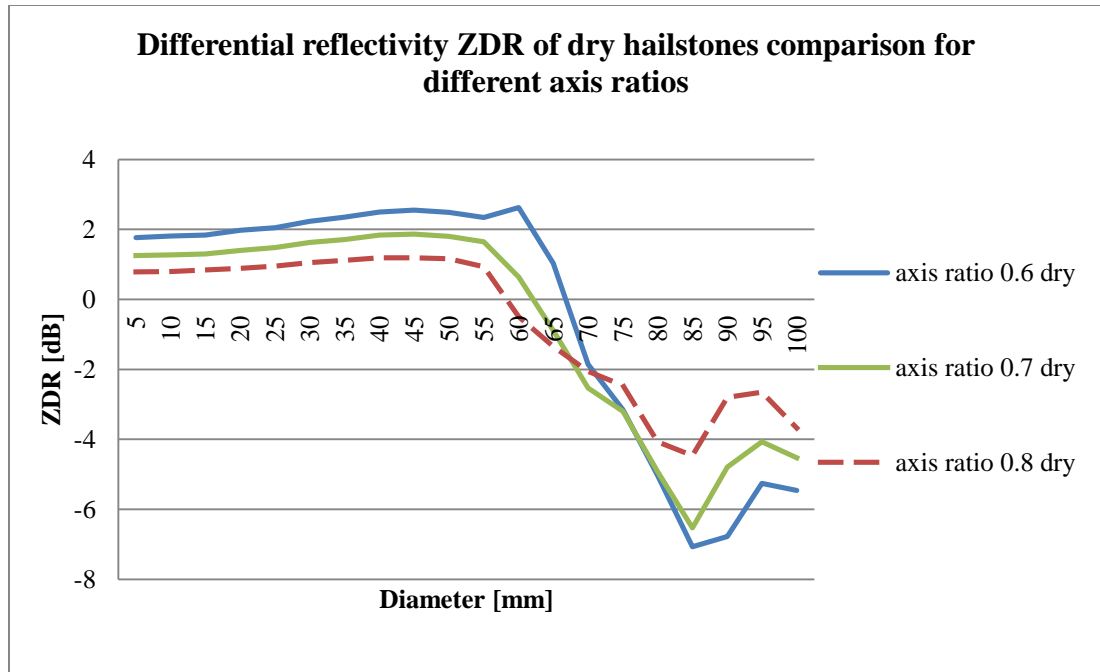


Figure 8.13 - Differential reflectivity (ZDR) for dry hailstones having the 2% M-type roughness and axis ratio of 0.6(solid blue), 0.7 (solid green), 0.8 (dashed red).

In the previous section effect of the water coating on the hailstones produced changes to the radar reflectivity factor. Similar effect is to be expected when it comes to the differential reflectivity. Due to the water coating effective (weighted average) permittivity of the hailstones will be increased, consequently wavelength as well positions of resonances as governed by the formula (2.6) will be shifted toward smaller diameters.

As in the dry hailstones differential reflectivity of axis ratio 0.6 is examined for two protrusion types M and R (Figs.8.14. and 8.15). Influence of protrusions to the differential reflectivity for smaller hailstone sizes are similarly to the dry hailstones mainly related to the increase of the local maxima magnitude and slight shifts of sizes where resonance effects are occurring. On the other hand for resonant sizes 45 to

70 mm influences to the Z_{DR} value, due to the protrusions, can be significant. Disregarding the roughness type oscillations around the median negative value at about 55 mm are heavily affected by the roughness value. For almost spheroidal hailstones (2% roughness) results are well correlated with those found in literature for pure spheroidal hailstone models (e.g. (Kumijan, 2012)). For increased roughness values results change once roughness value goes above 10%. Depending on the roughness type this value might be slightly more positive at 60 mm ranges for R-type roughness.

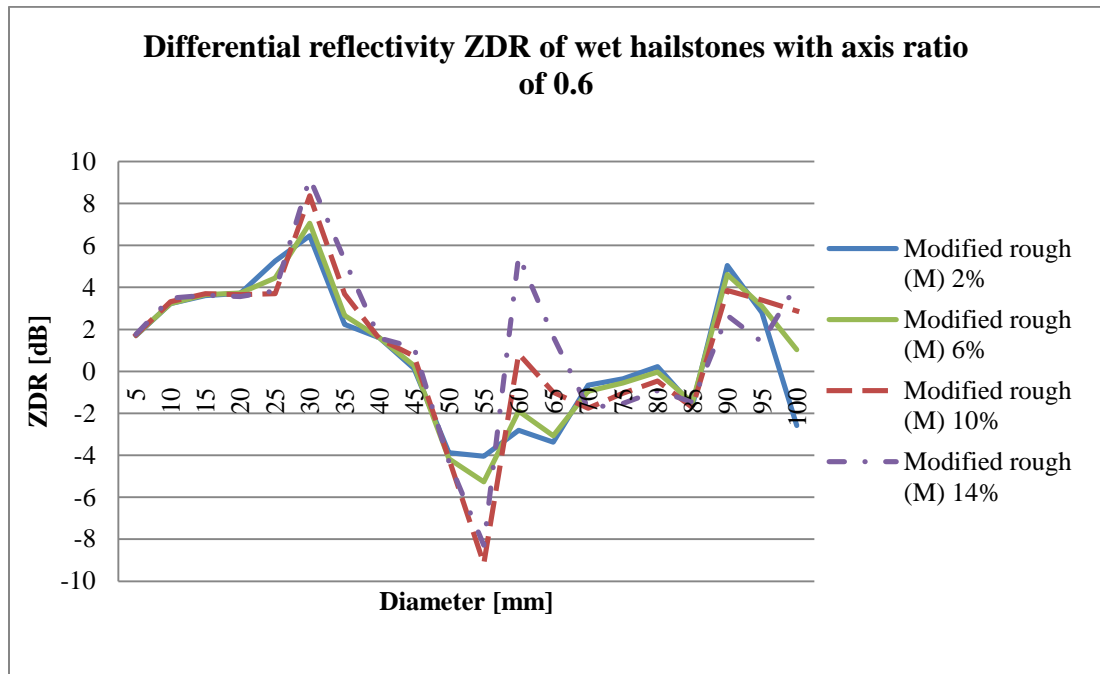


Figure 8.14 - Differential reflectivity (ZDR) for wet hailstones with axis ratio of 0.6 and M-type roughness of 2% (solid blue), 6% (solid green), 10% (dashed red) and 14% (dot-dashed violet).

The effect of roughness types may be illustrated in behavior of very rough wet hailstones is examined in Figs. 8.14 and 8.15 for 14% of roughness at 95 mm diameter. In the resonance region around 90 mm value of the Z_{DR} in case of R-type

roughness experiences a drop to slightly negative values which is not observed in the Z_{DR} for M- type roughness ensembles.

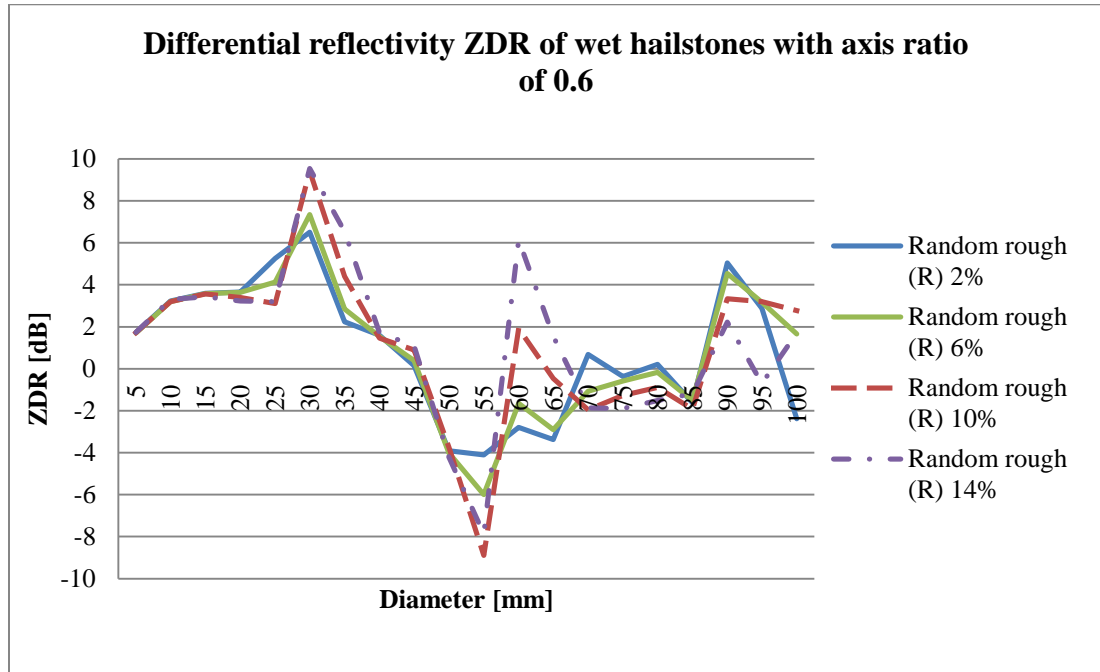


Figure 8.15 - Differential reflectivity (Z_{DR}) for wet hailstones with axis ratio of 0.6 and R-type roughness of 2% (solid blue), 6% (solid green), 10% (dashed red) and 14% (dot-dashed violet).

Differential reflectivity for wet hailstones of two roughness types and 0.7 axis ratio is presented in Figs. 8.16 and 8.17. Behavior of the Z_{DR} signature presented has similar effects as those described for wet hailstones of 0.6 axis ratio. Differences are mainly related to the Z_{DR} value, which is slightly lower as compared later. Effects of the protuberance value in the first resonance region (around 55 mm) are similar to those already discussed. Still in the second resonance region (95 mm) high roughness values tend to either shift the narrow region of Z_{DR} change in-between the variable calculation points, or create such scattering that this narrow negative region is extinct.

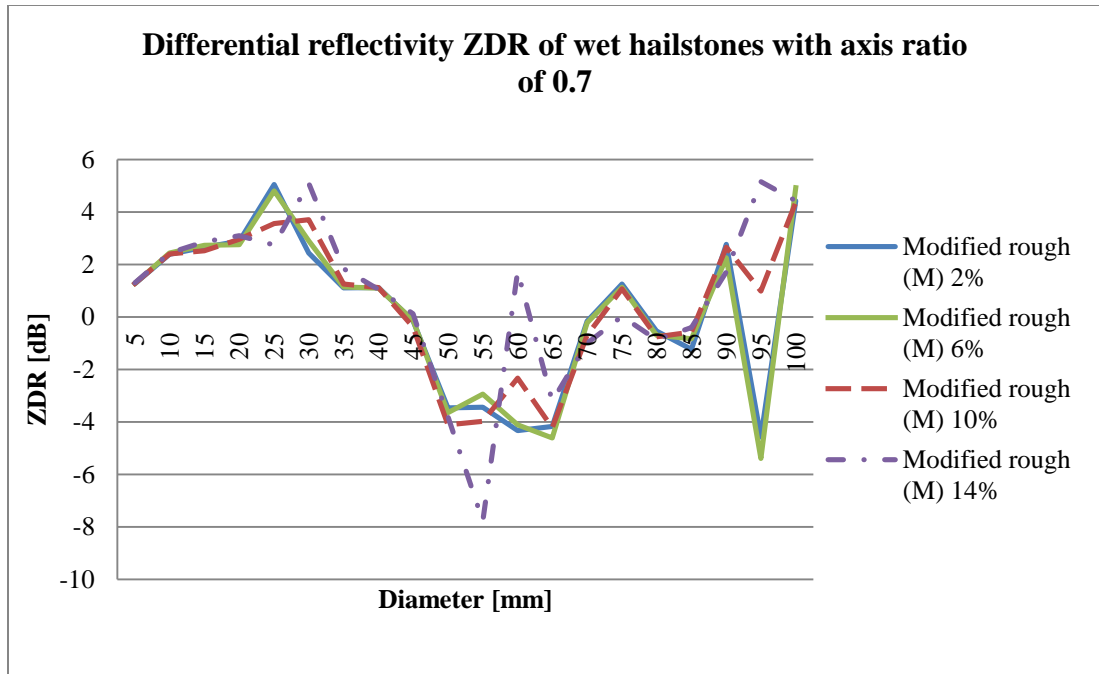


Figure 8.16 - Differential reflectivity (ZDR) for wet hailstones with axis ratio of 0.7 and M-type roughness of 2% (solid blue), 6% (solid green), 10% (dashed red) and 14% (dot-dashed violet).

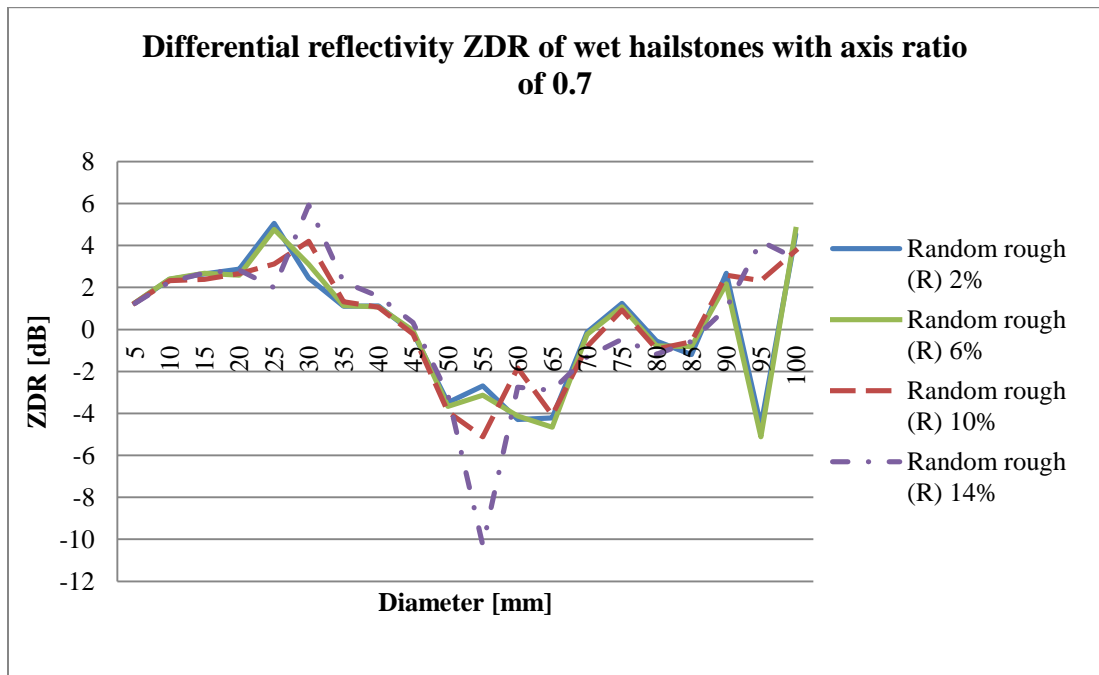


Figure 8.17 - Differential reflectivity (ZDR) for wet hailstones with axis ratio of 0.7 and R-type roughness of 2% (solid blue), 6% (solid green), 10% (dashed red) and 14% (dot-dashed violet).

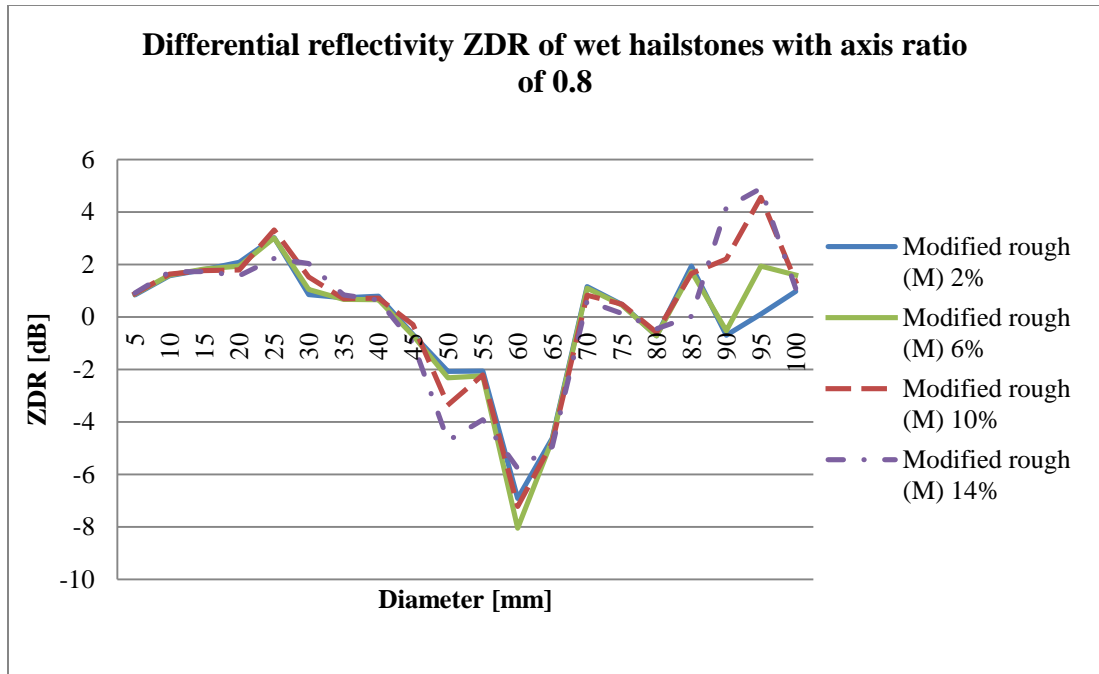


Figure 8.18 -Differential reflectivity (ZDR) for wet hailstones with axis ratio of 0.8 and M-type roughness of 2% (solid blue), 6% (solid green), 10% (dashed red) and 14% (dot-dashed violet).

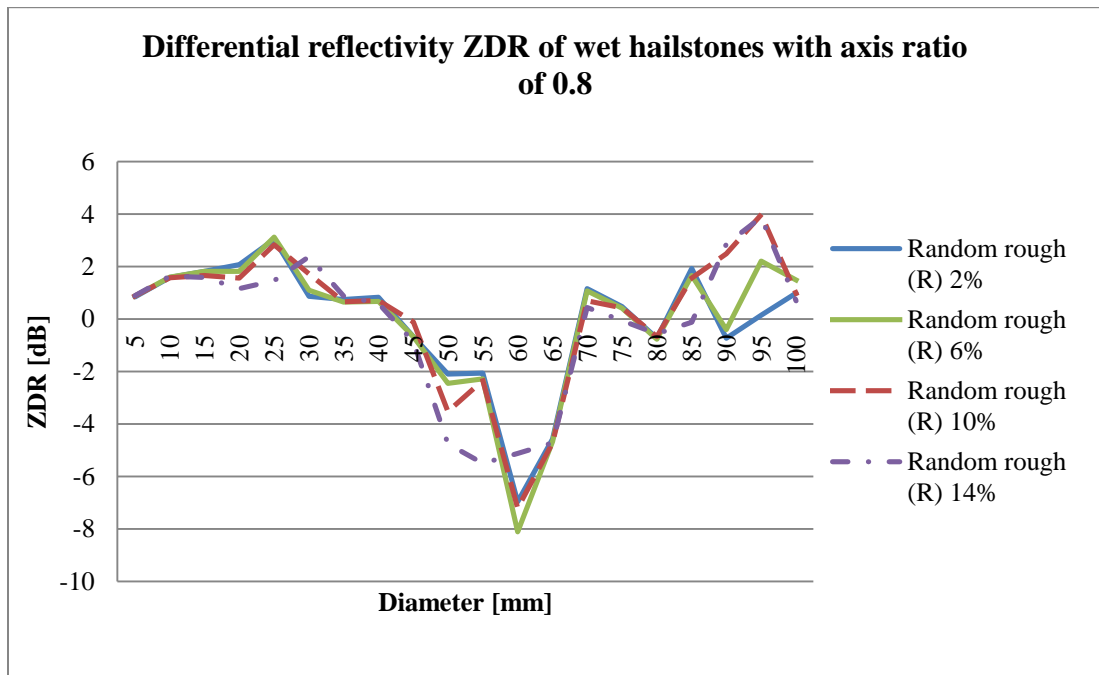


Figure 8.19 - Differential reflectivity (ZDR) for wet hailstones with axis ratio of 0.8 and R-type roughness of 2% (solid blue), 6% (solid green), 10% (dashed red) and 14% (dot-dashed violet).

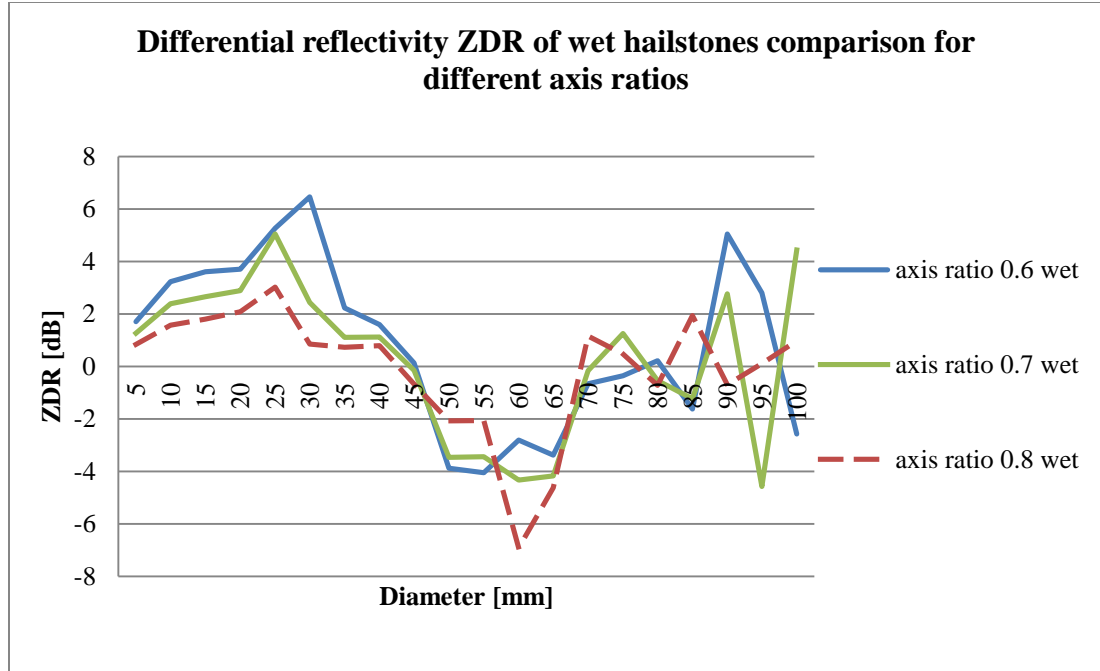


Figure 8.20 - Differential reflectivity (ZDR) for wet hailstones having the 2% M-type roughness and axis ratio of 0.6(solid blue), 0.7 (solid green), 0.8 (dashed red).

Co-polar correlation coefficient

Co-polar correlation coefficient represents the measure of similarity of returned signals. If the (5.10) is written in the format to separate its magnitude and phase, cases causing the drop of ρ_{HV} can be easily distinguished

$$|\rho_{HV}| = \frac{\sum_{i=0}^N |s_{hh}^i| |s_{vv}^i| e^{-j(\phi_{vv}^i - \phi_{hh}^i)}}{\sqrt{\sum_{i=0}^N |s_{hh}^i|^2 \cdot \sum_{i=0}^N |s_{vv}^i|^2}}, \quad (5.14)$$

where the exponential term is the backscatter differential phase for each hydrometeor $\delta^i = \phi_{vv}^i - \phi_{hh}^i$. Therefore the magnitude of each element contributing to ρ_{HV} is dependent mainly of the backscatter differential phase for that element. For the

ensemble of elements however, decrease in co-polar correlation coefficient occurs for particles when variation of shapes or orientations exist.

With aforementioned in mind it is expected that ρ_{HV} value, in cases of monodisperse size distribution and uniform distribution of orientations, will mainly be affected by resonant scattering effects. Additionally, the drop in ρ_{HV} will occur for larger protuberance values due to difference between scattering element values that have higher variance.

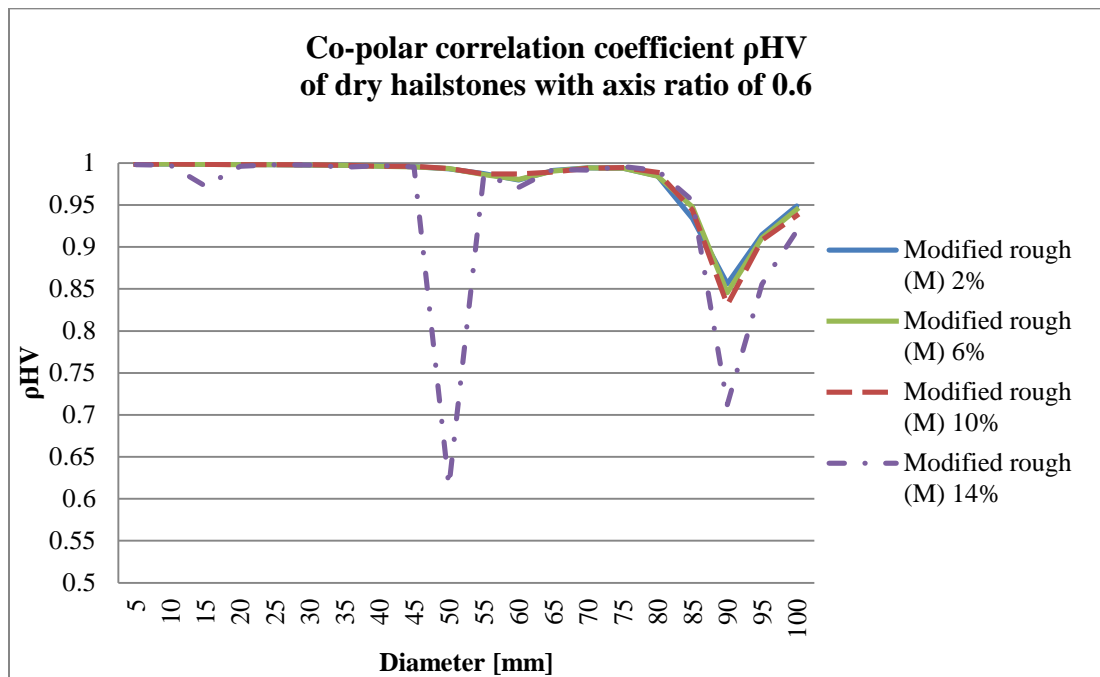


Figure 8.21 – Co-polar correlation coefficient (ρ_{HV}) for dry hailstones with axis ratio of 0.6 and M-type roughness of 2% (solid blue), 6% (solid green), 10% (dashed red) and 14% (dot-dashed violet).

Small, solid ice particles are known, in literature, to produce co-polar correlation coefficient close to unity. Detailed studies of the ρ_{HV} are seldom, and usually deal with larger purely spheroidal particles. Results in Figs. 8.21 and 8.22 represent behavior of ρ_{HV} for dry hailstones with axis ratio of 0.6 due to roughness value. In

both cases (M and R roughness types) co-polar correlation coefficient experiences drops at values of averaged physical diameter of 15, 50 and 90 mm. All three sizes are considered to be resonant sizes of for dry hailstones, which becomes clear once backscatter differential phase is examined in the following section. Additionally, slight drop of ρ_{HV} occurring at 75 mm for R-type roughness is most likely caused by the roughness value.

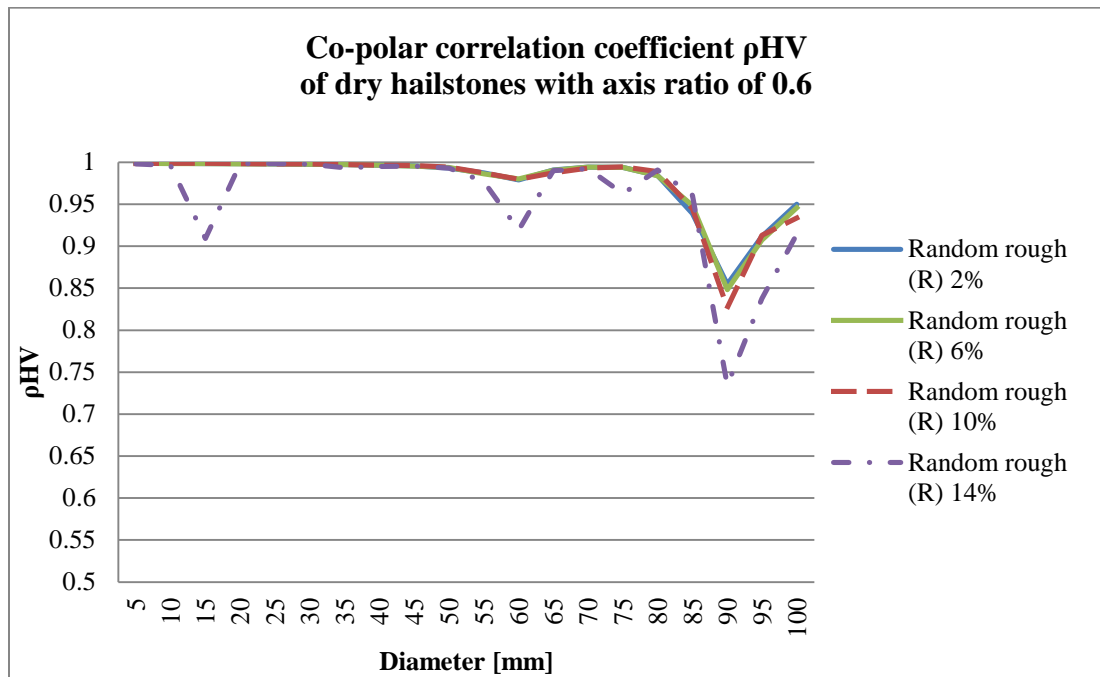


Figure 8.22 – Co-polar correlation coefficient (ρ_{HV}) for dry hailstones with axis ratio of 0.6 and R-type roughness of 2% (solid blue), 6% (solid green), 10% (dashed red) and 14% (dot-dashed violet).

For hailstones having axis ratio 0.7, ρ_{HV} is presented in Figs. 8.23 and 8.24. It is imperative to notice that the scale correlation coefficient value has changed from the previous case as drops occurring for hailstones having axis ratio 0.7 are slightly shallower than for 0.6 axis ratio hailstones. Additionally, drops in the case of R roughness are deeper than in case of M-type roughness.

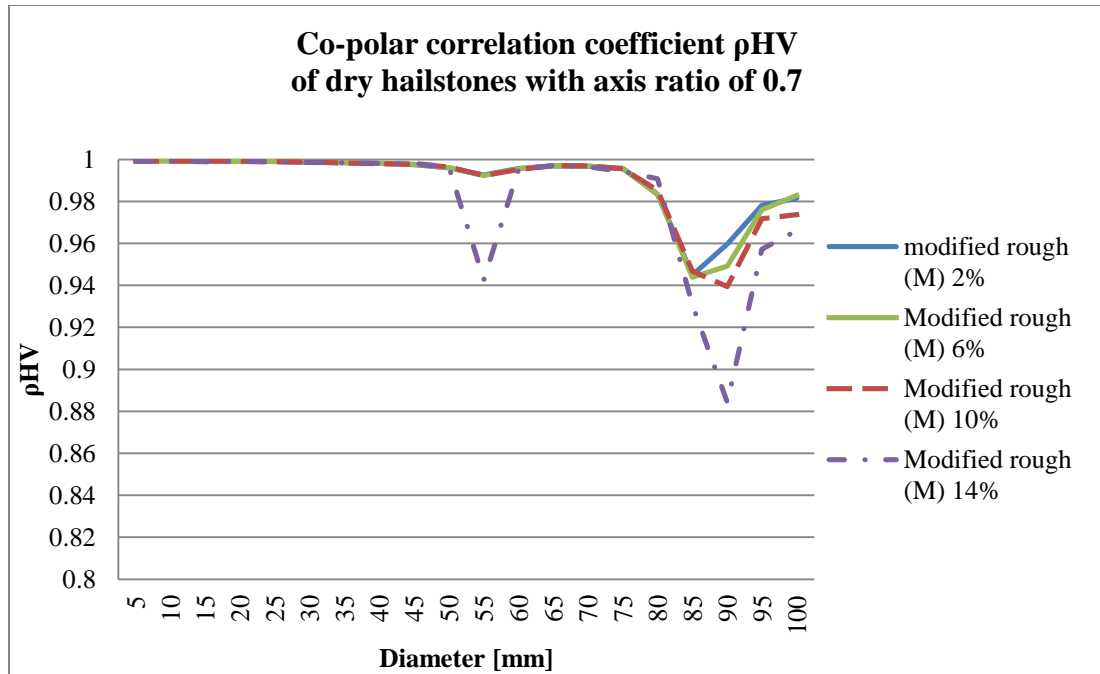


Figure 8.23 - Co-polar correlation coefficient (ρ_{HV}) for dry hailstones with axis ratio of 0.7 and M-type roughness of 2% (solid blue), 6% (solid green), 10% (dashed red) and 14% (dot-dashed violet).

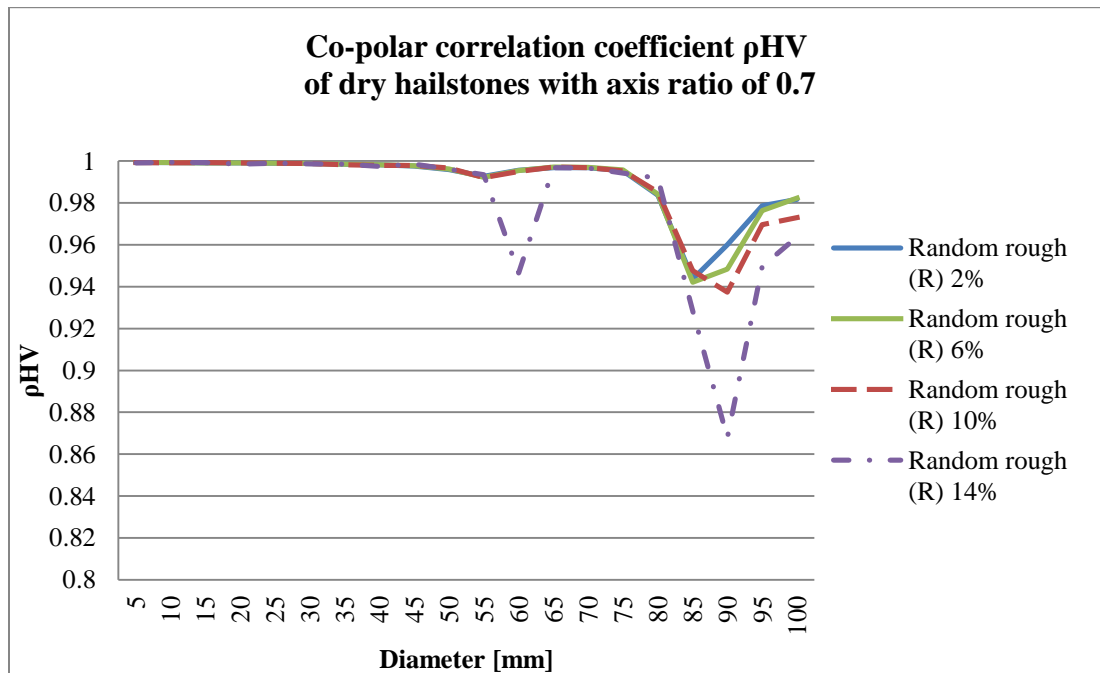


Figure 8.24 - Co-polar correlation coefficient (ρ_{HV}) for dry hailstones with axis ratio of 0.7 and R-type roughness of 2% (solid blue), 6% (solid green), 10% (dashed red) and 14% (dot-dashed violet).

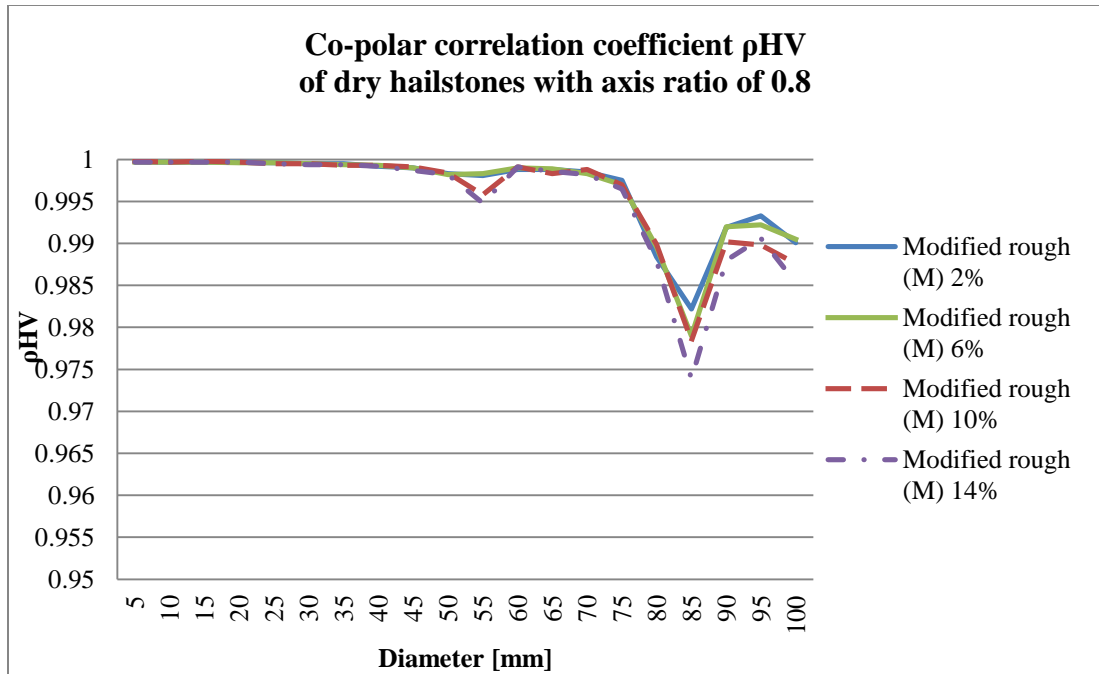


Figure 8.25 - Co-polar correlation coefficient (ρ_{HV}) for dry hailstones with axis ratio of 0.8 and M-type roughness of 2% (solid blue), 6% (solid green), 10% (dashed red) and 14% (dot-dashed violet).

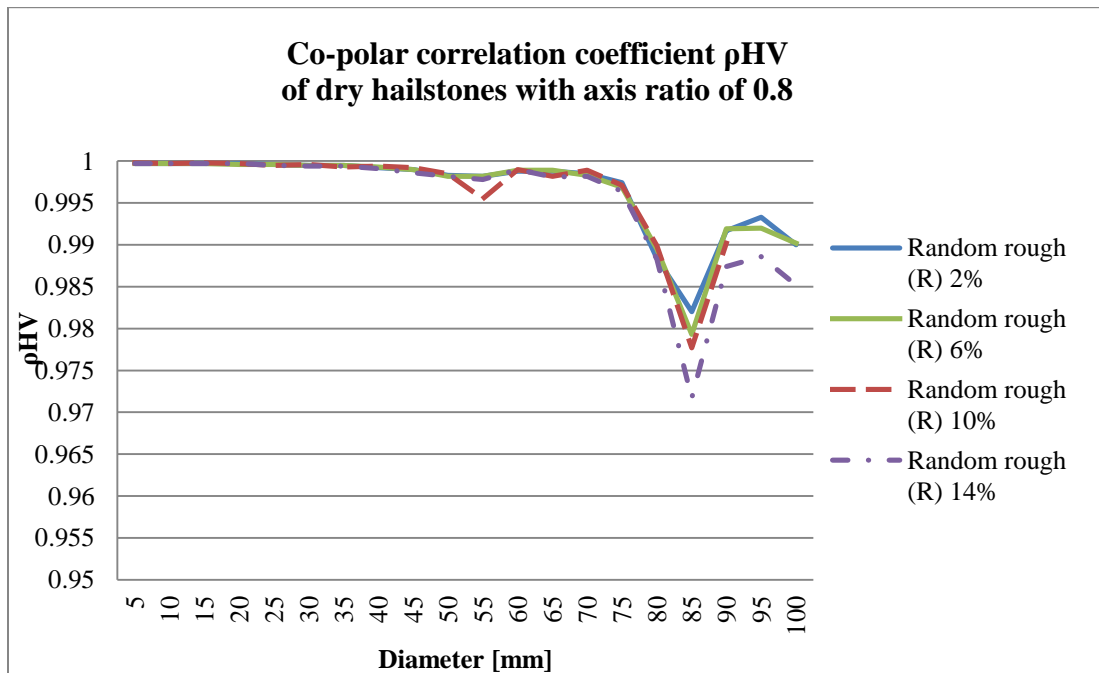


Figure 8.26 - Co-polar correlation coefficient (ρ_{HV}) for dry hailstones with axis ratio of 0.8 and R-type roughness of 2% (solid blue), 6% (solid green), 10% (dashed red) and 14% (dot-dashed violet).

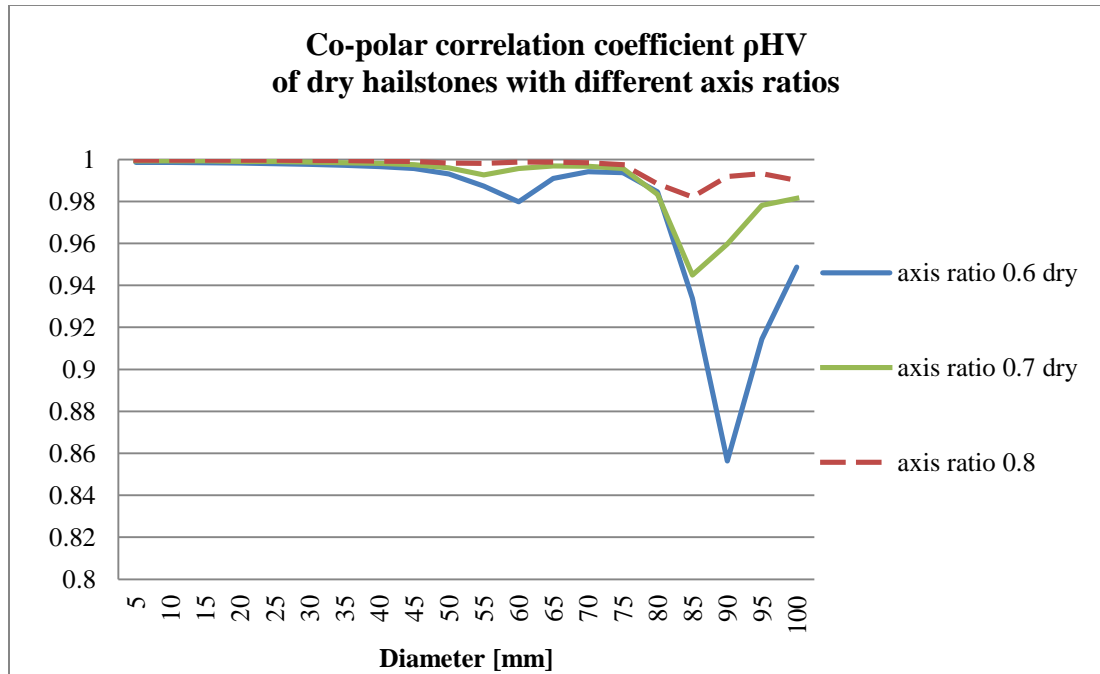


Figure 8.27 - Co-polar correlation coefficient (ρ_{HV}) for dry hailstones having the 2% M-type roughness and axis ratio of 0.6(solid blue), 0.7 (solid green), 0.8 (dashed red).

Behavior of the co-polar correlation coefficient for the water coated (wet) hailstones is substantially different than for dry hailstones. The reason for this behavior is the higher dielectric permittivity of these hailstones due to the liquid water film on their surface. Higher dielectric permittivity will result in higher backscattering returns and therefore a wider variety of backscattered values, providing an environment conducive to correlation coefficient drops. Presented below is the ρ_{HV} for 0.6 axis ratio wet hailstones (Figs. 8.28 and 8.29).

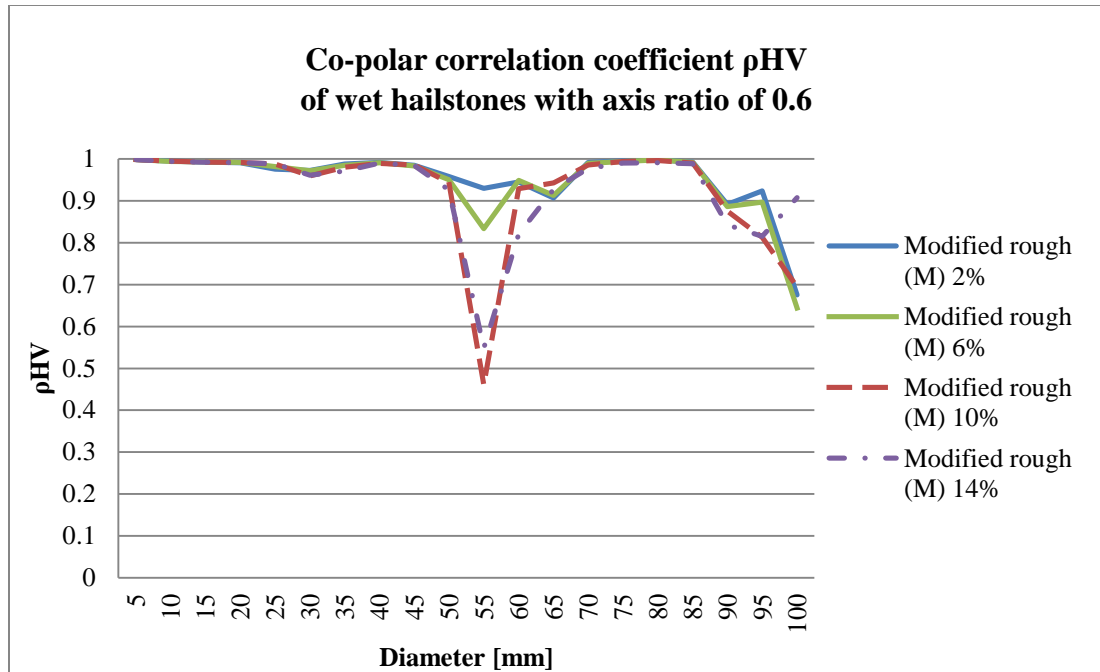


Figure 8.28 - Co-polar correlation coefficient (ρ_{HV}) for wet hailstones with axis ratio of 0.6 and M-type roughness of 2% (solid blue), 6% (solid green), 10% (dashed red) and 14% (dot-dashed violet).

As it was the case of dry hailstones of same axis ratio three drop regions could be identified for wet hailstones. It is important to emphasize the range of correlation coefficient values is changed if compared to previous graphs. Still, drop of the correlation coefficient value exist in places of resonances while the depth of the drop is directly proportional to the roughness value and type of protuberances (deeper for more uniform R type of roughness).

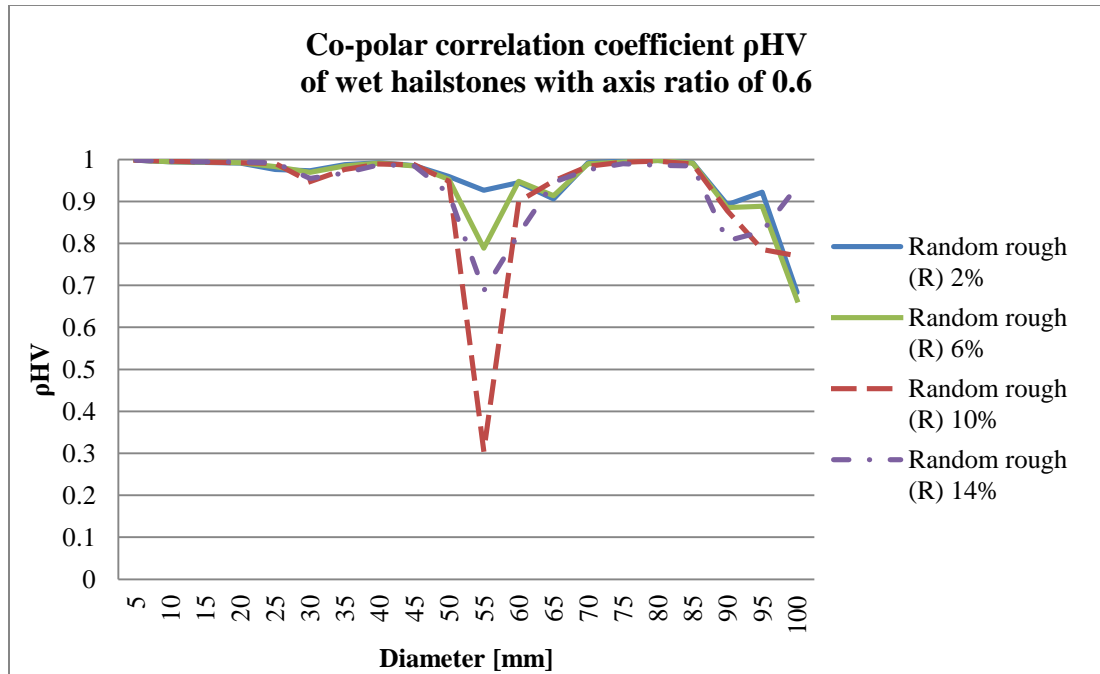


Figure 8.29 - Co-polar correlation coefficient (ρ_{HV}) for wet hailstones with axis ratio of 0.6 and R-type roughness of 2% (solid blue), 6% (solid green), 10% (dashed red) and 14% (dot-dashed violet).

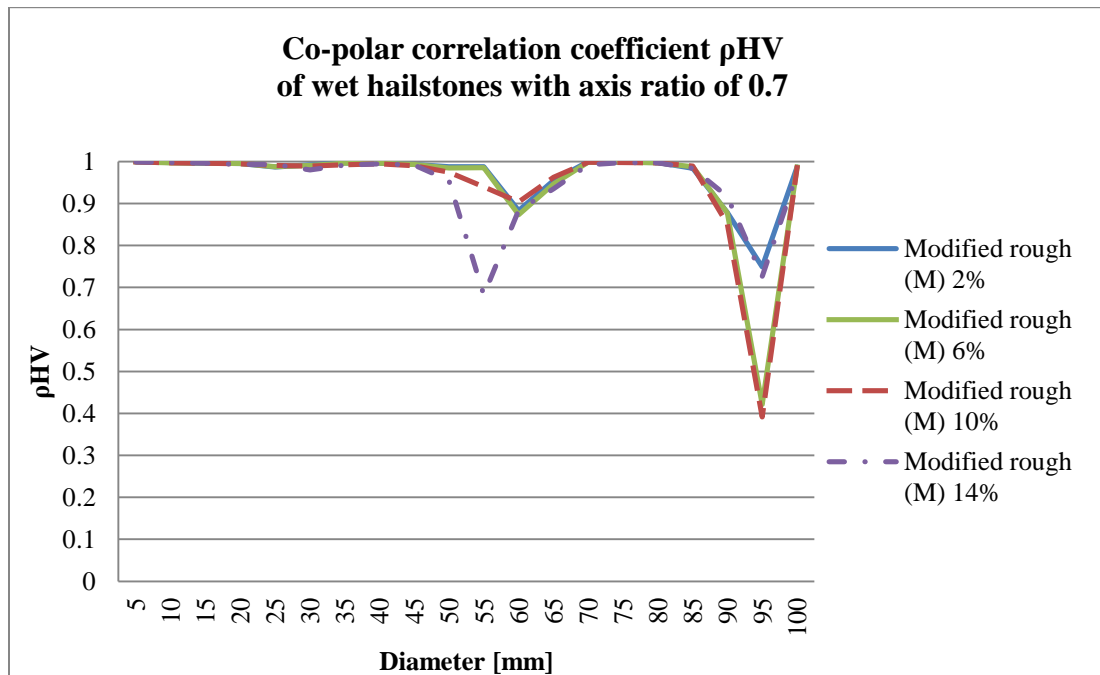


Figure 8.30 - Co-polar correlation coefficient (ρ_{HV}) for wet hailstones with axis ratio of 0.7 and M-type roughness of 2% (solid blue), 6% (solid green), 10% (dashed red) and 14% (dot-dashed violet).

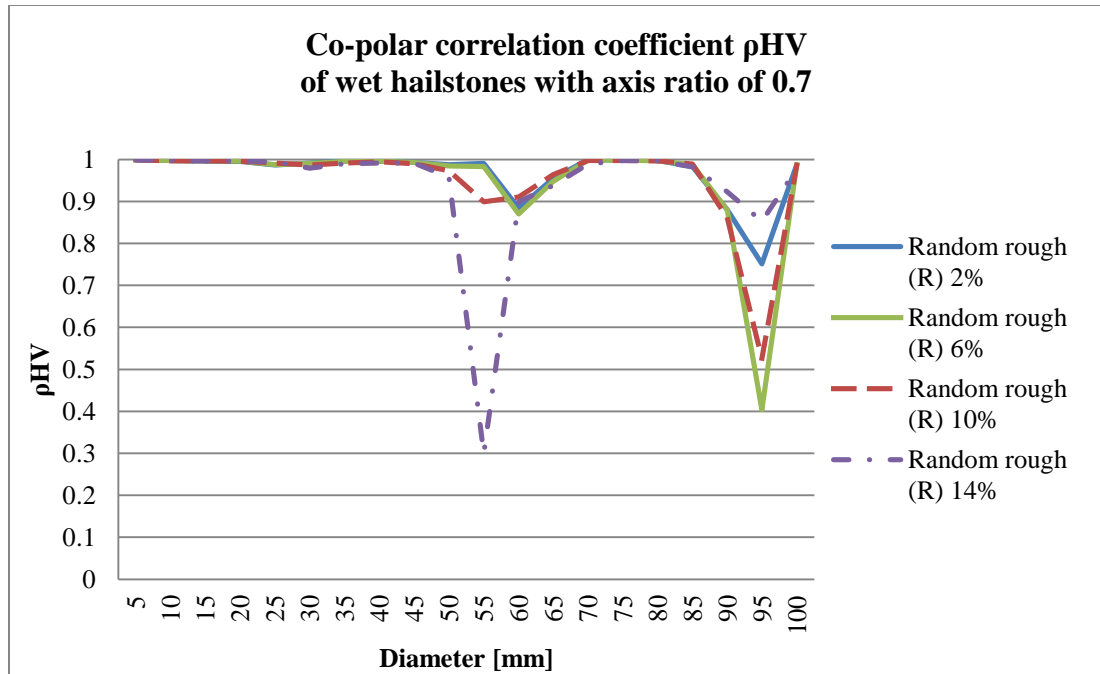


Figure 8.31 - Co-polar correlation coefficient (ρ_{HV}) for wet hailstones with axis ratio of 0.7 and R-type roughness of 2% (solid blue), 6% (solid green), 10% (dashed red) and 14% (dot-dashed violet).

As for the dry hailstones, wet hailstones of axis ratio 0.8 are examined (Figs. 8.32 and 8.33). The ρ_{HV} scale is changed in order to better present dynamic range of the correlation coefficient that is smaller than in cases of lower axis ratio hailstones.

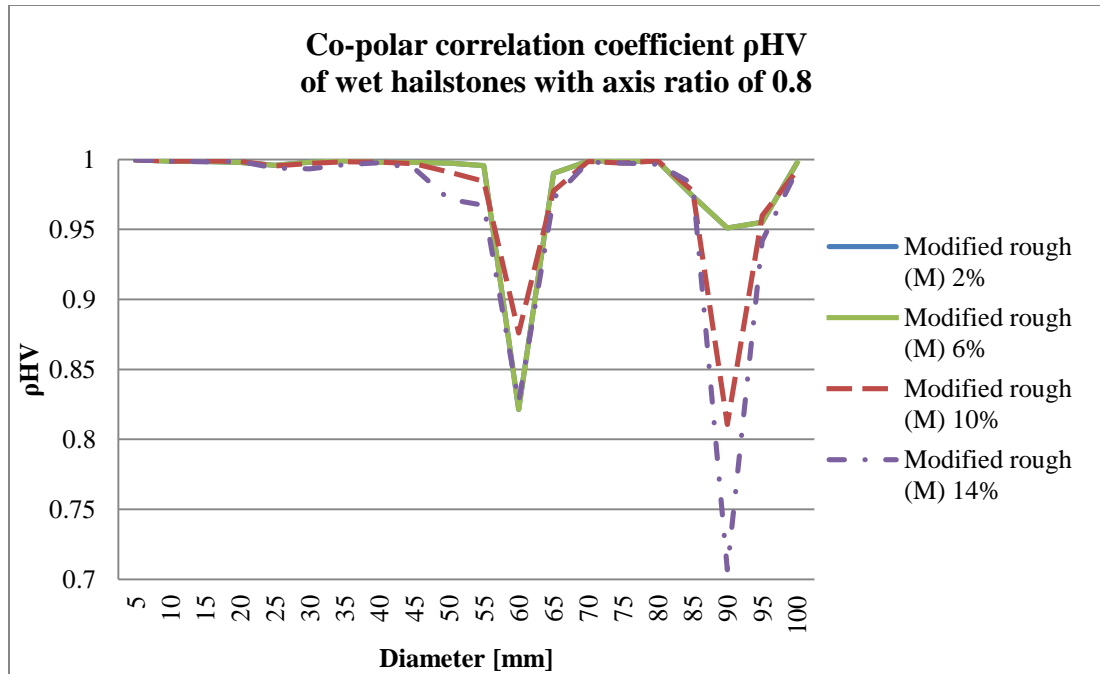


Figure 8.32 – Co-polar correlation coefficient (ρ_{HV}) for wet hailstones with axis ratio of 0.8 and M-type roughness of 2% (solid blue), 6% (solid green), 10% (dashed red) and 14% (dot-dashed violet).

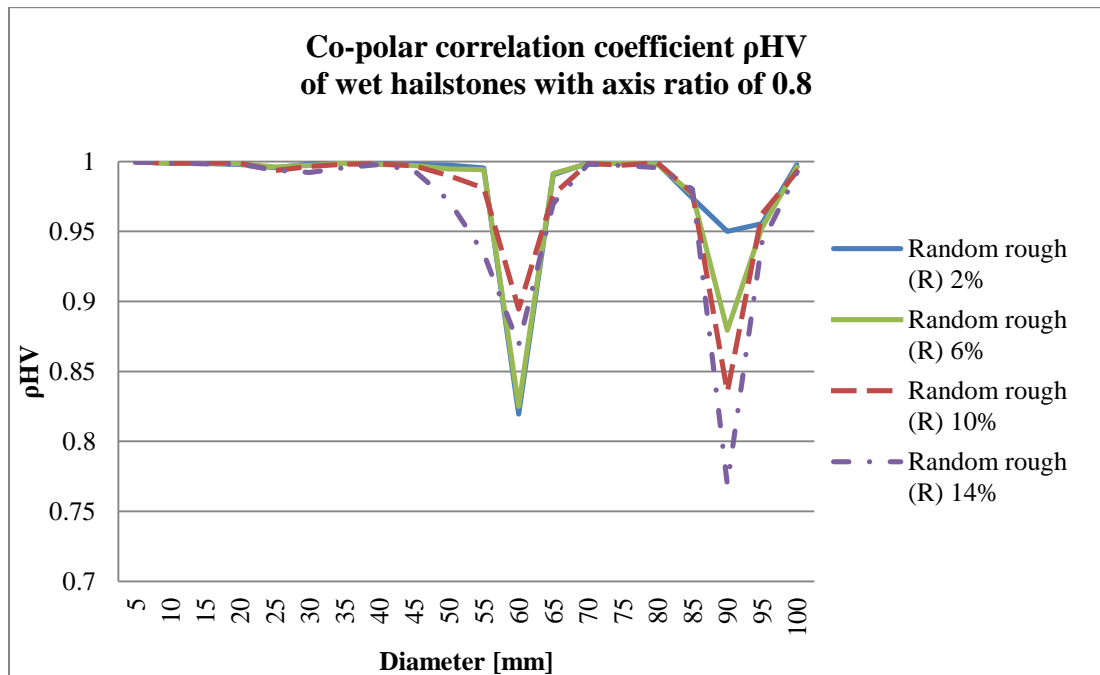


Figure 8.33 – Co-polar correlation coefficient (ρ_{HV}) for wet hailstones with axis ratio of 0.8 and R-type roughness of 2% (solid blue), 6% (solid green), 10% (dashed red) and 14% (dot-dashed violet).

Finally, co-polar correlation coefficient dependence on the axis ratio for 2% M type roughness particles is shown in Fig. 8.34. Expected value differences due to the higher sphericity of larger axis ratio are observed as well as wider ρ_{HV} drop ranges in case of lowest 0.6 axis ratio.

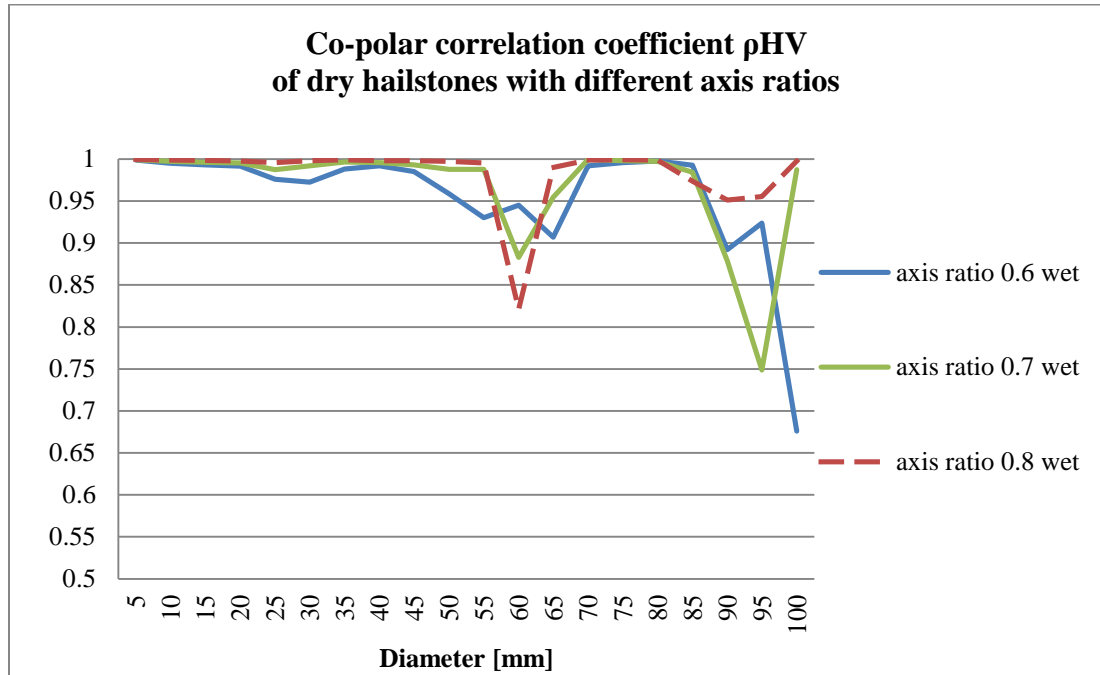


Figure 8.34 - Co-polar correlation coefficient (ρ_{HV}) for wet hailstones having the 2% M-type roughness and axis ratio of 0.6(solid blue), 0.7 (solid green), 0.8 (dashed red).

Backscatter differential phase

The backscatter differential phase synthesized using the PVS exists only due to the scattering effects happening with particular hailstone size. Moreover, as the monodisperse size distribution of scatterer sizes is assumed the backscatter differential phase is the best evidence of resonance effects happening in the scattering volume. This is evident from the (5.11) as the only term containing phase is the numerator. This phase will be exactly the difference of scattered fields phases of V

and H fields (5.14). As a conclusion, each abrupt change of the δ is caused by micro resonance or resonance effect, micro resonance due to roughness, or hailstone body resonance if this change of δ exists over a range of sizes.

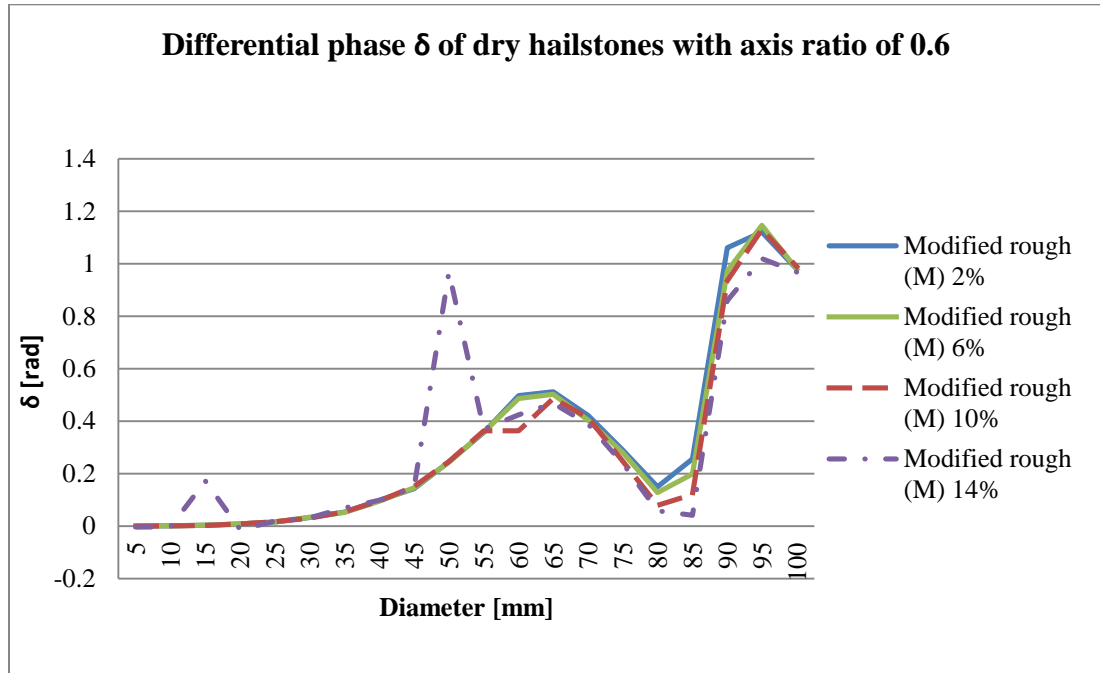


Figure 8.35 - Backscatter differential phase (δ) for dry hailstones with axis ratio of 0.6 and M-type roughness of 2% (solid blue), 6% (solid green), 10% (dashed red) and 14% (dot-dashed violet).

The backscatter differential phase results for dry hailstones with axis ratio 0.6 are presented in Figs. 8.35 and 8.36. These figures support explanations given for drops of co-polar correlation coefficient. It is evident that micro resonance effects are pronounced with peaks at 15 mm for both roughness type and 50 mm for 14% M-type roughness. Additionally, wider range of correlation coefficient drops are well aligned with the wider resonance effects observed in figures.

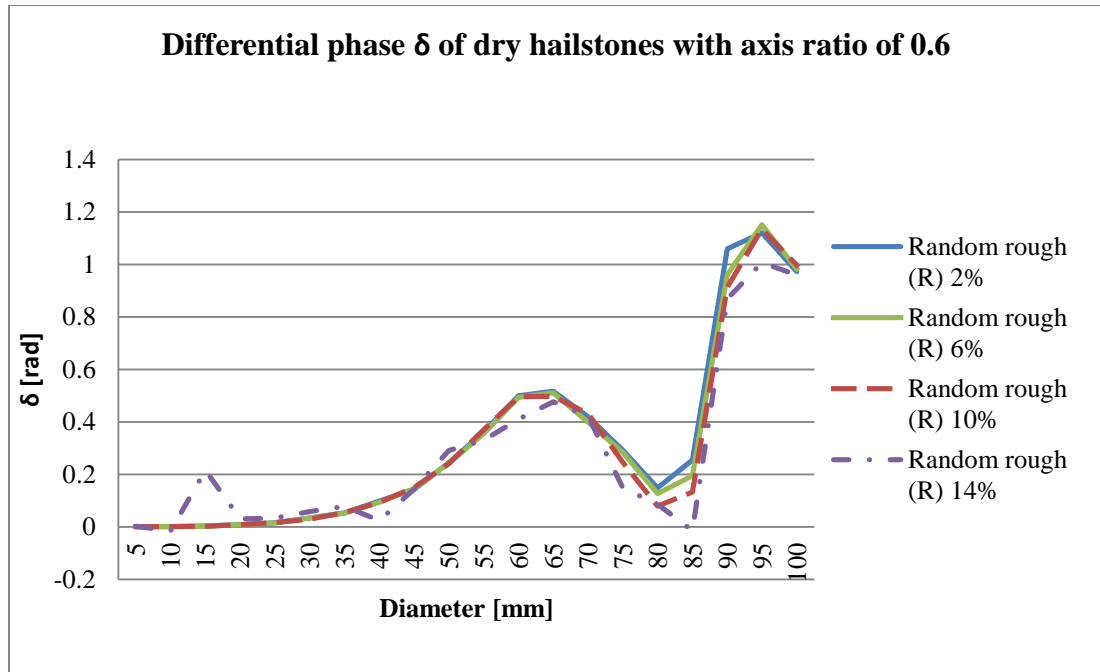


Figure 8.36 - Backscatter differential phase (δ) for dry hailstones with axis ratio of 0.6 and R-type roughness of 2% (solid blue), 6% (solid green), 10% (dashed red) and 14% (dot-dashed violet).

The backscatter differential case for monodisperse distribution of dry 0.7 axis ratio hailstones is given in Figs. 8.37 and 8.38. Figures best describe effects of roughness value to the resonances of hydrometeors. Depending on the roughness value, resonance effect will be pushed toward the larger diameters, which is illustrated around 80 mm, disregarding the roughness type. On the other hand for the R-type roughness abrupt change due to the micro resonance occurs at the top of the resonance regime (60 mm) causing additional increase of backscatter differential phase.

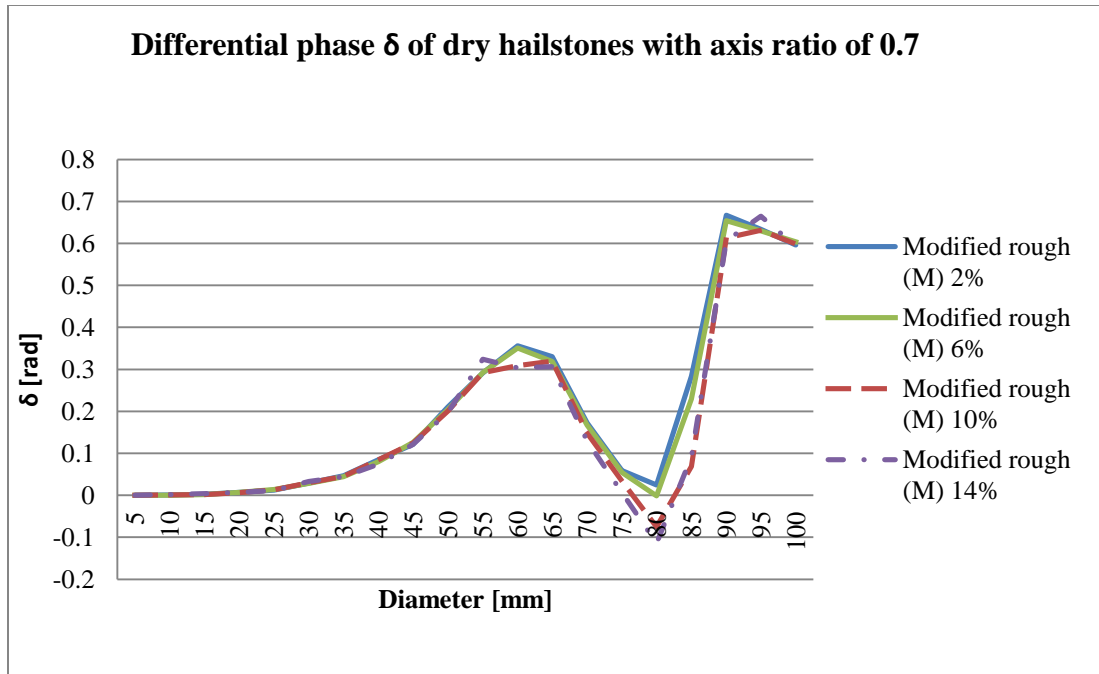


Figure 8.37 - Backscatter differential phase (δ) for dry hailstones with axis ratio of 0.7 and M-type roughness of 2% (solid blue), 6% (solid green), 10% (dashed red) and 14% (dot-dashed violet).

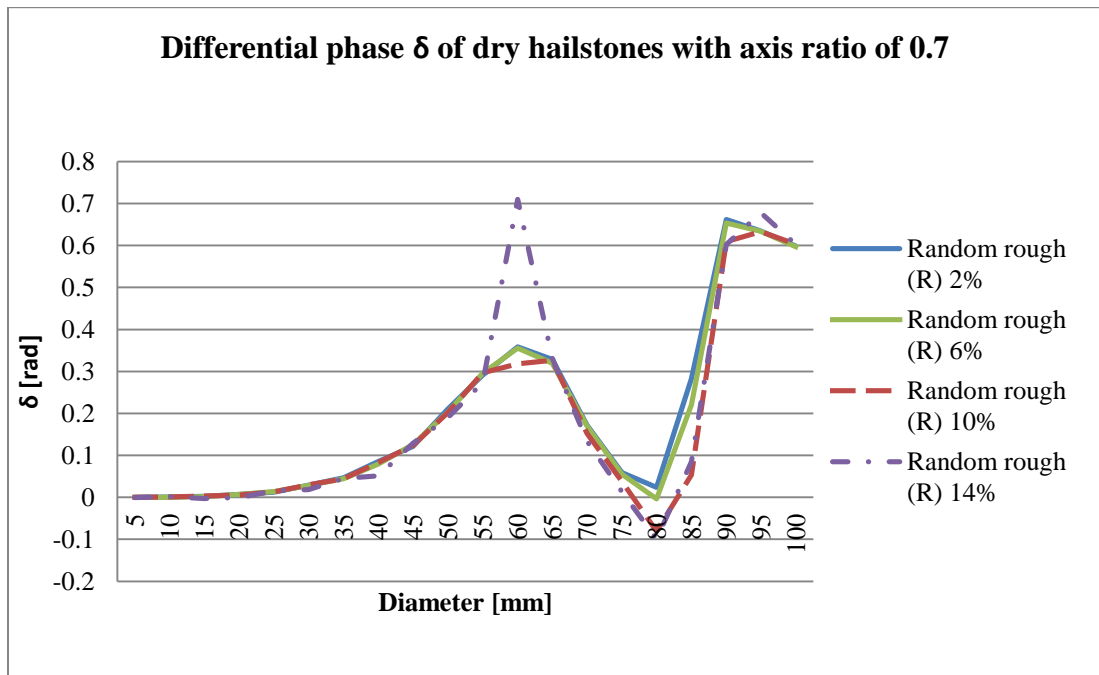


Figure 8.38 - Backscatter differential phase (δ) for dry hailstones with axis ratio of 0.7 and R-type roughness of 2% (solid blue), 6% (solid green), 10% (dashed red) and 14% (dot-dashed violet).

Effects similar to those observed for hailstones having axis ratio of 0.7 are observed in the case of 0.8 axis ratio hailstones. However, for the purpose of completeness, as well as specific interest in 0.8 axis ratio hailstones that are usually considered in the literature (e.g. (Kumijan, 2012)) calculated backscattering differential phase values are plotted (Figs. 8.39 and 8.40).

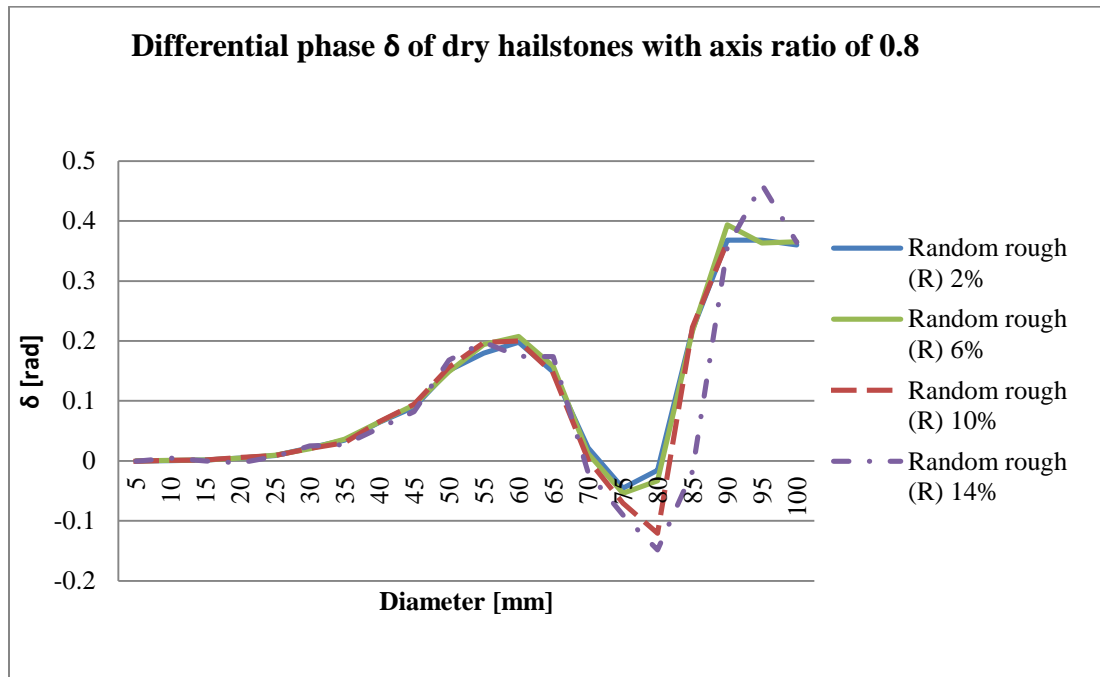


Figure 8.39 - Backscatter differential phase (δ) for dry hailstones with axis ratio of 0.8 and M-type roughness of 2% (solid blue), 6% (solid green), 10% (dashed red) and 14% (dot-dashed violet).

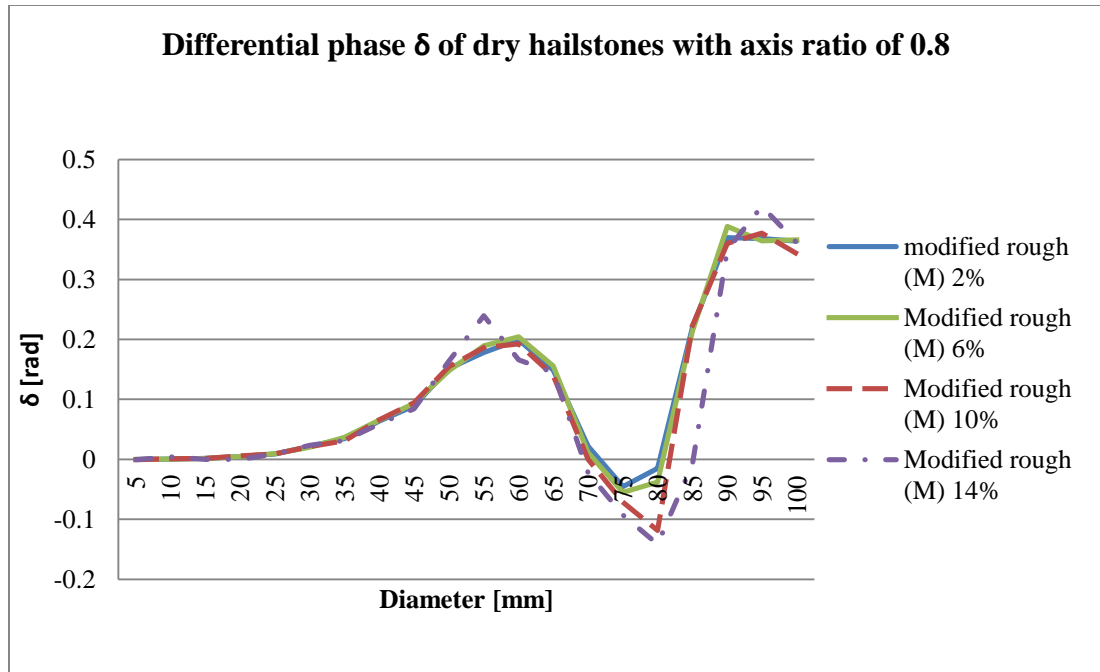


Figure 8.40 - Backscatter differential phase (δ) for dry hailstones with axis ratio of 0.8 and R-type roughness of 2% (solid blue), 6% (solid green), 10% (dashed red) and 14% (dot-dashed violet).

Comparison of δ for different axis ratios is presented by Fig. 8.41. Values of the backscatter differential phase are decreasing with respect to the increase of axis ratio, which was already identified to produce co-polar correlation coefficients closer to unity (Fig. 8.34). This effect can be explained by the smaller difference in backscatter phases as well as closer excitations of resonant modes between orthogonal fields. On the other hand, simplistic, straight forward logic is that as hailstones are closer to spherical shape values of backscatter differential phase have to approach those of a sphere (zero differential phase).

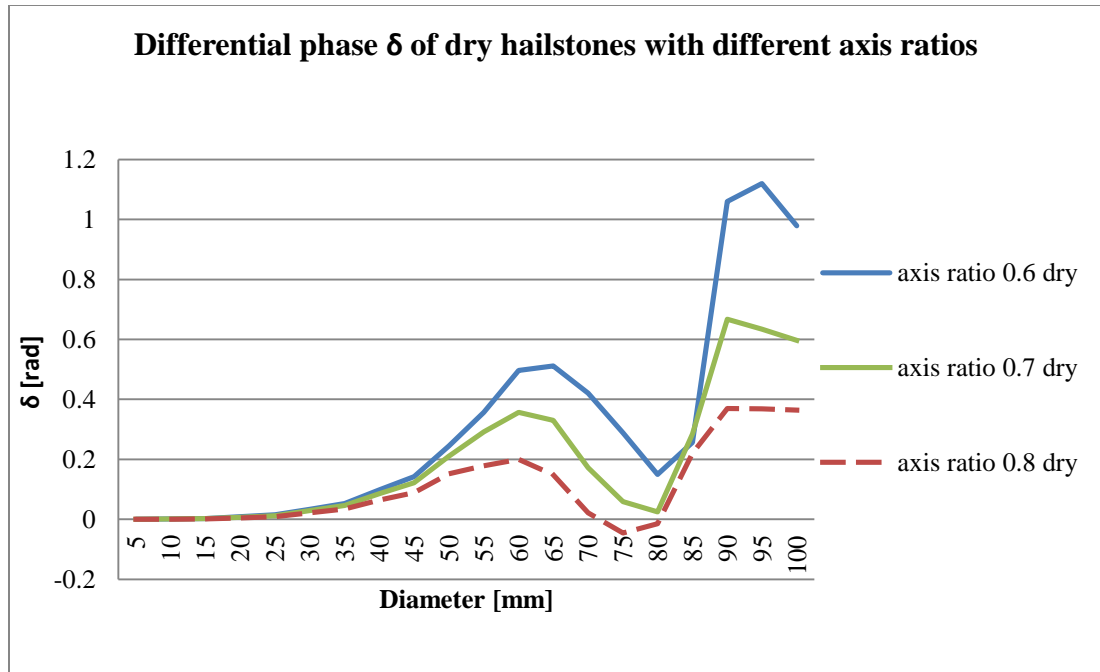


Figure 8.41 - Backscatter differential phase (δ) for dry hailstones having the 2% M-type roughness and axis ratio of 0.6(solid blue), 0.7 (solid green), 0.8 (dashed red).

The differential phase for wet hailstones of 0.6 axis ratio are plotted in Figs. 8.42 and 8.43. The backscatter differential phases are strongly affected with the change in the dielectric constant. Values of the differential phase due to the change in dielectric constant will experience dynamic range which is multiple times higher than I the case of dry hailstones.

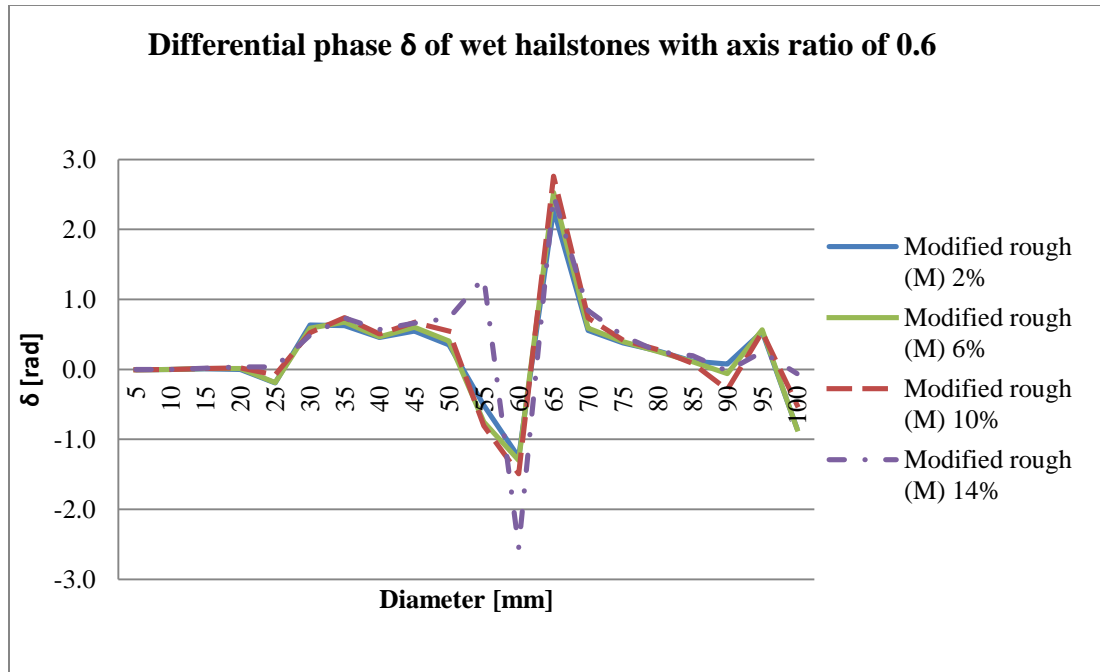


Figure 8.42 - Backscatter differential phase (δ) for wet hailstones with axis ratio of 0.6 and M-type roughness of 2% (solid blue), 6% (solid green), 10% (dashed red) and 14% (dot-dashed violet).

At the first glance, it is obvious that the position of resonance effects have changed from the case of dry hydrometeors. Values calculated for wet hailstone scattering are approximately at least two times higher for wet hailstones than for the dry ones, and as the main difference, change of the backscatter differential phase sign is observed for wet particles..

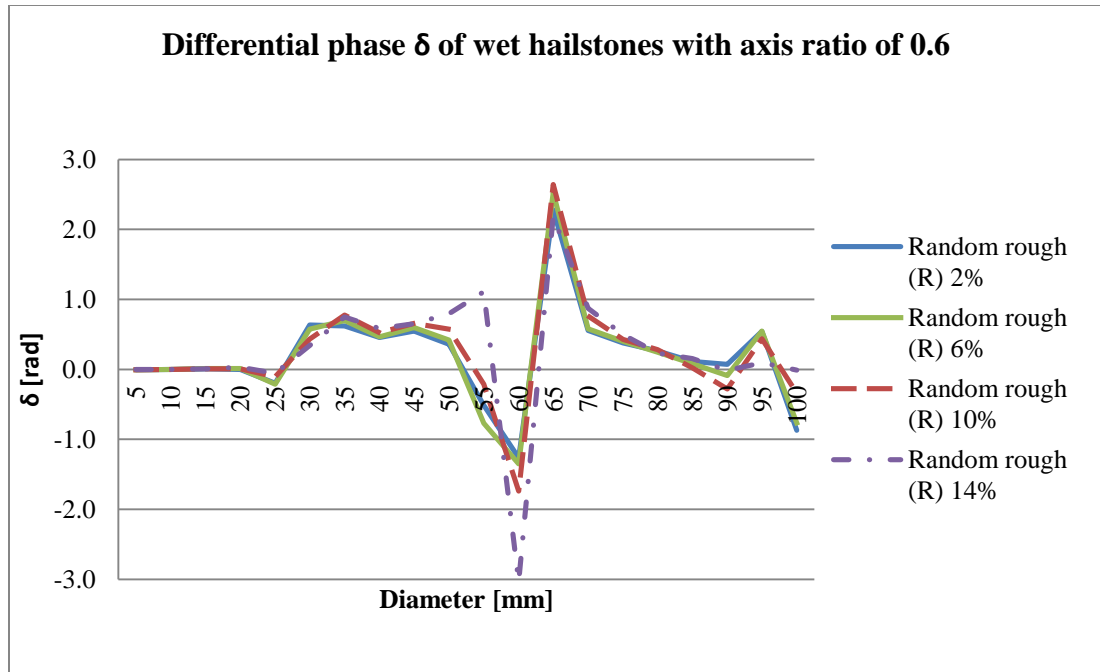


Figure 8.43 - Backscatter differential phase (δ) for wet hailstones with axis ratio of 0.6 and R-type roughness of 2% (solid blue), 6% (solid green), 10% (dashed red) and 14% (dot-dashed violet).

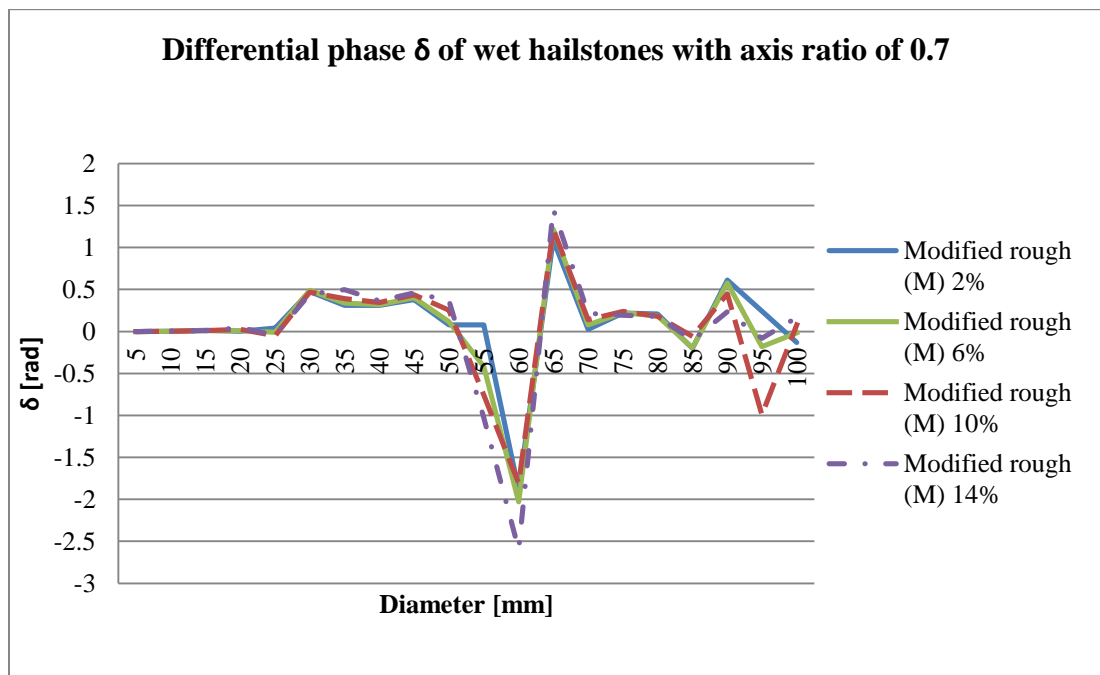


Figure 8.44 - Backscatter differential phase (δ) for wet hailstones with axis ratio of 0.7 and M-type roughness of 2% (solid blue), 6% (solid green), 10% (dashed red) and 14% (dot-dashed violet).

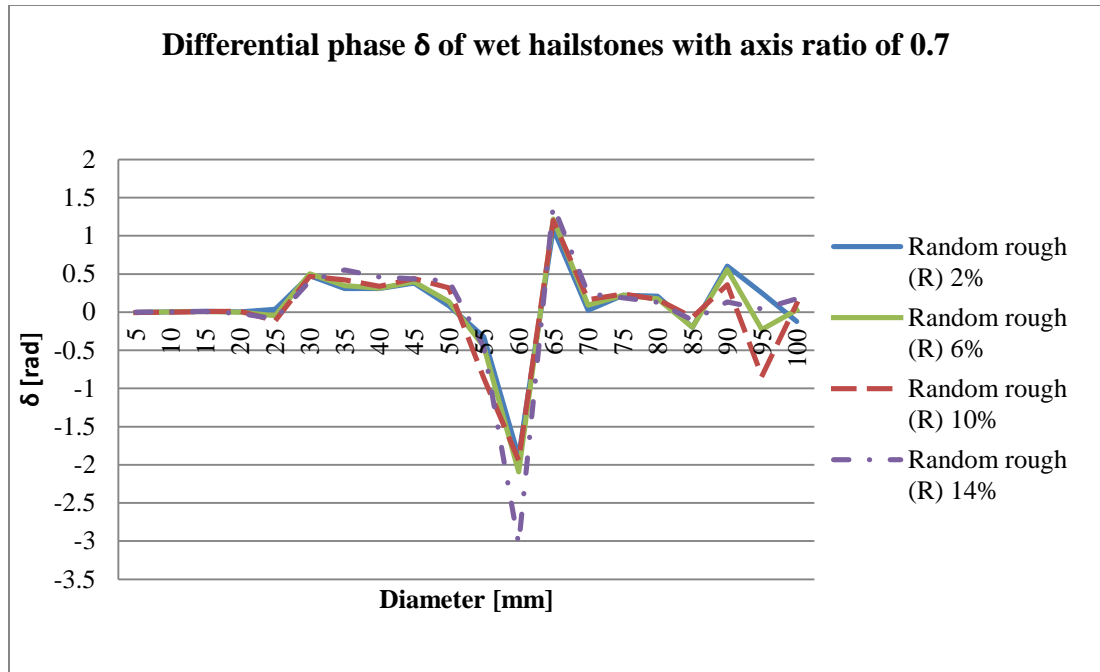


Figure 8.45 - Backscatter differential phase (δ) for wet hailstones with axis ratio of 0.7 and R-type roughness of 2% (solid blue), 6% (solid green), 10% (dashed red) and 14% (dot-dashed violet).

For the most spherical hailstone axis ratio (0.8) results are given in Figs. 8.46 and 8.47. Besides the previously described effects, it is interesting to notice that the resonant size of 60 mm backscatter differential phase in case of very rough (14%) hailstones will change the difference for more than 180 degrees and appear as the positive value in both figures. Actual difference from values calculated for other roughness values is not drastically larger, however its difference becomes positive value as phases are wrapped in $(-\pi, \pi)$ region.

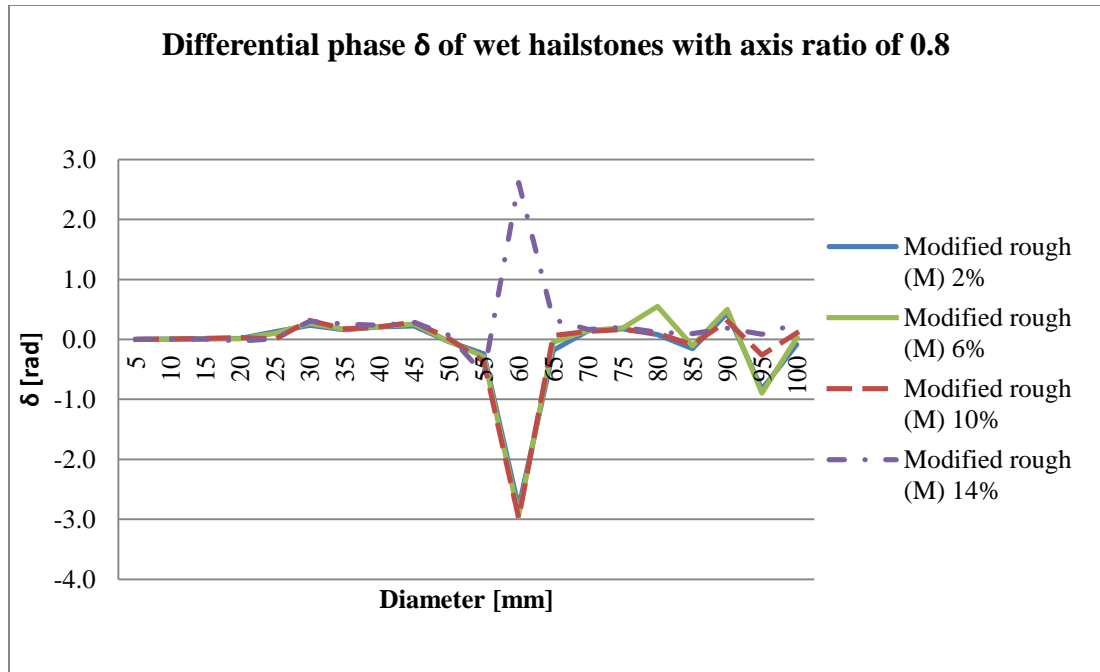


Figure 8.46 - Backscatter differential phase (δ) for wet hailstones with axis ratio of 0.8 and M-type roughness of 2% (solid blue), 6% (solid green), 10% (dashed red) and 14% (dot-dashed violet).

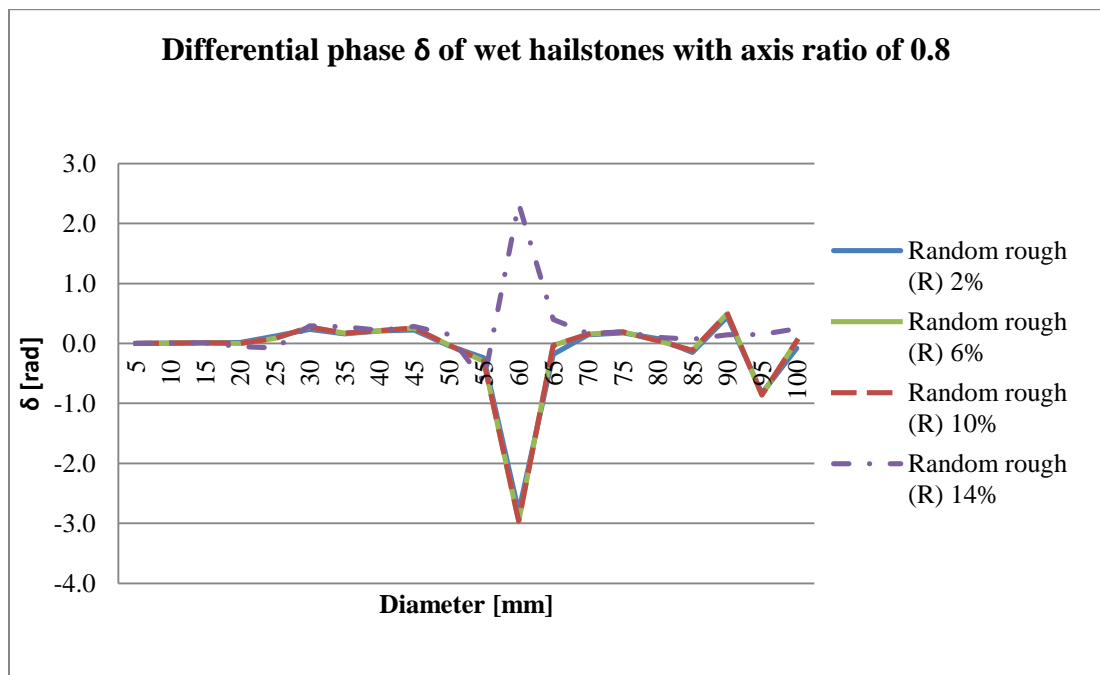


Figure 8.47 - Backscatter differential phase (δ) for wet hailstones with axis ratio of 0.8 and R-type roughness of 2% (solid blue), 6% (solid green), 10% (dashed red) and 14% (dot-dashed violet).

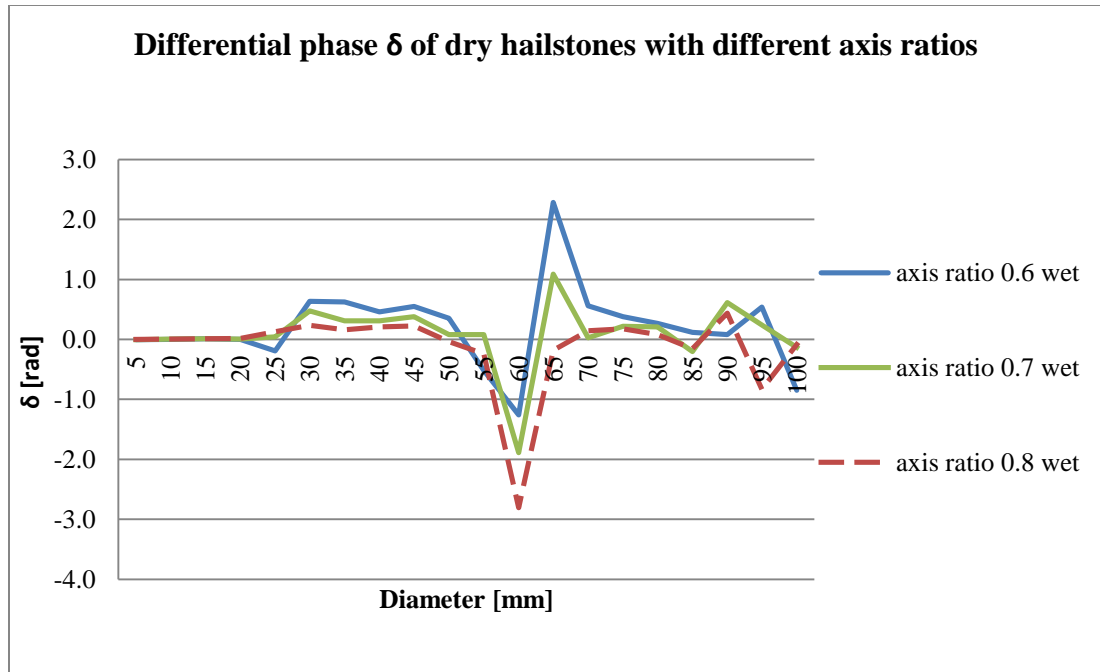


Figure 8.48 - Backscatter differential phase (δ) for wet hailstones having the 2% M-type roughness and axis ratio of 0.6(solid blue), 0.7 (solid green), 0.8 (dashed red).

Linear Depolarization Ratio

The linear depolarization ratio is the first among synthesized polarimetric variables that is not offered as a product from the operational WSR-88D network. Incapability to measure L_{DR} is intrinsic as the L_{DR} is a measure of the depolarization caused by the scattering volume, which for the WSR-88D network using simultaneous H and V mode is added to the orthogonal polarization return. Main factors causing depolarization in hydrometeor scattering are related to either orientation (canting) properties of hydrometeors, or irregularity of scatterer shapes.

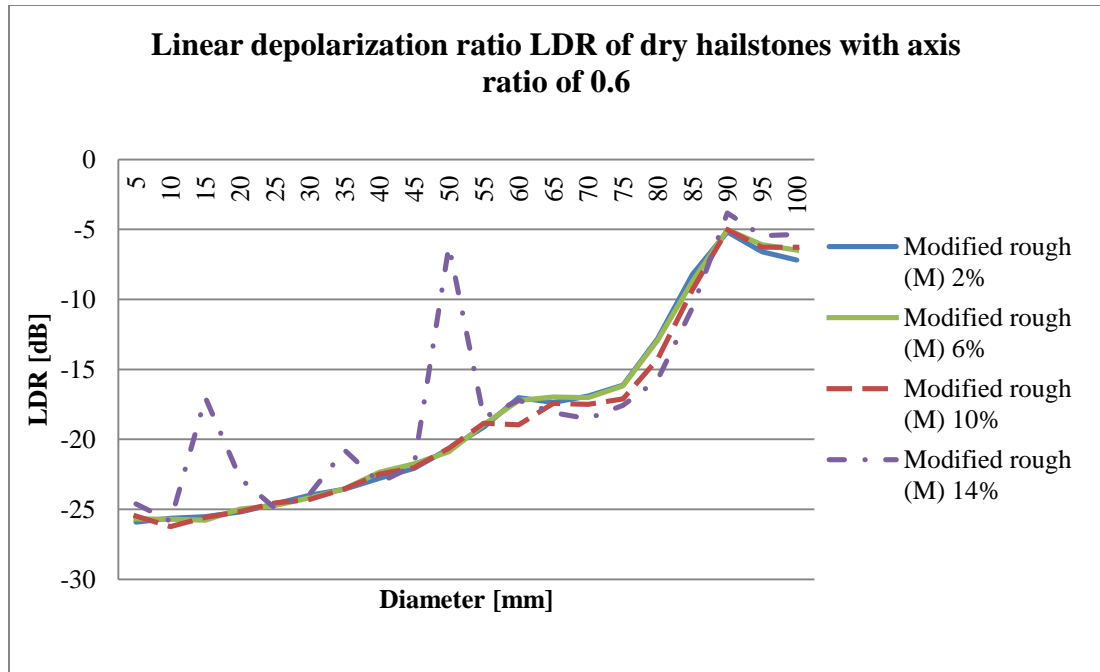


Figure 8.49 - Linear depolarization ratio (LDR) for dry hailstones with axis ratio of 0.6 and M-type roughness of 2% (solid blue), 6% (solid green), 10% (dashed red) and 14% (dot-dashed violet).

Expected behavior of the L_{DR} value is generally related to the size and roughness of scatterers in the scattering volume as well as their shape and dielectric permittivity. This is illustrated in Figs. 8.49 and 8.50 for hailstones with axis ratio of 0.6 for four different roughness values.

Increases of the L_{DR} in cases other than giant hailstones of wavelength sizes are clearly due to the high roughness of smaller hydrometeors (14%) which cause jumps in L_{DR} values at frequencies where other variables, experienced micro resonant behavior.

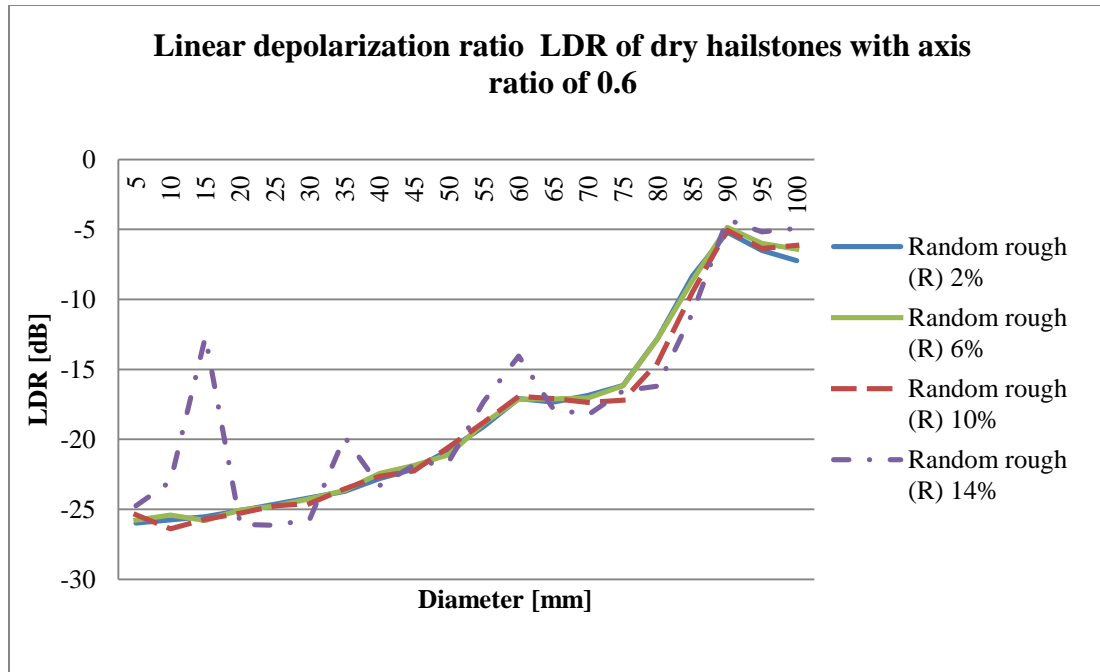


Figure 8.50 - Linear depolarization ratio (LDR) for dry hailstones with axis ratio of 0.6 and R-type roughness of 2% (solid blue), 6% (solid green), 10% (dashed red) and 14% (dot-dashed violet).

For hailstones with slightly higher axis ratio (0.7), L_{DR} is plotted in Figs. 8.51 and 8.52. Behavior of L_{DR} is quite independent of the roughness values, except for very high values (10% and 14%) where it introduces changes at resonant sizes (55-60 mm and 80-100 mm) dependent on the roughness type.

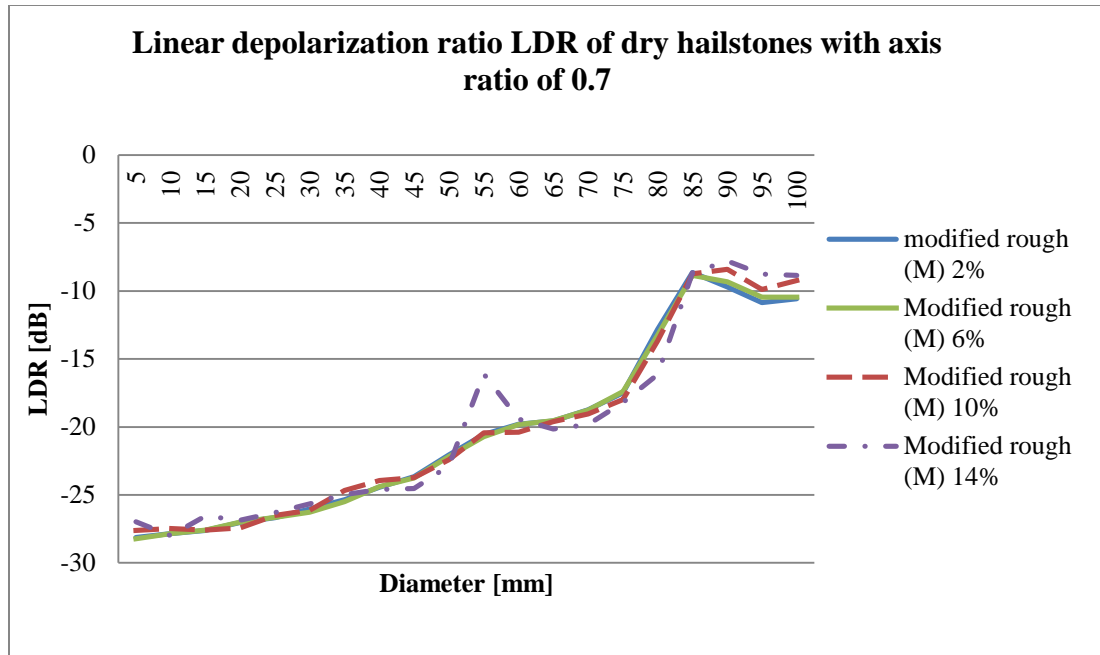


Figure 8.51 - Linear depolarization ratio (LDR) for dry hailstones with axis ratio of 0.7 and M-type roughness of 2% (solid blue), 6% (solid green), 10% (dashed red) and 14% (dot-dashed violet).

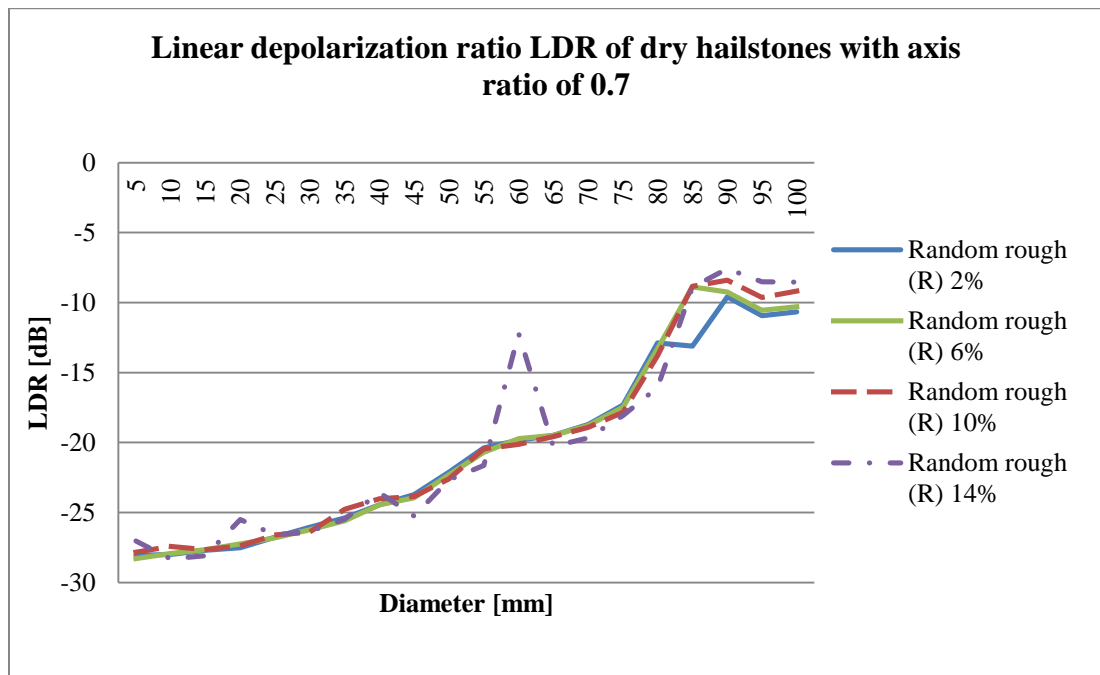


Figure 8.52 - Linear depolarization ratio (LDR) for dry hailstones with axis ratio of 0.7 and R-type roughness of 2% (solid blue), 6% (solid green), 10% (dashed red) and 14% (dot-dashed violet).

For hailstones of the highest sphericity (0.8 axis ratio) the L_{DR} is plotted in Figs. 8.53 and 8.54. Its behavior is similar to behavior of previously presented ones with the exception of the values.

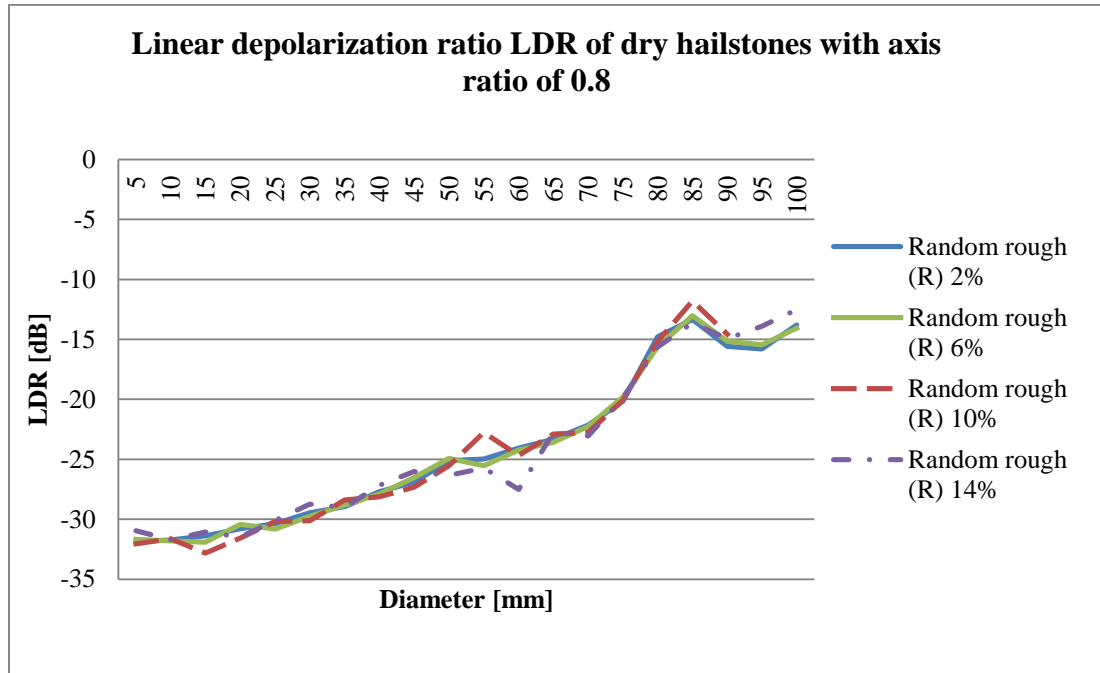


Figure 8.53 - Linear depolarization ratio (LDR) for dry hailstones with axis ratio of 0.8 and M-type roughness of 2% (solid blue), 6% (solid green), 10% (dashed red) and 14% (dot-dashed violet).

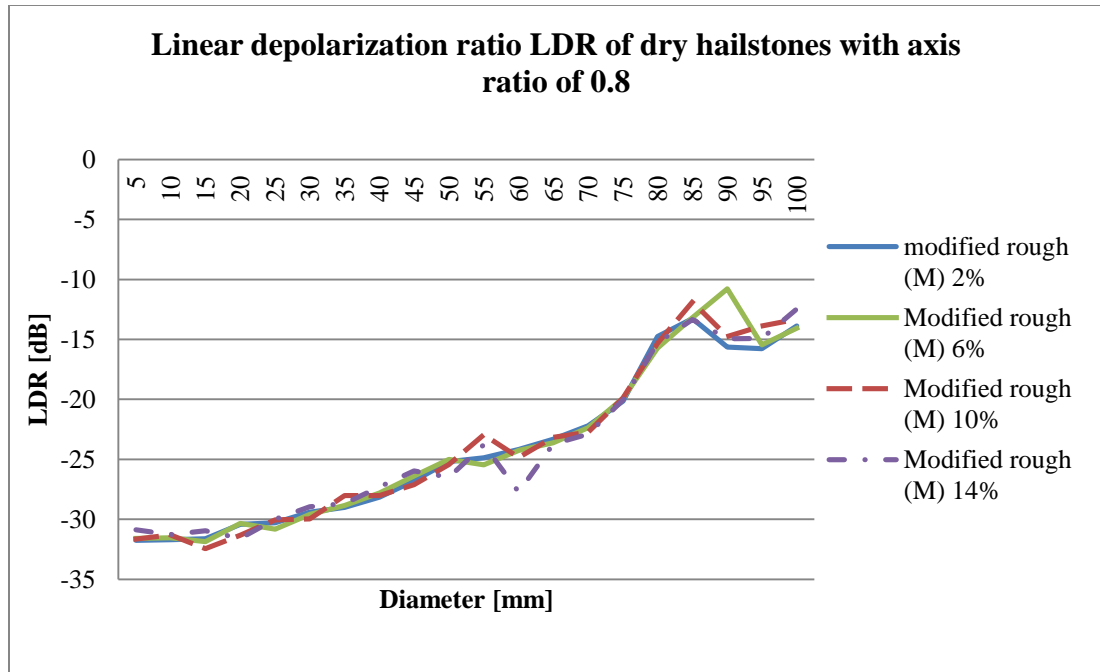


Figure 8.54 - Linear depolarization ratio (LDR) for dry hailstones with axis ratio of 0.8 and R-type roughness of 2% (solid blue), 6% (solid green), 10% (dashed red) and 14% (dot-dashed violet).

Sphericity of hailstones plays very important role in governing the L_{DR} value. Spherical scatterers do not cause any depolarization (cross-polar scattering) and for the same reasons it is expected that with the increase of sphericity L_{DR} values lower (Fig. 8.55). Additionally, positions of resonant jumps are shifted for the presented hailstones as the volume of particles having same (physical) diameter and axis ratios is not the same.

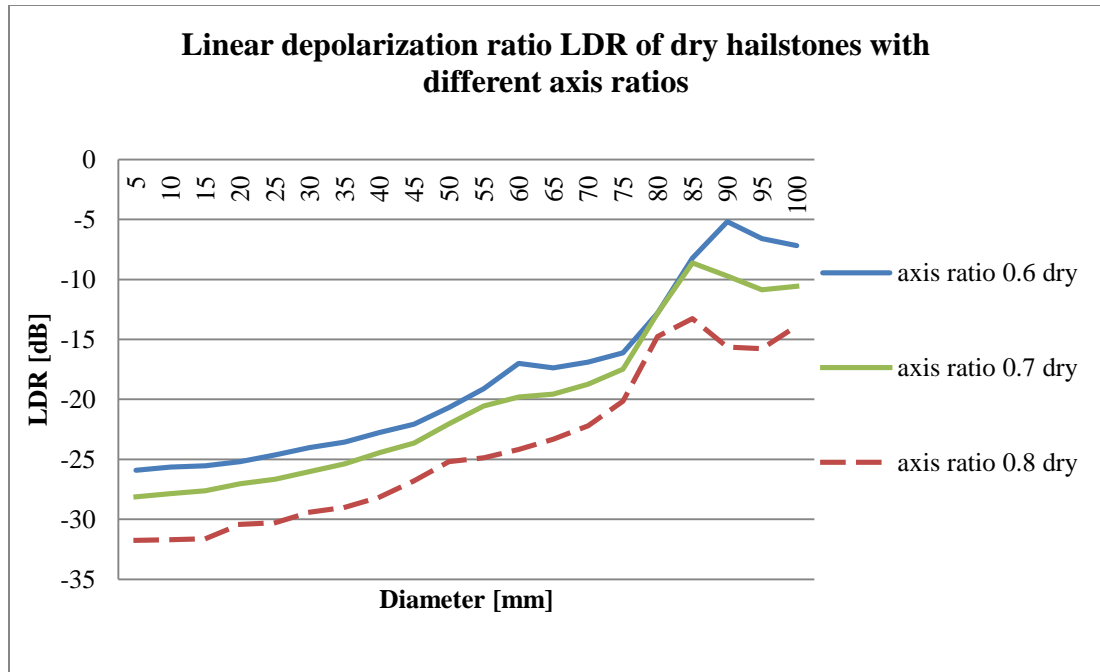


Figure 8.55 - Linear depolarization ratio (LDR) for dry hailstones having the 2% M-type roughness and axis ratio of 0.6 (solid blue), 0.7 (solid green), 0.8 (dashed red).

Water coating increases the backscattered returns and changes resonant behavior of hailstones. It causes significant increase in the linear depolarization ratio as the calculated results present.

The first considered are hailstones with 0.6 axis ratio (Figs. 8.56 and 8.57). The linear depolarization ratio for wet hailstones experiences dependence on the roughness value. These effects are pronounced around resonant regimes (50-60 mm) where roughness causes double the width of the high L_{DR} region. Besides increasing the width of the region slope of the L_{DR} value on the back edge of the resonant regime is less steep for high roughness values.

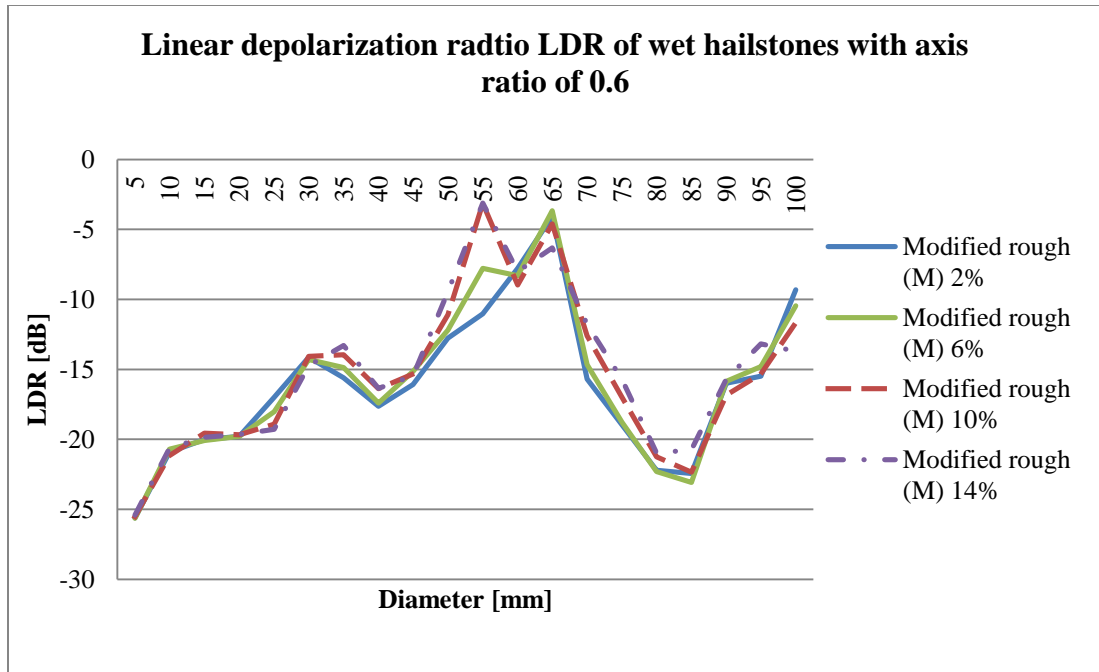


Figure 8.56 - Linear depolarization ratio (LDR) for wet hailstones with axis ratio of 0.6 and M-type roughness of 2% (solid blue), 6% (solid green), 10% (dashed red) and 14% (dot-dashed violet).

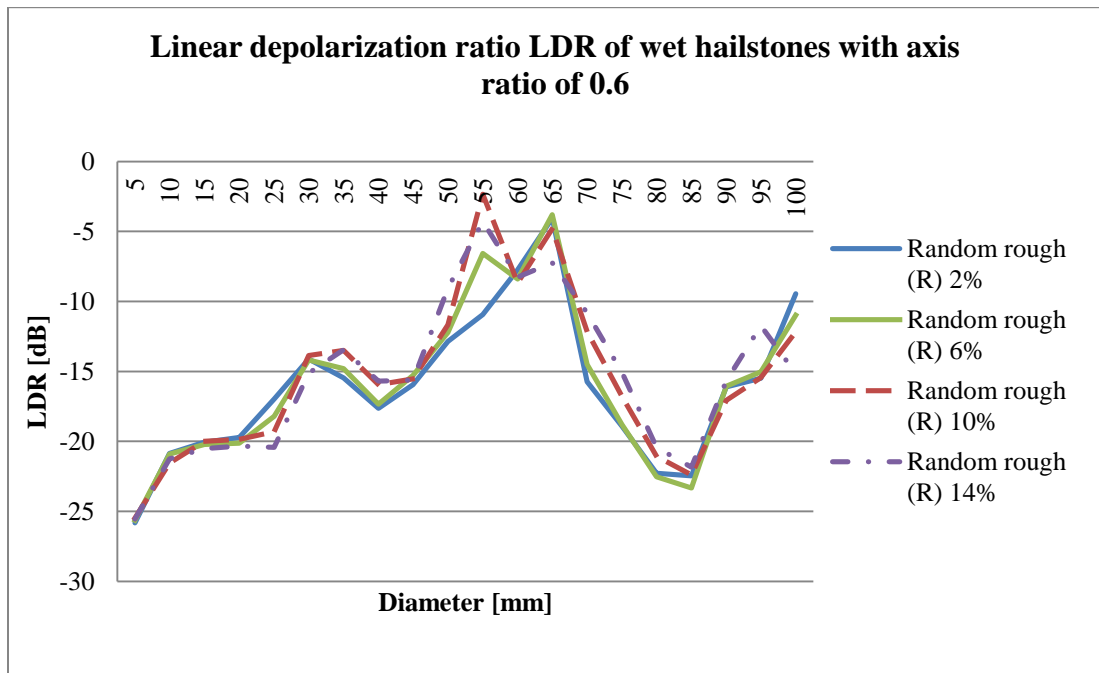


Figure 8.57 - Linear depolarization ratio (LDR) for wet hailstones with axis ratio of 0.6 and R-type roughness of 2% (solid blue), 6% (solid green), 10% (dashed red) and 14% (dot-dashed violet).

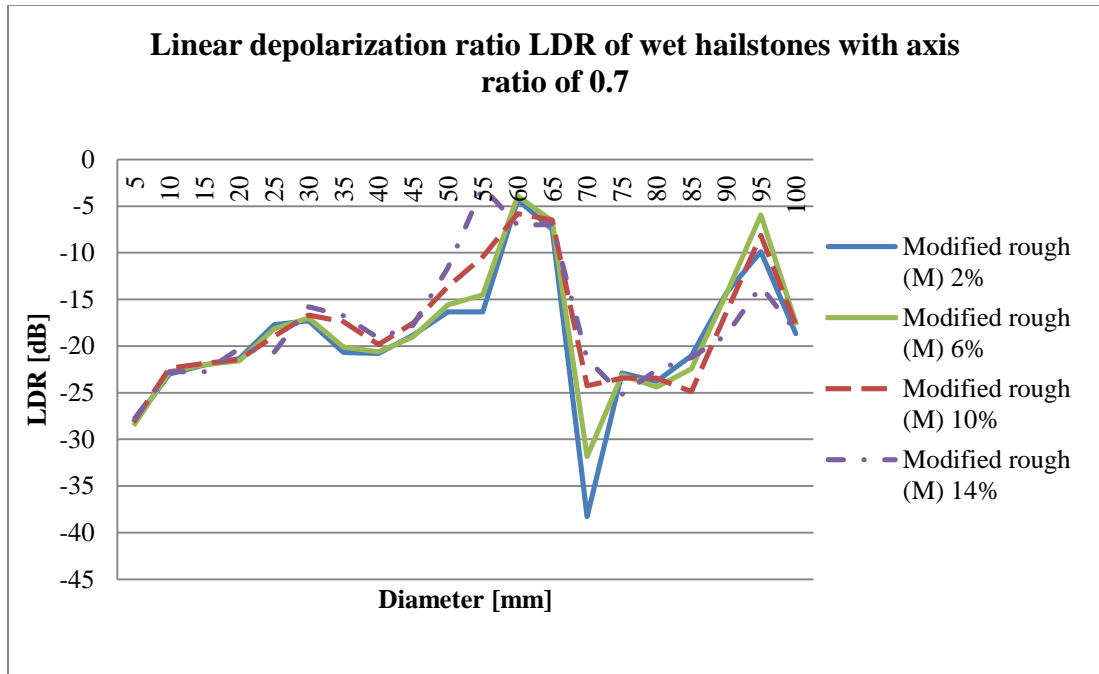


Figure 8.58 - Linear depolarization ratio (LDR) for wet hailstones with axis ratio of 0.7 and M-type roughness of 2% (solid blue), 6% (solid green), 10% (dashed red) and 14% (dot-dashed violet).

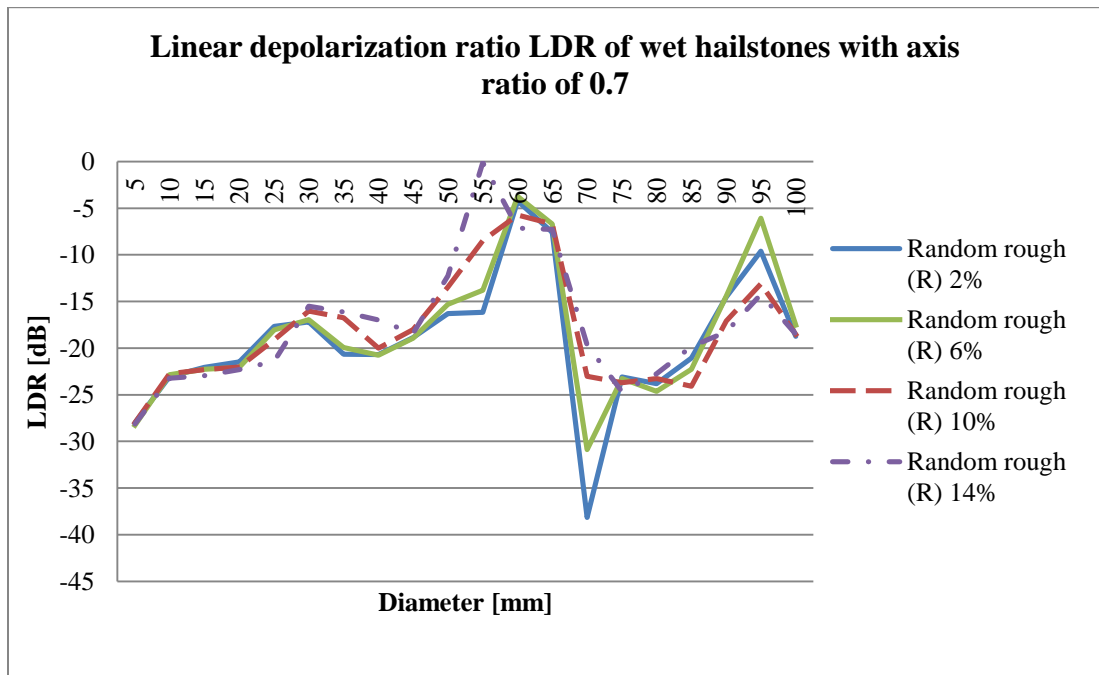


Figure 8.59 - Linear depolarization ratio (LDR) for wet hailstones with axis ratio of 0.7 and R-type roughness of 2% (solid blue), 6% (solid green), 10% (dashed red) and 14% (dot-dashed violet).

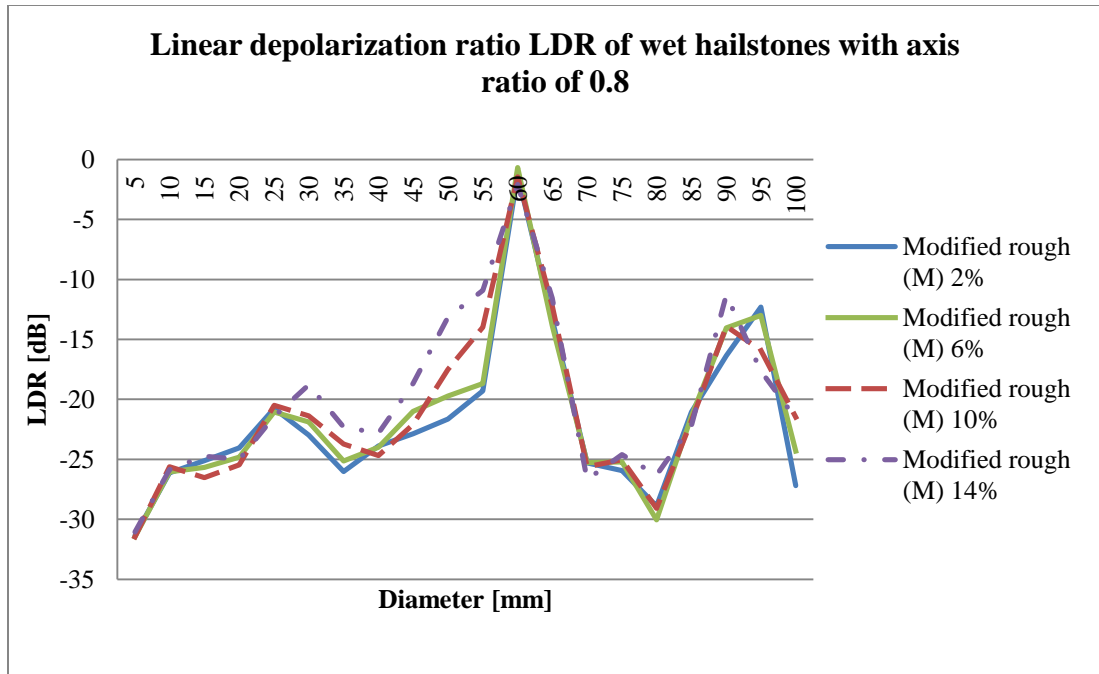


Figure 8.60- Linear depolarization ratio (LDR) for wet hailstones with axis ratio of 0.8 and M-type roughness of 2% (solid blue), 6% (solid green), 10% (dashed red) and 14% (dot-dashed violet).

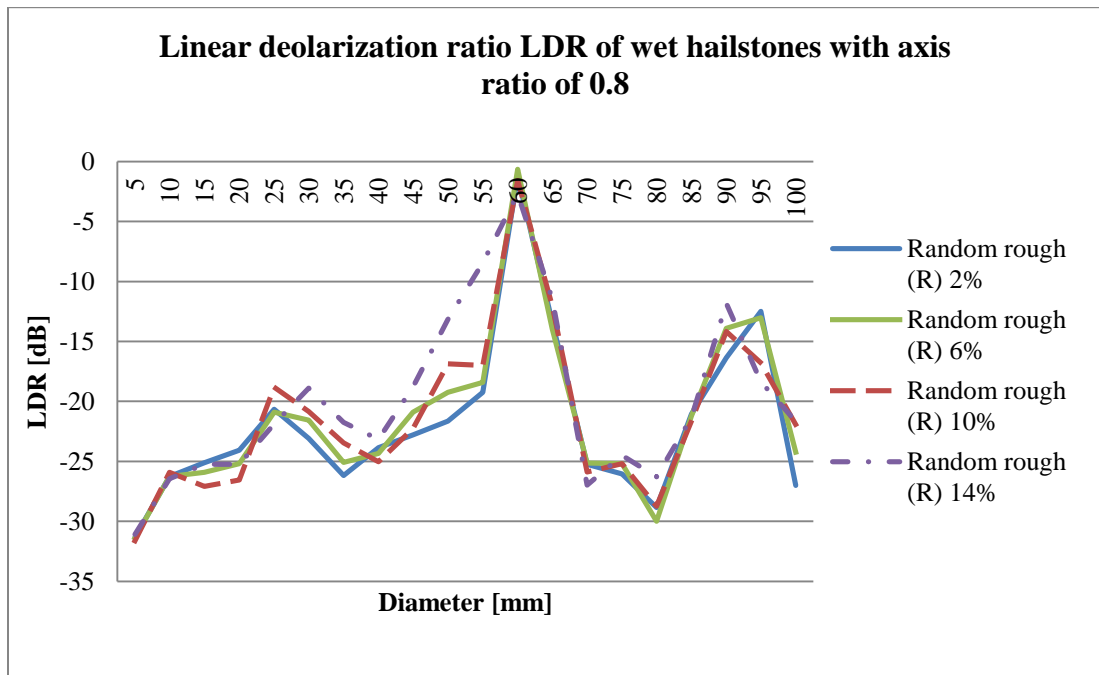


Figure 8.61 - Linear depolarization ratio (LDR) for wet hailstones with axis ratio of 0.8 and R-type roughness of 2% (solid blue), 6% (solid green), 10% (dashed red) and 14% (dot-dashed violet).

Dependence of the linear depolarization value due to the axis ratio is illustrated in Fig. 8.62. With the increase of the sphericity L_{DR} mean value is decreased, yet the maximum of the L_{DR} stays approximately constant at resonant sizes. In Fig. 8.62 this may not be best illustrated as the hailstone size modeling step of 5 mm omits the absolute maximum for 0.6 axis ratio hailstones. Nevertheless overall behavior of L_{DR} is well presented even with this coarse step size.

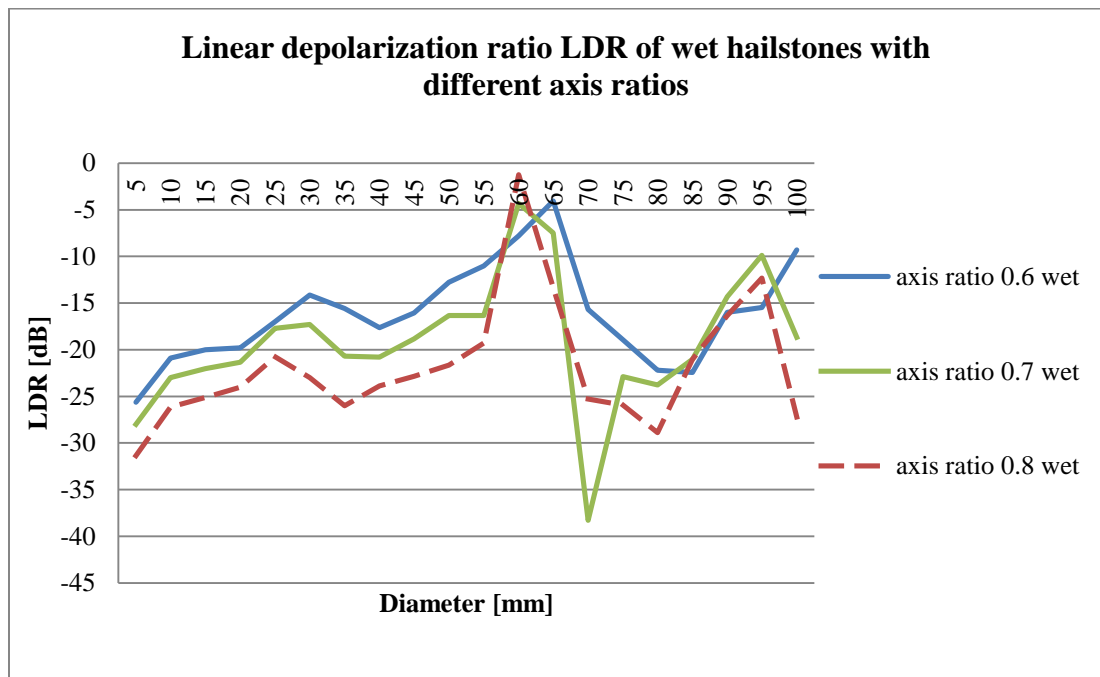


Figure 8.62 - Linear depolarization ratio (LDR) for wet hailstones having the 2% M-type roughness and axis ratio of 0.6(solid blue), 0.7 (solid green), 0.8 (dashed red).

Circular Depolarization Ratio

Values of CDR calculated for monodisperse size distribution of different hailstone types may be used for evaluation of Ryzhkov's claims (Ryzhkov, et al., 2014). Circular depolarization of dry hailstones with 0.6 axis ratio with respect to roughness values and types are illustrated in figures 8.63 and 8.64.

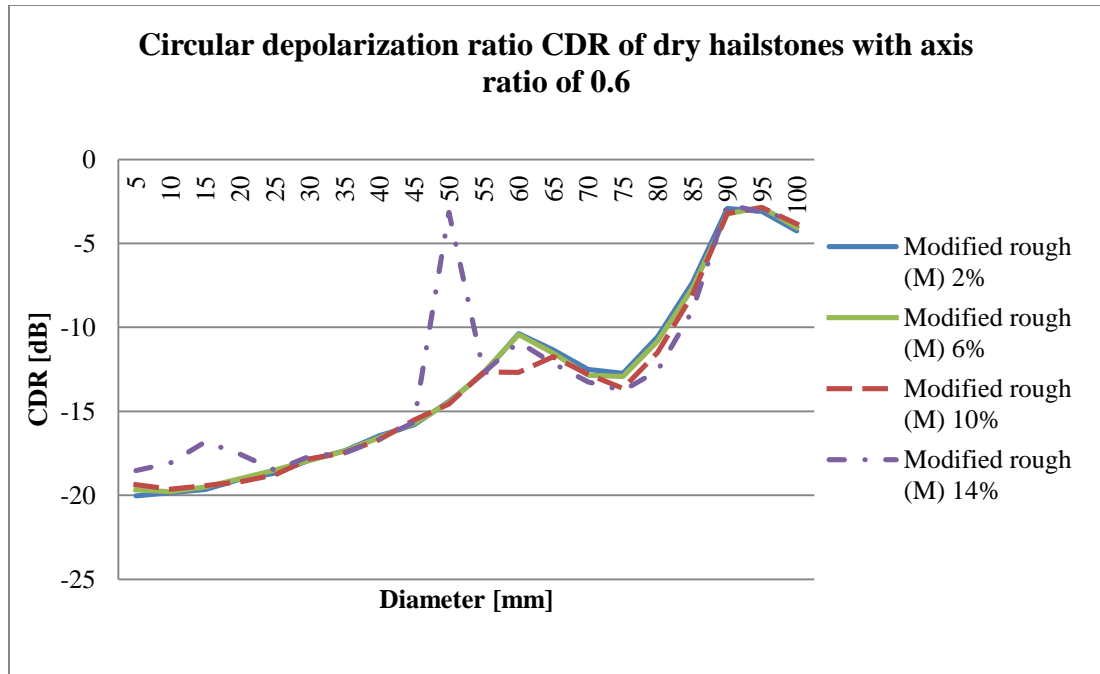


Figure 8.63 - Circular depolarization ratio (CDR) for dry hailstones with axis ratio of 0.6 and M-type roughness of 2% (solid blue), 6% (solid green), 10% (dashed red) and 14% (dot-dashed violet).

At the first glance it is obvious that CDR for dry hailstones follows monotonic growth directly proportional with the hailstone size. Monotonic increase of the CDR with size may be considered as a proof of claims by Ryzhkov providing relation between the hailstone sizes and the particular CDR value.

On the other hand, effects of the roughness value to the CDR are mainly obvious at micro resonant and resonant and resonant sizes where an abrupt increase of CDR value is correlated with changes of the backscatter differential phase.

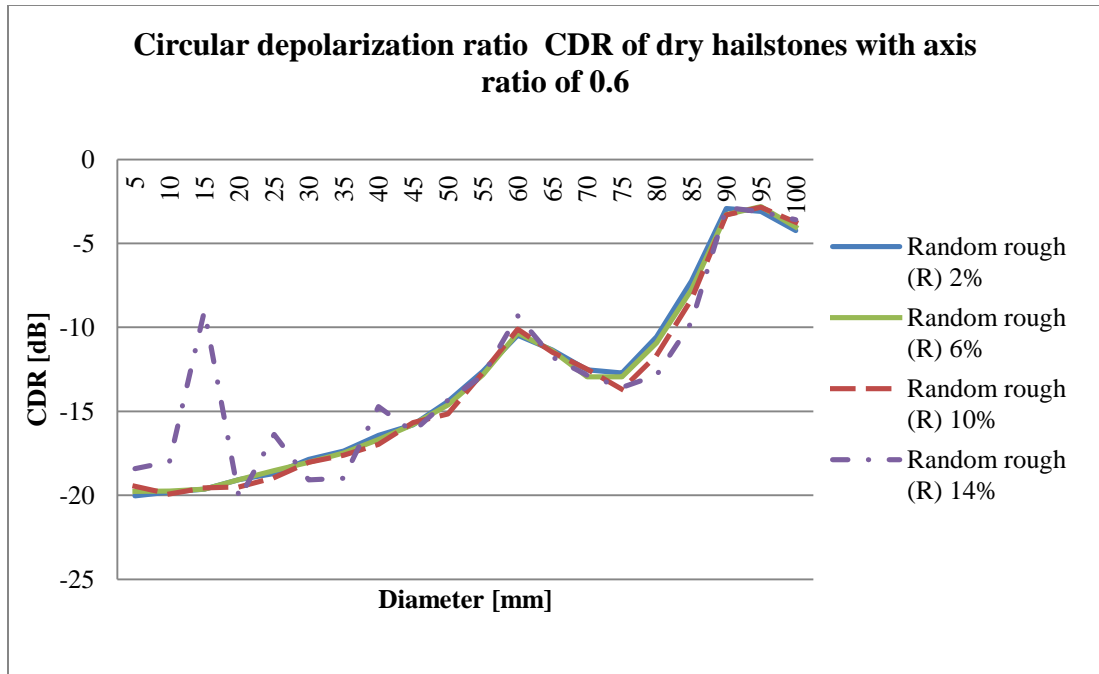


Figure 8.64 - Circular depolarization ratio (CDR) for dry hailstones with axis ratio of 0.6 and R-type roughness of 2% (solid blue), 6% (solid green), 10% (dashed red) and 14% (dot-dashed violet).

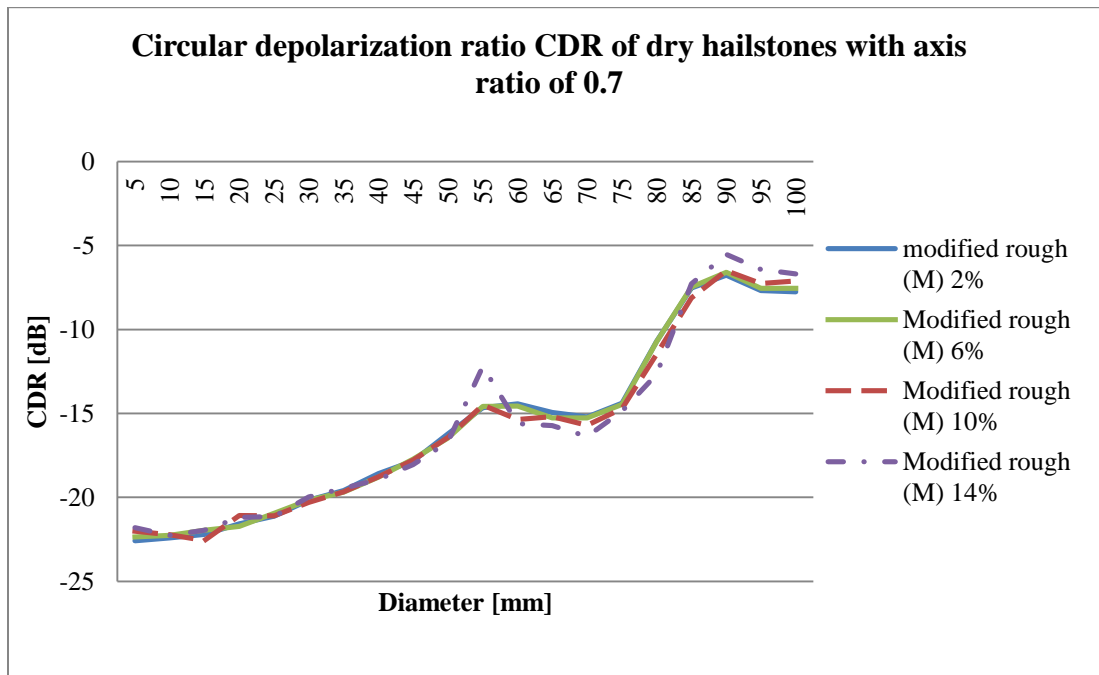


Figure 8.65 - Circular depolarization ratio (CDR) for dry hailstones with axis ratio of 0.7 and M-type roughness of 2% (solid blue), 6% (solid green), 10% (dashed red) and 14% (dot-dashed violet).

Similarly to the CDR behavior for 0.6 axis ratio hailstones circular depolarization is experiencing monotonic growth with minimal effects of roughness value except in resonant sizes.

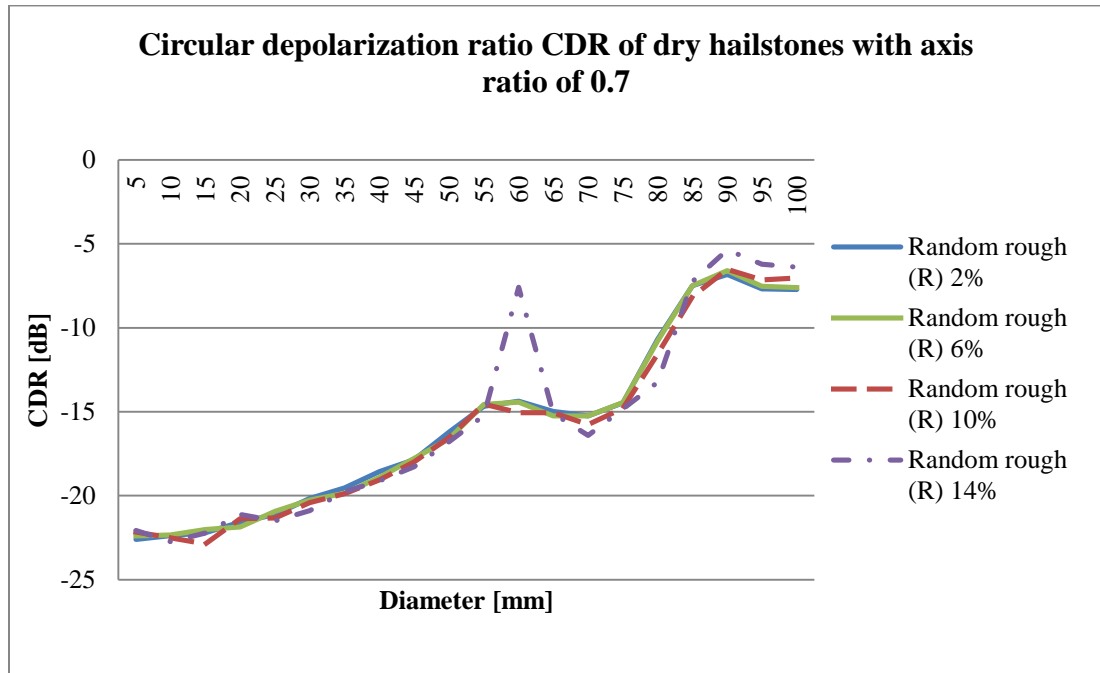


Figure 8.66 - Circular depolarization ratio (CDR) for dry hailstones with axis ratio of 0.7 and R-type roughness of 2% (solid blue), 6% (solid green), 10% (dashed red) and 14% (dot-dashed violet).

Finally, CDR is evaluated for 0.8 axis ratio hailstones and presented in Figs. 8.67 and 8.68. As it was the case with 0.6 and 0.7 axis ratio hailstones behavior of CDR is monotonic with minimal effects due to the size resonances.

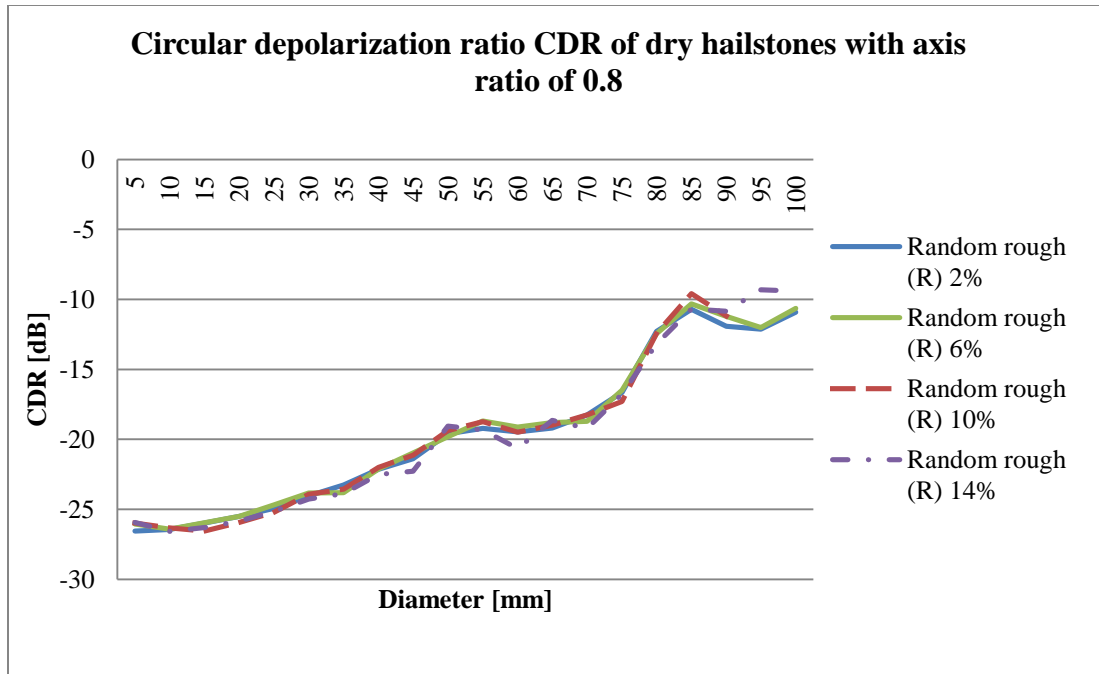


Figure 8.67 - Circular depolarization ratio (CDR) for dry hailstones with axis ratio of 0.8 and M-type roughness of 2% (solid blue), 6% (solid green), 10% (dashed red) and 14% (dot-dashed violet).

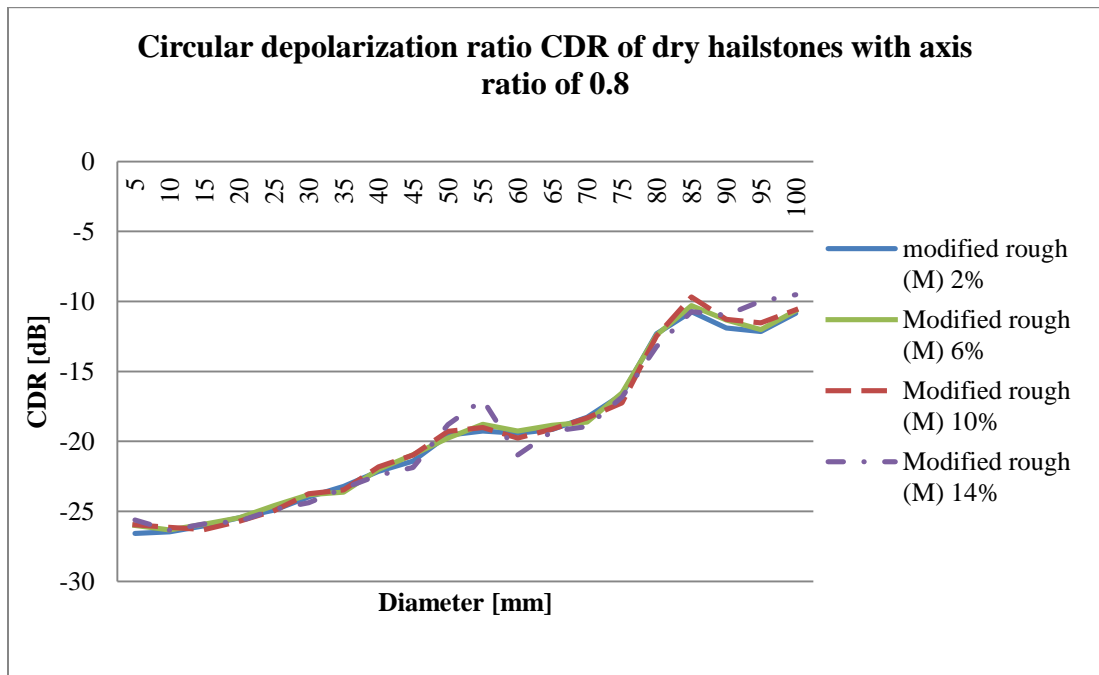


Figure 8.68 - Circular depolarization ratio (CDR) for dry hailstones with axis ratio of 0.8 and R-type roughness of 2% (solid blue), 6% (solid green), 10% (dashed red) and 14% (dot-dashed violet).

Comparison of CDR values for hailstones having minimal M type roughness are in Fig. 8.69. Significance of the comparison is in the quantification of CDR values for different axis ratio hailstones. Figure 8.69 provides important correlation of size to CDR value to be taken into account is one is to work on the quantification of hailstone sizes. From the figure it is immediately obvious that another polarimetric variable is required to help differentiate the actual size as same CDR values are obtained for different hailstone sizes depending on the different axis ratios.

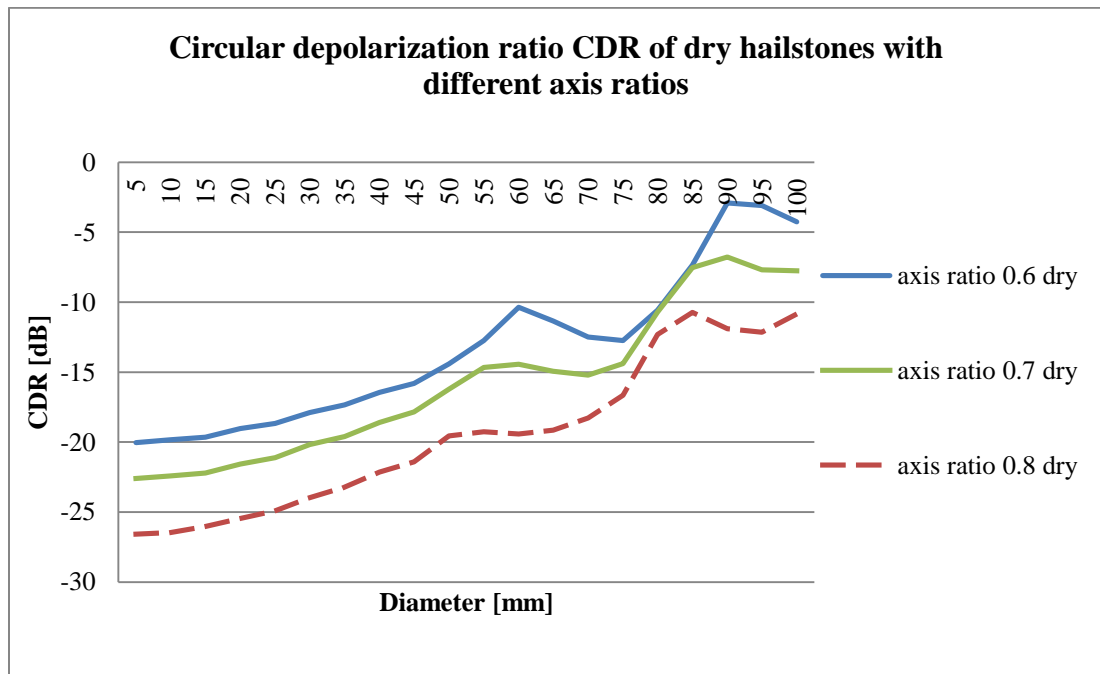


Figure 8.69 - Circular depolarization ratio (CDR) for dry hailstones having the 2% M-type roughness and axis ratio of 0.6 (solid blue), 0.7 (solid green), 0.8 (dashed red).

Water coated, (wet) hailstones are considered in the following portion of this section. Scattering properties off of these higher dielectric permittivity particles are generally more complex, which is depicted by all polarimetric variables so far. In the case of CDR of particularly interesting is the effect of scattering where differential phase

experiences large values. Contrarily to the linear depolarization ratio (L_{DR}) which for all isotropic media has to remain negative (in logarithmic scale), CDR may experience positive (in logarithmic scale) value if the differential phase shift is high. Such behavior is tied with the fact that opposite circularity (polarization) of the backscattered field is achieved if one of the two electric field vectors has shifted phase for 180 degrees.

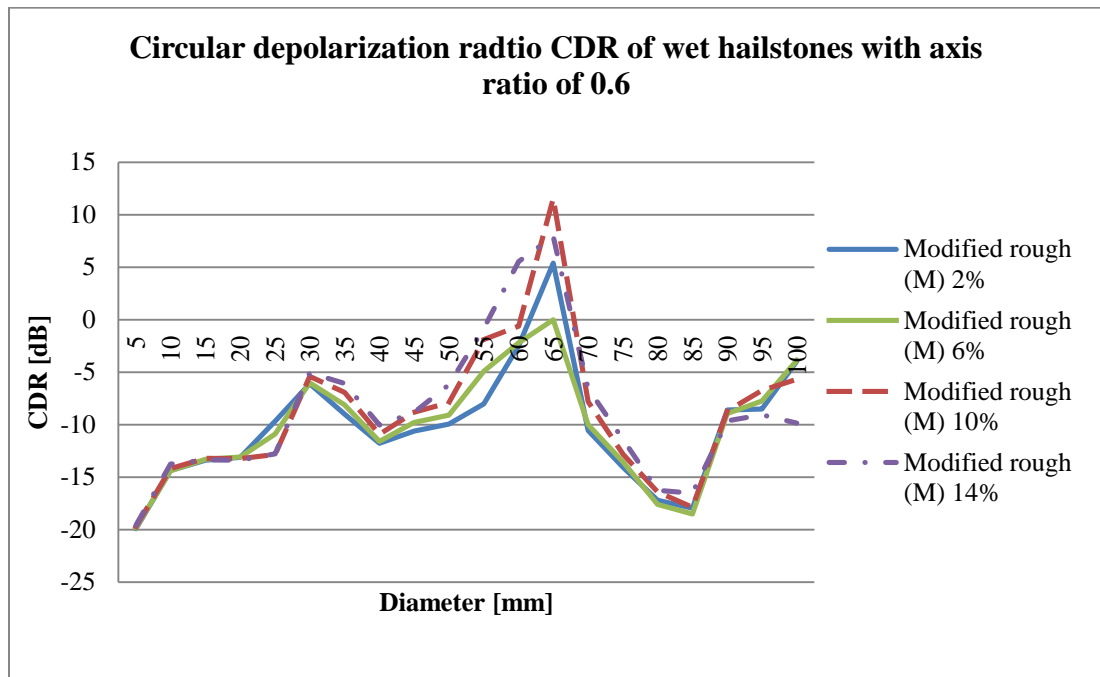


Figure 8.70 - Circular depolarization ratio (CDR) for wet hailstones with axis ratio of 0.6 and M-type roughness of 2% (solid blue), 6% (solid green), 10% (dashed red) and 14% (dot-dashed violet).

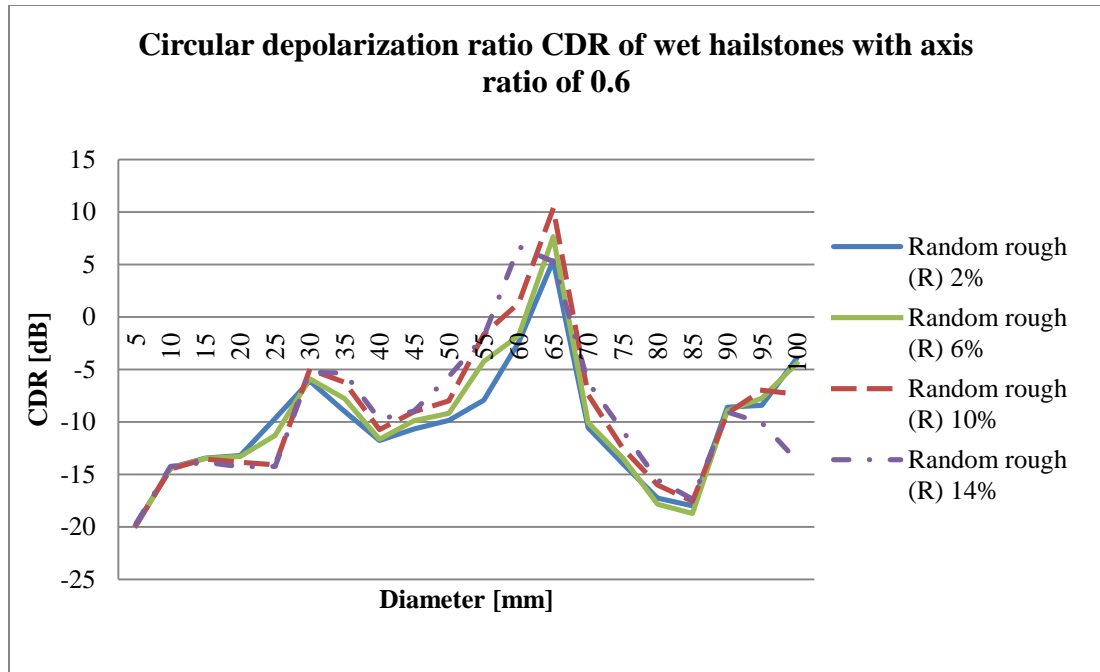


Figure 8.71 - Circular depolarization ratio (CDR) for wet hailstones with axis ratio of 0.6 and R-type roughness of 2% (solid blue), 6% (solid green), 10% (dashed red) and 14% (dot-dashed violet).

The effect of roughness values to polarimetric variables it evident in the width of resonant region, which is directly proportional to the roughness value. Values of local maxima are more pronounced with increase of the roughness value.

For the 0.7 axis ratio hailstones CDR values are plotted in Figs. 8.72 and 8.73. Similarly to the 0.6 axis ratio hailstones, effects observed in these figures are explained using same reasoning.

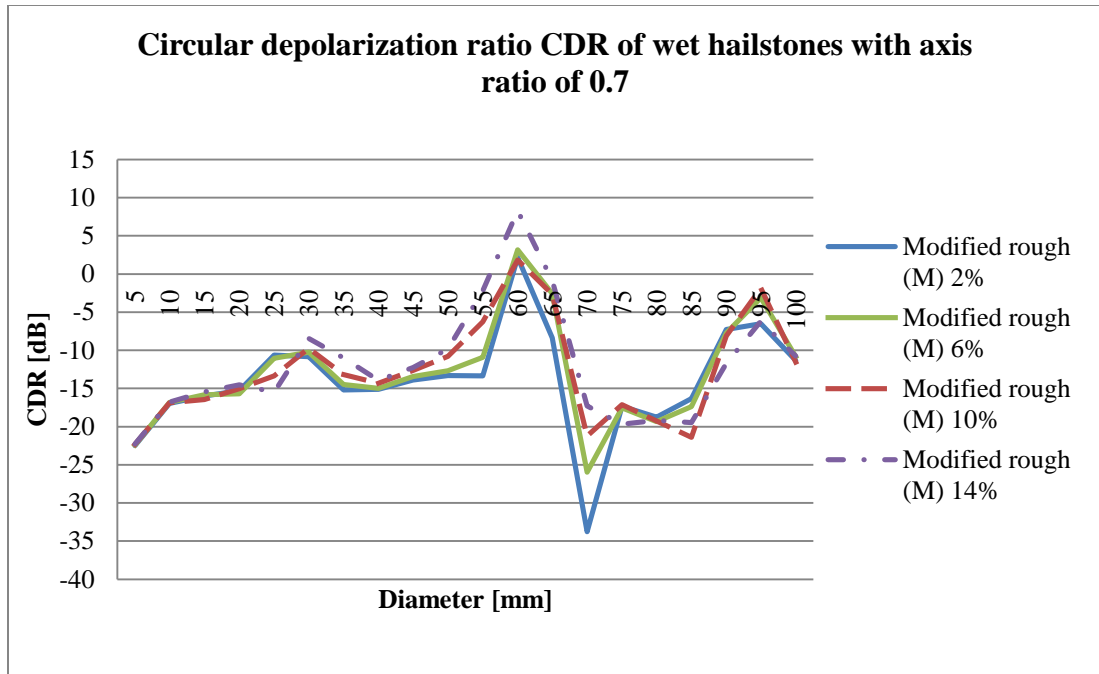


Figure 8.72 - Circular depolarization ratio (CDR) for wet hailstones with axis ratio of 0.7 and M-type roughness of 2% (solid blue), 6% (solid green), 10% (dashed red) and 14% (dot-dashed violet).

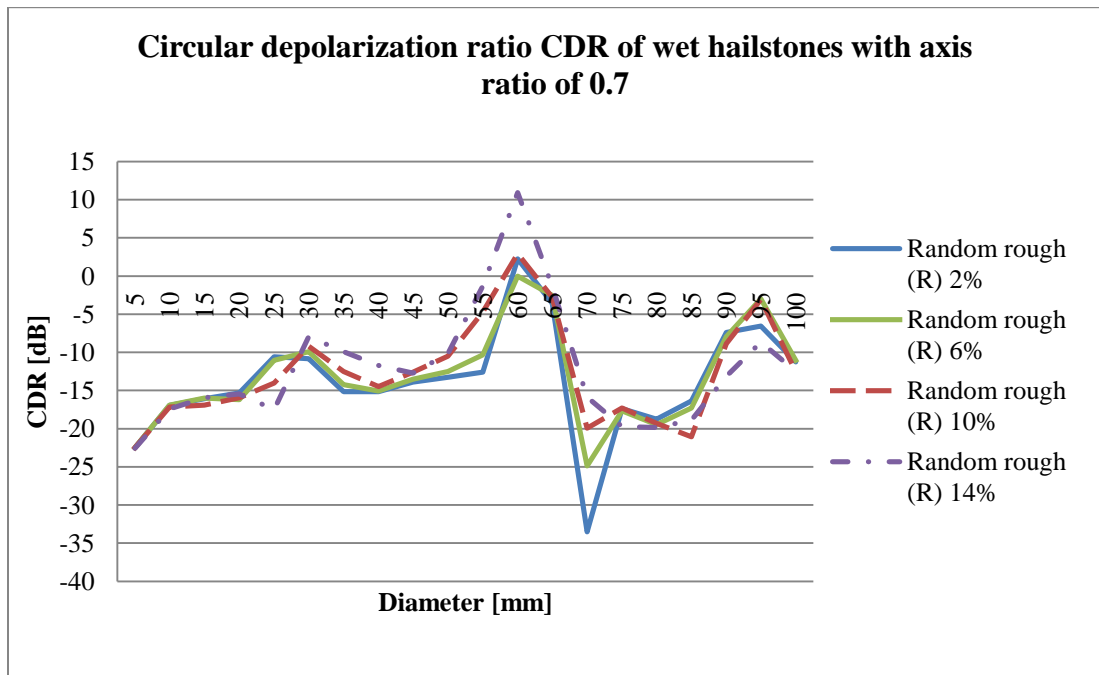


Figure 8.73 - Circular depolarization ratio (CDR) for wet hailstones with axis ratio of 0.7 and R-type roughness of 2% (solid blue), 6% (solid green), 10% (dashed red) and 14% (dot-dashed violet).

While for the 0.6 and 0.7 axis ratio hailstones CDR dynamic range was about 25dB in the case of 0.8 axis ratio hailstones (Figs. 8.74 and 8.75) is close to 30dB. Circular depolarization ratio signature of 0.8 axis ratio hailstones is distinctive for its low CDR values outside of resonances and narrow peaks at resonant values. All of which are caused by same physical mechanisms as discussed above.

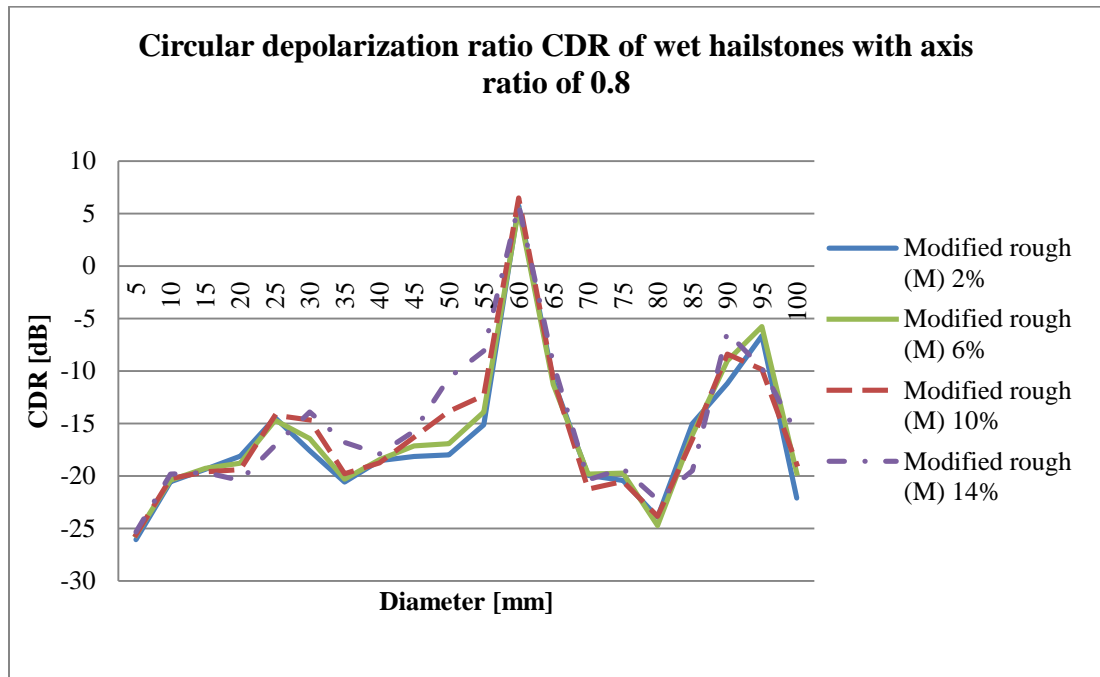


Figure 8.74 - Circular depolarization ratio (CDR) for wet hailstones with axis ratio of 0.8 and M-type roughness of 2% (solid blue), 6% (solid green), 10% (dashed red) and 14% (dot-dashed violet).

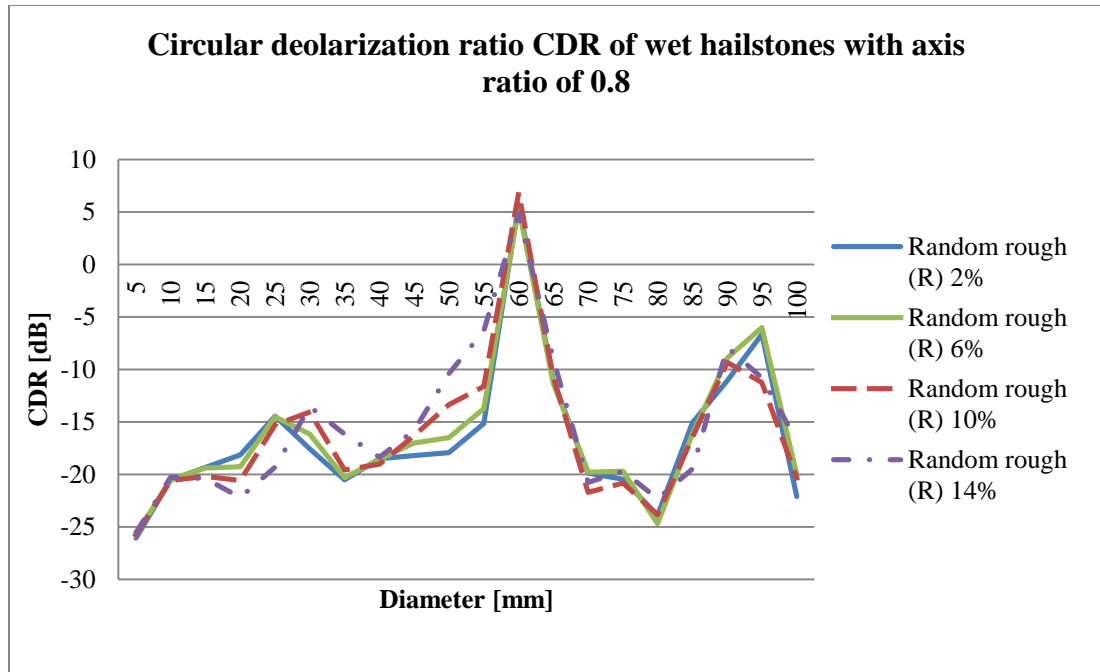


Figure 8.75 - Circular depolarization ratio (CDR) for wet hailstones with axis ratio of 0.8 and R-type roughness of 2% (solid blue), 6% (solid green), 10% (dashed red) and 14% (dot-dashed violet).

Comparison of CDR signatures for different axis ratios is plotted in figure 8.76. Except for the expected decrease of the CDR value due to higher sphericity of the hailstones no additional effects are noticeable. From the Fig. 8.76 it is clear that the global maximum of the CDR for 0.6 axis ratio hailstone is positioned at slightly larger diameter which is in-between calculated points, yet no significance for the particular graph exists in the exact position of the resonance peak.

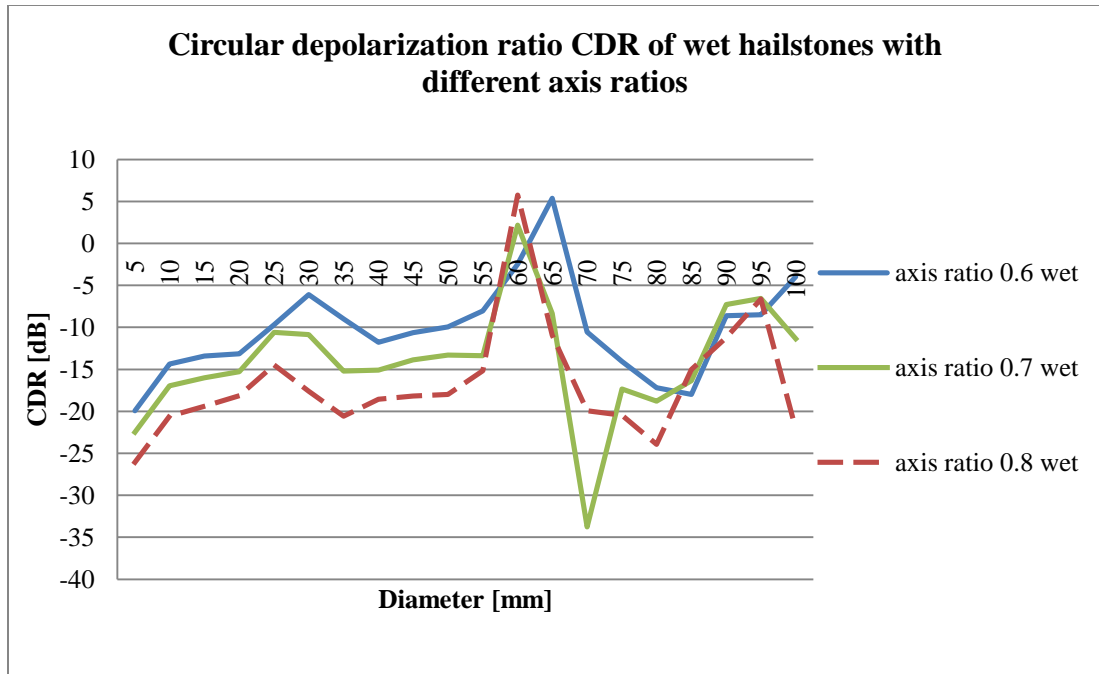


Figure 8.76 - Circular depolarization ratio (CDR) for dry hailstones having the 2% M-type roughness and axis ratio of 0.6 (solid blue), 0.7 (solid green), 0.8 (dashed red).